



HAL
open science

Transport processes in solar-type stars

Thibaut Dumont

► **To cite this version:**

Thibaut Dumont. Transport processes in solar-type stars. Solar and Stellar Astrophysics [astro-ph.SR]. Université Montpellier; Université de Genève (Genève, Suisse). Faculté des sciences, 2021. English. NNT : 2021MONT041 . tel-03441541

HAL Id: tel-03441541

<https://theses.hal.science/tel-03441541>

Submitted on 22 Nov 2021

HAL is a multi-disciplinary open access archive for the deposit and dissemination of scientific research documents, whether they are published or not. The documents may come from teaching and research institutions in France or abroad, or from public or private research centers.

L'archive ouverte pluridisciplinaire **HAL**, est destinée au dépôt et à la diffusion de documents scientifiques de niveau recherche, publiés ou non, émanant des établissements d'enseignement et de recherche français ou étrangers, des laboratoires publics ou privés.

THÈSE POUR OBTENIR LE GRADE DE DOCTEUR DE L'UNIVERSITÉ DE MONTPELLIER

En Physique

École doctorale Information Structures Systèmes

Unité de recherche : Laboratoire Univers et Particules de Montpellier

En partenariat international avec l'Université de Genève, SUISSE

Transport processes in solar-type stars

Présentée par Thibaut DUMONT

Le 20 mai 2021

Sous la direction de Ana PALACIOS, Directrice de thèse
et Corinne CHARBONNEL, co-Directrice de thèse

Devant le jury composé de

Mme. Yveline LEBRETON, Professeure, Observatoire de Paris / Rennes

M. Rafael A. GARCIA, Ingénieur-chercheur, CEA Paris

M. Jose Dias do NASCIMENTO, Professeur, UFRN Natal Brésil / Cambridge E.U.

M. Patrick EGGENBERGER, Maître d'enseignement et de recherche, Université de Genève

M. Fabrice MARTINS, Directeur de Recherche CNRS, LUPM Montpellier

Mme Ana PALACIOS, Astronome, LUPM Montpellier

Mme Corinne CHARBONNEL, Professeure, Université de Genève

Présidente

Rapporteur

Rapporteur

Examineur

Examineur

Directrice de thèse

Directrice de thèse



UNIVERSITÉ
DE MONTPELLIER

UNIVERSITE DE GENEVE
FACULTE DES SCIENCES
Département d'astronomie
Professeure Corinne CHARBONNEL

UNIVERSITE DE MONTPELLIER
FACULTE DES SCIENCES
Laboratoire Univers et Particules
Professeure Ana PALACIOS

THESE DE DOCTORAT

présentée à la Faculté des sciences de l'Université de Genève
pour obtenir le grade de Docteur ès sciences,
mention Astronomie et Astrophysique
et
en co-tutelle à la Faculté des sciences de l'Université de Montpellier
pour obtenir le grade de Docteur ès sciences,
mention Physique

Transport processes in solar-type stars

par
Thibaut DUMONT
de Poitiers (France)

Thèse N°5575

GENEVE
Observatoire Astronomique de l'Université de Genève
2021



**UNIVERSITÉ
DE GENÈVE**

FACULTÉ DES SCIENCES

**DOCTORAT ÈS SCIENCES, MENTION ASTRONOMIE ET
ASTROPHYSIQUE**

Thèse de Monsieur Thibaut DUMONT

intitulée :

«Transport Processes in Solar-Type Stars»

La Faculté des sciences, sur le préavis de Madame C. CHARBONNEL, professeure ordinaire et directrice de thèse (Département d'astronomie), Madame A. PALACIOS, docteure et codirectrice de thèse (Laboratoire Univers et Particules de Montpellier Place Eugène Bataillon, Université Montpellier II, Montpellier, France), Monsieur J.D.D. NASCIMENTO, professeur (Harvard Smithsonian Center for Astrophysics, Cambridge, United States), Monsieur P. EGGENBERGER, maître d'enseignement et de recherche (Département d'astronomie), Monsieur R. A. GARCIA, ingénieur-chercheur (Département d'astrophysique, CEA Saclay, Gif-sur-Yvette, France), Madame Y. LEBRETON, professeure (Observatoire de Paris, site de Meudon, Meudon, France), Monsieur F. MARTINS, directeur de recherche (Laboratoire Univers et Particules de Montpellier, Montpellier, France), autorise l'impression de la présente thèse, sans exprimer d'opinion sur les propositions qui y sont énoncées.

Genève, le 20 mai 2021

Thèse - 5575 -

Le Doyen

N.B. - La thèse doit porter la déclaration précédente et remplir les conditions énumérées dans les "Informations relatives aux thèses de doctorat à l'Université de Genève".

Thesis Outline

Transport processes occurring in the radiative interior of solar-type stars and low-mass open cluster stars are evidenced by the surface variation of light elements, in particular lithium (Li), and the evolution of their rotation rates. For the Sun, inversions of helioseismic data indicate that the radial profile of angular velocity in its radiative zone is nearly uniform, which implies the existence of angular momentum transport mechanisms that are efficient over evolutionary timescales. While there are many independent transport models for angular momentum and chemical species, there is a lack of self-consistent theories that permit stellar evolution models to simultaneously match the present-day observations. The aim of the PhD thesis is to explore how additional transport processes can improve the agreement between evolutionary models and observations for Li depletion, the rotation evolution of open cluster stars, and the solar rotation profile.

Observations include data of solar-type stars and low-mass stars from F- to G- spectral type. Low-mass stars of Population I are characterised by an important Li-depletion during their evolution from the pre-main sequence to the age of the Sun, and rotation-induced mixing has been seen as an insufficient process to fully explained the observed Li depletion. In addition, a strong coupling between the surface and the internal layers of the stars is required to explain the observations on the rotation surface velocity evolution in solar-type stars and on the solar rotation profile inferred by helioseismology. At a larger range of stellar masses ($0.8 M_{\odot}$ to $1.5 M_{\odot}$), we observe for a few open clusters, like the Hyades, a Li-dip, that appears at about 6600 K, corresponding to F-type stars. And, finally, besides the Li-depletion with time, stars in the cold-side of the Li-dip also exhibit a Li-depletion with decreasing masses.

We explored several transport processes from the literature with stellar evolution code STAREVOL (Geneva-Montpellier) and we constrained the resulting models with observational data.

We first optimised the treatment of atomic diffusion through the implementation of a more recent formalism that we validated thanks to the comparison with others stellar evolution codes. Then, we determined the optimal input physics for our models, including an update of the solar abundance reference, and calibrated our models on the Sun. We explore different additional transport processes for chemicals and for angular momentum such as penetrative convection, tachocline mixing, additional turbulence, and additional viscosity.

In Dumont et al. (2021, A&A, 646, A48), we computed models of solar-type stars including both atomic diffusion and rotation-induced mixing in the framework of observational data of solar-like stars for lithium and angular velocity. The constraints from the depletion of lithium and from the angular velocity in open cluster stars, solar twins and the Sun highlight the need for additional dynamical processes to transport both chemicals and angular momentum. Indeed, in the framework of the shellular rotation hypothesis the rotational induced mixing depends mainly on the meridional circulation and on the choice for the prescription of the turbulence shear and cannot answer the issue alone without additional processes. We showed the key role of the pen-

etrative convection dependent of rotation to transport chemicals in the pre-main sequence and the early main sequence. We considered as well an additional vertical viscosity ν_{add} , fixed or dependent of the rotation, and adjusted with the magnetic braking efficiency. It leads to efficient transport of angular momentum between the core and the envelope during the main sequence evolution and to solar-type models that match the observed profile of the Sun. However, this approach leads to a weaker depletion of lithium in the main sequence due to a weaker turbulent shear that results from the effect of ν_{add} . The addition of a parametric turbulence at the base of the convective zone allows us **to achieve simultaneously the reproduction of both the Li depletion and the rotational evolution, and to determine an optimal model**. However, we noted that we miss a physical motivation for the additional viscosity and the parametric turbulence. For the latter, we studied the promising effect of tachocline turbulence. We determined self-consistently in STAREVOL the tachocline thickness and the diffusion coefficient due to tachocline turbulence. The obtained thickness is compatible with estimations from helioseismology at the age of the Sun, but the diffusion coefficient has been found to be not adapted to the lithium evolution until the age of the Sun.

In a second paper (Dumont et al. 2021, revised), we explored stars with a larger range of masses (0.8 to 1.5 M_{\odot}) and metallicities ($[\text{Fe}/\text{H}] = -0.4$ to $[\text{Fe}/\text{H}] = 0.15$). We used the optimal model from Dumont et al. (2021) including the chemical and angular momentum transport processes (namely, rotation, convective penetration, parametric turbulence, parametric viscosity, and atomic diffusion) that have been tested against Li abundances and internal rotation and surface constraints for solar-type stars, and we confronted them to Li, Be and P_{rot} data for F-type and G-type stars from open clusters of various ages and metallicities.

We have shown that the optimal model developed for the solar-type stars is able to reproduce the cold side of the Li and Be dips, as well as the observed rotation rates for each cluster, independently of age and metallicity. An effect of metallicity is highlighted and we predict a higher depletion at high metallicity than at low metallicity. However, our models are in poorer agreement with the metal-poor observational data, which are more depleted in Li than predicted and would argue for a metal-dependence of the transport processes. Over the entire range of masses, metallicities, and ages explored, we reproduce the evolution of the surface rotation rates, and predict for the first time the observed anticorrelation between surface rotation rate and Li-depletion as a consequence of the penetrative convection prescription. Besides, the model predicts internal rotation profiles in good agreement with asteroseismic constraints in main sequence stars. However, we cannot reproduce the Li-dip (and Be-dip) observed in some open clusters with the same model which yields a too weak Li depletion for $M > 1.2M_{\odot}$. The Li-dip can only be reproduced considering a different prescription for the shear turbulent mixing and a mass dependent parametric viscosity ν_{add} to transport angular momentum. It is thus mandatory to have a clear theoretical discrimination between the different prescriptions currently available to account for the turbulent shear transport. It also calls for a new exploration of physical processes such as tachocline mixing for the transport of chemicals and internal gravity waves for the transport of angular momentum. Finally, we highlight the key constraint of Beryllium, which also exhibits a dip, correlated with Li. It provides additional and complementary constraints for the missing transport processes involved. We show that with the few data available, it is presently challenging to reconcile simultaneously the Li-dip and the Be-dip. It highlights the need of additional data for the beryllium abundance in main sequence F- and G-type stars of different ages and metallicities.

Résumé

Les processus de transport dans les étoiles de type solaire

Contexte

Les processus de transport qui se produisent dans les intérieurs radiatifs des étoiles de type solaire et des étoiles de faible masse dans les amas ouverts sont mis en évidence par la variation de surface des éléments légers, avec en particulier le lithium (Li) et le béryllium (Be) ainsi que par l'évolution de leur vitesse de rotation interne et de surface.

L'abondance en lithium

Le lithium est depuis longtemps considéré comme un élément utile et contraignant qui peut être utilisé pour comprendre le transport des éléments chimiques et du moment cinétique dans les intérieurs stellaires (e.g. Wallerstein & Conti 1969; Boesgaard 1976; Vauclair et al. 1978; Spite & Spite 1982a; Baglin et al. 1985; Vauclair 1988; Lebreton & Maeder 1987; Baglin & Lebreton 1990; Boesgaard 1991; Charbonnel et al. 1992, 1994; Deliyannis et al. 2000; Montalbán & Schatzman 1996; Montalbán & Schatzman 2000; Piau & Turck-Chièze 2002; Charbonnel & Talon 2005; Talon & Charbonnel 2010). Trimble & Leonard (1994) ont résumé la pertinence du lithium par une phrase que nous pouvons traduire par : "*Nous continuons à trouver légèrement déconcertant qu'un élément aussi peu commun que le lithium soit si important pour l'étude de la structure des couches externes des étoiles, sans parler de l'Univers primordial. Mais c'est bel et bien le cas.*". En raison de sa température de fusion relativement basse (~ 2.5 MK, proche de la température à la base de la zone convective des étoiles de type solaire), le Li est en effet facilement détruit par capture de protons dans les intérieurs stellaires. Selon la théorie classique de l'évolution stellaire, cette destruction devrait se manifester à la surface des étoiles de type solaire pendant la pré-séquence principale (PMS) sous la forme d'une diminution de l'abondance de Li en surface. Les modèles classiques qui n'incluent aucun processus de transport autre que la convection ne prédisent aucune autre variation du Li de surface jusqu'à ce que l'étoile devienne une étoile géante rouge.

Les observations spectroscopiques montrent cependant que l'abondance en lithium à la surface des étoiles de type solaire, du champ et dans les amas ouverts s'appauvrit le long de la séquence principale (e.g. King et al. 1997; Sestito & Randich 2005; Chen & Zhao 2006; Takeda et al. 2010; Smiljanic et al. 2011; Xing & Xing 2012; Delgado Mena et al. 2014; Waite et al. 2017; Cummings et al. 2017; Beck et al. 2017; Harutyunyan et al. 2018; Carlos et al. 2020). Cela est illustré par la

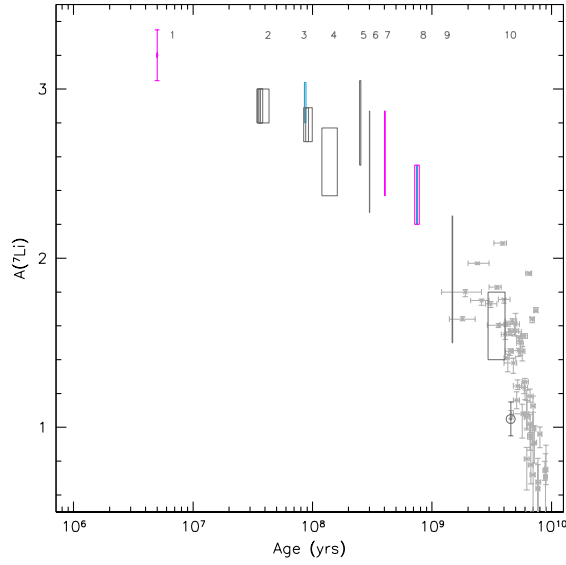


Figure 1 : Abondance de surface du Li vs l'âge. Les points individuels représentent les données (y compris l'âge) des jumelles solaires. (Carlos et al. 2019). Les boîtes correspondent aux observations du Li dans les étoiles de masse solaire dans différents amas ouverts (Sestito & Randich 2005; Carlos et al. 2020) avec les âges de Bossini et al. (2019)). Les numéros 1 à 10 identifient les amas [1) NGC 2264, 2) IC2391, IC2602 and IC4665, 3) α Per, Pleiades and Blanco I, 4) NGC2516, 5) M34, 6) NGC6475, 7) M35, 8) Praesepe et NGC6633, 9) NGC752 et 10) M67]. La couleur des boîtes indique la valeur de $[Fe/H]$: rose : -0.17 à -0.05; gris : -0.05 à 0.05; bleu clair : 0.05 to 0.16.

figure 1 qui donne l'abondance du Li dans différents amas en fonction de l'âge. Dans le cas du Soleil, le Li a diminué par rapport à sa valeur initiale (c'est-à-dire météoritique) de $A(^7Li) = 3.31^1$ à $A(^7Li) = 1.05$ (Greenstein & Richardson 1951; Schwarzschild et al. 1957; Asplund et al. 2009), ce qui témoigne d'une destruction importante du Li entre la formation du Soleil et son âge actuel. L'appauvrissement en Li a été clairement démontré comme s'accroissant avec le temps et avec la masse stellaire décroissante. La morphologie du comportement des abondances de Li en fonction de T_{eff} peut ainsi en être déduite (e.g. Deliyannis et al. 2000, pour une revue; et voir la figure 2 qui donne les observations du Li en surface pour 14 amas ouverts).

Elle présente en particulier deux comportements distincts pour les étoiles de faible masse à un âge donné. D'une part, les étoiles froides (de type G) présentent un appauvrissement progressif avec la température effective décroissante (masse décroissante). D'autre part, les étoiles de type F, de T_{eff} comprise entre 6400 K et 6800 K, forment ce que l'on appelle la brèche du Li (e.g. Wallerstein et al. 1965a; Boesgaard & Tripicco 1986; Hobbs & Pilachowski 1986; Soderblom et al. 1993; Balachandran 1995; Steinhauer & Deliyannis 2004; Anthony-Twarog et al. 2009; Cummings et al. 2012; Boesgaard et al. 2016). Celle-ci s'observe en particulier pour les Hyades et Praesepe où les étoiles F de la brèche présentent une abondance de surface de Li de 1 dex ou plus inférieure aux étoiles légèrement plus chaudes ou froides.

¹ $A(X) = \log_{10}(N_X/N_H) + 12$ (où N_X est la densité de nombre de l'élément X)

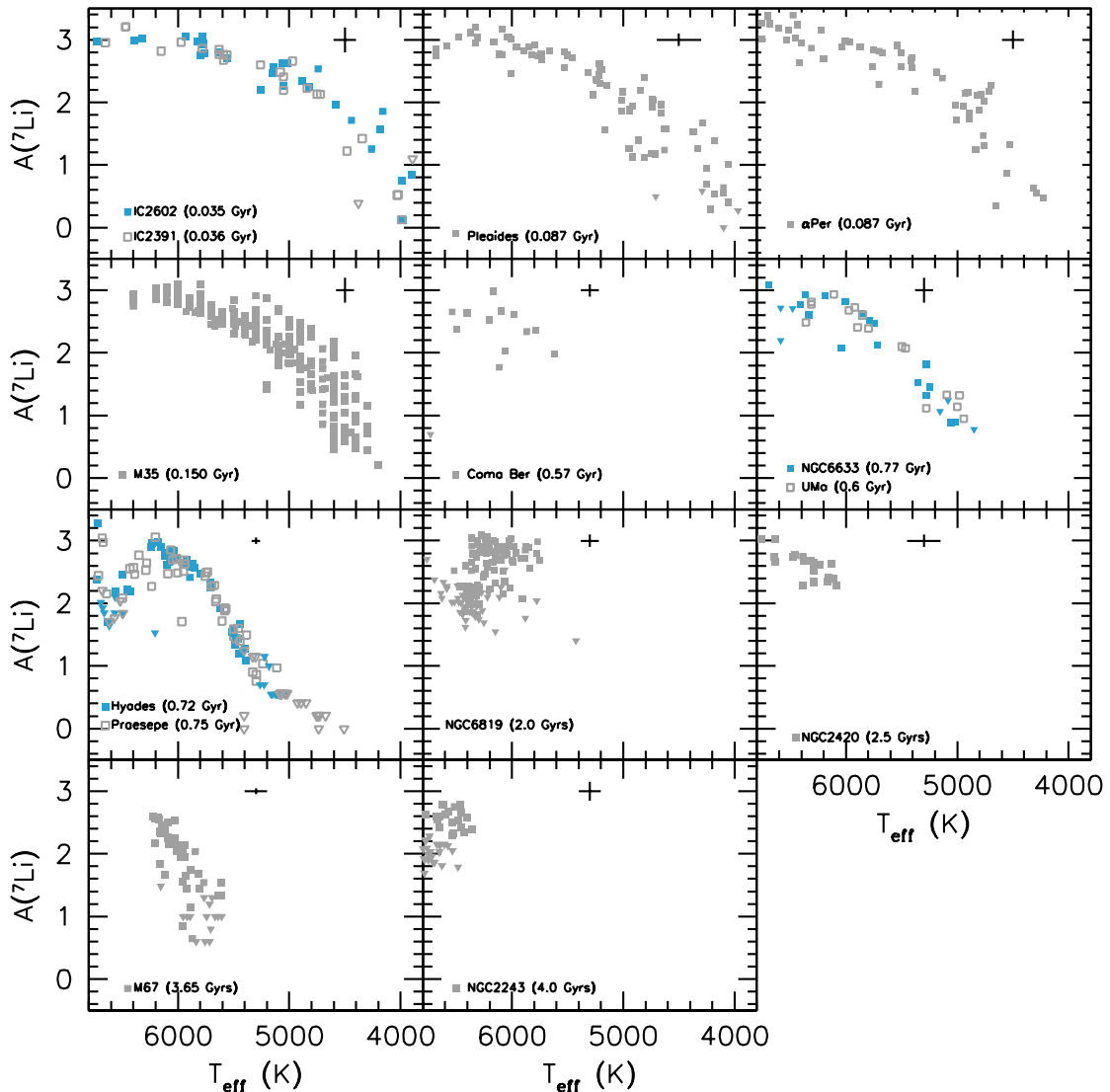


Figure 2 : Abondance de surface du Li vs T_{eff} pour 14 amas ouverts. La référence et les paramètres de chaque amas ouvert sont donnés en Tab. 1.1 ainsi que les erreurs typiques sur les mesures de Li et les corrections de LTE. (figure issue de Dumont et al. 2021, révisé)

Rotation de surface

La rotation en surface a également fait l'objet de multiples travaux qui ont permis la détermination des taux de rotation d'étoiles de type solaire à différents âges (e.g. Stauffer & Hartmann 1986; McQuillan et al. 2014; García et al. 2014; Gallet & Bouvier 2015; dos Santos et al. 2016; Lorenzo-Oliveira et al. 2020). La figure 3 présente les observations pour des étoiles de type solaire dans les amas ouverts. Ces observations établissent clairement que la rotation de surface de ces étoiles évolue dans le temps sous l'effet de processus multiples. Les interactions magnétiques entre l'étoile et son disque d'accrétion au début de la PMS et plus tard l'interaction avec le vent sont par exemple invoquées avec succès pour expliquer l'évolution et la dispersion des périodes de rotation (e.g. Matt et al. 2015a; Amard et al. 2016; Gallet et al. 2019, et références afférentes). Le rôle clef de la rotation a également été mis en évidence avec l'observation de la coïncidence

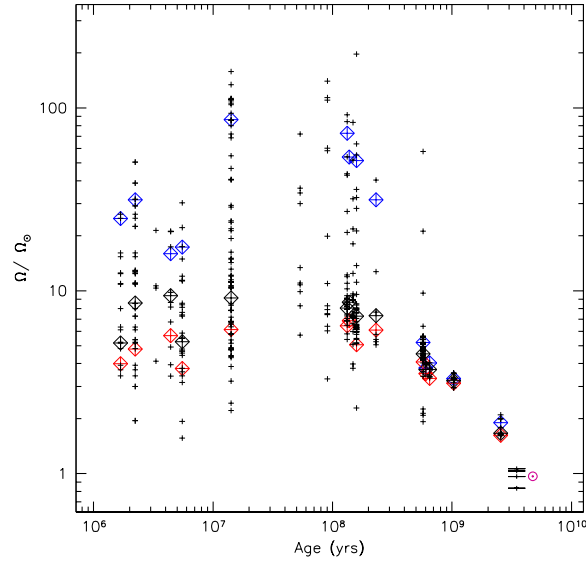


Figure 3 : Vitesse angulaire (en unités solaires; $\Omega_{\odot} = 2.86 \times 10^{-6} \text{ s}^{-1}$) vs l'âge. Les données observationnelles proviennent de Gallet & Bouvier (2015), exceptées les quatre étoiles de M67 qui viennent de Barnes et al. (2016). Les croix correspondent à des étoiles individuelles ; les diamants rouges, noirs et bleus vides indiquent les 25e, 50e et 90e percentiles de la distribution rotationnelle observée dans chaque amas, respectivement. Le Soleil est indiqué par le symbole usuel.

du bord froid de la brèche du Li avec ce que l'on appelle la rupture en rotation de Kraft, comme observée par exemple pour les Hyades (Boesgaard 1987) ou pour NGC 752 (Hobbs & Pilachowski 1986). La rupture de Kraft (Kraft 1967) correspond en effet à la transition entre les rotateurs lents (du côté froid de la brèche) et les rotateurs rapides (du côté chaud de la brèche) pour les étoiles de la séquence principale (MS) d'environ $1.2 M_{\odot}$ à métallicité solaire (étoiles de type F). Cette rupture dans la période de rotation est interprétée comme le résultat d'un freinage magnétique plus faible, ou inefficace, parmi les étoiles chaudes et plus massives par rapport aux étoiles plus froides et moins massives avec une enveloppe convective épaisse qui peut soutenir un freinage magnétique efficace par le vent stellaire (e.g. Schatzman 1962; Weber & Davis 1967; Matt et al. 2015b; Kawaler 1988a; Cummings et al. 2017; Deliyannis et al. 2019). La figure 4 donne les périodes de rotation observées pour 12 amas ouverts à différents âges. L'évolution rotationnelle des étoiles selon la masse et l'âge y est bien illustrée. La rupture de Kraft est également bien visible pour les étoiles les plus massives des amas les plus âgés.

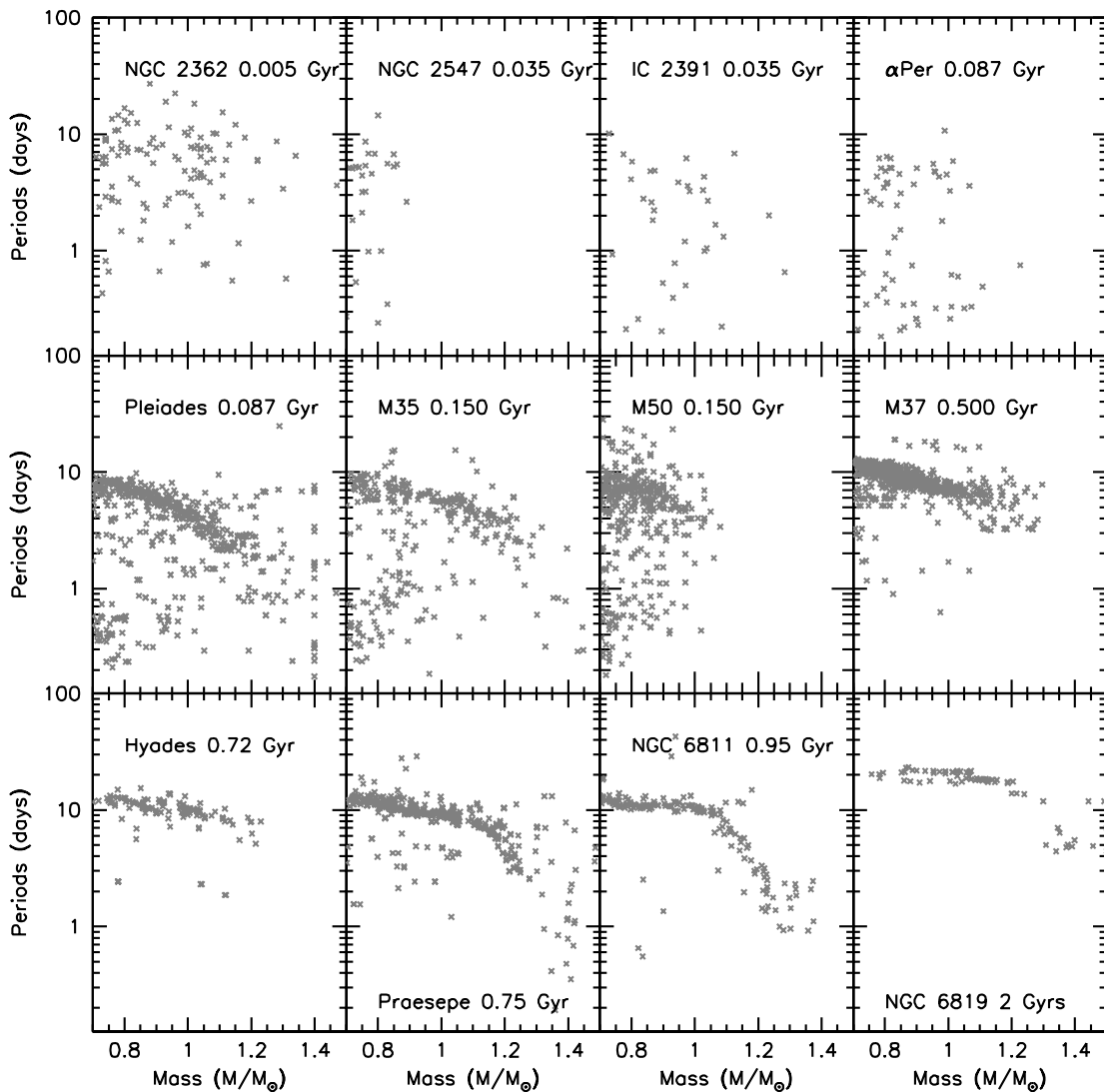


Figure 4 : Distribution de la période de rotation pour les étoiles MS de plusieurs amas ouverts (d'après Dumont et al. 2021, révisé)

Rotation interne

La rotation interne du Soleil est contrainte par l'héliosismologie. L'analyse des modes p donne accès au profil de rotation du Soleil entre environ $R = 0.2R_{\odot}$ et la surface (Kosovichev 1988; Elsworth et al. 1995; Thompson et al. 2003; Mathur et al. 2008; Eff-Darwich et al. 2008). La figure 5 présente le profil de rotation ainsi déduit pour le Soleil. Les inversions des données héliosismiques indiquent que le profil radial de la vitesse angulaire dans sa zone radiative est presque uniforme, ce qui implique l'existence de mécanismes de transport du moment cinétique efficaces au long de l'évolution. Il est généralement supposé que la rotation interne des étoiles de type solaire est similaire à celle du Soleil. Il est également possible de contraindre la rotation interne des étoiles de faible masse à des stades évolutifs plus avancés grâce à l'astérosismologie (i.e. pour les étoiles sous-géantes et les étoiles géantes rouges; e.g. Mosser et al. 2012; Deheuvels et al. 2012, 2014, 2015; Benomar et al. 2015; Gehan et al. 2018; García & Ballot 2019). L'analyse des modes mixtes dans les

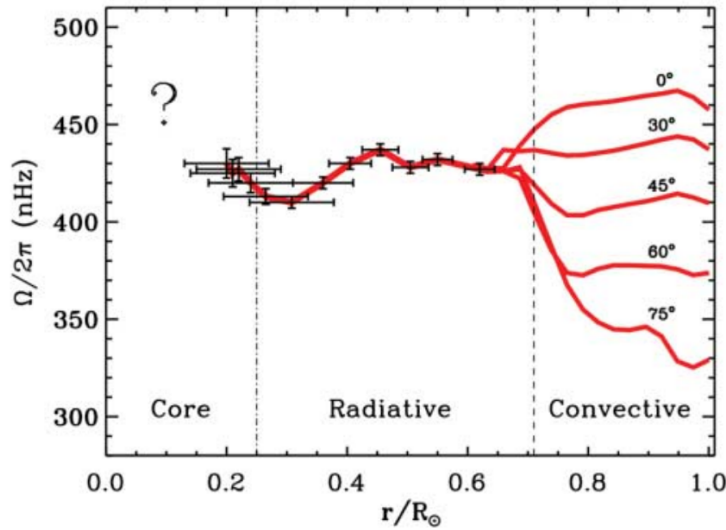


Figure 5 : Profil de rotation du Soleil à différentes latitudes extrait de García et al. (2007)

étoiles sous-géantes et géantes rouges de masse solaire présentant des oscillations de type solaire indique également un faible degré de rotation radiale différentielle dans le noyau. Ceci montre que le fort couplage trouvé à l'âge solaire est essentiellement maintenu au cours de l'évolution ultérieure (Eggenberger et al. 2017, 2019a; Mathis et al. 2018; Aerts et al. 2019). Il n'existe pas encore d'indice observationnel concernant la structure de la rotation interne au cours de l'évolution entre la PMS et le début de la MS, bien que l'analyse des données astérosismiques pour les étoiles de type solaire (Nielsen et al. 2014) et pour les étoiles de séquence principale de type F à G (Benomar et al. 2015) suggère que la rotation quasi solide de l'intérieur du soleil n'est probablement pas une exception.

Problématique et objectif de la thèse

Bien qu'il existe de nombreux modèles de transport pour le moment cinétique et les espèces chimiques, nous manquons de théories cohérentes permettant aux modèles d'évolution stellaire de reproduire simultanément les observations actuelles. L'objectif de la thèse est d'explorer comment des processus de transport supplémentaires peuvent améliorer l'accord entre les modèles d'évolution et les observations de l'abondance de Li en surface, de l'évolution de la rotation de surface des étoiles d'amas ouverts ainsi que du profil de rotation solaire.

Les observations comprennent les données pour des étoiles de type solaire (voir Fig. 1) et des étoiles de faible masse de type spectral F- à K- (voir Fig. 2). Les étoiles de faible masse de Population I (i.e. à métallicité solaire ou proche) sont caractérisées par une importante destruction du Li au cours de leur évolution de la pré-séquence principale à l'âge du Soleil et des études antérieures ont montré que le mélange induit par la rotation tel qu'il est inclus dans les codes d'évolution stellaire est insuffisant pour expliquer pleinement ces observations. De plus, un couplage fort entre la surface et les couches internes des étoiles est nécessaire pour expliquer l'évolution de la vitesse de rotation de surface dans les étoiles de type solaire (voir Fig. 3) et le profil de rotation solaire déduit par l'héliosismologie (voir Fig. 5). Dans une gamme plus large de masses stellaires ($0,8 M_{\odot}$ à $1,5 M_{\odot}$), nous observons également, pour quelques amas ouverts comme les Hyades, la brèche du Li qui apparaît à environ 6600 K (correspondant à des étoiles de type F) et coïncide avec la rupture rotationnelle de Kraft (voir Figs. 2-4). Enfin, outre l'épuisement du Li au fil de l'évolution, les étoiles du côté froid de la brèche du Li présentent un appauvrissement en Li avec des masses décroissantes (voir Fig. 2).

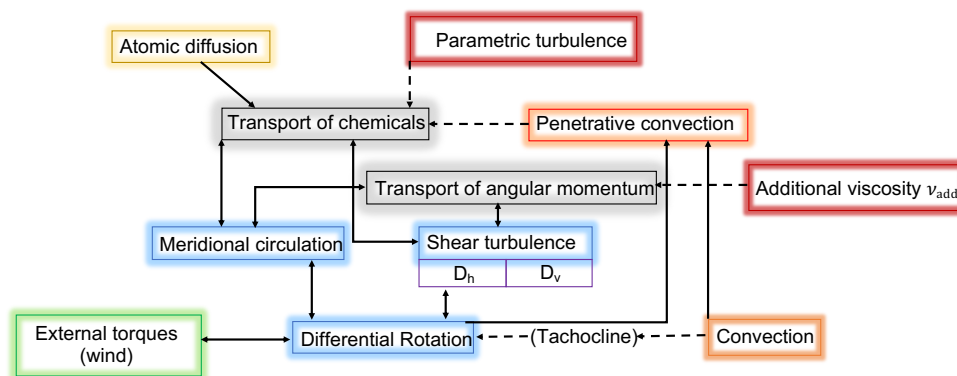


Figure 6 : Schéma des processus dynamiques et de leurs interactions qui conduisent au transport des éléments chimiques et du moment cinétique dans l'étoile. Les boîtes bleues font référence aux processus de rotation, les boîtes jaunes à la diffusion atomique, les boîtes vertes aux processus externes, les boîtes oranges à la convection, les boîtes rouges aux processus additionnels et les boîtes grises au type de transport qui en résulte (librement inspiré par la Fig. 1 d'après Mathis et al. 2007).

Nous explorons plusieurs processus de transport, du moment cinétique et des espèces chimiques, de la littérature avec le code d'évolution stellaire STAREVOL (Genève-Montpellier) que nous contraignons avec les données observationnelles.

Le premier objectif a été d'optimiser le traitement de la diffusion atomique par la mise en place d'un formalisme plus récent et mieux adapté à notre problématique (Paquette et al. 1986; Thoul et al. 1994), que nous avons ensuite validé grâce à une comparaison avec d'autres codes d'évolution stellaire. Nous avons ensuite déterminé les ingrédients de physique optimaux pour nos modèles, comprenant une mise à jour de la référence de l'abondance solaire (avec notamment l'enrichissement en Néon Asplund et al. 2009; Young 2018) et des opacités associées, et également la calibration de nos modèles sur le Soleil. Dans STAREVOL, la prise en compte des effets et du transport par la rotation suit le formalisme de la rotation "en coquille" développé par Zahn (1992) et Maeder & Zahn (1998), et déjà utilisé par exemple par Palacios et al. (2003); Decressin et al. (2009); Amard et al. (2019). Il fait intervenir deux processus dynamiques : la circulation méridienne et l'instabilité de cisaillement turbulente (verticale et horizontale). Il permet d'inclure un processus 3D dans un code d'évolution stellaire 1D avec l'hypothèse d'une turbulence anisotrope, c'est-à-dire avec un cisaillement horizontal plus fort que le cisaillement vertical. Ces processus conduisent à un mélange dans la zone radiative avec à la fois le transport de moment cinétique et celui des éléments chimiques dans l'étoile.

Afin d'optimiser les transports à la fois des éléments chimiques et du moment cinétique, au vu des observations, nous avons implémenté de nouveaux formalismes de pénétration convective dépendants ou non de la rotation (Baraffe et al. 2017; Korre et al. 2019; Augustson & Mathis 2019, 2020), une turbulence paramétrique (Richer et al. 2000; Richard et al. 2005), un mélange turbulent dû à la présence d'une tachocline (Spiegel & Zahn 1992; Brun et al. 1999) et une viscosité additionnelle (Eggenberger et al. 2012b, 2019b; Spada et al. 2016). L'interaction complexe des différents processus impliqués est illustrée en Figure 6. Le transport des éléments chimiques et du moment cinétique est le résultat de l'interaction de nombreux processus dans l'étoile (diffusion atomique, rotation différentielle) ou à l'extérieur de l'étoile (couplage magnétique externe). Les contraintes liées à l'évolution du lithium et à la vitesse angulaire dans les étoiles des amas ouverts, dans les jumelles solaires et dans le Soleil soulignent la nécessité de processus dynamiques supplémentaires afin de transporter à la fois les éléments chimiques et le moment cinétique. En effet, dans le cadre de l'hypothèse de la rotation "en coquille", le mélange induit par la rotation dépend principalement

de la circulation méridienne et du choix de la prescription pour la turbulence de cisaillement et ne peut reproduire toutes les observables sans l'ajout de processus supplémentaires.

Résultats

La destruction du lithium et le transport du moment cinétique dans les étoiles de type solaire

Nous avons précédemment décrit les contraintes observationnelles sur l'abondance de Li en surface et sur l'évolution rotationnelle et nous avons vu que l'évolution du Li dans différentes gammes de masse ou d'âge donne lieu à plusieurs divergences entre les observations et les prédictions des modèles. L'exploration des effets des processus additionnels que nous avons implémentés dans le code d'évolution stellaire STAREVOL a fait l'objet d'une première publication dans cette optique (Dumont et al. 2021).

Nous avons montré le rôle clef de la pénétration convective dépendante de la rotation pour transporter les éléments chimiques dans la pré-séquence principale et la séquence principale. Concernant le transport du moment cinétique, nous avons également considéré une viscosité verticale supplémentaire ν_{add} , fixe ou dépendante à la rotation, et ajustée à l'efficacité du freinage magnétique. Elle permet un transport efficace du moment cinétique entre le coeur et l'enveloppe lors de l'évolution en séquence principale et nous a permis de reproduire le profil observé pour le Soleil. Cependant, cette approche conduit à un appauvrissement moins important du lithium dans la séquence principale en raison d'une turbulence de cisaillement plus faible, résultant de l'effet de ν_{add} . L'ajout d'une turbulence paramétrique à la base de la zone convective nous permet de réaliser simultanément la reproduction de l'appauvrissement du lithium et de l'évolution rotationnelle et ainsi de déterminer un modèle optimal.

Cependant, les interprétations physiques pour la viscosité additionnelle et la turbulence paramétrique ne sont pas identifiées. Pour identifier cette dernière, nous avons étudié l'effet prometteur de la turbulence générée par la tachocline. Nous avons déterminé dans STAREVOL, et de manière auto-cohérente l'épaisseur de la tachocline et le coefficient de diffusion dû à la turbulence générée par la tachocline. L'épaisseur obtenue est compatible avec les estimations de l'héliosismologie à l'âge du Soleil, mais le coefficient de diffusion s'est avéré ne pas être adapté pour reproduire l'évolution du lithium jusqu'à l'âge du Soleil.

La figure 7 donne le résultat final obtenu avec le modèle optimal nommé $\nu R1_A^{T6.425}$ et calculé pour trois périodes de rotation initiales différentes : 1,6, 4,5 et 9,0 jours (rotation rapide (*F*), médiane (*M*) et lente (*S*)). Cela confirme le succès du modèle dit "optimal" pour reproduire simultanément les contraintes observationnelles.

La destruction du lithium et le transport du moment cinétique dans les étoiles de type F et de type G dans les amas ouverts galactiques

Dans un second temps, suivant les conclusions de Dumont et al. (2021) sur les différents processus de transport des produits chimiques et du moment cinétique, testés par rapport aux abondances de Li et aux contraintes de rotation interne et de surface pour les étoiles de type solaire, nous avons appliqué ces prescriptions à une gamme plus large en masse et en métallicité. Nous avons calculé des modèles pour une gamme de masse entre $0,8 M_{\odot}$ et $1,5 M_{\odot}$ ($\delta M = 0,1 M_{\odot}$), pour sept valeurs de $[\text{Fe}/\text{H}]$ (-0,4, -0,2, -0,1, -0,05, 0, +0,10, +0,15) qui couvrent la gamme de métallicité des amas ouverts présentés en figures 2 et 4. Les résultats de ce travail seront publiés dans la revue A&A (Dumont et al. 2021, soumis). La figure 8 donne un aperçu des résultats obtenus pour les cas spécifiques des Hyades et de Praesepe qui présentent les deux comportements du Li (et du Be). Nous avons montré que le modèle optimal développé pour le Soleil est capable de reproduire le côté froid de la brèche du Li pour chaque amas, indépendamment de l'âge et de la métallicité. Un

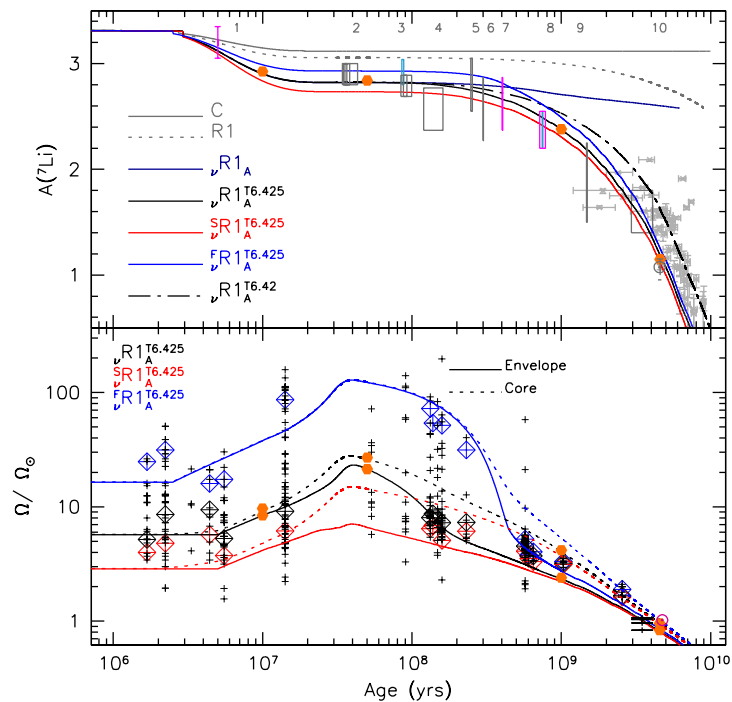


Figure 7 : Combinaison des figures 1 et 3 où sont ajoutés le modèle classique (C) et les modèles incluant la diffusion atomique et la rotation (R1). Le modèle optimal ($\nu R1_A^{T6.425}$) est calculé pour trois vitesses initiales différentes (F : rapide, M : median and S : lent). Il inclut l'*overshoot* comme proposé par Augustson & Mathis (2019): A , la turbulence paramétrique comme proposée par Richer et al. (2000) et Richard et al. (2005): $T6.425$ ($T6.42$ pour les jumelles solaires), et la viscosité additionnelle ν_{add} comme proposée par Eggenberger et al. (2012b, 2019b): ν . Les points oranges font référence à quatre âges auxquels les profils de coefficient de diffusion sont présentés dans la Fig. 7 de Dumont et al. (2021). Les carrés vides rouges, noirs et bleus donnent les 25ème, 50ème et 90ème percentiles des distributions rotationnelles observées dans chaque amas.

effet de la métallicité est mis en évidence et nous prédisons un appauvrissement plus élevé à haute métallicité qu'à basse métallicité. Cependant, nos modèles sont en moins bon accord avec les données observationnelles pour les métallicités faibles qui font apparaître des abondances en Li plus faibles que prédites et plaident pour une dépendance des processus de transport vis-à-vis des métaux. Sur toute la gamme de masses, métallicités et âges explorés, nous reproduisons l'évolution des taux de rotation de surface, et prédisons pour la première fois l'anticorrélation observée entre le taux de rotation de surface et l'appauvrissement en Li comme conséquence de la prescription de convection pénétrante. En outre, le modèle prédit des profils de rotation interne en bon accord avec les contraintes astérosismiques dans les étoiles de la séquence principale. En revanche, nous ne pouvons pas reproduire la brèche du Li observée dans quelques amas ouverts avec le même modèle du fait d'une trop faible destruction du Li pour les étoiles de masse $M > 1.2M_{\odot}$. Le brèche du Li ne peut être reproduit qu'en considérant une prescription différente pour le mélange turbulent de cisaillement et une viscosité paramétrique dépendant de la masse ν_{add} pour transporter le moment angulaire. En conclusion, nous mettons en évidence deux comportements du Li de chaque côté de la rupture de Kraft, une tendance reliant Li et T_{eff} et un comportement propre des étoiles de la brèche où nous avons vu la nécessité d'un processus de transport qui serait efficace dès lors qu'il atteint la rupture de Kraft. Cela encourage une clarification sur la théorie décrivant les processus turbulent dans les étoiles notamment lié au cisaillement. Et cela encourage

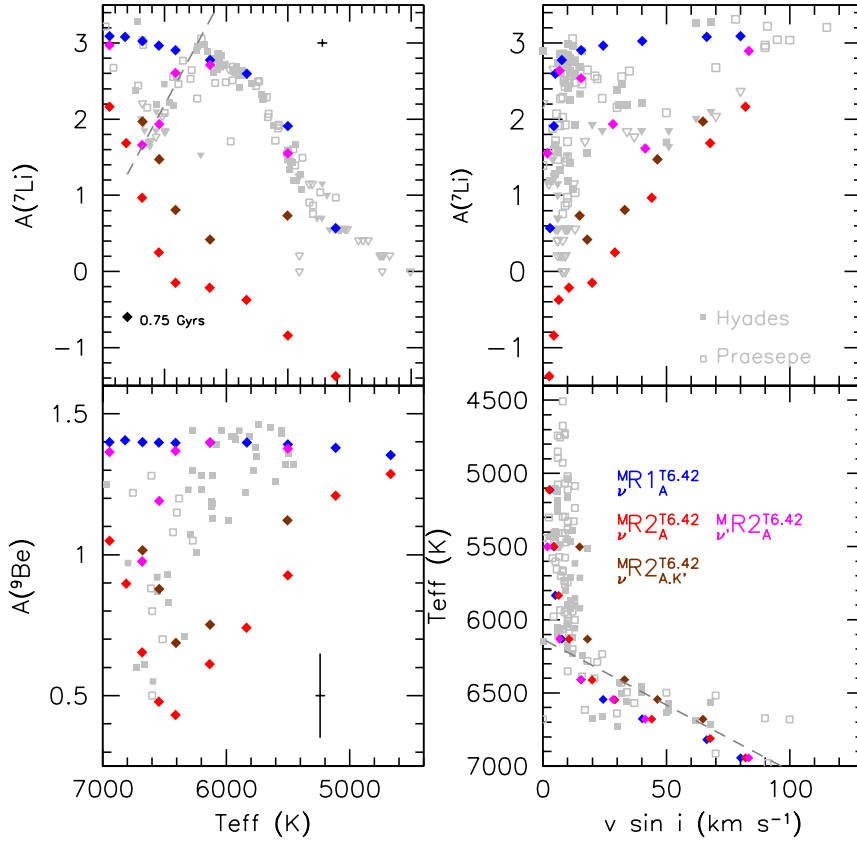


Figure 8 : Comparaison des modèles $\nu R1_A^{T6.42}$ (diamants bleus) et $\nu R2_A^{T6.42}$ pour différentes valeurs de ν_{add} et du paramètre de freinage magnétique K (code couleur) avec les observations dans les Hyades (carrés pleins) et Praesepe (carrés vides). Les modèles sont calculés avec une métallicité $[\text{Fe}/\text{H}] = +0,15$ pour 0,75 Gyr. Les observations proviennent de Cummings et al. (2017) à l’exception des observations de Be qui proviennent de Boesgaard et al. (2016). Les triangles inversés correspondent à des limites supérieures de Li. Les lignes grises en tirets représentent les corrélations linéaires empiriques trouvées par Cummings et al. (2017) pour le bord froid de la brèche dans les Hyades et Praesepe. Panneau supérieur gauche : Abondance de surface de Li en fonction de T_{eff} . Panneau supérieur droit : abondance de Li en surface en fonction de $v \sin i$. Panneau inférieur gauche : Abondance de surface de Be en fonction de T_{eff} . Panneau inférieur droit : température effective T_{eff} en fonction de $v \sin i$ (figure extraite de Dumont et al. 2021, soumis).

également une nouvelle exploration des processus physiques tels que le mélange tachocline pour le transport des espèces chimiques et les ondes de gravité internes pour le transport du moment angulaire. Enfin, la contrainte clef du Béryllium, qui présente également un brèche corrélé avec le Li (voir figure 9), est soulignée. Il fournit des contraintes supplémentaires et complémentaires pour les processus de transport manquants impliqués. Nous montrons qu’avec le peu de données disponibles, il est actuellement difficile de réconcilier simultanément la brèche du Li et celle du Be. Nous soulignons la nécessité de données supplémentaires sur l’abondance du béryllium dans les étoiles de type F et G de la séquence principale, à des âges et métallicités différents.

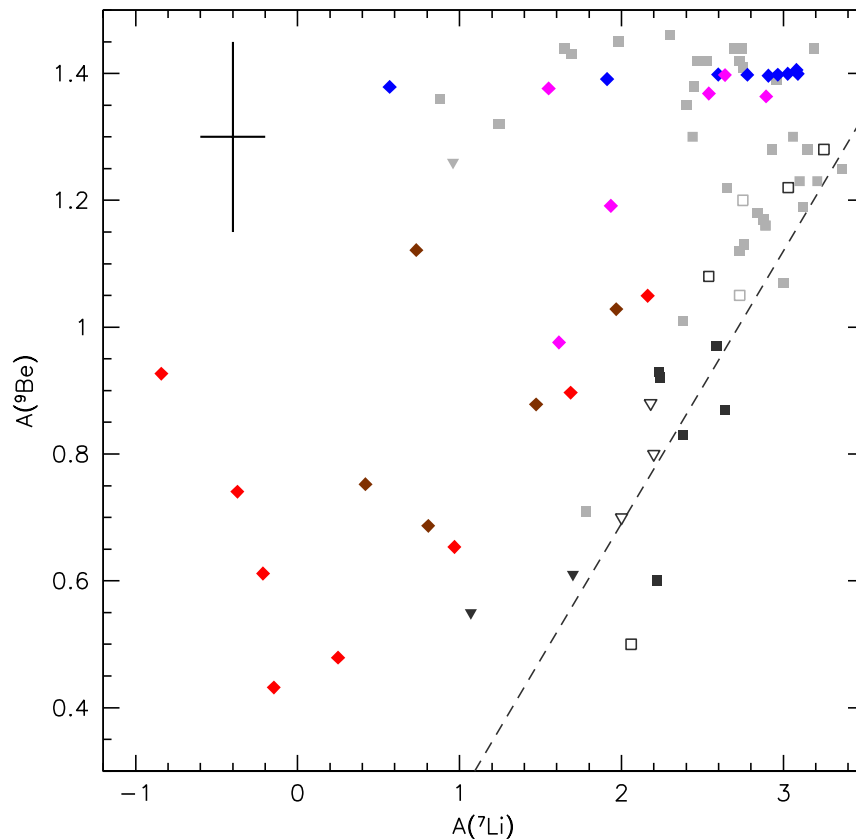


Figure 9 : Comparaison des modèles ${}^M_{\nu}R1_A^{T6.42}$ (diamants bleus), ${}^M_{\nu}R2_A^{T6.42}$ (diamants rouges), ${}^M_{\nu}R_{A,K'}^{T6.42}$ (diamants pourpres) et ${}^M_{\nu}R_{A,K'}^{T6.42}$ (diamants roses) avec des observations de surface de Li et Be dans les amas ouverts des Hyades (carrés pleins) et de Praesepe (carrés vides). Les triangles inversés correspondent à des limites supérieures de Li. Les étoiles correspondant à la brèche du Li ($6400 \text{ K} < T_{\text{eff}} < 6800$) sont représentées en gris foncé, les étoiles en dehors de la brèche sont représentées en gris clair. Les observations sont issues de Boesgaard et al. (2004, 2016). La ligne en tirets oranges représente la corrélation linéaire Li-Be trouvée par Boesgaard et al. (2020) pour les étoiles dans le bord froid de la brèche (figure extraite de Dumont et al. 2021, révisé).

Conclusion et perspectives

Conclusion

Au cours de cette thèse de doctorat, nous avons exploré comment des processus de transport supplémentaires peuvent améliorer l'accord entre les modèles d'évolution des étoiles en rotation et les observations pour l'épuisement du Li, l'évolution de la rotation de surface des étoiles, et le profil de rotation solaire. Nous avons utilisé les contraintes observationnelles du Soleil et des étoiles des amas ouverts, y compris les étoiles de type solaire et les étoiles de faible masse de type spectral F à K. Ces étoiles de la population I sont caractérisées par un appauvrissement important en Li au cours de leur évolution depuis la PMS jusqu'à l'âge du Soleil. L'appauvrissement en Li observé ne peut pas être entièrement expliqué par le mélange induit par la rotation qui est un processus insuffisant. De plus, les contraintes sur l'évolution de la vitesse de rotation dans les étoiles de type solaire et sur le profil de rotation solaire nécessitent un couplage fort entre la surface et les couches internes des étoiles afin de se rapprocher de la rotation presque solide déduite de l'héliosismologie. En considérant une gamme plus large de masses stellaires, nous observons pour

quelques amas ouverts, comme les Hyades, la brèche du Li, qui apparaît à environ 6600 K, et qui correspond aux étoiles de type F. Enfin nous avons observé, en plus de l'appauvrissement en Li avec le temps, que les étoiles du côté froid de la brèche présentent également un appauvrissement en Li pour des masses décroissantes.

La première tâche a été d'optimiser le code d'évolution stellaire STAREVOL pour calculer des modèles non standards adaptés à notre étude. Nous avons optimisé le traitement de la diffusion atomique par l'implémentation d'un formalisme plus récent, évitant l'hypothèse des éléments traces, que nous avons validé via la comparaison avec d'autres codes d'évolution stellaire. Nous avons ensuite déterminé la physique d'entrée optimale pour nos modèles, y compris une mise à jour de la référence d'abondance solaire, et calibré nos modèles sur le Soleil.

La deuxième tâche consistait à tester ces modèles, et à les comparer aux données observationnelles du Soleil et des étoiles de type solaire. Elle a mis en évidence l'insuffisance des modèles avec diffusion atomique et rotation seules pour reproduire simultanément la contrainte sur le Li et sur la vitesse de rotation. Des processus dynamiques supplémentaires sont en effet nécessaires pour transporter à la fois le moment cinétique et les éléments chimiques. Nous avons implémenté et étudié les effets de différents processus additionnels afin de déterminer une combinaison optimale pour reproduire les observations. Nous avons mis en évidence que l'appauvrissement en Li des étoiles de type solaire peut être reproduit en deux étapes : au niveau de la PMS avec l'ajout d'un processus d'*overshoot* dépendant de la rotation et au niveau de la MS avec l'ajout de deux processus paramétriques distincts de mélange turbulent pour le moment cinétique et pour les éléments chimiques. Nous avons également calculé pour la première fois un modèle incluant un traitement auto-consistant de la tachocline avec la prédiction de la même épaisseur que celle déduite par l'héliosismologie. Cependant, nous avons montré que le transport turbulent résultant de la tachocline ne permet pas de reproduire l'appauvrissement en Li observé, et également qu'il nous manque un développement analytique complet pour la tachocline. Nous avons finalement déterminé un modèle optimal qui reproduit toutes les observations à la fois. Nous avons cependant souligné le besoin de contraintes supplémentaires pour la rotation interne des jeunes étoiles de type solaire et aussi pour les abondances de béryllium des amas ouverts afin de tester les prédictions plus avant.

La troisième tâche consistait à tester notre modèle optimal, déterminé pour les étoiles de type solaire, dans le cadre d'une gamme plus large d'étoiles incluant les étoiles de faible masse de type F à K. Nous avons montré que notre modèle fonctionne bien avec le côté froid et le côté chaud de la brèche du Li, indépendamment de l'âge, de la métallicité et de la vitesse de rotation initiale. Cependant, la brèche elle-même ne peut pas être reproduite par ce modèle à moins de modifier la prescription pour le cisaillement turbulent ainsi que l'efficacité de la viscosité additionnelle ν_{add} . Et même alors, la transition entre côté froid de la brèche et la brèche elle-même reste difficilement prédictible. Cela met en évidence la nécessité de clarifier la théorie décrivant la turbulence de cisaillement dans les étoiles et le besoin d'explorer des processus physiques tels que le mélange tachocline pour le transport des espèces chimiques et les ondes de gravité internes pour le transport du moment angulaire. Enfin, la contrainte clef du Béryllium, qui présente également une brèche, et qui est corrélée avec le Li mais pour un niveau d'appauvrissement différent est également démontrée. Elle favorise un mélange dépendant de la rotation et fournit des contraintes supplémentaires et complémentaires pour les processus de transport manquants. Il est actuellement difficile de réconcilier simultanément la brèche du Li et celle du Be mais la nécessité de données supplémentaires sur l'abondance du béryllium dans les étoiles de type F et G de la séquence principale, à des âges et métallicités différents est à souligner.

Dans le contexte des contraintes observationnelles auxquelles nous avons accès, nous avons con-

firmé que des processus de transport sont nécessaires, en plus de la diffusion atomique, de la circulation méridienne et du cisaillement turbulent, pour expliquer le comportement de l'abondance de Li en surface et l'évolution de la rotation pour les étoiles de type solaire et les étoiles de faible masse et que des contraintes supplémentaires sur la rotation interne et sur le contenu en béryllium seraient une plus-value, ainsi que de nouvelles études théoriques pour résoudre l'incertitude de la turbulence dans les étoiles ainsi que du mélange tachocline.

Perspectives

Les travaux réalisés au cours de cette thèse ouvrent la voie à une analyse plus approfondie dans la continuité directe de l'étude de l'abondance du lithium et de la vitesse de rotation, mais aussi à l'extension à différents cadres d'étude où l'application de notre modèle optimal pourrait être pertinente.

- La première perspective directe de ce travail est l'extension de notre échantillon d'étoiles avec l'ajout des étoiles du champ. L'étude des étoiles du champ, dont l'abondance en Be a, par exemple, été déduite pour un échantillon d'une centaine d'étoiles, est disponible dans les travaux de Garcia Lopez & Perez de Taoro (1998); Santos et al. (2002, 2004b,a); Gálvez-Ortiz et al. (2011); Delgado Mena et al. (2012), et apporterait, en particulier, une contrainte complémentaire;
- La deuxième perspective directe serait d'élargir la gamme de masse stellaire considérée dans nos études vers des étoiles plus massives afin de tester les prédictions des modèles dans une gamme plus large d'étoiles. Cela impliquerait la considération des accélérations radiatives qui ne sont plus négligeables dès lors que la masse augmente sensiblement (ou lorsque la métallicité est faible, e.g. Deal et al. 2018, 2020, et voir la méthode d'implémentation en Annexe E);
- La troisième perspective directe serait l'implémentation et le test de nouveaux processus de transport des éléments chimiques et/ou du moment cinétique. Les ondes de gravité internes (e.g. Charbonnel & Talon 2005; Talon & Charbonnel 2008; Charbonnel et al. 2013), la dynamo de Tayler-Spruit (Spruit 2002), et le "pompage convectif" (Kissin & Thompson 2015) sont ainsi prometteurs;
- La quatrième perspective directe de notre travail est la poursuite de notre étude pour des étoiles plus évoluées : les étoiles sous-géantes et les étoiles géantes rouges. Le lithium peut également être utile pour l'étude de ces étoiles géantes évoluées (do Nascimento et al. 2000; Charbonnel et al. 2000, 2020). Le faible taux de rotation de ces étoiles permet en effet une détermination précise de l'abondance de surface en Li. De plus, à l'aide de l'astérosismologie, les étoiles évoluées ont pu être caractérisées avec précision (masse, rayon) et leur intérieur sondé au moyen de la méthode des modes mixtes² ce qui nous donne accès à la rotation interne des étoiles (e.g. Mosser et al. 2012; Gehan et al. 2018). Ainsi, les modes mixtes ouvrent de nouvelles opportunités pour étudier l'évolution du transport du moment cinétique dans les étoiles (voir par exemple Eggenberger et al. 2017, 2019b);
- Une autre perspective serait d'ajouter directement les contraintes astérosismiques pour les étoiles de la MS par le biais de l'étude des *glitches* acoustiques qui apparaissent sur les modes d'oscillation. Des méthodes d'analyse récentes, Verma et al. (2017); Verma & Silva Aguirre

²Les modes mixtes sont le résultat du couplage entre les modes p et les modes g lorsque l'étoile atteint des phases évoluées telles que SGB et RGB. Les caractéristiques mixtes de ces modes permettent de sonder les étoiles géantes du noyau à la surface.

(2019) et également Farnir et al. (2019), ont permis d'exploiter les informations fournies par les *glitches* acoustiques tant pour l'hélium que pour les zones de convection. Suite aux travaux réalisés par Monteiro et al. (2000); Appourchaux et al. (2015); Farnir et al. (2019); Verma et al. (2019), l'étude des *glitches* dans le cadre de notre modèle d'évolution stellaire non-standard serait un pas en avant pour comprendre et contraindre les processus de transport.

- Une dernière perspective serait d'appliquer notre modèle optimal dans le cadre des étoiles de Pop. II (métallicité faible) avec le cas spécifique des étoiles de faible masse dans les amas globulaires. La vision idéale des amas globulaires partageant des propriétés similaires telles que les abondances chimiques initiales est maintenant remise en question avec la détection des Populations Stellaires Multiples (MSP) (e.g. Gratton et al. 2012; Charbonnel 2016; Bastian & Lardo 2018). En effet, grâce au télescope spatial Hubble, des études photométriques à haute résolution ont permis de détecter de multiples séquences en différents points des diagrammes couleur-magnitude (CMD) des amas globulaires (e.g. Bedin et al. 2004; Piotto et al. 2007; Milone et al. 2008; Piotto 2009; Bellini et al. 2017). En outre, plusieurs analyses spectroscopiques de ces MSP ont apporté un éclairage nouveau sur leurs caractéristiques (Gratton et al. 2001; Carretta et al. 2009; Gratton et al. 2012). Ces études ont identifié au moins deux populations (ci-après P1 et P2) qui présentent des abondances chimiques différentes. Les étoiles P1 présentent ainsi une chimie comparable à celle des étoiles du champ et du halo tandis que les étoiles P2 ont une chimie exotique et unique. L'application de notre modèle à la modélisation des étoiles P1 de faible masse, en combinant les effets de la diffusion atomique et de la rotation à faible métallicité, serait une étape supplémentaire, après les études précédentes, par exemple, Richard et al. (2002b); Charbonnel (2016); Prantzos et al. (2017a); Chantreau et al. (2015), et cela apporterait notamment de nouvelles contraintes pour le scénario du pollueur initial.

Remerciements

Voici donc le temps des remerciements, dans la langue de Molière (il ne faut pas exagérer non plus), exercice singulier sur un fil entre texte sans relief et texte sans subtilité. C'est également le signe de la fin de la thèse et d'un cycle et le moment de rappeler que si tout n'a pas toujours été facile, cette aventure n'est pas toujours solitaire. Je citerais bien Alphonse Allais pour commencer ces remerciements mais je laisse le lecteur averti redécouvrir lui-même ce mot d'esprit.

Bien sûr, la tradition veut que les remerciements d'une thèse commence par là où tout a commencé. Mes premiers remerciements vont donc en premier lieu à Corinne et à Ana qui m'ont donné l'opportunité de faire cette thèse en physique stellaire (c'est déjà beaucoup !) il y a maintenant quatre ans, alors que je baguenaudais encore du côté du canal du midi toulousain. Merci pour m'avoir guidé tout au long de cette odyssee. Dans notre petit groupe de choc, je ne compte plus les discussions, les courriels et tous les échanges qui ont émaillés ces années. Nous avons tous les trois le mérite de ne nous être jamais découragés malgré un code récalcitrant digne de Sisyphe et les nombreux soucis liés à l'avancement d'une thèse. Nos échanges ont été ô combien nombreux et je voudrais particulièrement remercier Ana et Corinne pour toute leur aide afin de m'orienter dans les méandres du code STAREVOL, à travers les amas ouverts ou globulaires, à Genève ou à Montpellier et enfin et surtout pour leurs innombrables retours sur mon travail, avec comme point d'orgue ce manuscrit de thèse qui m'a mené vers une belle note finale.

A ces remerciements, je voudrais également joindre Florian Gallet, qui m'a permis de m'intégrer à Genève, m'a ouvert les portes de STAREVOL et m'a guidé sur de bons rails au début de ma thèse. Egalement Olivier Richard, qui m'a fait découvrir la diffusion atomique et ses nombreuses subtilités, tout en gardant humour et bienveillance. Enfin, merci pour toute l'aide amicale et plus que bienvenue de la part de William et Louis, mes vaillants prédécesseurs.

Si j'écris ces lignes, c'est également car mon travail de thèse a été étudié et validé par les différents membres de mon jury que je veux remercier ici. Merci donc à Yveline Lebreton pour avoir accepté d'être présidente de ce jury et pour avoir pris le temps de s'intéresser à mon travail ; à Jose do Nascimento pour avoir été rapporteur de mon manuscrit de thèse et pour avoir scrupuleusement vérifié que celui-ci était impeccable ; Fabrice Martins pour avoir accepté d'être examinateur de ma thèse et également pour toute son amitié pendant mes séjours à Montpellier. Enfin des remerciements particuliers pour les deux derniers membres de ce jury : tout d'abord un très grand merci à Rafael A. Garcia, qui a également rapporté ce manuscrit mais qui a surtout été celui qui m'a fait découvrir la recherche en physique stellaire et le champ fascinant de l'astérosismologie quelques années plus tôt et qui m'a gardé tout son soutien depuis lors ; ensuite un très grand merci à Patrick Eggenberger, pour son soutien sans faille, sa disponibilité, son humour et sa bienveillance durant toutes ces années de thèse jusqu'à la soutenance de celle-ci.

Ensuite, et maintenant que la tradition est respectée et que la forme est sauve, je veux remercier tous ceux qui n'apparaissent pas dans cette thèse mais qui ont joyeusement jalonné mes années à Genève et Montpellier. Tout d'abord parmi le groupe stellaire de Genève un grand merci à Gaël qui a été d'un soutien inestimable durant cette thèse et qui, malgré un sens de l'humour que d'aucuns qualifieraient de passablement douteux, m'a emporté plusieurs fous rires et toute ma reconnaissance (sans oublier Fatima bien sûr et toute son amitié). Merci également à Damien, mon camarade en désillusion, pessimisme et complaints en tout genre. Nos nombreuses discussions, toujours cyniques mais toujours avec bonne humeur ont été des prompts renforts à la fin de cette thèse.

Les lignes se remplissent et mon objectif n'étant pas d'écrire un roman, je veux remercier : Georges pour sa passion communicative, son sens de la narration et sa bienveillance ; Sylvia pour sa gentillesse et son soutien ; Lionel pour ces années partagées dans un même bureau, nos discussions passionnées sur l'arnaco-communisme, l'Unicef ou encore la fabuleuse Carouge vont me manquer ! Merci à Sébastien M, digne représentant relax du monde de l'ovalie, Camilla pour son amitié et sa grande gentillesse (*Grazie !*) mais aussi Arthur compagnon de thèse maintenant au plat pays, Slava mon vaillant successeur, Laurent pour ses nombreuses anecdotes truculentes, Devesh pour son esprit enjoué, et aussi pour leur amitié : Sébastien S, Sophie, Devina, Adam, Emilia, Marc, Manos et tous les autres que j'oublie et qui pourront très justement me le reprocher. Avec une note spéciale pour Jérôme qui avec ses opinions claires et tranchées comme une horloge suisse n'a pas dénoté dans notre bureau. Je veux aussi remercier à Montpellier, où chacun de mes séjours ont été de bons moments : Svetla pour son amitié (*Blagodarya*), Hervé pour son humour et toute sa sympathie, mais aussi Julien, Agnès, Fabrice (encore !), Yohann, Duncan, Loann et tous les autres ! Enfin, comme certains maintiennent qu'il y a d'autres domaines en astrophysique que la physique stellaire, une bien drôle d'idée, je veux remercier particulièrement Josephine, pour tout (*Danke sehr!*), mais aussi Elodie bien sûr, l'inénarrable Stéphane et ses analyses fines de la géopolitique et du genre humain en général (sans oublier Marine et les filles), Manu, Mahsa, Marianne, Adrien, Anne et bien d'autres. Avec eux, j'ai pu découvrir un petit bout de la Suisse et de son histoire, partager des cafés, des parties de foot endiablées, des escalades de Genève et autres semi-marathons, des restaurants et barbecues, une coupe du monde, un EURO ensorcelé, des visites suisses, des marches gessiennes, et de temps à autre même discuter d'astrophysique.

Je veux également dire toute ma reconnaissance à ceux qui m'ont encadrés avant cette thèse et qui m'ont dirigé vers ce curieux travail de la recherche : tout d'abord Benoît Canaud qui m'a bien mis à l'épreuve et qui a été un encadrant précieux, très formateur et très amical, Rafa bien sûr mais aussi Savita Mathur et Jérôme Ballot qui ont chacun fait preuve d'une grande bienveillance à mon égard et sont toujours d'un grand soutien.

Pour finir, et il serait temps, deux remerciements spéciaux.

Le premier d'abord pour le petit groupe des pauses cafés avec Patrick, Stéphane, Gaël, Damien, Lionel et Florian. Ces pauses où se sont côtoyées débats passionnés, méconnaissance de l'histoire française et de l'histoire de Poitiers (heureusement vite corrigée par mes soins), blagues à multiples degrés d'une qualité inimitable, mauvaise foi belgo-suisse et j'en passe. Ces moments (et les litres de cafés engloutis) ont une part immense dans le succès de cette thèse et dans la conservation d'un état psychologique presque correcte de son auteur.

Ensuite un grand merci à tous ceux qui ont jeté un oeil à ce manuscrit et dont l'aide m'a été très précieuse et pour qui j'ai une grande reconnaissance : Corinne et Ana évidemment (!), mon frère Etienne, mon beau-frère Pierre, mais aussi Josephine, Svetla et la toujours présente Marie.

Et avant de mettre un point final à cette histoire et comme il y a, paraît-il, un monde parallèle en dehors de la recherche astrophysique.... je veux donc remercier les amis de toujours ou presque

: Marie forcément mais aussi Boris, Floriane, Benjamin, Dimitri, Maxime, Antoine, Maud, Lisa, Paola, Aurélien, Amélie, Florian, Ugo, Clément, Saniya, Lise, Léo, Julien, sans oublier Zelda bien sûr ! A cela, je serais quelque peu indigne de ne pas citer mes parents sans qui j'aurai peut-être dû choisir la voie vers le BEP chômage et qui ont toujours su m'aider pour tout (avec un niveau en math toujours incroyable !). Sans compter mes frères et soeur : Perrine, Mathieu et Etienne dans le désordre pour une fois ainsi que bien sûr Pierre, Laure et Moni. Et sans oublier mes deux adorables petites nièces, Manon et Noémie.

Voilà, c'est la fin des remerciements, bravo aux courageux ayant été jusqu'au bout malgré l'échec patent de ma tentative d'écrire quelque chose sans en faire trop ni pas assez. La thèse est finie, deux diplômes de docteur en poche, quelques moments que je n'oublierai pas, une bonne chose de faite et ça fait ça de plus en moins. Et en fin de compte ce n'est déjà pas si mal.

Sur ces sujets, il est beau de chercher aussi à accroître sa connaissance, en dépit de points de départ réduits du fait qu'il y a une telle distance nous séparant des phénomènes de cette région.

ARISTOTE, *Περὶ Οὐρανοῦ* - *Traité du ciel, Livre II, Chapitre 12 : Deux difficultés concernant l'ordre des astres*

Soit dit en passant, c'est une chose assez hideuse que le succès. Sa fausse ressemblance avec le mérite trompe les hommes.

(...) Ils confondent avec les constellations de l'abîme les étoiles que font dans la vase molle du borbier les pattes des canards.

VICTOR HUGO, *Les Misérables, Livre Premier*

Je me demande (...) si les étoiles sont éclairées afin que chacun puisse un jour retrouver la sienne.

ANTOINE DE SAINT-EXUPÉRY, *Le Petit Prince, Chapitre 17*

Contents

Thesis Outline	i
Résumé en français	iii
Remerciements	xvii
List of Figures	xxvi
List of Tables	xxvii
I Introduction	3
1 Observational constraints on solar-type and low-mass stars	4
1.1 Introduction	4
1.2 Lithium abundances	4
1.2.1 Spectroscopic observations	5
1.2.2 The Sun	5
1.2.3 Solar-type stars	5
1.2.4 Low-mass stars: different masses and spectral-types	8
1.2.5 Summary	12
1.3 Surface Rotation	12
1.3.1 The Sun	13
1.3.2 Solar-type stars in open clusters	14
1.3.3 Low-mass stars: different masses and spectral-types	14
1.4 Internal rotation	17
1.4.1 Sun	17
1.4.2 Low-mass stars	18
2 Theoretical Interpretation	20
2.1 Lithium abundance	20
2.2 Rotation: surface and internal	22
2.3 Simultaneous analysis	23
II Stellar evolution code STAREVOL	25
3 STAREVOL: Input physics	26
3.1 Introduction	26

3.2	Generalities on the stellar evolution code STAREVOL	27
3.3	Equation of state	28
3.4	Nuclear reactions	29
3.5	Initial abundances	29
3.6	Opacity	30
3.7	Convection and penetrative convection	31
3.8	Surface boundary condition	35
3.9	Mass loss	37
4	Atomic Diffusion	38
4.1	Introduction	38
4.2	Principles of atomic diffusion	39
4.2.1	Atomic diffusion through the description of a multicomponent fluid	39
4.2.2	Paquette coefficients	41
4.3	Determination of the diffusion velocity	41
4.3.1	Hypothesis and Formalism of Montmerle & Michaud (1976)	42
4.3.2	Hypothesis and Formalism of Thoul et al. (1994)	43
4.3.3	Radiative accelerations	47
5	Rotation	48
5.1	Type I rotational mixing	48
5.1.1	Meridional circulation and shear turbulence	49
5.1.2	Diffusive treatment of the turbulent transport	51
5.2	Transport of angular momentum	54
5.2.1	Stellar winds and magnetic braking	54
5.2.2	Transport of angular momentum by additional viscosity	55
5.3	Transport of chemicals	55
5.3.1	Transport of chemicals in a rotating star	55
5.3.2	Tachocline	56
5.3.3	Parametric turbulent transport	57
5.4	To go beyond	58
III	Non-standard stellar evolution models: Results	59
6	Validation of the scheme for atomic diffusion	60
6.1	The Montréal/Montpellier stellar evolution code	60
6.1.1	Input physics of MoMo	60
6.1.2	Structure for benchmarking	61
6.2	Improvements on the original Thoul et al. (1994) algorithm	63
6.2.1	Partial ionisation and Paquette's coefficients	63
6.2.2	Terms involved in the diffusion velocity	65
6.3	Benchmarking of the Thoul et al. (1994) formalism	68
6.3.1	Comparison of the diffusion schemes: STAREVOL and MoMo	68
6.3.2	Comparison at two different evolution stages	70
6.3.3	Comparison for different stellar evolution codes at $X_c = 0.35$	73
6.4	Population I stars: evolution and structure	75
6.4.1	Evolution tracks and surface abundance variations	75
6.4.2	Structure: abundances, diffusion velocity and base of the convective envelope	78
6.5	Population II stars: evolution and structure	82

7	Solar calibrated models	86
7.1	Solar Calibration	86
7.2	A few elements of comparison: CSM, SSM and NSSM models	88
8	Lithium depletion and transport of angular momentum in solar-type stars	94
8.1	Preliminary work	94
8.2	Dumont et al. (2021, A&A, 646, A48)	97
9	Lithium depletion and angular momentum transport in F-type and G-type stars in Galactic open clusters	118
9.1	Dumont et al. 2021 (A&A, revised)	118
10	Conclusion and perspectives	137
10.1	Conclusion	137
10.2	Perspectives	138
A	Generation of new opacity tables	140
B	Addendum to atomic diffusion implementation	141
B.1	Friction coefficient with Paquette coefficients	141
B.2	K0 renormalisation	142
B.3	Test on Nacre I and Nacre II	143
C	Period rotation detection	145
D	Asteroseismology	148
D.1	Introduction	148
D.2	Rotation splittings	149
E	Radiative accelerations: perspectives and applications	150
F	Non-standard processes	153
F.1	Internal gravity waves	153
F.2	Tayler-Spruit instability	153
F.3	Advection-diffusion equation	154
	References	155

List of Figures

1.1	Schematic view of the architecture of a galaxy.	6
1.2	Pleiades open cluster. From the Space Telescope Science Institute (STScI) using the Hubble Space Telescope.	6
1.3	Li surface abundance vs the age for solar-type stars.	7
1.4	Li surface abundance vs T_{eff} for 14 open clusters.	9
1.5	Li and Be abundances observed in the Hyades open cluster	11
1.6	Lithium morphology evolution from Deliyannis et al. (2000)	12
1.7	Solar spots as drawn by Galileo in 1612	13
1.8	Angular velocity vs the age for a sample of open clusters	14
1.9	$v \sin(i)$ vs mass from Kraft (1967)	15
1.10	$v \sin i$ as a function of T_{eff} for MS stars of Hyades and Praesepe open clusters	15
1.11	Rotational period distribution for MS stars from several open clusters.	16
1.12	Rotational profile of the Sun at different latitudes from García et al. (2007)	18
1.13	Propagation of p-modes and g-modes.	18
1.14	Internal rotation as a function of the core-hydrogen abundance X_c derived from stellar modelling (from Benomar et al. (2015)).	19
2.1	Surface abundance profile of Li and Be as a function of the stellar mass fraction for a Zero Age Main Sequence (ZAMS) F-type star, and predictions of the classical model compared to Li observations of field stars	21
2.2	Li synthesis results from observations with WIYN/Hydra from Cummings et al. (2017)	22
3.1	Profile of normalised ionisation rate vs $\log T$ (K) from a STAREVOL solar model at solar age, and mean ionisation degrees from Schlattl (2002)	29
3.2	Relative differences in squared adiabatic sound speed between the Sun (obtained from seismic inversions), from Buldgen et al. (2019)	30
3.3	Schematic view of the penetrative convection in a solar-type stars	32
3.4	H-R diagram - Atmosphere	36
5.1	Scheme of the dynamical processes and their interactions that lead to transport of chemicals and of angular momentum in the star	49
5.2	Meridional circulation flow at three evolutionary stages of the PMS	50
5.3	Anisotropic turbulent transport in a stably stratified stellar radiative zone	50
5.4	Scheme of the dynamical processes and their interaction that lead to transport of chemicals and of angular momentum in the star where we consider the most promising physical phenomenon	58

6.1	Profiles of temperature, pressure and density at solar age: MoMo code	62
6.2	Mass fraction profiles: MoMo	62
6.3	Diffusion velocity with Paquette's coefficients at ZAMS	63
6.4	Normalised ionisation rate versus logarithm of temperature: STAREVOL, MoMo, MESA	64
6.5	Contribution of the different terms involved in atomic diffusion.	65
6.6	Profile of the pressure term A_p at ZAMS	66
6.7	Profile of the thermal term A_t at ZAMS	67
6.8	Diffusion velocities of ${}^4\text{He}$, ${}^{12}\text{C}$, ${}^{13}\text{C}$ and ${}^{16}\text{O}$ at ZAMS	68
6.9	Diffusion velocities for ${}^3\text{He}$, ${}^4\text{He}$, ${}^{12}\text{C}$, ${}^{13}\text{C}$ and ${}^{16}\text{O}$ at $X_c = 0.71$: STAREVOL and MoMo	69
6.10	Profile comparisons at two different stages: $X_c = 0.71$ and $X_c = 0.35$	71
6.11	Diffusion velocities for ${}^3\text{He}$, ${}^4\text{He}$, ${}^{12}\text{C}$, ${}^{13}\text{C}$ and ${}^{16}\text{O}$ at $X_c = 0.35$: STAREVOL and MoMo	72
6.12	Diffusion velocity of ${}^{16}\text{O}$ at the age of the Sun ($X_c = 0.35$)	74
6.13	Evolutionary tracks in the Hertzsprung-Russell diagram for STAREVOL and MoMo solar models with or without atomic diffusion	76
6.14	Time evolution of central hydrogen abundance (X_c). Time evolution of central helium abundance (${}^4\text{He}_c$). Effective temperature T_{eff} (K) versus X_c	76
6.15	Relative variation (decrease) of surface abundances as a function of central hydrogen mass fraction X_c for $1M_{\odot}$ Pop. I models of STAREVOL and MoMo	77
6.16	Evolution with T_{eff} of radius at the base of the convective zone (R_{bcz}) and temperature at the base of the convective zone (T_{bcz}) for the two codes STAREVOL and MoMo.	78
6.17	Mass fraction profiles of the main light elements (colour-coded) at solar age ($X_c=0.35$). STAREVOL and MoMo	80
6.18	Diffusion velocities profile of ${}^4\text{He}$, ${}^{12}\text{C}$, ${}^{14}\text{N}$, ${}^{16}\text{O}$ and ${}^{20}\text{Ne}$ at $X_c = 0.35$. STAREVOL and MoMo	81
6.19	Evolutionary tracks in the Hertzsprung-Russell diagram for Population II stars at $0.8M_{\odot}$ and $\text{Fe}/\text{H} = -1.75$	83
6.20	Time evolution of central hydrogen mass fraction (X_c). Time evolution of central helium mass fraction (${}^4\text{He}_c$). Effective temperature T_{eff} versus X_c . STAREVOL and MoMo	84
6.21	Relative variation (decrease) of surface abundances as a function of central hydrogen mass fraction X_c for $0.8M_{\odot}$, $\text{Fe}/\text{H}=-1.75$ models for STAREVOL and MoMo	85
7.1	Evolutionary tracks in the Hertzsprung-Russell diagram for the calibrated C model, D model and R1 model	88
7.2	Relative Surface abundances evolution of ${}^4\text{He}$, ${}^{12}\text{C}$, ${}^{14}\text{N}$, ${}^{16}\text{O}$ and ${}^{20}\text{Ne}$ versus the mass fraction of central hydrogen for solar models (D, R1 and R2 models)	89
7.3	Mass fraction profiles of the CSM, SSM and NSSM-R1 models at the turn-off	93
8.1	Li surface abundance evolution with time for the CSM (C), SSM (D) and NSSM (R1, R2, R3 and R4) model, and evolution of the angular velocity versus the age for R1, R2, R3 and R4 models	95
8.2	Profiles of the logarithm of the total transport coefficient $D_{\text{tot}} = D_{\text{eff}} + D_v$ at 8×10^7 years	96
8.3	Angular velocity profiles function of the relative mass fraction for the NSSM-R1 model	97
8.4	Angular velocity profiles versus the radius at solar age for model R1 computed with different values of additional viscosity ν_{add}	98

8.5	Li surface abundance evolution with time for the CSM (C), SSM (D) and NSSM (R1, R2, R3 and R4) model, and evolution of the angular velocity versus the age for R1, R2, R3 and R4 models. Both with the addition of the optimal model	99
8.6	Relative variations (decrease) of surface abundances for 4He and ^{12}C as a function of age for C and R1 models, and optimal model	100
B.1	Comparison of Nacre I or Nacre II for ^{12}C	143
B.2	Comparison of Nacre I or Nacre II for ^{13}C	144
C.1	Power spectrum density (PSD) of the CoRoT target HD52265	145
C.2	Detection of period of rotation: figure of analysis	147
D.1	Power spectrum density (in arbitrary units) of the Kepler target 16 Cyg A	148
D.2	Influence of the inclination angle i and of the rotational splitting on the structure of a mode	149
E.1	Impact of g_{rad} as function of the mass and the metallicity from Deal et al. (2018) . . .	152

List of Tables

1.1	Age estimates [*] , mean metallicity [†] , and reference for the lithium data of a sample of open clusters	10
1.2	Age estimates [*] and references for the rotational period of open clusters.	17
5.1	Turbulence shear prescriptions.	53
6.1	Comparative inputs physics in stellar evolution codes used for the validation of the atomic diffusion formalism.	61
6.2	Relative difference between diffusion velocities computed by STAREVOL and MoMo at $X_c = 0.71$ and $X_c = 0.35$	70
6.3	Relative decrease of surface abundances between the initial abundances and those at $X_c = 0.35$ for STAREVOL (left) and MoMo (right).	77
6.4	Results of the calibrations computed for two solar models of STAREVOL and MoMo for models with (SSM) or without (CSM) atomic diffusion	79
6.5	Parameters of the Population II, $[Fe/H] = -1.75$, $M = 0.8M_\odot$ models of STAREVOL and MoMo for models with (SSM) or without (CSM) atomic diffusion.	82
6.6	Relative decrease of surface abundances between the initial abundances and those at $X_c = 10^{-7}$ for STAREVOL (left) and MoMo (right).	85
7.1	Solar calibration results for different input physics: Classical Model (CSM - no transport other than convection), Standard Model (SSM - atomic diffusion) and Non-Standard Model (NSSM - atomic diffusion and type I rotation-induced transport) . .	87
7.2	Results of the calibrations for the three models C, D and R1 and adopted observational data for the Sun	90
7.3	Effective temperature T_{eff} , radius at the base of the convective envelope R_{bcz} , temperature at the base of the convective envelope T_{bcz} , mass at the base of the convective envelope M_{bcz} corresponding to the CSM, SSM and NSSM models.	92
8.1	Prescriptions for horizontal and vertical shear diffusivities	94
A.1	AGSS09 solar composition	140

Foreword

Stars are fundamental components of the Universe, they are age and distance indicators for astrophysics, and they are at the origin of the chemical evolution of all elements. Therefore, the impact of stars on their environment can be observed in a wide diversity of fields such as exoplanetology or galactic physics. The current description of stars by numerical models appears limited, and we are currently not able to reproduce all observational constraints at once. Indeed, nowadays powerful techniques (interferometry, spectropolarimetry, asteroseismology, etc.) provide a large amount of observational data allowing us to open new windows on the physics governing the evolution of stars. One of the main difficulties in producing reliable stellar models is related to the description of dynamical processes, that give birth to transport processes in stars. This description, as well as the identification of new processes that may impact the evolution of stars are presently at the heart of any significant progress in stellar physics.

We can divide the transport issue into two parts: the transport of chemicals and the transport of angular momentum. Thus, the identification and the characterisation of such chemicals and/or angular momentum transport processes is fundamental to understand the evolution of stars. If rotation is known to be one key element of the dynamical transport, the light element lithium (Li) has been revealed to be an unexpected and useful probe of these processes too.

Outline

The work presented in this thesis can be divided into three main parts.

- In Part 1, we introduce the framework of the PhD thesis. In Chapter 1, we focus on the observations obtained on lithium and also on the external and internal rotation of low-mass stars. In Chapter 2, we give an overview of the common interpretations of these observations. With the help of observational data for the Sun and for stars in open clusters, we highlight the discrepancies that are arising from the observation of surface lithium abundances and the challenge to consider them simultaneously with rotation;
- In Part 2, we present the stellar evolution code STAREVOL (Geneva/Montpellier). We describe the input physics of the code in Chapters 3. The next two chapters are dedicated to the work on atomic diffusion (Chapter 4) and on rotation and rotational-dependent processes (Chapter 5);
- In Part 3, we test the stellar models including the processes implemented during the PhD thesis and compare the modelling of solar-type stars and low-mass stars to the observations presented in Chapter 1. In Chapter 6, we present the work done to validate the formalism of atomic diffusion implemented in STAREVOL with the help of the Montreal/Montpellier

stellar evolution code. We highlight the fundamental effect of atomic diffusion in the evolution of solar-type stars. We show the effect of atomic diffusion, in particular, for the correct modelling of the stellar structure and the correct chemical abundance evolution. In Chapter 7, we provide the parameters of the models used during the PhD thesis and obtained from the implemented physics. It mainly focuses on the calibration of the models for the different sets of physics used. In Chapter 8, we present the tests and results obtained with the different processes implemented in STAREVOL in order to transport both chemicals and angular momentum in the context of observations of solar-type stars. In Chapter 9, we extend the study to a larger range of masses (between 0.8 and 1.5 M_{\odot}) and spectral-type stars (K-type to F-type stars). This chapter focus on the cold-side and the hot-side of the Li-dip and on the Li-dip itself. We present the results obtained by models already tested in the case of solar-type stars and discuss their relevance for surface Li observations. Finally, in Chapter 10, we discuss the results and give a conclusion. The futures perspectives of the PhD work are described in this chapter as well.

Part I

Introduction

Observational constraints on solar-type and low-mass stars

1.1 Introduction

Stars are among the most influential objects in the Universe and one of the main sources (with the Big Bang nucleosynthesis) of its chemical evolution. They are formed by interstellar material which they process and release again during their lives or when they die, and they are, in particular, at the origin of almost all the content in metals (in astronomy meaning any element heavier than helium) of the Universe. Numerous Solar-type and low-mass stars have been observed over a long period of time with the help of different techniques such as spectroscopy, photometry or asteroseismology. We now have access to data for a wide variety of stars at different masses, metallicities or ages in clusters or in the field. The surface chemical composition and its variations as well as the rotational evolution of these stars are of a particular interest in order to understand stellar evolution and stellar structure. Here, I present the main observational constraints that I have used in the present thesis: surface lithium abundance, as well as surface and internal rotation.

1.2 Lithium abundances

Lithium is the third lightest element in the Universe and one of the five isotopes created during the Big Bang nucleosynthesis, but its abundance is low compared to that of hydrogen or helium (primordial mass fractions of ^1H and ^4He are estimated at 0.7516 and 0.2484, respectively, and $^7\text{Li}/\text{H} = 5.61 \times 10^{-10}$, according to Coc & Vangioni 2017). However, lithium revealed itself as one of the most intriguing elements in astrophysics. Trimble & Leonard (1994) summarised the relevance of lithium: "*We continue to find it slightly disconcerting that so uncommon an element as lithium should be so important for studying the structure of outer layers of stars, not to mention the early Universe. But so it is*". Since then, the study of lithium evolution remains a relevant and important probe for stellar physics and beyond. It is a challenge, even today, to understand and explain the discrepancies that remain in stellar interiors and evolution models when compared to observations. We refer the reader to a series of papers by Deliyannis et al. (2000); Pinsonneault et al. (2000); Charbonnel et al. (2000) that give a good review of the challenges after two decades of works. A more recent review can be found in Charbonnel et al. (2010) (see in particular Eggenberger et al. 2009; Pinsonneault 2009; Randich 2009; Talon & Charbonnel 2009; Soderblom 2009; Spite & Spite 2009).

1.2.1 Spectroscopic observations

Observations of lithium can be achieved with the help of spectroscopy. The Li I resonance line can be detected at $\lambda \approx 6707 \text{ \AA}$ and the subordinate line at $\lambda \approx 6103 \text{ \AA}$. However, the accurate detection is challenging because of the blending effect of the CN and Fe I lines. The measurement of Li abundances is done from the Li equivalent width, which is sensitive to both the effective temperature (T_{eff}) uncertainties and photoionising UV radiation (Kiselman 1997). Besides, it was shown by Lind et al. (2009) that, although the departure from Local Thermodynamic Equilibrium (LTE) is relatively small, the use of Non-Local Thermodynamic Equilibrium (NLTE) corrections is relevant to achieve the required accuracy for Li measurements. For instance, Lind et al. (2009) showed that NLTE corrections give a shift for $A(\text{Li})$ [$A(X) = \log_{10}(N_X/N_H) + 12$, where N_X (N_H) is the number density of element X (H)] of about +0.15 dex for dwarf stars and of about +0.20 dex for giant stars. The details of the NLTE corrections for lithium abundances between -0.3 and 4.2 are given in Tab 2 and 3 in Lind et al. (2009) for the 6707 \AA line and the 6103 \AA line, respectively. These grids are computed in the ranges of $T_{\text{eff}} = [4000, 8000] \text{ K}$, $\log g = [1.0, 5.0]$, and $[\text{Fe}/\text{H}] = [-3.0, 0.0]$. The work by Lind et al. (2009) was recently extended by Wang et al. (2021) who computed a grid for a larger range of metallicities ($[\text{Fe}/\text{H}] = -4.0 \text{ dex to } +0.5 \text{ dex}$). Two isotopes of lithium, ${}^6\text{Li}$ and ${}^7\text{Li}$, can be observed with isotopic abundances of about 8% and 92%, respectively. Hereafter, we will not consider ${}^6\text{Li}$ as it has a negligible contribution to the Li stellar abundance.

1.2.2 The Sun

The Sun has been widely observed and several estimations of the solar chemical abundances were obtained over the past three decades with the help of detailed surface abundances from spectroscopy (e.g. Anders & Grevesse 1989; Grevesse & Noels 1993; Grevesse & Sauval 1998; Asplund et al. 2005, 2009; Caffau et al. 2011). The Li abundance in the solar photosphere was measured at $A({}^7\text{Li}) = 1.05$ (Greenstein & Richardson 1951; Schwarzschild et al. 1957; Asplund et al. 2009).

In the solar case, the lithium abundance can also be directly measured on meteoritic material. Indeed, meteorites are the witnesses of the protosolar nebula and give access to the primitive abundances of the solar system. Through their analysis, the meteoritic value of Li was inferred at $A({}^7\text{Li}) = 3.31$ (Lodders et al. 2009).

1.2.3 Solar-type stars

Beyond the solar case, we have access to data coming from the observation of solar-type stars in open clusters. We define solar-type stars as stars with an initial mass of $1.0 \pm 0.1 M_{\odot}$ and a value of $[Fe/H] = 0.0 \pm 0.2 \text{ dex}$, but possibly different ages. Open clusters are ideal laboratories to study stellar evolution. Located in the galactic disc (see Fig. 1.1), open cluster are young (a few Myrs to a few Gyrs) and typically composed of one hundred to one thousand stars¹. Figure 1.2 shows, for instance, the Pleiades open cluster observed by the Hubble Space Telescope. Each cluster gives access to a sample of stars sharing the same age and the same chemical composition thanks to a common origin (the same molecular cloud). It is thus possible to obtain a sample of stars at solar mass and metallicity, but for different open clusters at different ages and possibly with stars on the Pre Main Sequence (PMS) and/or on the Main Sequence (MS).

With the help of high resolution stellar spectroscopic data, the surface lithium abundances have

¹By contrast, globular clusters are old and massive clusters (from several Gyrs to almost the age of the Universe) composed up to millions of stars tightly bound by gravity. In this thesis, we focus on open cluster unless mentioned otherwise.

1.2. Lithium abundances

been obtained for several open clusters. We can, for instance, quote the results obtained by the WIYN² open cluster study that provides a large amount of data for open clusters stars (Mathieu 2000) and works on the spectrometer HIRES (Vogt et al. 1994), see references in Tab 1.1.

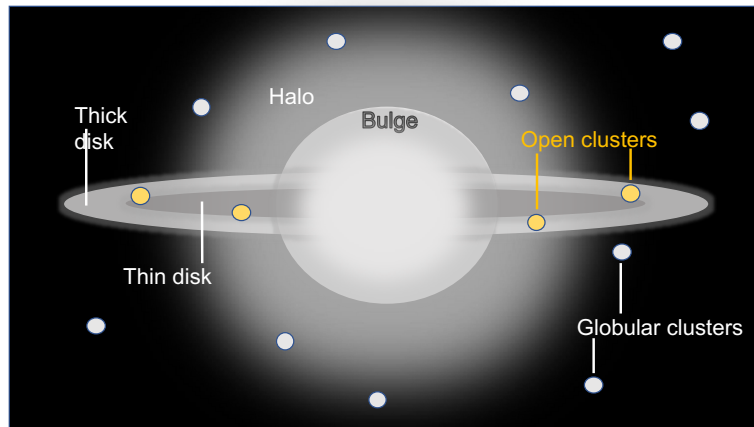


Figure 1.1: Schematic view of the architecture of a galaxy.



Figure 1.2: Pleiades open cluster. From the Space Telescope Science Institute (STScI) using the Hubble Space Telescope.

²Wisconsin, Indiana, Yale, NOAO.

Figure 1.3 gives the Li abundances provided by Sestito & Randich (2005) for a group of open clusters from which we established a sample of solar-types stars. For this sample, we computed

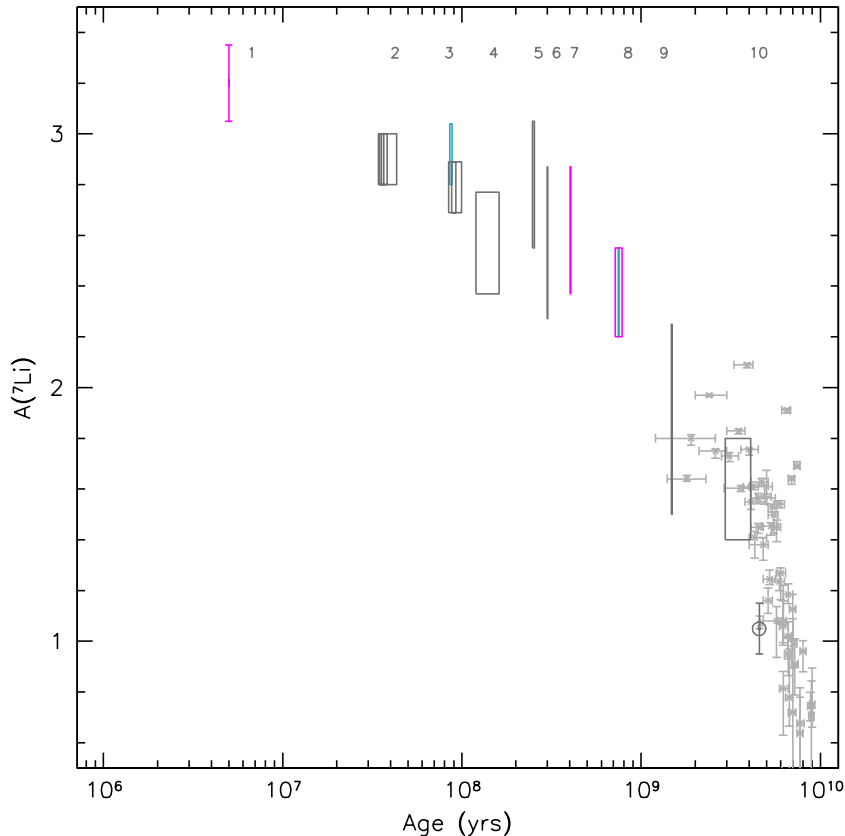


Figure 1.3: Li surface abundance vs the age. Individual points are data for solar twins (Carlos et al. 2019). Boxes are for Li observations of solar-mass stars in different open clusters (Sestito & Randich 2005; Carlos et al. 2020) with ages from Bossini et al. (2019). The numbers 1 to 10 identify the clusters: 1) NGC 2264, 2) IC2391, IC2602 and IC4665, 3) α Per, Pleiades and Blanco I, 4) NGC2516, 5) M34, 6) NGC6475, 7) M35, 8) Praesepe and NGC6633, 9) NGC752 and 10) M67. The colour of the boxes indicates the $[\text{Fe}/\text{H}]$ value: pink: -0.17 to -0.05; grey: -0.05 to 0.05; light blue: 0.05 to 0.16. The Sun is indicated with the usual symbol.

a stellar evolution model that predicts an effective temperature as a function of the age. Thus, for each cluster, we selected stars that have the same effective temperature, with an uncertainty of ± 100 K, than the predicted temperature at the age of each cluster. Sestito & Randich (2005) performed a homogeneous analysis of PMS/MS stars based on a group of open clusters available in the literature: NGC 2264, IC2391, IC2602, IC4665, α Per, Pleiades, Blanco I, NGC2516, M34, NGC6475, M35, Praesepe, NGC6633 and NGC752. Open clusters have $[\text{Fe}/\text{H}]$ values between -0.21 and +0.14. Moreover, we include recent measurements of the Li abundance of the M67 cluster provided by Carlos et al. (2020) and the abundances for a sample of solar twins³ observed by the HARPS spectrograph from Carlos et al. (2019). Li abundances were corrected from LTE in both sample: Sestito & Randich (2005) used the prescription of Carlsson et al. (1994) and Bossini et al.

³Stars are classified as solar twins when: $T_{\text{eff}} = T_{\text{eff},\odot} \pm 100$ K, $\log(g) = \log(g_{\odot}) \pm 0.1$, $[\text{Fe}/\text{H}] = [\text{Fe}/\text{H}]_{\odot}$, see also for instance Do Nascimento et al. (2009); do Nascimento et al. (2020); Delgado Mena et al. (2014).

(2019) used the *INSPECT* database⁴ (Lind et al. 2009).

These two additions complete the observational constraints at old age beyond the specific case of the Sun. Li abundances are provided as a function of the age of the clusters by Bossini et al. (2019) who determined ages by means of stellar isochrones with the help of Gaia DR2 astrometry and photometry (Gaia Collaboration et al. 2018), with the exception to the solar twins sample where the ages are from Carlos et al. (2019).

Photospheric Li abundance has long been known to decrease in solar-type stars along the PMS and the MS (e.g. King et al. 1997; Sestito & Randich 2005; Chen & Zhao 2006; Takeda et al. 2010; Smiljanic et al. 2011; Xing & Xing 2012; Delgado Mena et al. 2014; Waite et al. 2017; Cummings et al. 2017; Harutyunyan et al. 2018; Carlos et al. 2020). Figure 1.3 shows the evolution of surface Li abundance from the PMS to MS solar-type stars of several Gyrs (including the Sun) and highlights a continuous depletion between a value close to the meteoritic value of $A(^7\text{Li}) = 3.31$ to the solar photospheric value at $A(^7\text{Li}) = 1.05$. One additional element has to be noted: the sample of solar twins appears to be less Li-poor than the Sun at similar age. The Sun is consequently not typical of the Li evolution in solar-like stars.

1.2.4 Low-mass stars: different masses and spectral-types

The picture can be completed when considering a larger range of mass and stellar spectral-types. The observation of open cluster stars again provides precious information.

Figure 1.4 gives Li surface abundances⁵ for 14 open clusters at different ages and metallicities. We now consider different masses (or spectral types between F- and K-type stars⁶) of stars at the PMS and/or MS phase. References for lithium data are given in Tab 1.1 for each cluster. Ages are taken from Bossini et al. (2019); Gutiérrez Albarrán et al. (2020) for all clusters except Coma Ber and the Hyades (Netopil et al. 2016) and for the moving group Ursa Major (hereafter Uma), taken from Boesgaard et al. (2003a). Metallicities are given by Netopil et al. (2016) and Gutiérrez Albarrán et al. (2020), except UMa (Boesgaard et al. 2003a). Stellar effective temperatures range between 3800 K and 6800 K and masses are ranging between $0.8M_{\odot}$ and $1.5M_{\odot}$ from cool to warm stars.

Focusing on the cold-side (G- and K-type stars) at less than 6400 K, the Li surface abundance shows a continuous decrease with T_{eff} . On the hot-side ($T_{\text{eff}} > 6800$ K), stars appear to be characterised by a Li abundance close to the initial Li value $A(\text{Li}) = 3.31$. However, at an intermediate range of temperatures, we observe a dip of the Li abundance for stars between 6400 K and 6800 K for some clusters (see the Hyades and Praesepe in Fig. 1.4). At this range of masses and/or temperatures (early F-type stars), the picture becomes even more complex. Focusing on the specific case of the slight metal-rich Hyades open cluster (age close to 0.6 Gyr) we observe a group of stars that are Li-poor compared to stars at slightly higher or lower temperature. This feature is called the lithium-dip and it is clearly visible in the Hyades. The lithium-dip has been the object of studies for decades (e.g. Wallerstein et al. 1965b; Boesgaard & Tripicco 1986; Anthony-Twarog et al. 2009; Boesgaard et al. 2016; Cummings et al. 2017; Boesgaard et al. 2020).

⁴www.inspect-stars.com

⁵We computed 3D NLTE corrections ΔNLTE to the 1D LTE lithium abundances by using the code `Breidablik` (<https://github.com/ellawang44/Breidablik>) by Wang et al. (2021) to homogenise our sample.

⁶F-type, G-type and K-type stars correspond to MS stars with effective temperatures of about 6000-7500 K, 5200-6000 K and 3700-5200 K, respectively.

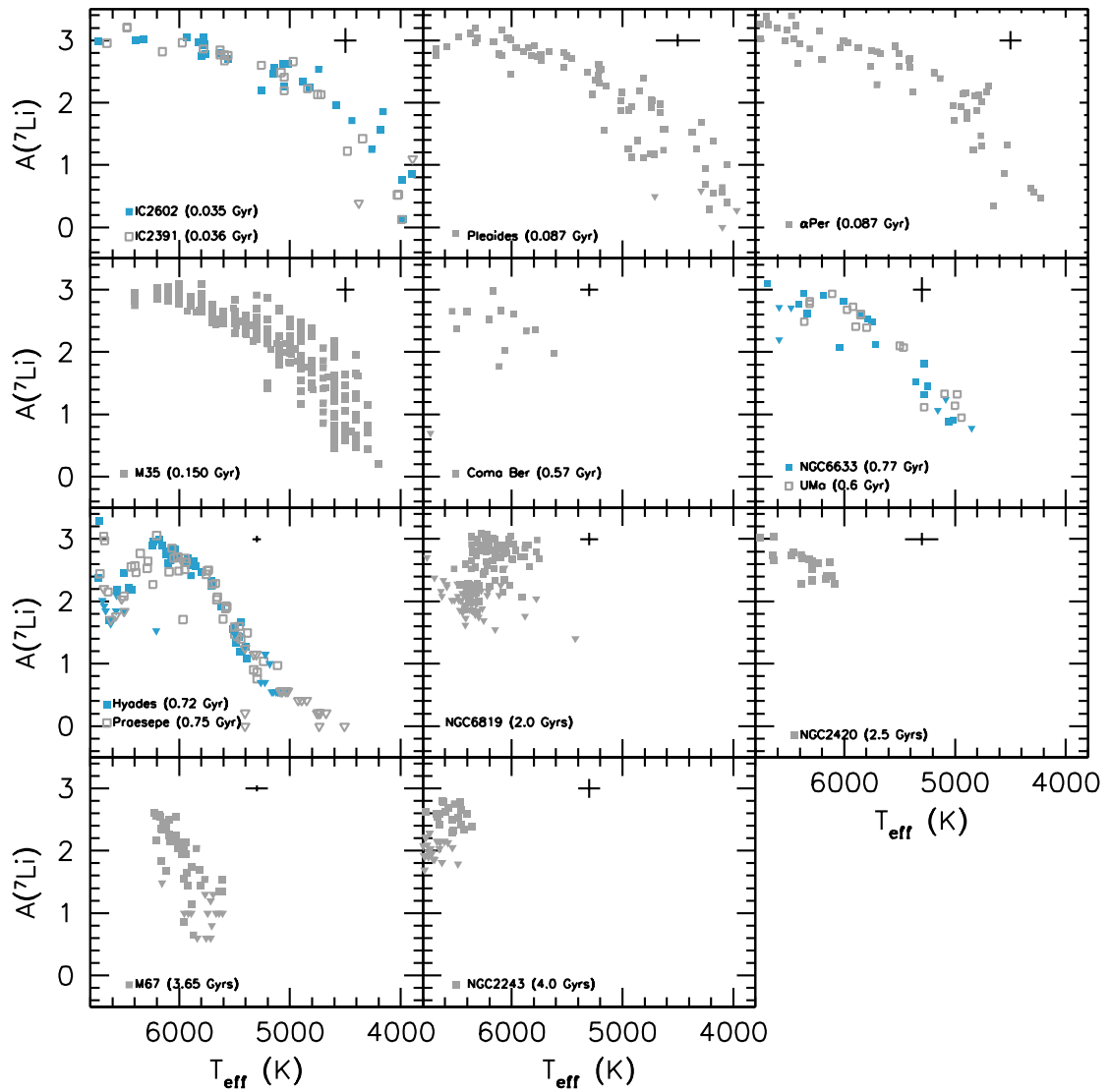


Figure 1.4: Li surface abundance vs T_{eff} for 14 open clusters. Reference and parameters of each open clusters is given in Tab. 1.1. Typical errors are represented by black crosses (from Dumont et al. 2021, revised)

Table 1.1: Age estimates*, mean metallicity†, and reference for the lithium data of a sample of open clusters

Name	Age (Myrs)	[Fe/H]	Ref Li	Typical error on A(Li)
IC 2602	35	-0.02±0.02	1	± 0.2
IC 2391	36	-0.03±0.02	1	± 0.2
Pleiades (Melotte 22)	87	-0.01±0.05	2	± 0.1
αPer (Melotte 20)	87	+0.14±0.11	3;4	± 0.2
M 35 (NGC 2168)	150	-0.17±0.01	5;6	± 0.2
Coma Berenices (Melotte 111)	570	0.00±0.08	7	± 0.1
UMa	600	-0.09	7	± 0.1
Hyades (Melotte 25)	720	+0.13±0.05	8	± 0.05
NGC 6633	770	-0.08±0.12	9;10	± 0.2
Praesepe (NGC 2632)	750	+0.16±0.08	8	± 0.05
NGC 6819	2000	+0.09±0.01	11	± 0.1
NGC 2420	2500	-0.05±0.02	12	± 0.1
M67 (NGC 2682)	3640	-0.01±0.04	13	± 0.05
NGC 2243	4000	-0.38±0.04	14	± 0.15

References.

* Boesgaard et al. (2003a); Netopil et al. (2016); Bossini et al. (2019); Gutiérrez Albarrán et al. (2020).

† Boesgaard et al. (2003a); Netopil et al. (2016); Gutiérrez Albarrán et al. (2020).

1: Randich et al. (2001); 2: Bouvier et al. (2018); 3: Boesgaard et al. (2003b); 4: Balachandran et al. (2011); 5: Barrado y Navascués et al. (2001); 6: Jeffries et al. (2021); 7: Boesgaard et al. (2003a); 8: Cummings et al. (2017); 9: Jeffries (1997); 10: Jeffries et al. (2002); 11: Deliyannis et al. (2019); 12: Semanova et al. (2020); 13: Pace et al. (2012); 14: François et al. (2013).

Figure 1.5, extracted from Boesgaard et al. (2020)), is illustrative of this phenomenon.

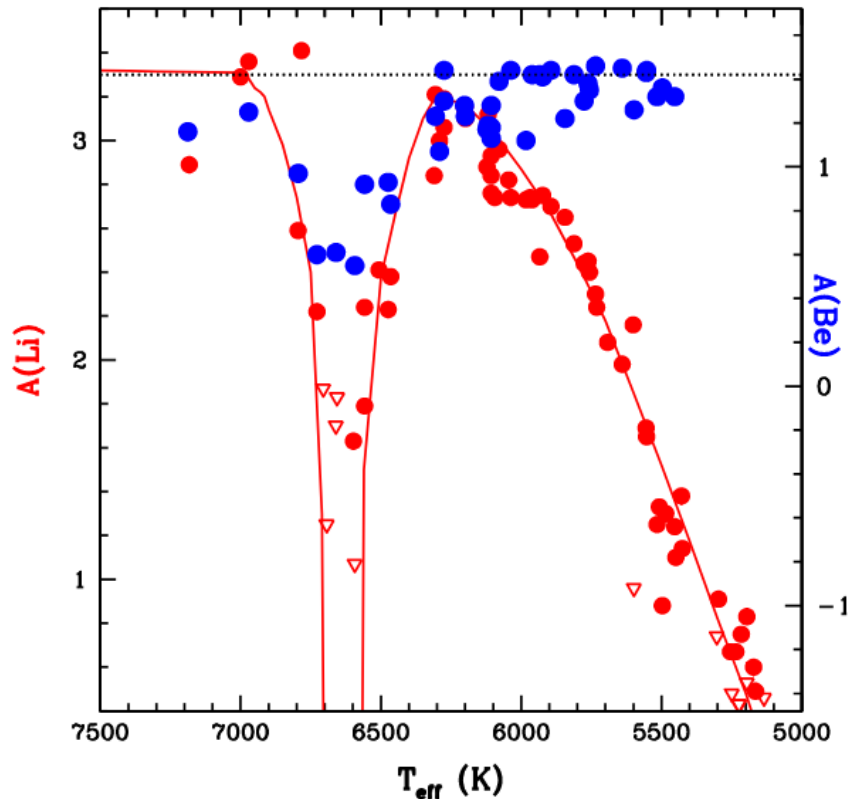


Figure 1.5: Li and Be abundances observed in the Hyades open cluster (≈ 0.6 Gyr) by Boesgaard et al. (2016) on the same scale and normalised to their respective solar system values ($A(^7\text{Li}) = 3.31$, $A(^9\text{Be}) = 1.41$). The Li-dip is observed between about 6400 K and 6800 K. A Be-dip is also observed. The red solid line represents a fit through the Li-temperature data. (Plot from Boesgaard et al. 2020).

Since, the observation in the Hyades cluster, the Li-dip has been searched and observed in several open clusters including, for instance, M35 (100 Myrs, Steinhauer & Deliyannis 2004), Praesepe (0.75 Gyr, Cummings et al. 2017), NGC 6819 (2.25 Gyrs, Deliyannis et al. 2019) but not for instance in the younger (≈ 87 Myrs) Pleiades and α Per open clusters (e.g. Boesgaard et al. 1988, 2003b) or the older (≈ 3.65 Gyrs) M67 open cluster (Pace et al. 2012) where the more massive stars had already left the Li-dip region.

It is also interesting to observe the behaviour of beryllium in the same clusters (e.g. Boesgaard et al. 2003a,b, 2004, 2016, 2020). For the case of the Hyades cluster, beryllium behaves similarly as lithium, and we observe the apparition of a Be-dip (see Fig. 1.5) at the range of temperature between 6400 K and 6800 K. However, the cold-side of the Be-dip appears to be close to the initial value of $A(^9\text{Be}) = 1.41$, contrary to Li. Indeed, the Li/Be ratio has been shown to constrain the general view of the dip bringing complementary evidence for a similar behaviour (e.g. Boesgaard 1976; Boesgaard et al. 2016, 2020). However, the observation of beryllium is challenging⁷ and has been inferred only for a few stars in a few open clusters.

⁷Observed with the help of Be II resonance line at 3130 Å in the UV.

1.2.5 Summary

Figure 1.6 summarises the observations on surface lithium abundances for open clusters (and halo field stars) at the MS at different ages and masses. The three groups identified in the previous sections appear and show the different behaviours of Li surface evolution. A first group corresponds to solar-like stars, close to solar metallicity and including the Sun. At the same temperature and metallicity but different age, the Li surface abundance is depleted but this depletion is different between the clusters, depending on the age, in particular, with a Li-poor Sun. A second group corresponds to cold stars that include solar-like stars, the Sun and the cold-side (< 6400 K) of the open clusters. It shows a Li-depletion as a function of decreasing T_{eff} and as a function of age. A last group corresponds to the stars that show the Li-dip at about 6600 K. Only the Hyades and Praesepe open clusters of close ages show the behaviour where the surface Li abundance drops. Finally, the parameters that govern the Li depletion are identified as the mass (or T_{eff}) and the age. We note that a last group can be identified: the stars of the so-called Spite Li plateau (Spite & Spite 1982a,b), composed of old metal-poor dwarf halo stars, that appear at an almost not depleted Li abundance value. However, the Li plateau is beyond the scope of this thesis and will not be detailed here.

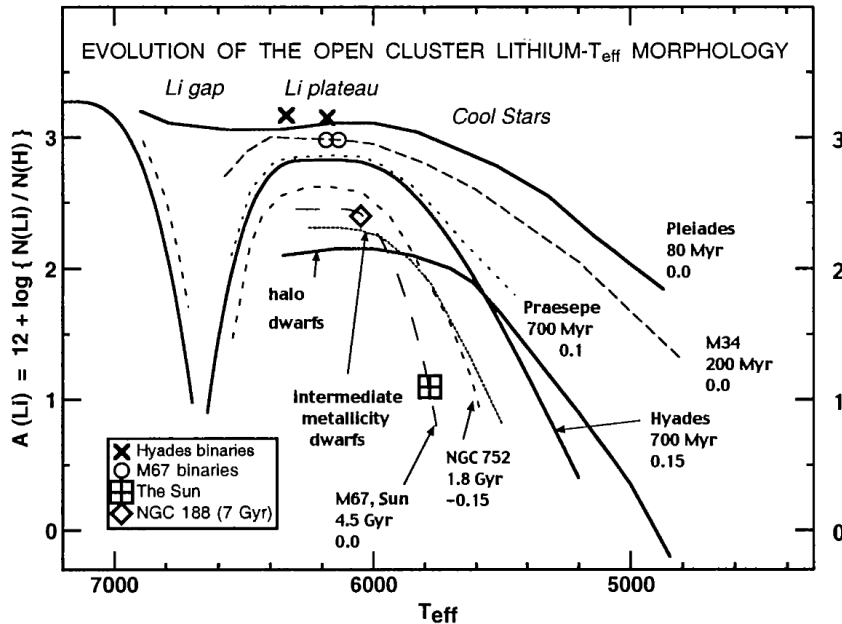


Figure 1.6: Surface Li abundances function of T_{eff} for the Sun, several open clusters and halo field stars at different ages and different metallicities. Lithium morphology evolution from Deliyannis et al. (2000).

1.3 Surface Rotation

The observation of spots on the surface of the Sun at the beginning of the 17th century by Galileo (see Fig. 1.7) and Scheiner showed that the Sun was rotating. Scheiner determined a rotation period of about 27 days in *Rosa Ursina sive Sol* in 1630. However, it is only at the beginning of the 20th century that Frank Schlesinger discovered that other stars than the Sun were rotating too (e.g. Schlesinger 1910, 1916). Since then, rotation has been observed for a tremendous number of stars and its behaviour as stars evolve is still far from being understood. Rotational observations

for solar-type and low-mass stars at the Main-Sequence (MS) phase are described below. We invite the reader to refer to Chapter 1 in the book of Tassoul (1978) for a historical summary of rotation observations.



Figure 1.7: Solar spots as drawn by Galileo in 1612 (taken from Malherbe (2016) - POSNER funds scanning, Carnegie Mellon)

Since the first inference of solar and stellar rotation by Galileo and Schlesinger, surface rotation has been observed for numerous stars with the help of mainly two techniques. The first method is based on spectroscopy and consists of measuring the projected broadening of spectral lines that appear as a consequence of rotation in order to determine the value of $v \cdot \sin(i)$ (e.g. Kaler 1989)⁸. The second method uses photometry and is based on the study of light curve modulations that arise as a consequence of stellar spots. The numerous data provided by the *Kepler* satellite⁹ allowed for instance the detection of the period of rotation (P_{rot}) for thousands of stars on the MS and on the RGB¹⁰ (e.g. McQuillan et al. 2014; García et al. 2014; Aigrain et al. 2015; do Nascimento et al. 2020; Breton et al. 2021). The measurement of the rotation period is carried out indirectly through the effect of star spots on the light curves. Different techniques are used to analyse the light curves and detect this effect: spot-modelling, power spectrum, auto-correlation, wavelet decomposition (see for instance Figure C.2 in Appendix C). The main difficulty is the correct identification of the period of rotation among the other periodic effects appearing on the light curve (e.g. seismic oscillations, granulation, exoplanets, instrumental noise), see Figure C.1 in Appendix C.

1.3.1 The Sun

The surface angular velocity of the Sun was measured at $\Omega_{\odot} = 2.86 \times 10^{-6} \text{ s}^{-1}$, which corresponds to a period close to 25 days or a surface velocity of about $12 \text{ km} \cdot \text{s}^{-1}$. However, this measurement refers to the equatorial latitude. Indeed, the rotation of the Sun is not homogeneous, and we can observe variations. For the Sun, latitudinal differential rotation was observed by the measurement of the poles period at about 36 days. In other words, the equator is rotating faster than the poles (the solar-type rotation¹¹).

⁸Where i refers to the angle of inclination between the rotation axis and the line of sight, and the absorption line profile will be defined by $\Delta\lambda = \lambda \frac{v \cdot \sin(i)}{c}$, with λ the wavelength, v the velocity and c the speed of light.

⁹The *Kepler* mission was continued with the K2 space mission that also gave detections for solar-type stars as for instance in Rebull et al. (2016); Douglas et al. (2019); Gordon et al. (2021)

¹⁰Red Giant Branch.

¹¹Few stars have been found to be anti-solar-type, for instance star HD 31993 (Kitchatinov & Rüdiger 2004)

1.3.2 Solar-type stars in open clusters

The period of rotation of solar-type stars has been observed extensively for large samples including open clusters stars (e.g. Stauffer & Hartmann 1986; Gallet & Bouvier 2015; Barnes et al. 2016), samples of solar twins (dos Santos et al. 2016; Lorenzo-Oliveira et al. 2020; do Nascimento et al. 2020) and see also the pioneer works of R. Kraft in a series of papers between 1965 and 1967 (Kraft 1967, and references therein). From these observations, we can plot the evolution of surface rotation velocity for solar-type stars at different ages. Fig. 1.8 shows the angular velocity obtained by Gallet & Bouvier (2015) for a sample of open clusters, where we added four solar-type stars of M67, extracted from the analysis by Barnes et al. (2016). The coloured diamonds represent the 25th, 50th and 90th percentiles of the observed rotational distribution in each cluster. At young ages, we observe a large dispersion. The velocity increases until a threshold close to 100 Myrs before a progressive decrease that extends until the age of the Sun at a few Gyrs.

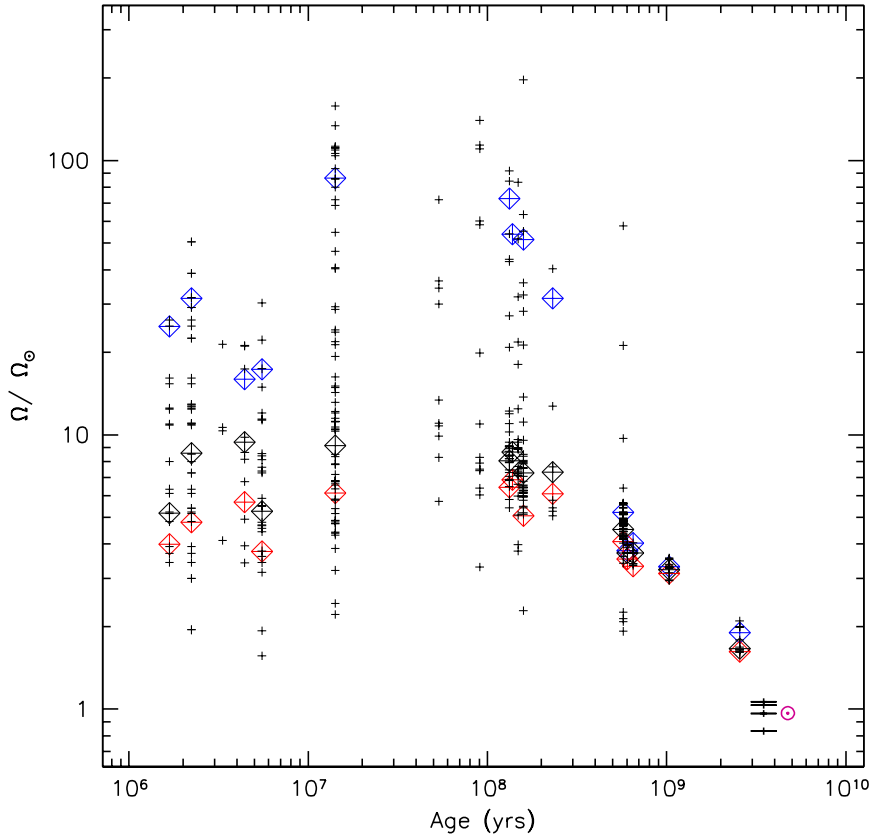


Figure 1.8: Angular velocity (in solar units; $\Omega_{\odot} = 2.86 \times 10^{-6} \text{ s}^{-1}$) vs the age. The observational data comes from Gallet & Bouvier (2015), except one of the four stars of M67 that comes from Barnes et al. (2016). Crosses are for individual stars; open red, black and blue diamonds show the 25th, 50th and 90th percentiles of the observed rotational distribution in each cluster, respectively. The Sun is indicated with the usual symbol.

1.3.3 Low-mass stars: different masses and spectral-types

Similarly to solar-type stars, the rotational velocity for low-mass stars at different masses was also observed with, e.g. stars in the Hyades and Praesepe (e.g. Cummings et al. 2017), NGC 6819

(Deliyannis et al. 2019) or Pleiades and αPer (e.g. Kraft 1967; Stauffer & Hartmann 1986).

For Hyades and Praesepe, Kraft (1967) and Stauffer & Hartmann (1986) observed that F-type stars have large rotational velocities and G- and K- type stars present a sharp decline with small rotational velocities at the same age (see Figs. 1.9 and 1.10)¹².

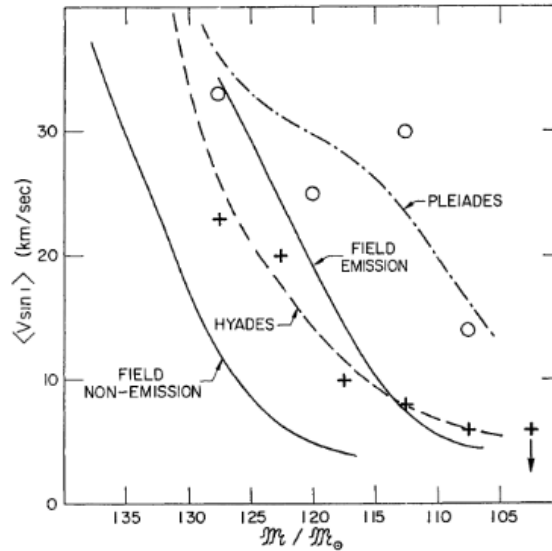


FIG. 8.— $\langle V \sin i \rangle$ as a function of (M/M_{\odot}) for field and cluster stars. Crosses and open circles correspond, respectively, to mean values for the Hyades and Pleiades.

Figure 1.9: From Kraft (1967)

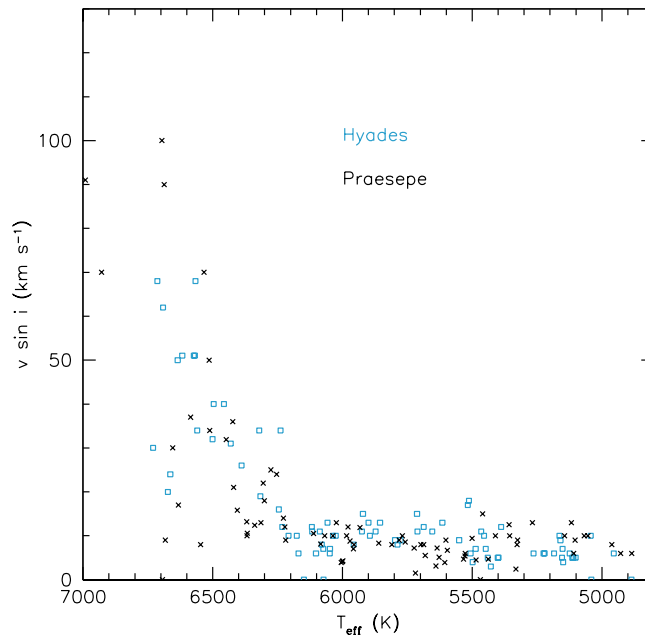


Figure 1.10: $v \sin i$ as a function of T_{eff} for MS stars of Hyades (open blue squares) and Praesepe (black crosses) open clusters. Data from Cummings et al. (2017).

¹²See also Fig. 1 of Kraft (1967) where the break in the rotational velocities is highlighted for low-mass field stars

1.3. Surface Rotation

Figure 1.11 gives the rotational period distribution for stars obtained from 12 different open clusters as a function of the mass (see Tab. 1.2). Works from Gallet & Bouvier (2015), Godoy-Rivera et al. (2021), and reference therein, give access to a large sample of rotation periods for open cluster stars. This sample shows a large dispersion at young age with Prot lower than 10 days, whereas at older ages of a few Gyrs, the period of rotation increases to stabilise at about 10-20 days.

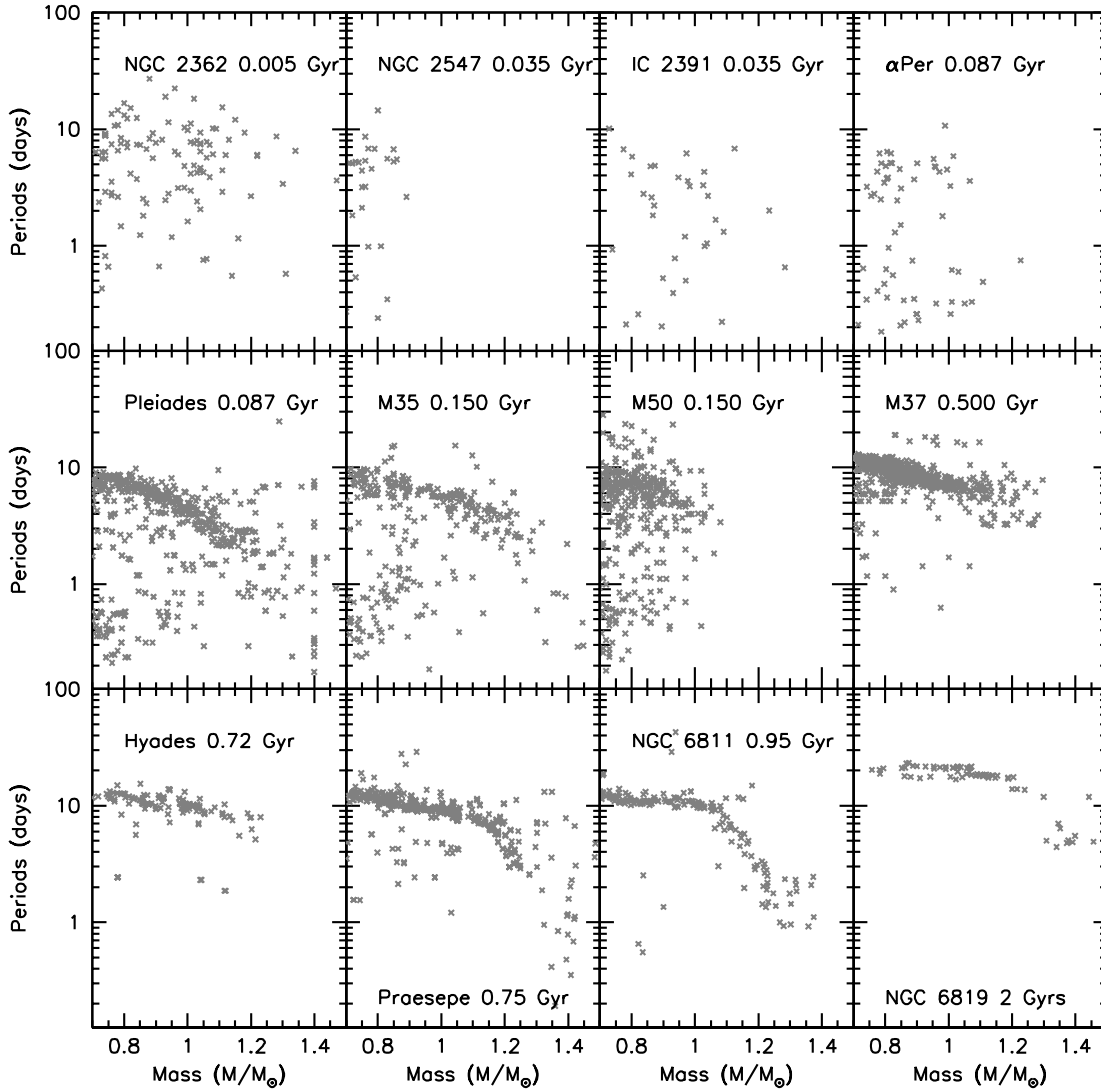


Figure 1.11: Rotational period distribution for MS stars from several open clusters. See Tab. 1.2 for references (from Dumont et al. 2021, revised.)

Table 1.2: Age estimates* and references for the rotational period of open clusters.

Name	Age* (Myrs)	Ref. Prot
NGC 2362	5	1
NGC 2547	35	2
IC 2391	36	3
Pleiades (Melotte 22)	87	2;4
α Per (Melotte 20)	87	3
M 35 (NGC 2168)	150	5
M 50 (NGC 2323)	150	2;6
M 37 (NGC 2099)	500	2;7
Hyades (Melotte 25)	720	8;9
Praesepe (NGC 2632)	750	2;10;11;12
NGC 6811	950	2;13
NGC 6819	2000	14

References.

* Douglas et al. (2016); Netopil et al. (2016); Bossini et al. (2019); Gutiérrez Albarrán et al. (2020); 1: Irwin et al. (2008); 2: Godoy-Rivera et al. (2021); 3: Irwin & Bouvier (2009); 4: Hartman et al. (2010); 5: Meibom et al. (2009); 6: Irwin et al. (2009); 7: Hartman et al. (2008); 8: Delorme et al. (2011); 9: Douglas et al. (2016); 10: Agüeros et al. (2011); 11: Douglas et al. (2017); 12: Douglas et al. (2019); 13: Meibom et al. (2011); 14: Meibom et al. (2015).

1.4 Internal rotation

1.4.1 Sun

The radial differential rotation (Brown 1985), that corresponds to a differential rotation velocity within the solar interior, was inferred thanks to helioseismology (e.g. Christensen-Dalsgaard et al. 1985a), especially with the observations from the MDI-GOLF-GONG¹³ that detected the presence of acoustic modes at the solar surface (see Fig. C.1 in Appendix C). The analysis of acoustic oscillations (p-modes for which pressure gradient is the restoring force) at the surface of the Sun gives access to the rotation profile of the Sun between about $R=0.2 R_{\odot}$ and the surface (Elsworth et al. 1995; Thompson et al. 2003; García et al. 2007; Mathur et al. 2008; Eff-Darwich et al. 2008), illustrated in Fig. 1.12 and the left panel of Fig. 1.13.

Figure 1.12 shows an almost flat core and radiative rotation at about 425 nHz between $0.2 R_{\odot}$ and $0.7 R_{\odot}$. When reaching the convective zone there is a splitting in latitude, with low latitudes rotating faster than higher ones.

Concerning the core rotation itself, additional information could be provided by the detection of gravitational oscillations (g-modes for which buoyancy acts as the restoring force) that propagate only in the central and radiative regions of the Sun and carry information on the central core. However, these modes are evanescent in the convective zone (see right-panel of Fig. 1.13) and their detection is challenging (Appourchaux et al. 2010). The detection of g-modes was presented in García et al. (2007); Fossat et al. (2017) but it remains uncertain and is highly debated in the helioseismic community (e.g. Schunker et al. 2018).

¹³MDI: Michelson Doppler Imager (Scherrer et al. 1995), GOLF: Global Oscillations at Low Frequencies (Gabriel et al. 1995). These instruments are on-board the SOLar and Heliospheric Observatory (SOHO) spacecraft of ESA/NASA (Domingo et al. 1995). GONG is the Global Oscillation Network Group (e.g. Howe et al. 2020, and references therein).

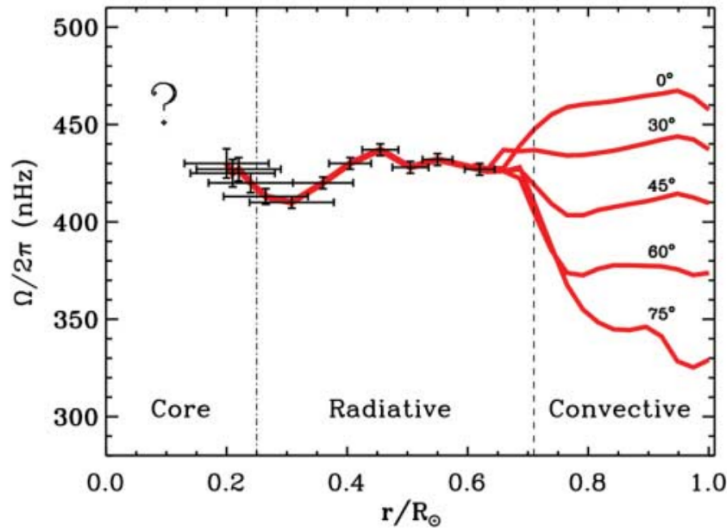


Figure 1.12: Rotational profile of the Sun at different latitudes from García et al. (2007)

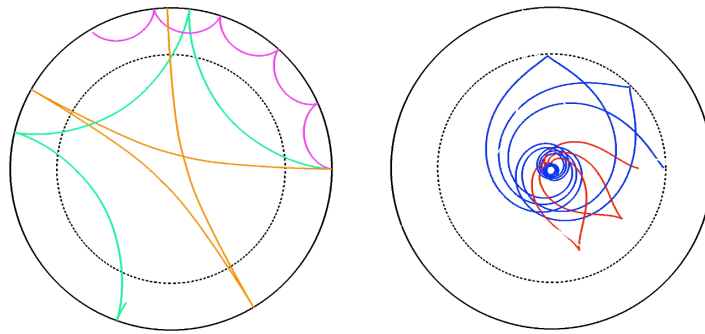


Figure 1.13: (Left) Propagation of three different degrees of pressure modes. The detection of p-modes can be achieved due to the high amplitude of p-modes close to the surface. (Right) Propagation of two different degrees of gravity modes. The g-modes are trapped in the radiative zone and have a very small amplitude at the surface. The dotted line refers to the base of the convection zone. (L. Alvan, CEA)

1.4.2 Low-mass stars

The situation is more complex for the internal rotation of low-mass stars. Contrary to the Sun¹⁴, the stellar surface of other stars is not resolved and we cannot achieve a sufficiently high resolution to observe high degree p-modes ($l > 3$) in these stars. Indeed, we (often) only have access to the radial ($l=0$), dipole ($l=1$), quadrupole ($l=2$) and octupole ($l=3$) modes that propagate through the entire star, which is not enough to determine the accurate radial rotational profile (Chaplin & Miglio 2013). Consequently, there are no measurement of internal rotation for these stars. However, the dipole and quadrupole modes are also sensitive to the rotation by the way of the Coriolis force (octupole modes are usually poorly observed). It gives birth to the rotational splitting in the modes, see e.g. Ballot et al. (2006), Fig. 1 in Chaplin & Miglio (2013) and Appendix D. The

¹⁴And excluding the specific case of γ dor where g modes have been detected that allow to probe the deep layers of the stars (see for instance Keen et al. 2015)

sensitivity of the modes to the rotation in the different regions of the star is represented by the rotational kernels (commonly noted $K_{n,l}$). Low-degree modes are not sensitive to the core but to the convective and radiative zones. Thus, it is possible to estimate the internal rotation of stars knowing the surface rotation velocity, and under a few assumptions (the convection zone velocity is uniform and equal to the surface velocity and the rotational splitting is relatively uniform). According to this method, Benomar et al. (2015) showed that the internal rotation of solar-like MS stars of different masses is nearly uniform, as is the case for the Sun (see Fig. 1.14). However, it stays a global estimation of the internal rotation that does not take into account the core and that is not providing an accurate radial profile as for the Sun (see also the work presented in Ceillier 2015).

Asteroseismology is able to constrain the core rotation of stars only at advanced evolutionary stages where mixed-modes appear.

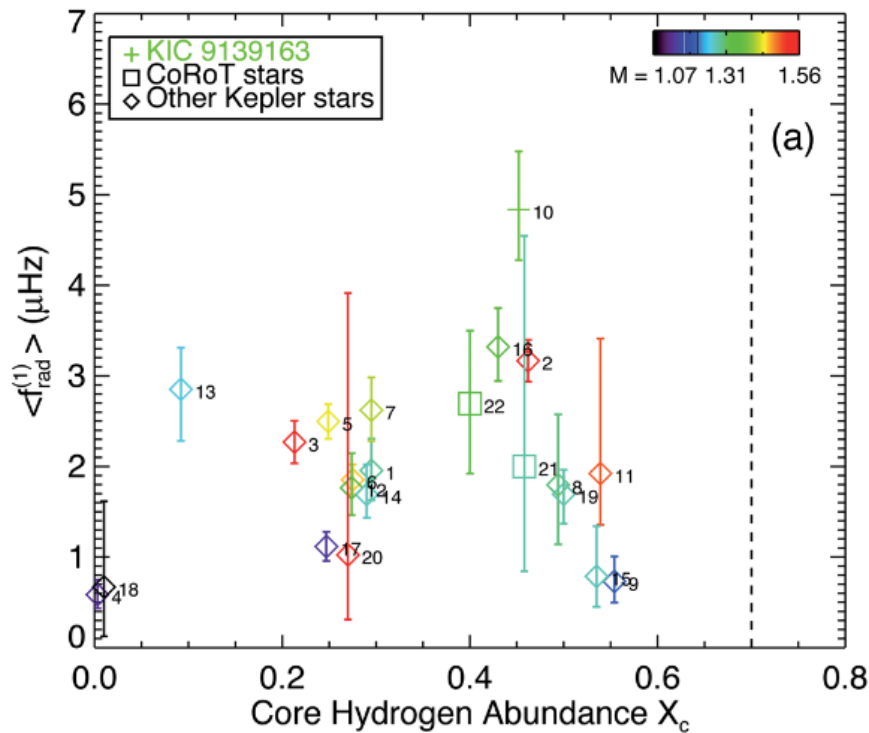


Figure 1.14: Internal rotation rate (f_{rad}) as a function of the core-hydrogen abundance X_c derived from stellar modelling. The vertical dotted line indicates the initial hydrogen abundance. Selected stars (identified by a number) cover different masses and a large part of the MS, but no evident slowing down of the interior is observed (from Benomar et al. 2015).

Theoretical Interpretation

In this Chapter, I will first interpret the observations of surface Li abundance, and of surface and internal rotation, shown in Chapter 1. Then, I will show how the interpretations highlight simultaneous constraints on the transport of chemicals and the transport of angular momentum, both in solar-type stars and in low-mass stars.

2.1 Lithium abundance

Lithium has long been used as a constraint on the transport of chemicals and on angular momentum in stellar interiors (e.g. Wallerstein & Conti 1969; Boesgaard 1976; Vauclair et al. 1978; Spite & Spite 1982a; Baglin et al. 1985; Vauclair 1988; Lebreton & Maeder 1987; Baglin & Lebreton 1990; Boesgaard 1991; Charbonnel et al. 1992, 1994; Deliyannis et al. 2000; Montalbán & Schatzman 1996; Montalbán & Schatzman 2000; Piau & Turck-Chièze 2002; Charbonnel & Talon 2005; Talon & Charbonnel 2010). This is due to the relatively low burning temperature of lithium at about 2.5 MK (close to the temperature at the base of the convective zone in solar-type stars) where Li is destroyed by proton capture reactions (p,γ).

The left side of Fig. 2.1 gives an overview of the situation. Because lithium is destroyed at a temperature of about 2.5 MK, it is burned in the internal region of the star. According to classical stellar evolution theory, Li destruction is expected to manifest at the surface of solar-type stars during the PMS and leads to a decrease of the surface Li abundance. During this phase, the convection zone is deep enough to reach a sufficient temperature to burn Li. Classical models that do not include transport processes beyond the convection zone predict no further surface Li variation until the first dredge-up episode¹ when stars evolve towards the RGB. However, the right side of Fig. 2.1 shows that classical models² fail to reproduce the Li evolution. It appears that an additional transport process should be involved. Spectroscopic observations show that the abundance of lithium at the surface of field and open cluster solar-type stars decreases along the MS (see Fig. 1.3 and Fig. 1.6 that presents stars in the PMS and MS phases, and Section 1.2.3). The observed depletion of Li is then interpreted as the evidence of (and a constraint on) an additional chemical transport, in particular at the base of the convection zone.

Similarly, beryllium, with a higher burning temperature of 3.5 MK, gives an additional constraint on the transport process. If the surface Li is depleted but not the surface Be, the ratio Li/Be will be

¹The first dredge-up corresponds to the point where the maximal depth of the convective envelope is reached along the RGB.

²See definition in introduction of Chapter 3.

changed depending on how deep the chemical mixing has gone in the stellar interior (e.g. Boesgaard et al. 2016, 2020; Deliyannis et al. 2019), as illustrated in Fig. 2.1. Besides, at older ages and/or for more massive and hotter stars, it could be an additional constraint in addition to the one linked to lithium.

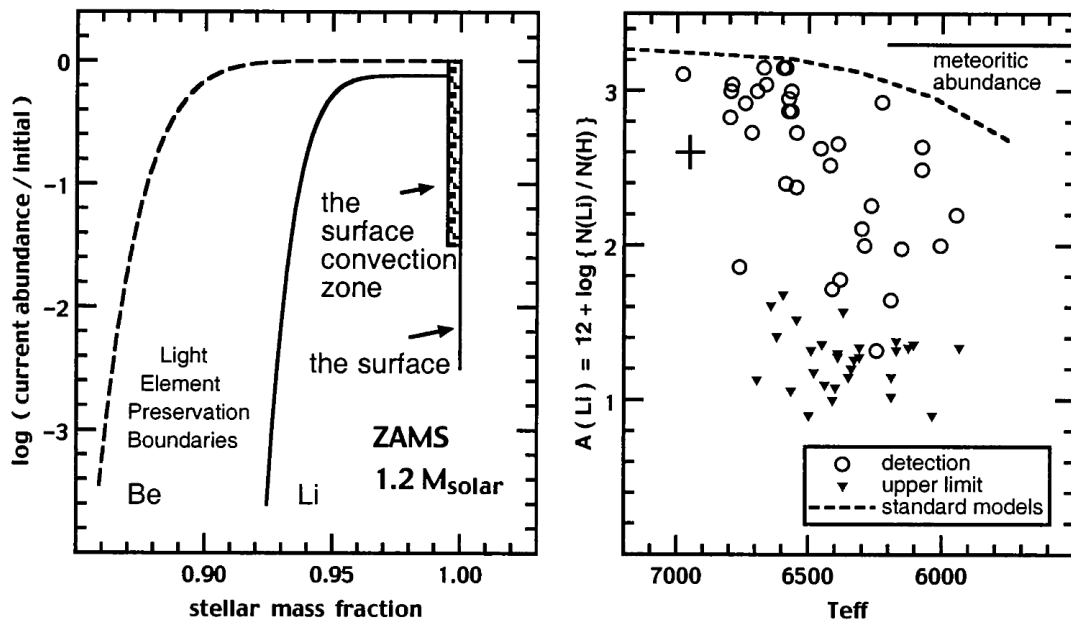


Figure 2.1: Left: Surface abundance profile of Li and Be as a function of the stellar mass fraction for a Zero Age Main Sequence (ZAMS) F-type star. Right: Predictions of the classical model compared to Li observations of field stars (from Deliyannis et al. 2000).

In Section 1.2, we showed that the surface lithium abundance was depleted as a function of the age of solar-like stars observed in open clusters (e.g. Jeffries 2000; Sestito & Randich 2005; Cummings et al. 2017; Deliyannis et al. 2019; Boesgaard et al. 2020). The dynamical processes at the origin of the Li-evolution should be effective during the PMS and the MS before reaching the evolved phases. It indicates that several processes could be at the origin of the two distinct depletions, the first one during the PMS and the second one during the MS with a shallower convective envelope. It indicates that during the MS phase, some dynamical processes are making a connection between the Li-burning layers of solar-like stars and their surface. In addition, when comparing the Li abundances of the Sun to a sample of 51 solar twins at similar ages in Fig. 1.3, we observed that the Sun is slightly Li-poor for its age. This deficiency in Li seems to indicate that the Sun is not a reliable benchmark for Li-depletion (as already demonstrated by Carlos et al. 2019) as well as for the constraint of the dynamical processes involved.

When increasing the range of stellar masses or stellar spectral-types, the surface Li abundance also shows discrepancies with the classical stellar evolution theory. Figure 2.2 shows the case of the surface Li abundance of the Hyades as a function of the effective temperature compared to two classical models (no atomic diffusion and no rotation). On the cold-side of the Li-dip described previously, these models do not deplete Li enough and highlight the lack of a chemical transport. The picture is even worse for the specific case of the Li-dip (between 6400 K and 6800 K) where classical models predict almost no depletion of the surface Li abundance. Figure 1.6 shows the general picture of lithium evolution, and illustrates the key parameters, such as mass and age. However, in view of the Li-dip, the interpretation has to be more complex. The specific location in temperature of the Li-dip (typically F-type stars) seems to indicate that there exists a threshold at

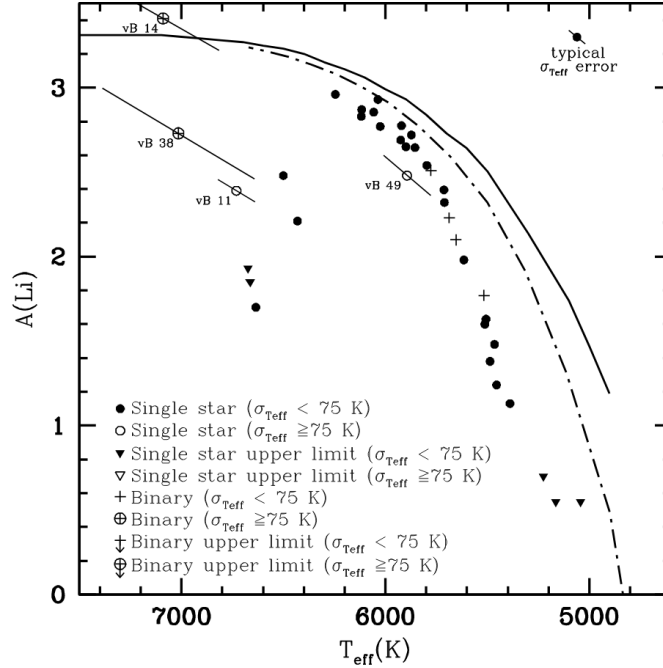


Figure 2.2: Li synthesis results from observations with WIYN/Hydra. The symbols are explained in the figure. The solid curve and dashed-dotted curve are Li isochrones from the classical (no rotation, diffusion, mass loss, etc) models of Pinsonneault (1997) and Somers & Pinsonneault (2014), respectively, for the Hyades age and metallicity. (From Cummings et al. 2017).

which different processes are involved.

Classical stellar evolution appears not adapted to reproduce these behaviours (Sun, solar-type stars, low-mass stars) and rotation-induced transport and mixing processes have been invoked to transport chemicals (e.g. Lebreton & Maeder 1987; Pinsonneault et al. 1990; Charbonnel et al. 1992; Richard et al. 1996; Do Nascimento et al. 2009).

2.2 Rotation: surface and internal

Rotational mixing is constrained by the rotation evolution of stars, shown for instance in Fig. 1.8 for solar-type stars. The angular velocity increases from its initial velocity during the stellar contraction that follows the disappearance of the disc at several Myrs to 10 Myrs. The behaviour is mainly driven by the extraction of angular momentum at the surface via magnetised winds (in other words, it corresponds to the magnetic braking). Finally, at older ages, we observe a decrease of the angular velocity that was found to follow the so-called law of Skumanich (1972) that accurately reproduces solar-type stars older than about 1 Gyr. This means that the processes at the origin of the two distinct depletions have to be efficient during the PMS for a high rotation velocity and during the MS at lower rotation velocity.

When considering different masses as in Figs. 1.9 and 1.10 the most massive stars ($1.2M_{\odot} < M < 1.5M_{\odot}$) showed higher rotation velocity at the same age than less massive stars ($M < 1.3M_{\odot}$). Kraft (1967) showed that the distribution of rotational velocities for stars hotter than mid-F-type, drops by an order of magnitude compared to ones cooler than mid-F-type. This break in the rotational period is interpreted as the result of a weaker, or ineffective, magnetic braking among the hotter and more massive stars ($> 1.2 M_{\odot}$) as a consequence of the transition from convective to

radiative atmosphere (Deliyannis et al. 2019). This is another indication of the need of dynamical processes for different rotation velocities and different masses.

The last constraint is shown in Fig. 1.12 that presents the rotational profile of the Sun as inferred by helioseismology. If the rotation of the core is unknown, the rotation in the radiative zone and in the convective envelope appears to be heterogeneous. In the radiative zone, the flat rotation profile is compatible with solid-body rotation. This means that a strong rotational coupling is involved between the different layers of solar-like stars. An efficient transport process for angular momentum is consequently expected to take place in these stars (see also Gallet & Bouvier 2013; Lanzafame & Spada 2015; Spada & Lanzafame 2020, who predicted strong transport for angular momentum). Moreover, the analysis of mixed modes in solar-mass subgiant (hereafter SGB) and RGB presenting solar-like oscillations also points to a low degree of radial differential rotation in the core. This means that the strong coupling found at solar ages is essentially maintained during the further evolution (Eggenberger et al. 2017, 2019a; Mathis et al. 2018; Aerts et al. 2019). No observational clue exists yet regarding the structure of the internal rotation during the PMS and the early MS evolution. Although there are hints that the quasi solid-body rotation of the solar interior may not be an exception to the analysis of asteroseismic data for solar-type stars (Nielsen et al. 2014) and for F-type to late G-type MS stars (Benomar et al. 2015).

2.3 Simultaneous analysis

We saw in the previous section that the abundance of Li and the stellar rotation are closely linked. Indeed, to explain the Li behaviour, the key role of rotational-mixing is now demonstrated (e.g. Steinhauer 2003). For instance, Boesgaard (1987) noted that the minimum in $A(\text{Li})$ in the Hyades coincides in T_{eff} with the break in the Kraft curve (or Kraft break) (see also Cummings et al. 2017; Deliyannis et al. 2019). Observations indicate that fast rotating stars possess higher Li abundances than slow rotating stars, which is linked to the PMS rotational evolution (e.g. Bouvier 2008; Somers & Pinsonneault 2015). In particular, it has been related to the difference in the disc lifetime between fast and slow rotators (e.g. Eggenberger et al. 2012a) or alternately to the correlation between rotation and penetrative convection (e.g. Baraffe et al. 2017).

Rotation in stars gives rise to instabilities that lead to both the transport of chemicals and of angular momentum. However, the correct modelling of rotation is challenging and the potential effect of additional transport processes is still under debate (e.g. Cummings et al. 2017; Amard et al. 2019; Deliyannis et al. 2019). Rotation involves several processes like meridional circulation, shear induced turbulence, magnetic braking through magnetised winds (see for instance comparative studies of Amard et al. 2016, 2019; Gossage et al. 2020). Besides, the failure to reproduce the internal rotation rates evidenced by helio- and asteroseismology (e.g. Mosser et al. 2012; Deheuvels et al. 2012, 2014, 2015, 2020; Ceillier et al. 2013; Marques et al. 2013; Benomar et al. 2015; Eggenberger et al. 2017, 2019a; Gehan et al. 2018; García & Ballot 2019; Mathis et al. 2018; Amard et al. 2019; Aerts et al. 2019) is another constraint to take into account. With the simultaneous evolution of the surface Li abundance and the surface rotation, it highlights the existence of dynamical processes other than rotation-mixing that transport both angular momentum and chemicals but potentially dependent on rotation (e.g. Do Nascimento et al. 2009, 2010; Somers & Pinsonneault 2016).

Several processes that are neglected in classical models are able to transport chemicals and/or angular momentum. Processes have been invoked to transport chemicals such as penetrative convection (e.g. Schlattl & Weiss 1999; Baraffe et al. 2017), which refers to the penetration of convective

cells in the radiative zone of the stars that leads to a chemical transport; tachocline³ mixing (Spiegel & Zahn 1992; Brun et al. 1999) that results in turbulent chemical transport at the interface between the convective envelope and the radiative zone, and planet accretion (ingestion of chemicals) during the MS (Montalbán & Rebolo 2002).

Processes have been invoked to transport angular momentum such as mass loss (Guzik & Mussack 2010), internal gravity waves that arise at the interface of the convective zones and propagate in the radiative zone transporting angular momentum (Montalban 1994; Charbonnel & Talon 2005), magnetic processes and instabilities (Gough & McIntyre 1998; Spruit 2002; Eggenberger et al. 2005, 2010b, 2019b,c; Fuller et al. 2014, 2019; Belkacem et al. 2015; Pinçon et al. 2017), mainly including the Tayler instability (Tayler 1973) that gives birth to a dynamo in the radiative interior leading to the transport of angular momentum. These mechanisms also impact the transport of chemicals induced by rotation and influence the way Li is depleted with time in solar-type stars (e.g. Charbonnel & Talon 2005; Talon & Charbonnel 2005; Eggenberger et al. 2010a).

Nevertheless, no current prescription is able to reproduce simultaneously both chemicals and angular momentum constraints (defined by both the surface angular velocity evolution and the solar rotation profile for solar-type stars).

It is now clear that a period(rotation)-age-mass relation exists for Li evolution in low-mass stars (e.g. Deliyannis et al. 2019) and that the correct characterisation of processes depending on these parameters would be key to understand Li evolution and bring any significant progress in stellar modelling.

The objective of the present thesis is to test the impact of different processes involved in the transport of chemicals and of angular momentum in low-mass stars. We have access to observational constraints, on Li abundance as well as on the surface rotational evolution, for solar-like stars as well as for low-mass stars from the K-type to the F-type spectral type, and with the additional constraint of the solar internal rotation. It opens the way to a better comprehension of the evolution of solar-type stars and low-mass stars through the support of a simultaneous analysis.

³See Section 5.3.2

Part II

Stellar evolution code STAREVOL

STAREVOL: Input physics

3.1 Introduction

Today, stellar modelling is still a difficult challenge. The difficulty comes from the identification and the description of different physical phenomena that involve different time-scale and space-scale. The combined effects on the structure, the chemical evolution, the rotation, etc, of the star lead to a complex and interdependent scheme that has to be taken into account.

Since the first stellar evolution models several decades ago, stars are in general modelled in one dimension to simplify the computation and consider a purely spherical geometry. The physical phenomena that exist in two or three dimensions in reality are then implemented in the 1D-codes. They are included by the way of 1D prescriptions or constraints from theoretical developments or theoretical assumptions or in the best cases from the average effects of the processes, obtained from specific 2D or 3D hydrodynamical or magnetohydrodynamical numerical simulations. However, depending on the process considered, the 1D approximation is more or less suitable.

In this PhD thesis, we present stellar evolution models of different types and adopt the following terminology:

- Classical Stellar Model (CSM). This model considers only the mixing in the convection zones and nuclear reactions.
- Standard Stellar Model (SSM). Model that also includes the atomic diffusion, efficient in the radiative zone.
- Non-Standard Stellar Model (NSSM). This model includes some complex physical phenomena such as stellar rotation, overshooting, etc. These processes are studied and described with the help of theoretical developments or hydrodynamic and magneto-hydrodynamic simulations. Their incorporation in 1D stellar codes is often complex.

To compute a stellar evolution model, we then need to assume the initial chemical composition and the mixing length parameter of the convection (α_{MLT}). To determine these parameters, models are calibrated on the Sun. Depending on the physical ingredients involved in the model, the calibration will be impacted and will lead different parameters. The calibration consists in a solar calibration of a one solar mass model. In other words, the aim is to reproduce, at the age of the Sun, the solar luminosity, the solar photospheric radius and the solar ratio ($\frac{Z}{X}$)_⊙. The free parameters of the calibration are: the mixing length parameter of the convection (α_{MLT}), the initial helium abundance (Y_{ini}) and the initial metal abundance (Z_{ini}).

As a consequence, we will calibrate each model that we shall use to obtain the initial parameters adapted for each case (CSM, SSM and NSSM).

It has to be kept in mind that a solar calibration is a calibration on one point, the Sun, however it gives a common benchmark for the different stellar evolution codes used in the community. It will be the object of Chapter 7, where we will describe the main calibrations done and used during the PhD thesis.

3.2 Generalities on the stellar evolution code STAREVOL

The stellar evolution code STAREVOL is a lagrangian 1D code that solves the equations of stellar structure (Eqs 3.1-3.5). These equations are solved in the framework of a spherical geometry, where we follow a mass element m_r during the evolution applying the Henyey method (finite differences). Solutions to the equations are then found from the previous time-step by the way of the iterative Newton-Raphson method.

Continuity equation

$$\frac{\partial r}{\partial m_r} = \frac{1}{4\pi r^2 \rho}, \quad (3.1)$$

with r the radius, m the mass, ρ the density.

Continuity of motion

$$\frac{\partial u}{\partial t} \frac{1}{4\pi r^2} = - \left(\frac{\partial P}{\partial m_r} + \frac{Gm_r}{r^4} \right), \quad (3.2)$$

where t is the time, $u = \partial r / \partial t$, P is the pressure, G is the gravitational constant¹. with the hydrostatic equilibrium as:

$$\frac{\partial P}{\partial m_r} = \frac{-Gm_r}{4\pi r^4}, \quad (3.3)$$

Energy conservation

$$\frac{\partial L_r}{\partial m_r} = \epsilon_n - \epsilon_\nu + \epsilon_{\text{grav}}, \quad (3.4)$$

with L_r the luminosity, ϵ_n the energy produced by nuclear reactions, ϵ_ν the energy loss by escaped neutrinos and ϵ_{grav} the gravitational energy (<0 if the star is contracting and >0 if the star is expanding).

Energy transport

$$\frac{\partial T}{\partial m_r} = - \frac{Gm_r}{4\pi r^4 P} \nabla, \quad (3.5)$$

where the gradient of temperature ∇ is defined as:

$$\nabla = \frac{\partial \ln T}{\partial \ln P} = \begin{cases} \nabla_{\text{rad}} = \frac{3}{16\pi a c G} \frac{\kappa L_r P}{m T^4} \\ \nabla_{\text{conv}} = \left(\frac{\partial \ln T}{\partial \ln P} \right)_{\text{ad}} \end{cases} \quad (3.6)$$

with κ the Rosseland opacity, $a = 4\sigma/c$, c the light speed velocity², and σ the Stefan constant³

The work of this thesis is mainly based on the use and the development of the stellar evolution code STAREVOL (Geneva-Montpellier). This chapter is dedicated to the description of the

¹ $G = 6.6738 \times 10^{-11} \text{ m}^3 \cdot \text{kg}^{-1} \cdot \text{s}^{-2}$

² $c = 2.99792458 \times 10^8 \text{ m} \cdot \text{s}^{-1}$

³ $\sigma = 5.67 \times 10^{-8} \text{ J} \cdot \text{s}^{-1} \cdot \text{m}^{-2} \cdot \text{K}^{-4}$

physical inputs used in the STAREVOL code. These ingredients allow the computation of the three types of model described previously. After a brief introduction on the main ingredients of stellar modelling I will describe the improvements realised during the PhD. In Sections 3.3, 3.4, 3.5, and 3.6 we present the choices for the treatment of the equation of state, nuclear reactions, initial abundances, and the opacity. Section 3.7 presents the treatment for convection and penetrative convection. Section 3.8 gives the details for the boundary conditions and Section 3.9 presents the mass loss used in STAREVOL.

3.3 Equation of state

The EOS provides the needed quantities for the stellar structure and evolution equations the pressure P and the entropy s , as well as their derivative on the temperature T and the density ρ . The Equation Of State (EOS) is based on the principle of Helmholtz free energy minimisation and follows Eggleton et al. (1973) and Pols et al. (1995) where a change of variable from ρ to free energy f is applied in order to optimise the computation by a better description of the electronic degenerescence in the star, and to determine the gravity energy ϵ_{grav} (Dufour 2000; Siess et al. 2000). It is thus easier to solve the Saha equation that gives the relative concentrations of atoms in the different ionisation degrees.

In the previous versions of STAREVOL code, partial ionisation was activated only for hydrogen and helium and total ionisation was assumed for others elements. However, Saha equation in STAREVOL allows to compute partial ionisation for elements from hydrogen to chlorine (see Section 3.4). During the thesis we relaxed total ionisation assumption and consider partial ionisation for all available elements in STAREVOL. Indeed, the ionisation rate has an important effect for particles interaction and consequently for the atomic diffusion process that will be described in Chapter 4. Ionisation happens when a bound electron is ejected from the atom. This ejection needs energy and is connected to the temperature and the pressure of the surrounding medium. In the deep interior of stars, P and T are large and the total ionisation is a good approximation (at the exception to the heaviest element as iron). However, when approaching the surface, T and P are decreasing and the degree of ionisation becomes smaller. The ionisation is only partial. Solving the Saha equation in all the star, we determine the profile of ionisation rate. The normalised ionisation rate is defined as $Z_{\text{mean}} = \frac{Z_{\text{ionise}}}{Z} = 0$ if the gas is neutral, and $Z_{\text{mean}} = \frac{Z_{\text{ionise}}}{Z} = 1$ if the gas is completely ionised. Normalised ionisation rate as a function of the logarithm of temperature is shown Fig. 3.1 left panel.

Total ionisation is imposed for temperatures higher than $T = 5 \times 10^6$ K ($\log T = 6.7$) or if $\ln(f) > 100$ as justified by Schlattl (2002). The right panel of Fig. 3.1 shows the results obtained by Schlattl (2002) for the Sun (a) and for a $1.1M_{\odot}$ star (b). At $\log T = 6.7$, He, C and O are totally ionised ($\bar{\zeta}/Z = 1$ where $\bar{\zeta} = Z_{\text{mean}}$ is the mean ionisation degrees and Z the charge number), and Fe always partially ionised, for the Sun and also for the metal-poor model of $1.1M_{\odot}$ near the Turn-off.

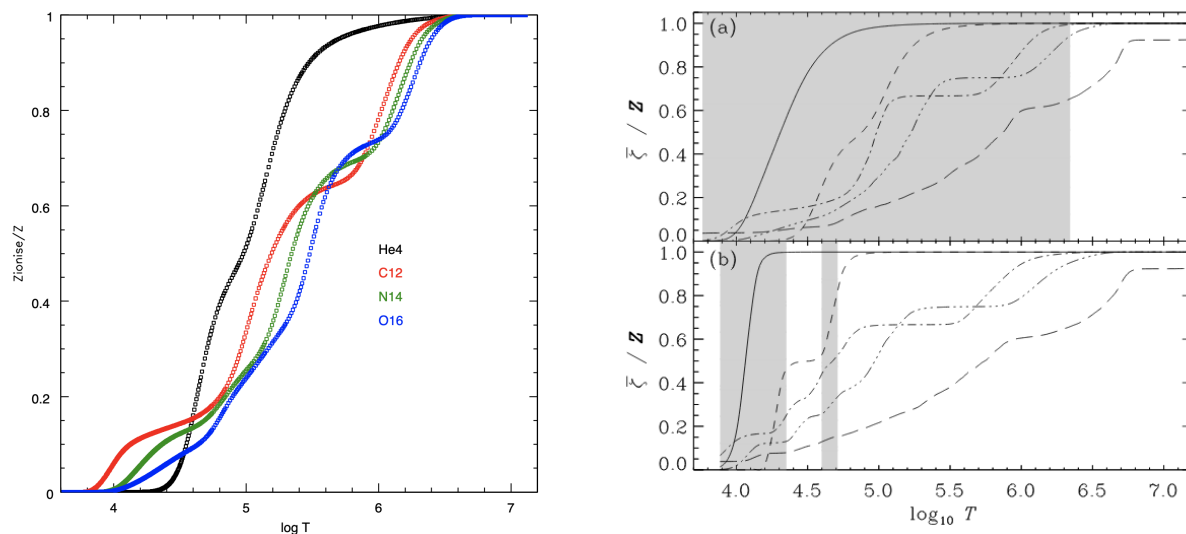


Figure 3.1: (Left) Profile of normalised ionisation rate vs $\log T$ (K) from a STAREVOL solar model at solar age. (Right) Mean ionisation degrees $\bar{\zeta}$ of H (solid line), He (short-dashed line), C (dash-dotted line), O (dash-dot-dot-dotted line), and Fe (long-dashed line) normalised to their respective charge number Z . (a) The Sun. (b) Metal-poor star with $[\text{Fe}/\text{H}] = -1.3$, of $1.1 M_{\odot}$ near the Turn-off. The grey area refers to the convective envelope (from Schlattl 2002).

3.4 Nuclear reactions

STAREVOL follows the evolution of 54 chemical species from ^1H to ^{37}Cl that are involved in 185 nuclear reactions. The rates of thermonuclear reactions are extracted from the NACRE II database according to Xu et al. (2013b) via the NetGen web interface (Xu et al. 2013a). The screening factors are computed using the formalisms of Graboske et al. (1973) and Mitler (1977).

3.5 Initial abundances

When computing stellar models, we rely in most cases on the solar reference abundances and on the relative abundances of individual isotopes. Solar abundances are determined from the spectroscopic study of the solar photosphere. The choice of the solar reference abundances will affect the resulting opacity and impact the results of stellar modelling (e.g. Serenelli 2016). In the last decades, they have been revised multiple times (e.g. Anders & Grevesse 1989; Grevesse & Noels 1993; Grevesse & Sauval 1998; Asplund et al. 2005, 2009; Caffau et al. 2011; Young 2018). The main changes come from the introduction of the 3D radiation hydrodynamics models of the solar atmosphere, the improvement of atomic data and the inclusion of non-local thermodynamic equilibrium (NLTE) corrections. It led mainly to a change in metallicity Z from $Z_{\odot} = 0.0201$ according to Anders & Grevesse (1989) to $Z_{\odot} = 0.0134$ according to Asplund et al. (2009). At the beginning of the thesis, in STAREVOL, we were using the abundances from Asplund et al. (2009).

From the abundances of Grevesse & Sauval (1998), widely used in the solar community, to the abundances recommended more recently by Asplund et al. (2009), the abundance of C, N and O were decreased by factors of 1.3-2. This yields a decrease of Ne and of the opacity in the stars, as Ne is the third contributor to stellar opacity (Blancard et al. 2012). Indeed, the Neon abundance is estimated by the mean of the ratio Ne/O. Recently, Landi & Testa (2015) pointed out the issue when estimating the abundance of Neon by the way of this ratio that depends on a good measure of O abundance. Besides, it was already suggested by Cunha et al. (2006), who observed a Neon

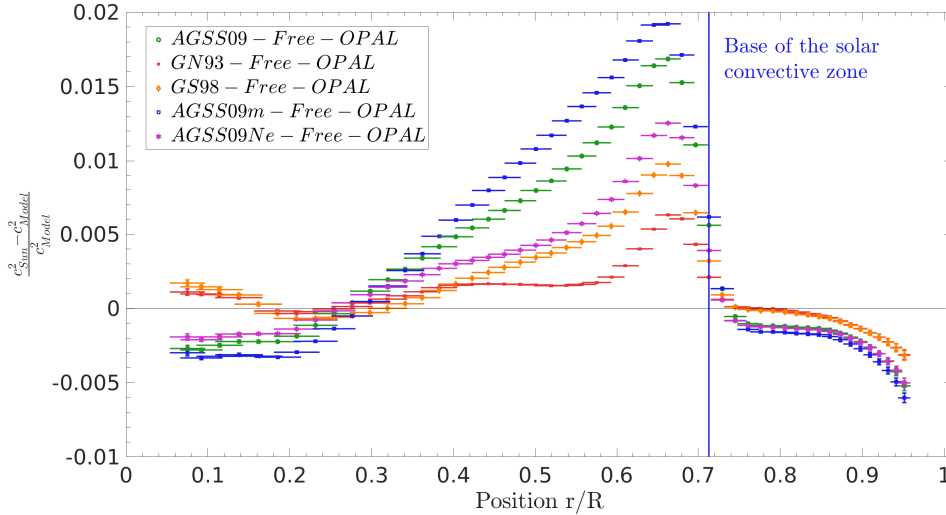


Figure 3.2: Relative differences in squared adiabatic sound speed between the Sun (obtained from seismic inversions) and calibrated solar models for different choices for the solar reference abundances (from Buldgen et al. 2019). AGSS09: Asplund et al. (2009), GN93: Grevesse & Noels (1993), GS98: Grevesse & Sauval (1998), AGSS09m: C, N, O, Ne and Ar taken from meteoritic values as done in Serenelli et al. (2009), AGSS09Ne: Young (2018).

enhancement in B stars. When using these recent abundances in stellar models the results are in less agreement with helioseismology than older references (e.g. Serenelli et al. 2009). For instance, it is the case for the sound speed as shown in Fig. 3.2 where the model using Asplund et al. (2009) (AGSS09) is plotted in green. This discrepancy has been identified as a consequence of the opacity reduction in the radiative zone (Serenelli et al. 2009). Observing the Sun, Landi & Testa (2015) then showed that the ratio Ne/O is not constant in the solar atmosphere, both in time and at different heights. The photospheric value of Ne should be increased by about 40 % to be closer to the true value. Indeed, it was shown by Buldgen et al. (e.g. 2019) that taking the abundances of Asplund et al. (2009) plus Ne-enhancement (Young 2018) allows to obtain better results regarding helioseismology (for instance for the sound speed profile). It is what we observe in Fig. 3.2 where the track plotted in magenta shows the model including Ne-enhancement (AGSS09Ne).

It is today a common hypothesis that was already used by Lagarde et al. (2012) who computed STAREVOL models following recommendations from Cunha et al. (2006) or, for instance, by Zhang et al. (2019) who followed abundances from Young (2018). Three references for initial abundances were initially available in STAREVOL: abundances from Grevesse & Noels (1993, GN93), Asplund et al. (2005, AGS05) and Asplund et al. (2009, AGSS09). I implemented the new reference with the enhancement for neon (increased of 40 %) recommended by Landi & Testa (2015); Young (2018, AY18).

However, differences and the so-called "solar abundance problem" (Serenelli et al. 2009) remain, see for instance Fig. 3.2, and is discussed as a future major improvement if solved (see for instance by Montalbán et al. (2006); Serenelli (2016); Vinyoles et al. (2017); Buldgen et al. (2019); Capelo & Lopes (2020).

3.6 Opacity

The opacity of a star is the ensemble of the frequency-dependent interactions (photo-absorption) between radiations and matter in the star. In the STAREVOL code, the opacity profiles are interpolated within opacity tables that give possible interactions at each step of the evolution. They

provide the Rosseland mean opacity κ for a range of temperatures, densities and chemical compositions (He, CNO and Z). Different opacity tables are available in the literature: OPAL: Iglesias & Rogers (1996), OP: Seaton (2005), OPAS: Mondet et al. (2015), OPLIB: Colgan et al. (2016). OPAL and OP give similar values and are at the origin of improvements in the explanations of β Cephei pulsations (see e.g. Cox et al. 1992; Salmon et al. 2012). However, an advantage of OPAL is that it provides a public and fully consistent EOS alongside the opacity tables (Rogers et al. 1996). This is not the case of OPAS and OPLIB for which the EOS is not available. Differences between the EOS used by OPAS and OPLIB on one side and by OPAL and OP on the other may also explain large differences observed at high temperatures. In addition, Richer et al. (1998) showed that the amplitudes of radiative accelerations are very similar for both OPAL and OP opacity tables. In STAREVOL, only OPAL opacity tables are implemented and used.

Rosseland opacities are interpolated in STAREVOL according to the scheme of A. Boothroyd (livopaint table⁴) among the OPAL opacity tables (Iglesias & Rogers 1996) for high temperatures ($T > 8000$ K). At lower temperatures ($T < 8000$ K), we use the Wichita opacity database from Ferguson et al. (2005). The opacity tables were generated on the OPAL website⁵ at the exception to lower temperatures that were directly provided by J. W. Ferguson. They were consistently updated for the AY18 abundances (see Appendix A).

3.7 Convection and penetrative convection

The treatment of convection is done following the so-called Mixing Length Theory (MLT) according to Böhm-Vitense (1958) and Kippenhahn et al. (1991). The mixing length is defined as $\Lambda = \alpha_{\text{MLT}} H_P$ with H_P the local pressure scale height ($H_P = \frac{dr}{d \ln P}$) and α_{MLT} the mixing length parameter. Convective boundaries between a radiative zone and a convective zone are determined by the Schwarzschild criterion.

Penetrative convection

The MLT formalism associated to the Schwarzschild criterion for the instability to describe the extent of the convective regions is known to be flawed as the convective edges are defined according to null acceleration instead of null velocity of convective eddies. Convection actually penetrates in the sub-adiabatic layers below (for the convective envelopes) the superadiabatic unstable region. This generates mixing beyond the convective region down to where convective eddies are braked or eroded (e.g. Zahn 1991). This concretely results in the penetration of convective eddies in the adjacent stable radiative zone leading to an additional mixing at the interface. The depth of penetration d_{ov} is defined as the distance between the interface of the radiative and the convective zone defined by the Schwarzschild criteria and the point of convective mixing extension (see Fig. 3.3). At this point, we note that penetrative convection and overshoot are not always well defined in the literature and that they are sometimes confused in one single process. In this manuscript, we follow Zahn (1991) and define the general process as penetrative convection. Overshoot (in the case of penetrative convection below the convective zone, we could also use undershoot term) then involves only the transport of chemicals at the base of the convective zone (or from the convective core if applicable) but does not take into account the effects on the temperature gradient ∇T expected from the penetrative convection process. Penetrative convection or overshoot can be described based on the MLT theory and several formalisms have been

⁴<https://www.cita.utoronto.ca/boothroyd/>

⁵<https://opalopacity.llnl.gov/opal.html>

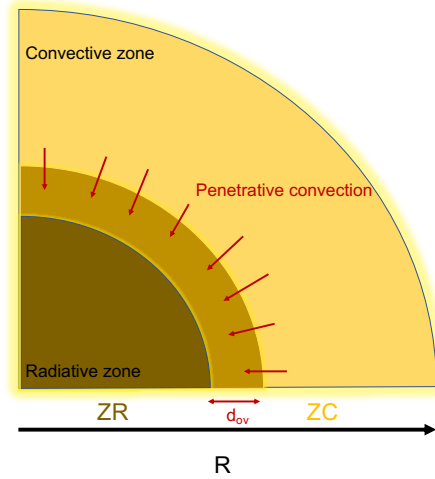


Figure 3.3: Schematic view of the penetrative convection in a solar-type star. The penetration depth d_{ov} determines a zone in the radiative zone where convection apply.

described and implemented in stellar evolution codes. We will focus on the penetrative convection between the convective envelope and the radiative zone of solar-type stars.

In the PhD thesis, we always treated penetrative convection as overshoot (without impacting ∇T). There are two ways to implement overshoot: the *step overshoot* as e.g. Ekström et al. (2012) where the convection zone is simply extended by a factor dependent of the pressure scale height H_P and the *diffusive overshoot* where a diffusion coefficient is added in the equation of chemical species transport (Herwig et al. 1997). In order to improve the overshoot formalism, hydrodynamical simulations and/or additional constraints are needed. Hereafter, I will briefly present the step overshoot and three different formalisms for the diffusive overshoot that were especially implemented and studied thorough the PhD thesis.

Step overshoot

The *step overshoot* consists in imposing a radial extension to the convective zone limited by a free parameter α_{over} and dependent on the pressure scale height H_P . The new radius of the base of the convective envelope is then: $R_{bcz,new} = R_{bcz,old} - \alpha_{over}H_P$ where $R_{bcz,old}$ is the base of the convective envelope determined with the Schwarzschild criterion. Step overshoot is commonly used in stellar evolution to obtain a more realistic extension of the convection zones, highlighted by helioseismic observations to be beyond the limits defined by the Schwarzschild criteria (e.g. Basu et al. 1994; Christensen-Dalsgaard et al. 2011). Also, the new size of the convective envelope, imposed by the step overshoot, necessary includes the corresponding ∇T .

Formalism by Baraffe et al. (2017)

During the PhD thesis, we implemented the formalism proposed by Baraffe et al. (2017). It is based on 2D and 3D hydrodynamic simulations of a young Sun on the PMS at 1 Myr and at solar metallicity (Pratt et al. 2017). These simulations allow them to characterise the depth of the penetrative convection below the convection zone and show the existence of extreme events (deep penetrating plumes), which can have an outsized impact on transport mechanisms, especially those that are meant to be inviscid. The diffusion coefficient obtained by Pratt et al. (2017) and reproduced here in Eq. (3.7), describes the mixing in the penetration layers and is characterised by

the cumulative distribution function of the maximal penetration depth obtained in the simulations:

$$D_B(r) = D_0 \left[1 - \exp \left(- \exp \left(- \frac{r_{\text{bcz}} - r}{R} - \mu \right) \right) \right] \quad (3.7)$$

where r is the local radius, r_{bcz} is the radius at the base of the convective zone, R is the total radius of the star. The coefficients $\lambda = 6 \times 10^{-3}$ and $\mu = 5 \times 10^{-3}$ are constants as prescribed by Baraffe et al. (2017) and obtained from the simulations of Pratt et al. (2017). D_0 refers to the convective turbulent diffusivity obtained from MLT:

$$D_0 = \frac{v_{\text{conv}} H_p \alpha_{\text{MLT}}}{3} \quad (3.8)$$

with v_{conv} the mean velocity of the convective elements obtained from MLT, H_p the pressure scale-height and α_{MLT} the mixing length parameter. The effect of penetrative convection is treated as overshoot below the convective envelope (the temperature gradient stays unchanged in the concerned region). The penetration depth of the overshooting is limited by the free parameter d_{ov} linked to the pressure scale-height and adjusted to take into account the limiting effect of stellar rotation. Baraffe et al. (2017) determined that this parameter should be $d_{\text{ov}} \approx 0.30H_p - 0.35H_p$ to reproduce the solar lithium abundance if d_{ov} is a constant. Baraffe et al. (2017) also proposed to vary the depth of the overshooting zone depending on rotation, as supported by numerical studies (Ziegler & Rüdiger 2003; Brummell 2007; Brun et al. 2017). They adopted $d_{\text{ov}} = 0.1H_p$ when the star is rapidly rotating ($\Omega > 5\Omega_{\odot}$, i.e. typically on the late PMS and around the ZAMS) and a much deeper overshooting zone ($d_{\text{ov}} = 1H_p$) for slower, more evolved rotating stars.

However, in this case, the rotation dependence, is not self-consistent. Formalisms for penetrative convection, self-consistent with rotation, have been, nevertheless, realised, and two formalisms were implemented during the PhD thesis. Indeed, a high stellar rotation will tend to decrease the depth of penetration by the action of the centrifugal force. It is consequently possible to define a time-dependent overshoot that evolving with the stellar rotation.

Formalism by Augustson & Mathis (2019)

We implemented the formalism by Augustson & Mathis (2019) as an overshoot process. It is based on a new model of rotating convection in stellar interiors. Contrary to Eq (3.7), the derivation of the penetration depth follows Zahn (1991). In his work, Zahn (1991) linearised the equations of motion in the region of penetration and the depth of penetration is then derived in order to give the velocity at the upper boundary of that region, which is assumed to reside in the convection zone. In Augustson & Mathis (2019), the impact of rotation on the convection is accounted for using a modal convection model for rotating Rayleigh-Benard convection (Barker et al. 2014) where it is assumed to be locally valid in the region of penetration. This model has the asymptotic property that the velocity scales as $(v/v_0) \propto \text{Ro}^{1/5}$, with $\text{Ro} = \frac{\text{inertial}}{\text{Coriolis}} = \frac{v}{2\Omega l \sin(\varphi)}$ the Rossby number⁶, which is inversely proportional to the angular velocity in the convective region. The depth of the overshooting zone then depends on the pressure scale-height, the convective Rossby number (hence angular velocity), and the thermal diffusivity, and is dynamically estimated. The depth of the overshoot is however controlled with the free parameter d_{ov} . Using this model for penetrative convection and the functional form proposed by Pratt et al. (2017), Augustson & Mathis (2019) derived a new expression for the diffusion coefficient (their Eq. (70)):

$$D_A(r) = \left(\frac{5}{2} \right)^{1/6} \frac{\alpha H_{P,0} v_0 h}{3\sqrt{z}} \left[1 - \exp \left(- \exp \left(\frac{r - r_{\text{bcz}}}{\lambda L_p} + \frac{\mu}{\lambda} \right) \right) \right] \quad (3.9)$$

⁶ Ω is the angular velocity, l is the mean free path, v is the velocity, φ is the angle between the rotation axis and the direction of the fluid motion

3.7. Convection and penetrative convection

where r , r_{bcz} , μ , λ are the same as in Eq. (3.7), $\alpha = \alpha_{MLT}$, $H_{P,0}h = H_P$, h is the scale-height ratio, L_P is the penetration depth, z is a normalised wave-vector.

In the code STAREVOL, we approximate that expression, using:

$$D_A(r) \approx D_0 \left[1 - \exp \left(- \exp \left(\frac{r - r_{\text{bcz}}}{d_{\text{ov}} \times \left(\frac{v}{v_0} \right)^{3/2} + \frac{\mu}{\lambda}} \right) \right) \right] \quad (3.10)$$

where D_0 is given Eq. (3.8) and (v/v_0) is the ratio of the rotating to the non-rotating velocity of the convective elements. Eq. (69) from Augustson & Mathis (2019) gives:

$$\left(\frac{v}{v_0} \right)^{3/2} = \frac{L_P}{L_{P,0}} = \left(\frac{5}{2} \right)^{1/4} z^{-3/4} \quad (3.11)$$

This implies that the diffusion coefficient in Eq. (3.10) is smaller when the star rotates faster, mimicking the fact that fast rotation inhibits penetrative convection to penetrate deep into the stable stratified region below. Thus, this model is a combination of the Baraffe et al. (2017) fitted to their numerical stellar convective penetration simulations and the theoretical results of Augustson & Mathis (2019).

Formalism by Korre et al. (2019)

We implemented the formalism by Korre et al. (2019) as an overshoot process. It is based on hydrodynamical simulations of penetrative convection and overshooting in a non-rotating Boussinesq spherical shell⁷. Korre et al. (2019) propose a diffusive prescription suitable for 1D stellar evolution code. In comparison to the simulations of Pratt et al. (2017), these simulations include an explicit diffusion, being the Navier-Stokes equations rather than an approximation of the Euler equations. The prescription is given by Eq. (45) of Korre et al. (2019):

$$D_K(r) = D_0 \exp \left(- \frac{(r - r_{\text{bcz}})^2}{2\delta_G^2} \right), \quad (3.12)$$

where D_0 (noted D_{cz} in the original paper) is the same as in Eq. (3.7) and δ_G controls the depth of the penetration and is defined as:

$$\delta_G \approx 1.2 \left(\frac{E_0 Pr}{S Ra_0} \right)^{1/2}, \quad (3.13)$$

where E_0 is the mean kinetic energy in the non-rotating convection zone, $Pr = \nu/\kappa_T$ is the Prandtl number defined as the ratio between the viscosity ν and the thermal diffusivity κ_T , S is the stiffness that measures the stability of the interface between the radiative zone and the convective zone and Ra_0 is the Rayleigh number defined in Korre et al. (2019) as:

$$Ra_0 = \frac{\alpha_{\text{th}} g \left| \frac{dT_0}{dr} - \frac{dT_{\text{ad}}}{dr} \right| r_0^4}{\kappa_T \nu}, \quad (3.14)$$

with α_{th} the thermal expansion coefficient, g the gravity, $\frac{dT_{\text{ad}}}{dr}$ the adiabatic temperature gradient, $\frac{dT_0}{dr} = \frac{dT_{\text{ad}}}{dr} |_{r=r_0}$, r_0 the outer radius of the convection zone and ν the viscosity.

We use Eq. (3.15) (instead of Eq. (3.12)), which is a result of fits to the numerical penetrative convection simulations carried out in Korre et al. (2019) where the overshooting length is adapted to

⁷The approximation of Boussinesq assumes an incompressible medium with no density variations except for the determination of the buoyancy force (see e.g. Maeder 2009).

contain information about the local rotation rate through the convective model of Augustson & Mathis (2019) and its implications for a linearised convective penetration model:

$$D_K(r) \approx D_0 \exp\left(-\frac{(r - r_{bcz})^2}{d_{ov}^2 \times \left(\frac{v}{v_0}\right)^2}\right). \quad (3.15)$$

δ_G is approximated using the same principle as for $D_A(r)$ and adding the velocity dependence (v/v_0) (Augustson & Mathis 2020)

$$\delta_G \approx d_{ov} \times \frac{v}{v_0}. \quad (3.16)$$

Due to this inverse dependence on rotation, $D_K(r)$ is also smaller when the star rotates faster. Regarding the initial numerical simulation of Korre et al. (2019), the way that we adapted the rotational dependence with the help of the Augustson & Mathis (2019), combining the two, should be taken with precautions when used. However, in the framework of slow-rotators ($\Omega < 5\Omega_\odot$), it is a relevant assumption to use.

3.8 Surface boundary condition

The atmosphere of the star is defined with the help of the optical depth τ that gives a consistent stratification of the outer layers of a star where the density is weak. The inner edge of the atmosphere is usually defined for $\tau = 2/3$ with τ as:

$$\tau = \int_R^\infty \kappa \rho dr = \bar{\kappa} \int_R^\infty \rho dr \quad (3.17)$$

where $\bar{\kappa}$ is the Rosseland mean opacity, average over the stellar atmosphere.

The atmosphere can be treated in a stellar evolution code with two main approaches. The first one is based on analytical relations between the optical depth τ and the temperature $T(\tau)$. The second one is based on the use of stellar atmosphere model tables.

For the present thesis, we used two analytical expressions for the temperature profile in the atmosphere as outer boundary conditions to the stellar structure equations.

The grey atmosphere relation also known as the Eddington approximation gives the temperature function of the optical depth τ as:

$$\frac{4}{3} \left(\frac{T(\tau)}{T_{\text{eff}}}\right)^4 = \frac{2}{3} + \tau, \quad (3.18)$$

that gives $T(\tau = 2/3) = T_{\text{eff}}$.

The linear approximation of 3.18 can be corrected using the Hopf function $q(\tau)$ according to Hopf (1930); Morel et al. (1994) as:

$$\frac{4}{3} \left(\frac{T(\tau)}{T_{\text{eff}}}\right)^4 = q(\tau) + \tau, \quad (3.19)$$

at a given optical depth τ , T_{eff} being the temperature of the equivalent black body and $T(\tau)$ the temperature profile.

We also used the analytical expressions, scaled on the Sun, from Krishna Swamy (1966) (hereafter KS66) that give $q(\tau)$ as:

$$q(\tau) = 1.39 - 0.815 \exp^{-2.54\tau} - 0.025 \exp^{-30\tau}. \quad (3.20)$$

3.8. Surface boundary condition

These relations are independent of the metallicity and the KS66 was derived for G and K dwarf stars only. In order to have a more realistic treatment of the atmosphere, taking into account variation of the surface gravity and of the chemical composition, one could use tabulated model atmospheres.

This other method provides tables adapted for a defined range of effective temperatures, metallicities and/or effective gravity (e.g. ATLAS: Kurucz (1970), PHOENIX: Allard et al. (2012) and Amard et al. (2019)).

Figure 3.4 shows a comparison of evolutionary tracks in the Hertzsprung-Russell diagram for three calibrated models using different treatments of atmosphere: Grey, KS66 and PHOENIX (from Amard et al. 2019). The results obtained with KS66 and PHOENIX are in good agreement, but different from the grey atmosphere in the PMS and RGB phases. The analytical expressions from KS66 are then a good assumption in the case of a solar model.

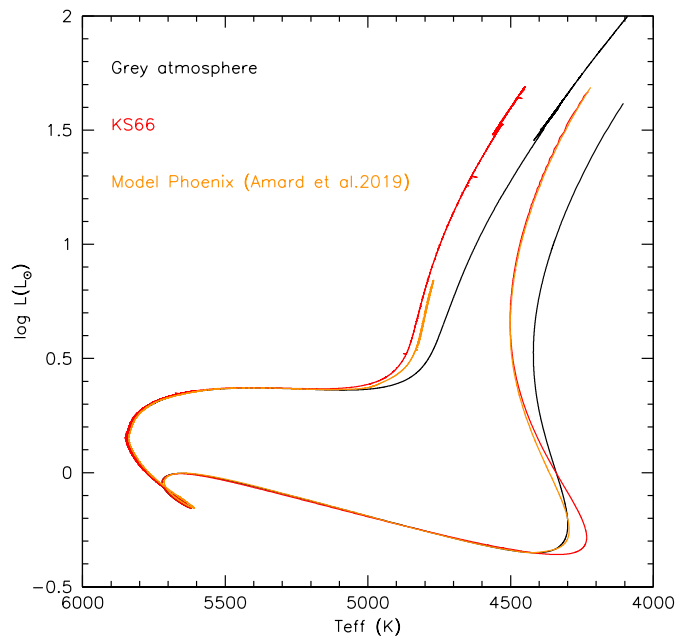


Figure 3.4: Evolutionary tracks in the Hertzsprung-Russell diagram of three solar models with different treatments of the atmosphere, computed with STAREVOL. The black line gives the model using the grey approximation, the red line gives the model with KS66 formalism and the orange line gives the track obtained by Amard et al. (2019) for the PHOENIX atmosphere.

We finally fix a value for the attachment location of the atmosphere, or in others words the point where the temperature profile is given by mean of the τ and not any more by the structure equations. According to VandenBerg et al. (2008) and Choi et al. (2018), the attachment location of the atmosphere does not impact the effective temperature in the case of a solar-calibrated model. The atmosphere is then integrated up to an optical depth of $\tau_0 = 0.005$ and the connection to the atmosphere made at $\tau_{ph} = 2$.

In this PhD, we used for all models the analytical expression from Krishna Swamy (1966) for $q(\tau)$, unless mentioned otherwise.

3.9 Mass loss

In our CSM and SSM models, we assume the prescription for the stellar mass loss given by Reimers (1975):

$$\dot{M} = -3.98 \times 10^{-13} \eta_R \frac{LR}{M} M_{\odot} \cdot yr^{-1}, \quad (3.21)$$

where η_R is a free parameter dependent on the evolution phase and/or the metallicity. Results from McDonald & Zijlstra (2015) give a median determined from 56 GCs of $\eta_R = 0.477 \pm 0.07$. As advocated by McDonald & Zijlstra (2015) and Guo et al. (2017) for solar-type stars based on observational constraints on the red giant branch, we shall take 0.5 for our models.

In case of rotating models, we use the mass loss prescription according to Cranmer & Saar (2011). This prescription takes into account the effects of rotation on stellar activity, and consequently mass loss. Cranmer & Saar (2011) gave an expression made of two components. A first hot component carried by a hot stellar corona ($T \geq 10^6$ K) and dependent to the radiative pressure at the surface:

$$M^{\text{hot}} = \rho u A = \frac{4\pi R_{\star}^2 f_{\text{TR}}}{V_{\text{esc}}^2} (F_{H,TR} - F_{\text{cond}}), \quad (3.22)$$

with ρ the density, u the radial stellar wind velocity, $A = 4\pi r^2 f$ the cross-sectional area of the total stellar surface covered by flux tubes opened to the stellar winds (f : a dimensionless filling factor), R_{\star} the stellar radius, $V_{\text{esc}} = (2GM_{\star}/R_{\star})^{1/2}$ the escape velocity, f_{TR} is a dimensionless filling factor at the transition region⁸, $F_{H,TR}$ the heat flux at the transition region and F_{cond} the energy flux transported by heat conduction along the field.

A second cold component is carried by pressure waves generated by the Alfvén waves and consequently by the stellar magnetic field⁹.

$$M^{\text{cold}} = 4\pi r_{\text{crit}}^2 u_{\text{crit}} \rho_{\text{crit}} \quad (3.23)$$

with r_{crit} the critical radius and ρ_{crit} the critical density, both defined at the radius where the wind velocity is equal to the sound velocity (Holzer et al. 1983). u_{crit} is the critical point velocity defined as $u_{\text{crit}}^2 = \frac{\nu_{\perp}^2}{4} \frac{1+3M_A}{1+M_A}$ where ν_{\perp}^2 is the transverse velocity amplitude of Alfvén waves in the photosphere and $M_A = u/V_A$ is the Alfvén Mach number with V_A the Alfvén velocity.

The combined mass loss is defined by:

$$\dot{M} \approx M^{\text{cold}} + M^{\text{hot}} \exp^{-4M_{A,TR}^2}, \quad (3.24)$$

with $M_{A,TR}$ the Alfvén Mach number at the transition region.

⁸Defined by Cranmer & Saar (2011) as the limit between the chromosphere and the corona.

⁹The cold component is consequently dependent on the choice for the magnetic braking.

Atomic Diffusion

The implementation of an optimised formalism for atomic diffusion in STAREVOL was one of the main objectives of the PhD thesis. In this Chapter, we describe the formalisms studied during the PhD thesis and the way how we proposed to improve the treatment of atomic diffusion in the code. Details about the validation of the new implementation are provided in Chapter 6.

The transport of chemical elements in the stellar interior is described by the diffusion equation that involves the different physical processes operating in the star:

$$\rho \frac{\partial X_i}{\partial t} = \underbrace{\frac{1}{r^2} \frac{\partial}{\partial r} \left(r^2 \rho D \frac{\partial X_i}{\partial r} \right)}_{\text{Turbulent diffusion}} - \underbrace{\frac{1}{r^2} \frac{\partial}{\partial r} \left(r^2 \rho X_i v_i \right)}_{\text{Atomic diffusion}} + m_i \underbrace{\left[\sum_j r_{ji} - \sum_k r_{ik} \right]}_{\text{Nuclear reactions}}, \quad (4.1)$$

where ρ is the density, X_i refers to the mass fraction of element i , r is the radius, $D = \sum_j D_j$ is the total coefficient for turbulent diffusion, written as the sum of the j different diffusion coefficients describing turbulent processes such as shear, penetrative convection or any other process, v_i is the diffusion velocity of element i , m_i is the mass of nuclei i , and r_{ij} is the reaction rate producing nuclei j from nuclei i .

4.1 Introduction

The existence of atomic diffusion was discovered by means of theoretical and experimental physics studies of the behaviour of a mixture of gas submitted to a gradient of temperature, a gradient of pressure or a gradient of concentration. Chapman (1917a,b) first introduced the possible impact of atomic diffusion processes in stars that give place to these gradients. In the following years, it was studied and developed, in particular, in the context of the solar chromosphere (Chandrasekhar 1933) but it was argued by Eddington (1926) that chemical separation does not play a main role in photospheric solar abundances. It is only after a few decades that atomic diffusion became again of a prime interest following the work by Aller & Chapman (1960). They introduced the thermal term of diffusion defined by Chapman (1917b) into a diffusion velocity equation, already accounting for the pressure term, the concentration term and the term of external forces (see their Eq. (2.1)) and re-evaluated the effect below the convective envelope. Since then, atomic diffusion has been shown necessary in stellar modelling in the framework of abundances anomalies observed for instance in AmFm stars¹ (e.g. van't-Veer-Menneret et al. 1988; Richer et al. 2000),

¹AmFm stars are main sequence Population I stars with $7000 \leq T_{\text{eff}} \leq 10000$ K that are characterised by small

white dwarfs (e.g. Chapter 13 of Michaud et al. 2015) or even to reproduce the solar observations. In particular, it was highlighted with the help of helioseismology that we cannot neglect this process for solar-type stars. For instance, this applies to constraints on the radius at the base of the convective envelope (e.g. Christensen-Dalsgaard et al. 1985b) or to the helium mass fraction measured in the convective envelope (e.g. Richard et al. 1996) that cannot be reproduced by models not including atomic diffusion.

The reader can find more details in Vauclair & Vauclair (1982) where a good review of the history of atomic diffusion and its challenge with notably the results of helioseismology (see e.g. Christensen-Dalsgaard et al. 1993) can be found. Besides, the process and its effects were largely described in the literature, see Michaud et al. (2015) for a review.

4.2 Principles of atomic diffusion

Atomic diffusion is one of the fundamental transport processes in stars and a main ingredient in the Standard Stellar Model. Atomic diffusion occurs in the stable radiative zone of stars and lead to chemical stratification. Atomic diffusion is led by means of three gradients: a gradient of pressure or gravity, a gradient of concentration and a gradient of temperature.

In radiative stellar interiors, the gradients of pressure and temperature drive the hydrogen toward the outer layers and the heavy and charged elements toward the centre. The concentration gradient drives the elements in the opposite way. Radiative accelerations also lead to an atomic diffusion process, but are neglected in the SSM model (see Section 4.3.3).

The problem is therefore the following:

- i Solve the Boltzmann equation of a dilute plasma with the integration of a suitable particle interaction physics;
- ii Derive from (i) the velocity of the different elements with respect to the different terms of atomic diffusion;
- iii Deduce the chemical stratification and its evolution using diffusion velocities in Eq. (4.1).

4.2.1 Atomic diffusion through the description of a multicomponent fluid

The stellar plasma is a charged fluid composed of ions, of electrons and of different element species. To express the different terms of diffusion we have to consider the interactions of particles that impact the diffusion velocity. For this purpose, one uses the equation of the kinetic theory of gases from Boltzmann which describes the evolution of a multi-component and charged fluid (see Michaud et al. 2015).

Binary interaction is assumed to be the main interaction and a classical interaction at a single temperature for the two particles. In addition, it is assumed that one can apply the ideal gas equation of state.

Then the collision integrals Ω_{ij} , between two particles i and j , are defined according to Paquette et al. (1986) and Michaud et al. (2015), as:

$$\Omega_{ij}^{(\alpha\beta)} = \left(\frac{k_B T}{m M_i M_j} \right)^{1/2} \int_0^\infty \int_0^\infty \exp^{-g^2} g^{2\beta+3} \underbrace{(1 - \cos^\alpha \chi_{ij})}_{\phi_{ij}^{(\alpha)}} b db dg, \quad (4.2)$$

anomalies for elements species with an atomic mass lower than iron peak elements.

4.2. Principles of atomic diffusion

with $\alpha = i, j$, $\beta = j, i$, k_B the Boltzmann constant, T the temperature, m the sum of the masses of the particles i and j , $M_i = m_i/m$, $M_j = m_j/m$, b the impact parameter, g is a dimensionless velocity and with the scattering angle χ_{ij} :

$$\chi_{ij} = \pi - 2 \int_{r_{ij}^{\min}}^{\infty} b dr \left[r^2 \left(1 - \frac{b^2}{r^2} - \frac{V_{ij}(r)}{g^2 k_B T} \right)^{1/2} \right]^{-1}, \quad (4.3)$$

and where r_{ij}^{\min} is the distance of the closest approach of particles and V_{ij} is the potential between two particles i and j .

Ω_{ij} describe the classical collisions between particles of species i and j interacting via the potential $V_{ij}(r)$. $\phi_{ij}^{(\alpha)}$ are the collision cross-sections for a given energy.

It is assumed that particles are interacting by means of a Coulomb potential suitable for a stellar plasma and that binary ion interactions is the main and relevant interaction. According to Paquette et al. (1986), a screened Coulomb potential (or Debye-Hückel potential) can be used to describe the interaction between two charged particles i and j as:

$$V_{ij}(r) = Z_i Z_j \frac{e^2 \exp^{-r/\lambda_D}}{r}, \quad (4.4)$$

where Z_i (Z_j) is the charge of element i (j), e the electronic charge, r is the distance and the Debye length is defined as:

$$\lambda_D = \left(\frac{k_B T}{4\pi e^2 \sum_i n_i Z_i^2} \right)^{1/2}, \quad (4.5)$$

with n_i the number density of charged particles of species i . It represents the distance where the screening effect is effective. This equation of the Debye length is appropriate in the case of low densities ($\lambda_D \gg a_0$) but it will not be the case any more for higher densities ($\lambda_D \ll a_0$) where we will take consequently the interionic distance itself $a_0 = (3/4\pi \sum_{\text{ions}} n_i)^{1/3}$ itself, according to Paquette et al. (1986).

These collision integrals cannot be solved analytically. The potential can be approximated as a pure Coulomb potential ($V_{ij}(r) = Z_i Z_j e^2 / r$). The cross-section for Coulomb scattering between an element i and an element j is then written

$$\phi_{ij} = 2\sqrt{\pi} \left(\frac{e^2 Z_i Z_j}{k_B T} \right)^2 \ln(\Lambda_{ij}), \quad (4.6)$$

where it is also assumed that the integration over the impact parameter b has been limited to $b = \lambda_D$ and that the term g^2 in Eq. (4.3) can be approximated by an average value, and where $\ln(\Lambda_{ij})$ is the Coulomb logarithm. The expression obtained by Iben & MacDonald (1985) using numerical results writes:

$$\ln(\Lambda_{ij}) = \frac{1.6249}{2} \ln \left[1 + 0.18769 \left(\frac{4k_B T \lambda}{Z_i Z_j e^2} \right)^{1.2} \right], \quad (4.7)$$

where $\lambda = \max(\lambda_D, a_0)$ (dependent on the density condition for screening distance).

Finally, the collision integrals write:

$$\Omega_{ij}^{(\alpha\beta)} \approx \left(\frac{k_B T}{2\pi m M_i M_j} \right)^{1/2} \left(\frac{Z_i Z_j e^2}{2k_B T} \right)^2 \ln(\Lambda_{ij}), \quad (4.8)$$

4.2.2 Paquette coefficients

Paquette et al. (1986) showed that the usual methods used to solve the Boltzmann equation introduce systematic errors in the limit of a dilute plasma. They argued that an analytical way to solve collision integrals should be avoided in order to limit errors. They proposed to use the Paquette's coefficients that are estimated by a high-accuracy fit of collision integrals.

They made the following assumptions and simplifications:

- i The interionic diffusion is the main variable and the effects of electron-ion collisions are neglected;
- ii Inelastic collisions are ignored;
- iii The temperature is the same for all elements;
- iv The thermal velocity is larger than the diffusion velocities;
- v The ideal gas equation of state applies.

Paquette et al. (1986) define:

$$\Omega_{ij}^{\alpha\beta} = \epsilon_{ij} F_{ij}^{\alpha\beta}, \quad (4.9)$$

where $F_{ij}^{\alpha\beta}$ is a dimensionless integral obtained as a function of the dimensionless collision integral $\phi_{ij} = \ln[\ln(1 + \Lambda_{ij}^2)] \approx 2\ln\Lambda_{ij}$ (in our system of notation²), and

$$\epsilon_{ij} = \pi \left(\frac{Z_i Z_j e^2}{2k_B T} \right)^2 \left(\frac{k_B T}{2\pi m M_i M_j} \right)^{1/2}, \quad (4.10)$$

with $m = m_i + m_j$ the sum of the masses of the particles i and j , $M_i = m_i/m$, $M_j = m_j/m$. The proportionality to the element charges implies that the assumption of total / partial ionisation for elements i and j may have an important impact on the values of the collision integrals. We will see in Chapter 6 the particular influence of Paquette's coefficients on the diffusion velocity.

4.3 Determination of the diffusion velocity

Atomic diffusion consists in a global motion of particles (ions, electrons, protons) following gradients and forces in presence. In addition to the collision integrals, the velocity of the particles due to diffusion need to be defined.

The mean fluid velocity u_i of each species i and the mean fluid velocity u are defined by Thoul et al. (1994), respectively, as:

$$u_i = \int v F_i dv, \quad (4.11)$$

$$u = \frac{1}{\rho} \sum \rho_i v_i, \quad (4.12)$$

where v is the velocity, $F_i(x, v, t)$ is the distribution function for a species i .

As a result, the diffusion velocity for species i writes:

$$v_i = u_i - u. \quad (4.13)$$

Thereby, from the equation of mass conservation we can determine the mass fraction evolution due to atomic diffusion with the equation of diffusion for an element i depending on the velocity v_i as:

$$\rho \frac{\partial X_i}{\partial t} = -\frac{1}{r^2} \frac{\partial}{\partial r} (\rho r^2 X_i v_i), \quad (4.14)$$

²In Paquette et al. (1986), ϕ is called ψ and Λ is called γ .

4.3. Determination of the diffusion velocity

with t the time, ρ the density, r the radius and X_i the mass fraction of the element i

$$X_i = \frac{n_i A_i m_u}{\rho}, \quad (4.15)$$

with the mass number A_i , the atomic mass unit m_u and n_i the number of particles i .

Several methods have been developed to compute the diffusion velocity v_i (Eq. (4.13)) and solve the diffusion equation. Hereafter, we describe two of them.

The first formalism is based on the Chapman-Enskog theory described in Aller & Chapman (1960) and Chapman & Cowling (1970). It follows a simple approach of the problem by solving the equations element by element with respect to a reference element³. The implementation in STAREVOL follows Montmerle & Michaud (1976).

A second formalism comes from equations developed by Burgers (1969) (see also introduction of Paquette et al. 1986). They used a more robust approach and solved equations of heat transfer and of flux simultaneously for all the elements. The implementation in STAREVOL follows Thoul et al. (1994).

In STAREVOL, the first formalism was already implemented at the beginning of the PhD thesis, and the second one was implemented and tested during the PhD thesis to optimise the treatment of atomic diffusion. Verifications and tests of the first one and implementation of the second one was a main part of the work during the first year of the PhD thesis.

4.3.1 Hypothesis and Formalism of Montmerle & Michaud (1976)

The first formalism implemented in the STAREVOL code for the atomic diffusion is the one described by Montmerle & Michaud (1976), hereafter M&M, based on the works by Wildt (1937); Aller & Chapman (1960); Chapman & Cowling (1970).

It considers that the total distribution function of a given element can be written as a convergent series whose different terms represent successive approximations of the distribution function. This calculation is made for a trace element in relation to the surrounding medium (usually hydrogen in the stellar case), considering electron scattering and the effect of the electric field. This gives a diffusion velocity with respect to hydrogen.

Hydrostatic equilibrium is assumed and atomic diffusion is considered as a first-order perturbation of this equilibrium. The hydrostatic equilibrium writes, according to M&M:

$$\frac{-1}{p_i} \frac{dp_i}{dr} + \frac{F_i}{k_B T} = \sum_j \alpha_{ij} c_j \frac{d \ln T}{dr}, \quad (4.16)$$

where p_i is the partial pressure of atomic species i , α_{ij} is the thermal diffusion coefficient, c_j is the actual concentration of element j with respect to the medium, F_i is the sum of the forces that applies on the element i (gravity, electrical force, radiative force), and where the right term of the equation corresponds to the temperature gradient. Thus, if one assumes that the diffusion velocity of an element i with respect to protons is proportional to the difference between the equilibrium and the initial state, one has the velocity:

$$v_{pi} = D_{pi} \left[\frac{\partial \ln p_{i,eq}}{\partial r} - \frac{\partial \ln p_{i,ini}}{\partial r} \right]. \quad (4.17)$$

³It is assumed that a trace element evolves in a medium composed of the reference element that is the most abundant one in the star, typically hydrogen.

This equation can be written under the form:

$$v_{pi} = D_{pi} \left(- \underbrace{\nabla \ln c_i}_{\text{Concentration gradient}} - \underbrace{\kappa_p \nabla \ln P}_{\text{Pressure gradient}} + \underbrace{\kappa_T \nabla \ln T}_{\text{Thermal gradient}} - \underbrace{\frac{f_i}{k_B T}}_{\text{External forces}} \right), \quad (4.18)$$

where D_{pi} is the diffusion coefficient between protons and trace element i , κ_T is the thermal diffusivity and κ_p is defined as:

$$\kappa_p \nabla \ln P = \left(A_i - \frac{Z_i}{2} - \frac{1}{2} \right) \frac{m_p G m_r}{k_B T r^2}, \quad (4.19)$$

where A_i is the mass number, Z_i is the charge of element i , m_p is the proton mass, G is the gravitational constant, m_r is the mass below radius r .

Eq. (4.18) can be rewritten as:

$$v_{pi} = D_{pi} \left[-\nabla \ln c_i + \frac{A_i m_p}{k_B T} (g_{\text{rad}}, i - g) + \frac{(Z_i + 1) m_p g}{2 k_B T} + \kappa_T \nabla \ln T \right], \quad (4.20)$$

where the radiative forces g_{rad} are considered to be external forces and the electric field term is $\frac{(Z_i + 1) m_p g}{2 k_B T}$.

One of the main assumptions is the one of the trace element. In other words, the diffusion velocity of an element, the trace element, is computed with respect to hydrogen. This assumption is true as long as the surrounding medium of the trace element is mainly composed of hydrogen. It can be assumed to be the case in main-sequence stars where hydrogen is the most abundant element. However, the helium may become the more abundant element in the central regions even during the main-sequence and the trace element approximation is not valid any more for helium. M&M proposed corrections to take into account this issue and defined a specific velocity for helium with:

$$v_{He} = \langle D_{He} \rangle \left((1 + \gamma_{He}) \left[-\nabla \ln c_{He} + \overline{\Phi}_{He} + \frac{(A_{He} - 1) + K_{P,E}(A_{He} - \overline{Z}_{He})}{(1 + A_{He} \gamma_{He}) \lambda_{He}} \nabla \ln P + \kappa_T \nabla \ln T \right] - \frac{\langle f_{He} \rangle}{k_B T} \right), \quad (4.21)$$

where D_{He} is the average diffusion coefficient of all ionisation states of He, $\gamma_{He} = \frac{N(A_{He}, Z_{He})}{N_{1H}}$, $\overline{\Phi}_{He}$ gives the average contribution of the ionisation of helium, $K_{P,E}$ is a coefficient close to 1, \overline{Z}_{He} is the average charge of helium, $\lambda_{He} = 1 + \gamma_{He}(Z_{He} - 1)(\gamma_{He} - 1)$ and where $\langle f_{He} \rangle$ is the average radiative force applied to helium.

However, although this formalism gives good results, it is limited by the assumption of a trace element. Despite the corrections of M&M, the abundance of helium is still an issue, and it will be even more critical when the star will reach more evolved phases where helium becomes the most abundant element in the core. A solution could be to adapt the definition of the trace element from a hydrogen surrounding medium to a helium surrounding medium. But it would imply to adapt the diffusion equation for each different layer according to the current more abundant element all along the evolution of the star and could lead to errors. In conclusion, to obtain a relevant treatment of atomic diffusion, we need a more general formalism, suitable at different evolutionary phases and chemical abundances.

4.3.2 Hypothesis and Formalism of Thoul et al. (1994)

During the PhD thesis, we implemented the formalism developed by Thoul et al. (1994) on the base of Burgers equations. We used the routine distributed by Thoul et al. (1994) and implemented it in STAREVOL. We also included additional modifications with the computation

of Paquette' coefficients and corrections from Hu et al. (2011).

Burgers (1969) solved rigorously the Boltzmann equation for a multicomponent fluid. With this method, the computation of the velocity of each element with respect to each other is possible. Equations of flux and of heat transfer are solved simultaneously for all the elements. Burgers' equation for hydrostatic equilibrium writes:

$$\frac{dp_i}{dr} + \rho_i(g - g_{\text{rad},i}) - \rho_{ei}E = \sum_{i \neq j} K_{ij}[(w_j - w_i) + z_{ij}(x_{ij}r_i - y_{ij}r_j)], \quad (4.22)$$

and the heat transfer equation writes:

$$\frac{5}{2}n_i k_B \frac{dT}{dr} = \sum_{i \neq j} K_{ij} \left[\frac{5}{2}z_{ij}x_{ij}(w_i - w_j) - y_{ij} [0.8z''_{ij}x_{ij}(r_i + r_j) + Y_{ij}r_i - (3 + z'_{ij})x_{ij}r_j] \right] - 0.4z''_{ij}K_{ii}r_i, \quad (4.23)$$

with p_i the partial pressure of atomic species i , r the radius, $\rho_i = n_i m_i$ the mass density of atomic species i , g the gravitational acceleration, g_{rad} the radiative accelerations, $\rho_{ei} = n_i q_i$ the charge density of atomic species i , E the electric field, w_i (w_j) is the mean velocity of atomic species i (j), and where K_{ij} is the friction coefficient (defined Eq. 4.31), r_i (r_j) is the residual heat flow velocity (defined Eq. 4.27), z_{ij} , z'_{ij} and z''_{ij} are the resistance coefficients (defined Eqs. 4.28-4.30), and with:

$$x_{ij} = \frac{m_j}{m_i + m_j}, \quad (4.24)$$

$$y_{ij} = \frac{m_i}{m_i + m_j}, \quad (4.25)$$

$$Y_{ij} = 3y_{ij} + z_{ij}x_{ij}\frac{m_i}{m_j}, \quad (4.26)$$

where m_i (m_j) is the mass of particle i (j).

The residual heat flow velocity r_i represents the velocity that reflects the local heat flow transported by a particle i divided by the partial pressure of this particle. It will be particularly relevant for the thermal gradient (see Burgers 1969) and is defined as:

$$r_i = \left[\frac{m_i}{2k_B T} \int F_i(v - u)|v - u|^2 dv - \frac{5}{2}w_i \right] \quad (4.27)$$

where u , v and F_i were defined in Eqs. (4.11) and (4.12).

The resistance coefficients (Burgers 1969; Paquette et al. 1986) are three heat flux terms that describe interactions between elements i and j and can be expressed in terms of the reduced collision integrals $\Omega_{ij}^{\alpha\beta}$ as:

$$z_{ij} = 1 - \frac{2}{5} \frac{\Omega_{ij}^{(12)}}{\Omega_{ij}^{(11)}}, \quad (4.28)$$

$$z'_{ij} = \frac{5}{2} - \frac{2}{5} \frac{5\Omega_{ij}^{(12)} - \Omega_{ij}^{(13)}}{\Omega_{ij}^{(11)}}, \quad (4.29)$$

$$z''_{ij} = \frac{\Omega_{ij}^{(22)}}{\Omega_{ij}^{(11)}}. \quad (4.30)$$

The friction coefficient K_{ij} is defined as:

$$K_{ij} = \frac{2}{3} \mu_{ij} \left(\frac{2k_B T}{\mu_{ij}} \right)^{1/2} n_i n_j \phi_{ij}, \quad (4.31)$$

with $\mu_{ij} = m_i m_j / (m_i + m_j)$ the reduced mass for species i and j , n_i (n_j) the particle number density of species i (j) and ϕ_{ij} the cross section defined Eq. (4.6) (see also Appendix B).

In Thoul et al. (1994), following approximations for resistance coefficients are used: $z_{ij} = 0.6$, $z'_{ij} = 1.3$ and $z''_{ij} = 2.0$. However, applying the Paquette's coefficients from Paquette et al. (1986) we integrate the resistance coefficients of the Burgers' method (Burgers 1960, 1969), according to Eqs. (4.28-4.30) with Ω_{ij}^{11} the collision integral defined in Eq. (34) in Paquette et al. (1986) and dependent of the Coulomb logarithm defined in Eq. (4.7). In Thoul et al. (1994) the friction coefficient is renormalised using κ_{ij} with $\kappa_{ij} = K_{ij}/K_0$. We note that we used the coefficient of renormalisation K_0 to obtain the result in cgs units at the end of the computation (see demonstration Appendix B). Besides, z_{ij} , z'_{ij} , z''_{ij} are computed for each element i compared with each element j in each layer of the star. It allows to relax the approximation used by Thoul et al. (1994).

Finally, we must also satisfy the local mass conservation and the current neutrality, respectively as:

$$\sum_i A_i m_i \omega_i = 0, \quad (4.32)$$

$$\sum_i Z_i m_i \omega_i = 0, \quad (4.33)$$

where ω_i is the velocity of element i in regard to the centre of mass.

Thus, we can solve equation (21) from Thoul et al. (1994) that writes:

$$\frac{p}{K_0} \left(\underbrace{\alpha_i \frac{\partial \ln p}{\partial r}}_{\text{Pressure term}} + \underbrace{\beta_i \frac{\partial \ln T}{\partial r}}_{\text{Thermal term}} + \sum_{\substack{j=1 \\ j \neq e, 2}}^S \underbrace{\gamma_{ij} \frac{\partial \ln c_j}{\partial r}}_{\text{Concentration term}} \right) = \sum_{j=1}^{2S+2} \Delta_{ij} W_j, \quad (4.34)$$

with S the number of species considered, where the sum over the concentration term does not account for electrons and helium ($j \neq e, 2$). According to Hu et al. (2011), we can include ${}^4\text{He}$ in the determination of the concentration term without the generation of issues as:

$$\frac{p}{K_0} \left(\alpha_i \frac{\partial \ln p}{\partial r} + \beta_i \frac{\partial \ln T}{\partial r} + \sum_{\substack{j=1 \\ j \neq e}}^S \gamma_{ij} \frac{\partial \ln c_j}{\partial r} \right) = \sum_{j=1}^{2S+2} \Delta_{ij} W_j \quad (4.35)$$

The others parameters are given in Thoul et al. (1994).

The diffusion coefficients α , β , γ follow equations (30-32) and write:

$$\alpha_i = \begin{cases} \frac{C_i}{C} & \text{for } i = 1, 2, \dots, S, \\ 0 & \text{for } i = S+1, \dots, 2S+2, \end{cases} \quad (4.36)$$

$$\beta_i = \begin{cases} 2.5 \frac{C_{i-S}}{C} & \text{for } i = S+1, \dots, 2S, \\ 0 & \text{for } i = 1, \dots, S \text{ and } i = 2S+1, 2S+2, \end{cases} \quad (4.37)$$

$$\gamma_i = \begin{cases} \frac{C_i}{C} \left[\left(\delta_{ij} - \frac{C_j}{C} \right) - \left(\delta_{i2} - \frac{C_2}{C} \right) \frac{Z_j C_j}{Z_2 C_2} \right] & \text{for } i = 1, \dots, S, \\ 0 & \text{for } i = S+1, \dots, 2S+2 \end{cases} \quad (4.38)$$

4.3. Determination of the diffusion velocity

Parameter Δ follows equations (33-36) and writes:

$$\Delta_i = \begin{cases} -\sum_{k \neq i} \kappa_{ik} & \text{for } j=i, \\ \kappa_{ij} & \text{for } j = 1, \dots, S \text{ and } j \neq i, \\ \sum_{k \neq i} z_{i,j-S} \kappa_{ik} x_{ik} & \text{for } j=i+S, \\ z_{ij} \kappa_{i,j-S} y_{i,j-S} & \text{for } j=S+1, \dots, 2S \text{ and } j \neq i+S, \\ Z_i C_i & \text{for } j = 2S+1, \\ -A_i C_i & \text{for } j=2S+2, \end{cases} \quad (4.39)$$

for $i = 1, \dots, S$;
it writes

$$\Delta_i = \begin{cases} \sum_{k \neq j} -2.5 z_{i-S,j} \kappa_{i-S,k} x_{i-S,j} & \text{for } j=i-S, \\ -2.5 z_{i-S,j} \kappa_{i-S,k} x_{i-S,j} & \text{for } j=1, \dots, 2S \text{ and } j \neq i-S, \\ -\sum_{k \neq i} \kappa_{i-S,k} y_{i-S,k} (0.8 z''_{i-S,k} x_{i-S,k} + Y_{i-S,k}) - 0.4 z''_{i-S,i-S} \kappa_{i-S,i-S} & \text{for } j=i, \\ \kappa_{i-S,j-S} y_{i-S,j-S} x_{i-S,j-S} (3 + z'_{i-S,j-S} - 0.8 z''_{i-S,j-S}) & \text{for } j=S+1, \dots, 2S \text{ and } j \neq i, \\ 0 & \text{for } j = 2S+1, 2S+2, \end{cases} \quad (4.40)$$

for $i = S+1, \dots, 2S$;
it writes

$$\Delta_i = \begin{cases} Z_j C_j & \text{for } j=1, \dots, S, \\ 0 & \text{for } j = S+1, \dots, 2S+2, \end{cases} \quad (4.41)$$

for $i = 2S+1$;
and it writes

$$\Delta_i = \begin{cases} A_j C_j & \text{for } j=1, \dots, S, \\ 0 & \text{for } j = S+1, \dots, 2S+2, \end{cases} \quad (4.42)$$

for $i = 2S+2$.

The parameter W follows equations (29) from Thoul et al. (1994) and writes:

$$W_i = \begin{cases} w_i & \text{for } i=1, \dots, S, \\ r_{i-S} & \text{for } i = S+1, \dots, 2S, \\ K_0^{-1} n_e e E & \text{for } i=2S+1, \\ K_0^{-1} n_e m_0 g & \text{for } i = 2S+2. \end{cases} \quad (4.43)$$

where we put back the z_{ij} , z'_{ij} and z''_{ij} for which we do not use constant values and where κ_{ij} can be written (Eq. (37) from Thoul et al. 1994) as:

$$\kappa_{ij} = \frac{A_i A_j}{A_i + A_j}^{1/2} C_i C_j Z_i^2 Z_j^2 \ln \Lambda_{ij}. \quad (4.44)$$

with C_i (C_j) the concentration of species i (j).

We remind that radiative accelerations are neglected in the work of Thoul et al. (1994) as well as in STAREVOL.

Finally, the dimensionless diffusion velocity can be written from Eq. (4.35) as:

$$v_i = \alpha_i \frac{\partial \ln p}{\partial r} + \beta_i \frac{\partial \ln T}{\partial r} + \sum_{\substack{j=1 \\ j \neq e}}^S \gamma_{ij} \frac{\partial \ln c_j}{\partial r} \quad (4.45)$$

This way, we determine in STAREVOL the diffusion velocity (in cgs after renormalisation) in all the star for 31 not radioactive isotopes: 1H , 2H , 3He , 4He , 6Li , 7Li , 9Be , ^{10}B , ^{11}B , ^{12}C , ^{13}C , ^{14}N , ^{15}N , ^{16}O , ^{17}O , ^{18}O , ^{19}F , ^{20}Ne , ^{21}Ne , ^{22}Ne , ^{23}Na , ^{24}Mg , ^{25}Mg , ^{26}Mg , ^{27}Al , ^{28}Si , ^{31}P , ^{32}S , ^{35}S , ^{35}Cl , ^{36}Cl . This velocity is computed for each element with respect to each other.

At the end, we obtain the diffusion velocity inside the stellar interior for these elements and see how atomic diffusion impacts abundances during the evolution of a low-mass star. Thus, we should obtain a complete treatment of atomic diffusion in STAREVOL code with the consideration of each involved effects whatever the stellar evolution phase.

4.3.3 Radiative accelerations

Radiative accelerations are the result of an interaction between photons which radiate in stars and elements which are diffused within the stars. This interaction leads a transfer of momentum between the elements and the radiative field. It should be included for the complete treatment of atomic diffusion.

However, their computation requires a large database of atomic physics and opacities. This could imply a large time-consumption to compute radiative accelerations for each element and at each step. Moreover, Richer et al. (1998); Turcotte et al. (1998b); Deal et al. (2018, 2020) showed that the effect of radiative accelerations is weak for stars with $M < 1.1 - 1.2M_{\odot}$ and solar metallicity. Consequently, the contribution of g_{rad} is often neglected for solar-type stars and we will neglect it for the present thesis.

Appendix E gives an overview of this process and how it could be included in order to study more massive stars and/or metal-poor stars for perspectives purpose (see Section 10.2).

Rotation

Until now and with the exception to the overshoot process, we described what compose a standard stellar model (or SSM). However, to achieve a more complete modelling, we have to include non-standard processes. This chapter is dedicated to stellar rotation.

Stellar rotation, and in particular differential rotation (radial and latitudinal), triggers the transport of both angular momentum and chemicals species in the radiative zone during stellar evolution. It generates the large-scale currents of the meridional circulation and several hydrodynamical instabilities that eventually become turbulent as the vertical and horizontal shear instabilities. The inclusion of stellar rotation in stellar evolution models may consequently be of a great significance. For a detailed review of dynamical processes in stars, see e.g. Mathis (2013).

In this Chapter, we present the "Type I rotational mixing" that includes meridional circulation and shear turbulence in Section 5.1. During this thesis, we implemented rotational dependent transport processes from the literature and tested them in the framework of the observational constraints obtained from Open Clusters. It includes a transport of angular momentum, described in Section 5.2 and several additional transports of chemicals described in Section 5.3. We did not investigate the effects of internal gravity waves, magnetic fields or magnetic instabilities. However, they are quickly described in Appendix F as promising processes to add for stellar modelling.

5.1 Type I rotational mixing

In STAREVOL, the implementation of rotation follows the formalism of shellular rotation developed by Zahn (1992) and Maeder & Zahn (1998), and already used for instance by Palacios et al. (2003); Decressin et al. (2009); Amard et al. (2019). It involves two dynamical processes: meridional circulation and turbulence shear instability (vertical and horizontal). It allows to include a 3D process into a 1D stellar evolution code with the assumption of an anisotropic turbulence. The horizontal shear is stronger than the vertical one. These processes lead to a mixing in the radiative zone with both the transport of angular momentum and chemicals in the star.

The challenge is then to give a good description of the different intrinsically 3D processes involved into 1D codes. The complex interaction of the different processes involved is illustrated in Figure 5.1. Transport of chemicals and angular momentum is the result of the interaction of numerous processes in the star (atomic diffusion, differential rotation) or outside the star (external torque). The sophistication of this model allows to consider more specific processes as penetrative convection, turbulence, etc and will be introduced in the coming sections.

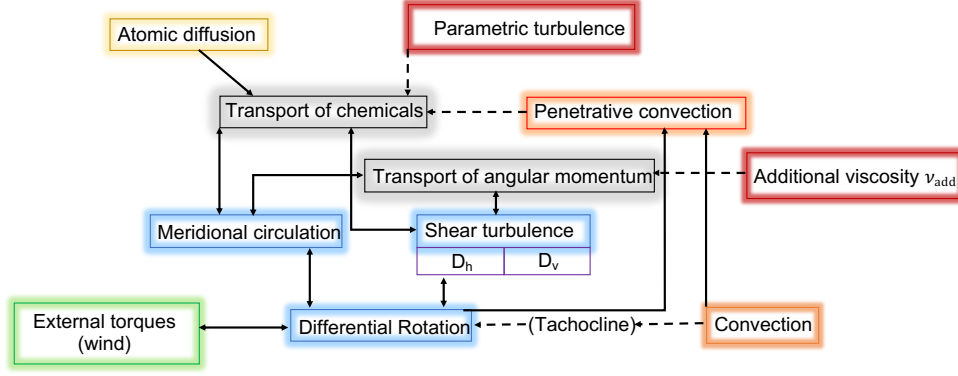


Figure 5.1: Scheme of the dynamical processes and their interactions that lead to transport of chemicals and of angular momentum in the star. Blue frames refer to rotation processes, yellow frame refers to atomic diffusion, green frame refers to external processes, orange frame refer to convection, red frames refer to additional processes and grey frames refer to the resulting transport (freely inspired from Fig. 1 from Mathis et al. 2007).

5.1.1 Meridional circulation and shear turbulence

The meridional circulation is a large-scale transport of matter in meridian planes as illustrated in Fig. 5.2. It is generated because of the thermal imbalance created by rotation in the star (see for instance Zahn (1992); Maeder & Zahn (1998); Palacios et al. (2003); Rieutord (2006); Espinosa Lara & Rieutord (2013)). It transports both the chemical species and the angular momentum. The expression of the circulation velocity is derived from the equation of energy conservation (Maeder & Zahn 1998) and writes:

$$\vec{U}_M = U_2(r)P_2(\cos\theta)\hat{e}_r + V_2(r)\frac{dP_2(\cos\theta)}{d\theta}\hat{e}_\theta, \quad (5.1)$$

with U_2 the amplitude of the radial component of the meridional circulation velocity and V_2 the amplitude of the horizontal component, (r, θ) the spherical coordinates, $P_2(\cos\theta)$ is the second Legendre polynomials and \hat{e}_r (\hat{e}_θ) the radial (colatitudinal) unit vector. V_2 and U_2 are related by:

$$V_2 = \frac{1}{6\rho r} \frac{d(\rho r^2 U_2)}{dr}. \quad (5.2)$$

The radial component U_2 writes:

$$U_2(r) = \frac{LP}{M_{\text{eff}}C_P\bar{\rho}\bar{T}\bar{g}} \frac{1}{\nabla_{\text{ad}} - \nabla_{\text{rad}} + \frac{\varphi}{\delta}\nabla_\mu} [u_B + u_{\text{Th}} + u_{\text{N-G}} + u_{\text{NS}}], \quad (5.3)$$

with L the luminosity, P the pressure, M_{eff} is effective mass of the star, C_P the specific heat at constant pressure, $\nabla_{\text{ad}} = \nabla_{\text{conv}}$ and ∇_{rad} are the adiabatic and radiative temperature gradients (defined Eq. (3.6)), respectively, $\nabla_\mu = \frac{d\ln\mu}{d\ln P}$ is the mean molecular gradient, $\varphi = \frac{d\ln\rho}{d\ln\mu}\Big|_{P,T}$ and $\delta = -\frac{d\ln\rho}{d\ln T}\Big|_{P,\mu}$. The four last terms are different contributions to the meridional circulation: u_B takes into account the baroclinicity or in other words the fact that the isobars and isodensities do not coincide, u_{Th} is the thermal contributor, $u_{\text{N-G}}$ refers to the nuclear energy production and heating due to gravitational adjustments, and u_{NS} stands for non-stationary processes (Zahn 1992; Mathis & Zahn 2004; Decressin et al. 2009).

On the other hand, the differential rotation that results of the angular momentum transport by the

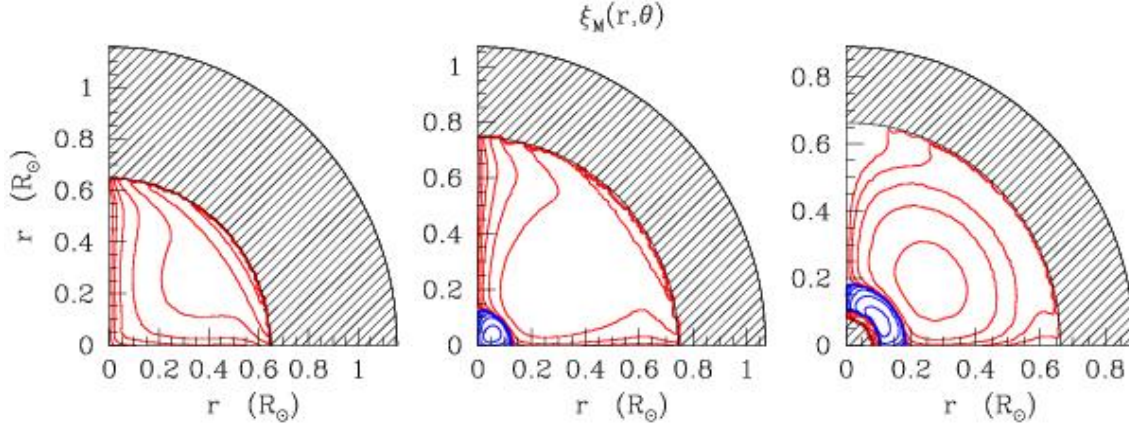


Figure 5.2: Meridional circulation flow (represented in terms of the stream function $\xi_M(r, \theta) = \frac{1}{2}U_2(\cos^3\theta - \cos\theta)$, see Decressin et al. 2009) for a $1.0M_\odot$ at three evolutionary stages of the PMS: from left to right: 14 Myrs, 35 Myrs and 55 Myrs. Blue and red lines indicate clockwise ($U_2 > 0$) and counterclockwise ($U_2 < 0$) circulation, respectively. The hatched areas refer to convective regions (from Charbonnel et al. 2013)

meridional flow, leads also to the apparition of several hydrodynamic instabilities. Differential rotation generates shear and turbulence associated to it when it becomes unstable (stability is determined using Reynolds and Rayleigh criteria). The resulting shear turbulence impacts both the transport of chemical species and of the angular momentum.

In the framework of the shellular rotation proposed by Zahn (1992), the shear is strongly anisotropic and can be divided in two components: the vertical shear and the horizontal shear (see Fig. 5.3). The horizontal turbulence propagates along the isobars and is strong thanks to the Coriolis acceleration that acts as its restoring force. At the opposite, the vertical shear is inhibited by the buoyancy force and the stratification density of the star in the radial direction.

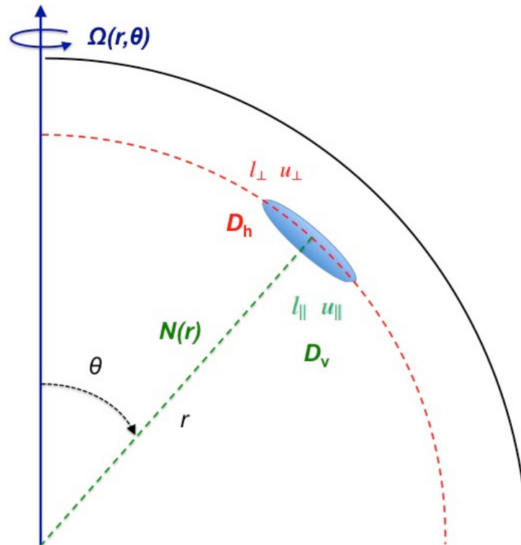


Figure 5.3: Anisotropic turbulent transport in a stably stratified stellar radiative zone with a buoyancy frequency N rotating with an angular velocity Ω . u_{\parallel} and u_{\perp} refer to the characteristic velocities, and l_{\parallel} and l_{\perp} refer to the length scales of a turbulent "pancake" in the direction of the entropy stratification and in the horizontal one, respectively (from Mathis et al. 2018).

5.1.2 Diffusive treatment of the turbulent transport

The transport of angular momentum by meridional circulation and turbulent shear (vertical and horizontal) obeys the advection-diffusion equation

$$\rho \frac{d}{dt}(r^2\Omega) = \underbrace{\frac{1}{5r^2} \frac{\partial}{\partial r}(\rho r^4 \Omega U_2)}_{\text{Advection term}} + \underbrace{\frac{1}{r^2} \frac{\partial}{\partial r} \left(\nu_v r^4 \frac{\partial \Omega}{\partial r} \right)}_{\text{Diffusive term}}, \quad (5.4)$$

where ρ , r , Ω and ν_v are the density, the radius, the angular velocity, and the vertical shellular component of the turbulent viscosity, respectively. Meridional circulation appears through its velocity U_2 in Eq. (5.4) for the transport of angular momentum, and can be described as a diffusion coefficient D_{eff} in Eq. (4.1) for the transport of chemicals as shown by Chaboyer & Zahn (1992). The turbulent shear in the vertical and horizontal directions appears as a viscosity ν_v (ν_h) in Eq. (5.4) and as a diffusivity D_v (D_h) in Eq. (4.1), which is proportional to the corresponding viscosity, with a proportionality factor of 1 as usually assumed in stellar evolution models (Zahn 1992; Eggenberger et al. 2008; Ekström et al. 2012; Mathis et al. 2018).

Several prescriptions exist for both (D_v, ν_v) and (D_h, ν_h) , and one may find in the literature stellar evolution models computed with different combinations of them. As demonstrated by Meynet et al. (2013) and Amard et al. (2016) this choice strongly affects the outcome of the models. There are several prescriptions implemented in STAREVOL. Each prescription allows to describe the coefficient associated to the turbulent viscosity (horizontal or vertical).

Prescription for the vertical shear

In the framework of the "shellular" rotation hypothesis and assuming the anisotropy of the turbulence, Zahn (1992), hereafter Za92, proposed a definition of D_v , v as:

$$D_{v,v} = \frac{Ri_c}{3} \kappa_T \left(\frac{r \sin\theta}{N_T} \frac{d\Omega}{dr} \right)^2, \quad (5.5)$$

where $Ri_c = 1/4$ is the critical Richardson number beyond which the initial instability exists, κ_T is the thermal diffusivity, θ is the spherical coordinate and $N_T = \frac{g\delta}{H_P}(\nabla_{\text{ad}} - \nabla)$ is the thermal term of the Brunt-Väisälä frequency with gravity g , H_P the pressure scale height, $\delta = -\left. \frac{d \ln \rho}{d \ln T} \right|_{P,\mu}$, $\nabla_{\text{ad}} = \left. \frac{\partial \ln T}{\partial \ln P} \right|_{\text{ad}}$, $\nabla = \left. \frac{d \ln T}{d \ln P} \right|$.

The Richardson number gives an estimation of the ratio of the buoyancy term to the flow shear term and writes

$$Ri = \frac{N_T^2}{(dV/dz)^2} = \frac{N_T^2}{(r \sin\theta \frac{d\Omega}{dr})^2}, \quad (5.6)$$

where V is the fluid velocity, z is the radial component perpendicular to the rotation axis, (dV/dz) is the shear rate and N_T^2 is the thermal Brunt-Väisälä frequency.

Talon & Zahn (1997), hereafter TZ97, developed another version of D_v that considers the effect of thermal and chemical stratifications. The Richardson criterion was then modified; it now involves $N_\mu = \frac{g\varphi}{H_P} \nabla_\mu$, the chemical term of the Brunt-Väisälä frequency, where $\varphi = \left. \frac{d \ln \rho}{d \ln \mu} \right|_{P,T}$ and

5.1. Type I rotational mixing

$\nabla_\mu = \frac{d \ln \mu}{d \ln P}$. The coefficient $D_{v,v}$ becomes:

$$D_{v,v} = \frac{1}{4} Ri_c \left(\frac{N_T^2}{\kappa_T + D_h} + \frac{N_\mu^2}{D_h} \right)^{-1} \left(r \sin \theta \frac{d\Omega}{dr} \right)^2, \quad (5.7)$$

where $N^2 = N_T^2 + N_\mu^2$ is the Brunt-Väisälä frequency and θ is the spherical coordinate.

Prescription for the horizontal shear

Zahn (1992) (Za92) defined the horizontal turbulent diffusion coefficient generated by horizontal shear D_h as:

$$D_h = \frac{1}{c_h} r |2V_2 - \alpha U_2|, \quad (5.8)$$

with c_h a free parameter close to 1, $\alpha = \frac{1}{2} \frac{d \ln(r^2 \bar{\Omega})}{d \ln r}$ the shear rate ($\alpha = 1$ means uniform rotation), V_2 the latitudinal component defined in Eq. (5.2) and U_2 the radial component of the meridional circulation developed to the second order as:

$$U_2 = \frac{5}{\rho r^4 \Omega} \left(\Gamma(m) - \rho \nu_v r^4 \frac{d\Omega}{dr} \right), \quad (5.9)$$

where $\Gamma(m)$ refers to the gain or loss of angular momentum in the isobar enclosing $m(r)$.

Mathis et al. (2004), hereafter MPZ04, proposed a new expression for D_h base on Couette-Taylor flow laboratory experiments (Richard & Zahn 1999). D_h writes

$$D_h = \left(\frac{\beta}{10} \right)^{1/2} (r^2 \bar{\Omega})^{1/2} [r |2V_2 - \alpha U_2|]^{1/2}, \quad (5.10)$$

where $\beta = 1.5 \times 10^{-5}$ (Maeder 2009).

Mathis et al. (2018), hereafter Mathis18, accounted for the fact that horizontal turbulence is generated from both horizontal and vertical shears. The coefficient D_h then writes as: $D_h = D_{h,h} + D_{h,v}$ and D_h in Eqs. (5.8) and (5.10) actually refers to $D_{h,h}$. The first index means the direction of the transport and the second index refers to the shear that generate the transport. Mathis et al. (2018) derive a prescription for the diffusion coefficient associated to the horizontal turbulence generated by vertical shear, $D_{h,v}$. This source of transport is active only if the vertical shear does not fulfil the Reynold's criterion ($Re > Re_{e;c}$ with $Re_{e;c} = 7\nu_m$ with ν_m the molecular viscosity in STAREVOL).

$$D_{h,h} = \left(\frac{\beta}{10} \right)^{1/2} (r^2 \Omega)^{1/2} [r |2V_2 - \alpha U_2|]^{1/2}, \quad (5.11)$$

$$D_{h,v} = \begin{cases} \frac{\tau^2 N^4}{2\Omega^2} D_{v,v} & \text{if } Re > Re_{e;c} \\ 0 & \text{if } Re < Re_{e;c} \end{cases}. \quad (5.12)$$

Here $D_{v,v} \equiv D_v$ from Eq. (5.5), and τ is a characteristic timescale for the turbulence, taken to be equal to the time characterising the radial shear, $\tau = 1/S$, where $S = r \sin \theta \partial_r \Omega$.

We summarise the prescriptions that we used during the PhD thesis in Tab. 5.1. Others prescriptions have been derived for both transport coefficients but we will not use them for the present PhD work. We can quote, for instance, Maeder (1997); Maeder & Zahn (1998); Maeder & Meynet (2001); Maeder (2003); Prat et al. (2016).

Table 5.1: Turbulence shear prescriptions.

Prescription	Reference
D_v	Zahn (1992) - Za92
D_v	Talon & Zahn (1997) - TZ97
D_h	Zahn (1992) - Za92
D_h	Mathis et al. (2004) - MPZ04
D_h	Mathis et al. (2018) - Mathis18

Several numerical simulations have been realised to test the vertical shear coefficient D_v defined by Za92 (e.g. Prat & Lignières 2013, 2014; Prat et al. 2016; Garaud et al. 2017; Gagnier & Garaud 2018). However, we miss equivalent studies for the others prescriptions, in particular for the horizontal turbulence coefficient.

5.2 Transport of angular momentum

The transport of angular momentum follows the advection-diffusion equation defined Eq. (5.4).

5.2.1 Stellar winds and magnetic braking

Stars are magnetic objects with their own magnetic field. The magnetic field generated by the star interacts, in particular, with the stellar winds and affects the charged particles. Due to this link, the particles stay connected in corotation with the star. The magnetic lines are distended to a large distance from the star (Alfvén radius¹) and this leads to a loss of angular momentum. This interdependence can be illustrated by the famous example of the rotating ice skater. When the skater closes his arms (small magnetic field lines), his rotation is fast but at the moment he opens his arms (large magnetic field lines) his rotation velocity decreases. The deformation of the field lines by the stellar wind generates a torque on the surface of the star and a loss of angular momentum for the star occurs as soon as particles escape from its Alfvén radius; the so-called magnetic braking (Schatzman 1962). The magnetic braking will depend on the characteristics of the stellar magnetic field, on the rotation and on the mass of the star. It appears as a boundary condition to the transport of angular momentum equation. From Zahn (1992), the boundary condition writes:

$$\frac{\partial}{\partial t} \left[\Omega \int_{r_{bcz}}^R r^4 \rho dr \right] = -\frac{1}{5} r^4 \rho \Omega U_2 + \mathcal{F}_\Omega \quad (5.13)$$

with \mathcal{F}_Ω the torque applied at the stellar surface.

Several expressions were proposed in the literature to describe the loss of angular momentum during the stellar evolution (e.g. Skumanich (1972); Kawaler (1988b); Matt et al. (2012, 2015a) and see also the comparative work of Amard et al. (2016)).

For the models presented in this thesis, the extraction of angular momentum at the stellar surface due to magnetised winds is according to the formalism by Matt et al. (2015a). The loss of angular momentum writes as:

$$\frac{dJ}{dt} = -\tau_0 \left(\frac{\tau_{cz}}{\tau_{cz\odot}} \right)^p \left(\frac{\Omega_\star}{\Omega_\odot} \right)^{p+1} \quad \text{if unsaturated,} \quad (5.14)$$

$$\frac{dJ}{dt} = -\tau_0^p \left(\frac{\Omega_\star}{\Omega_\odot} \right)^{p+1} \quad \text{if saturated,} \quad (5.15)$$

where τ_0 :

$$\tau_0 = K \left(\frac{R_\star}{R_\odot} \right)^{3.1} \left(\frac{M_\star}{M_\odot} \right) \gamma^{2m}, \quad (5.16)$$

with $\gamma = \sqrt{1 + (f/0.072)^2}$, see Eq. (8) of Matt et al. (2012). Saturation refers to the magnetic field that reach saturation above a certain value of the surface angular velocity (Amard et al. 2016; Wright et al. 2011).

We use the adjusted values for the parameters $m = 0.22$ and $p = 2.1$ as in Amard et al. (2019). They refer respectively to an exponent related to the magnetic field geometry and to the exponent relating rotation and activity. We take $\chi = 14 \equiv \frac{Ro_\odot}{Ro_{\text{sat}}}$, the ratio of the solar Rossby number to the saturation value of the Rossby number (at which the magnetic activity indicators saturate). At this point there is no further increase of the magnetic field, it defines when the saturation effect is reached.

We also remind that the Rossby number is defined as:

$$Ro = (\Omega \tau_{cz})^{-1}, \quad (5.17)$$

¹The Alfvén radius is defined as the radius beyond which particles escape the influence of the stellar magnetic field.

where τ_{cz} is the convective turnover timescale, defined by the ratio between the size of a convective region and the convective velocity. τ_{cz} gives the time for a convective cell to cover a mixing length l (for the Sun: $\tau_{cz,\odot} = 2 \times 10^2$ days). Then we have $\chi \equiv \frac{\Omega_{\text{sat}} \tau_{cz}}{\Omega_{\odot} \tau_{cz,\odot}}$.

These parameters (p , m , χ) are fitted on clusters of different ages in order to reproduce the rotation velocity dispersion according to Amard et al. (2019). However, we note that the value of Ω_{sat} , the rotation limit to reach saturation, has also been shown to be mass dependent. Indeed, observations suggest a faster decrease of rotation velocities with time for higher masses ($\approx 1.2 - 1.3M_{\odot}$) that implies a higher value of Ω_{sat} .

Finally, a last additional parameter linked to magnetised wind braking, K , is adjusted to reproduce the surface rotation of the Sun at $K = 6.3 \cdot 10^{30}$ (Matt et al. 2019)².

5.2.2 Transport of angular momentum by additional viscosity

Several processes (e.g. internal gravity waves, magnetic instabilities and see Section 5.4) have been proposed to explain the strong coupling between the core and the surface of low-mass stars, and to flatten the angular velocity profile at the solar age and beyond. To estimate the efficiency of the missing process(es), parametric studies have been realised by mean of the addition of an additional viscosity. Eggenberger et al. (2012b, 2019b, see also Lagarde et al. 2014 and Spada et al. 2016) proposed to introduce a parametric vertical viscosity ν_{add} in the equation describing the transport of angular momentum to reproduce the core rotation rates of SGB and RGB stars. In this context, Eq. (5.4) becomes:

$$\rho \frac{d}{dt} (r^2 \Omega) = \frac{1}{5r^2} \frac{\partial}{\partial r} (\rho r^4 \Omega U_2) + \frac{1}{r^2} \frac{\partial}{\partial r} \left((\nu_v + \nu_{\text{add}}) r^4 \frac{\partial \Omega}{\partial r} \right). \quad (5.18)$$

Eggenberger et al. (2012b) proposed ν_{add} as constant and uniform in time. However, the authors remind that it does not mean that they expect an unknown physical process that would result of a constant viscosity in stellar radiative zones. In addition, Spada et al. (2016) proposed a rotation dependant viscosity ν_{add} . Their Eq. (3) assumed an angular momentum transport efficiency dependent on the radial rotational shear, i.e.:

$$\nu_{\text{add}}(t) = \nu_0 \times \left(\frac{\bar{\Omega}_{\text{rad}}}{\bar{\Omega}_{\text{conv}}} \right)^{\alpha}, \quad (5.19)$$

where ν_0 and α are free parameters, and $\bar{\Omega}_{\text{rad}}$ and $\bar{\Omega}_{\text{conv}}$ are the mean angular velocity in the radiative interior and convective envelope, respectively.

The additional viscosity ν_{add} was already implemented before the beginning of the thesis. We added the rotational dependence and tested both approaches in different configurations for rotation in Chapter 8 in the framework of Li and rotational observations described in Chapter 1.

5.3 Transport of chemicals

5.3.1 Transport of chemicals in a rotating star

We remind here the general diffusion equation already given Eq. (4.1).

$$\rho \frac{\partial X_i}{\partial t} = \underbrace{\frac{1}{r^2} \frac{\partial}{\partial r} \left(r^2 \rho D \frac{\partial X_i}{\partial r} \right)}_{\text{Turbulent diffusion}} - \underbrace{\frac{1}{r^2} \frac{\partial}{\partial r} (r^2 \rho X_i v_i)}_{\text{Atomic diffusion}} + m_i \underbrace{\left[\sum_j r_{ji} - \sum_k r_{ik} \right]}_{\text{Nuclear reactions}}, \quad (5.20)$$

²One notes that in STAREVOL the value is normalised multiplying by 2/3.

It describes the evolution of chemical abundances under the effect of nuclear reactions and transport processes. $D = \sum_j D_j$ with j the sum of different diffusion coefficients describing turbulent processes. According to e.g. Chaboyer & Zahn (1992), it includes the transport due to the vertical shear (coefficient D_v) and the diffusion coefficient D_{eff} from meridional circulation that depends on the horizontal shear (coefficient D_h), and writes:

$$D_{\text{eff}} = \frac{(rU_2)^2}{30D_h} \quad (5.21)$$

Additional transport processes can be included in the total coefficient D for turbulent diffusion.

5.3.2 Tachocline

The tachocline (Spiegel & Zahn 1992), named by analogy with the thermocline of oceanography, where "Táchos-" (ancient greek: $\tau\alpha\chi\omicron\varsigma$) means fast in the sense of the fast change of Ω , is a transition layer located at the base of the external convection zone, where the latitudinal rotation profile goes from differential in the convective envelope, to flat in the radiative interior (Christensen-Dalsgaard & Schou 1988). First modelled by Spiegel & Zahn (1992) in a hydrodynamical framework, it is considered the seat of strong turbulence that can be parametrised with respect to the Brunt-Väisälä frequency, the thickness of the tachocline and the horizontal turbulent viscosity within it. This turbulence is then highly linked to rotational-mixing processes. In particular, the tachocline thickness is expected to be thin in case of strong horizontal turbulence. The tachocline turbulence can be treated as an additional coefficient of diffusion as described by Brun et al. (1999). From Eq. (15) and (16) in Brun et al. (1999) the coefficient for tachocline mixing is defined as:

$$D_{\text{Tach}}(\zeta) = \frac{1}{180} \frac{1}{4} \left(\frac{8}{3}\right)^2 \nu_H \left(\frac{d}{r_{\text{bcz}}}\right)^2 \mu_4^6 Q_4^2 \exp(-2\zeta) \cos^2(\zeta) \quad (5.22)$$

where ν_H is the horizontal turbulent viscosity; r_{bcz} is the radius at the base of the convective envelope; $\zeta = \mu_4(r_{\text{bcz}} - r)/d$ is a non-dimensional depth; $\mu_4 = 4.933$; $Q_4 \approx \hat{\Omega}/\Omega$, with $\hat{\Omega} = d\Omega(r, \theta)/d\theta$ is the latitudinal differential rotation at the base of the convective envelope; and d is a measure of the tachocline thickness h , with $h \approx d/2$:

$$d(t) = r_{\text{bcz}} \left(\frac{2\Omega}{N}\right)^{1/2} \left(\frac{4\kappa_T}{\nu_H}\right)^{1/4} \quad (5.23)$$

Eq. (5.22) can be solved independently of time. However, the depth of the convective envelope r_{bcz} , the angular velocity Ω , the horizontal viscosity ν_H , the thermal diffusivity κ_T and the Brunt-Väisälä frequency N , all vary in time, as predicted by the structure and rotation equations. During this thesis, we were able, for the first time, to solve self-consistently the Eq. (5.23) (see Chapter 8). Defining:

$$C = \frac{1}{180} \frac{1}{4} \left(\frac{8}{3}\right)^2 \mu_4^6 \exp(-2\zeta) \cos^2(\zeta) \quad (5.24)$$

we can compute the fully time-dependent equation of D_{Tach} as:

$$D_{\text{Tach}}(t) = C \times \nu_H \left(\frac{d}{r_{\text{bcz}}}\right)^2 \left(\frac{\hat{\Omega}}{\Omega}\right)^2 \propto \Omega \nu_h^{1/2} \left(\frac{\hat{\Omega}}{\Omega}\right)^2 \quad (5.25)$$

The treatment of the meridional circulation in the framework of Zahn's theory is based on the expansion of all the physical quantities, including meridional circulation, in Legendre polynomials. The meridional circulation velocity is expanded to the second-order Legendre polynomials in the original works by Zahn (1992) and Maeder & Zahn (1998), which is the formalism adopted in

STAREVOL. In that case, as shown by Mathis & Zahn (2004), the differential rotation in latitude is not explicitly accounted for. An expansion to the fourth-order of the departures from spherical symmetry is required to simultaneously treat the bulk of a radiative region and its tachocline, which is beyond the scope of this study. Hence, we need a prescription to evaluate $\hat{\Omega}/\Omega$, and we adopt the same proportionality as in Brun et al. (1999), namely $\hat{\Omega} \propto \Omega^{0.7 \pm 0.1}$, which in turn comes from the paper from Donahue et al. (1996), and has been confirmed since then (e.g. Saar 2009; Brun et al. 2017), even if some uncertainties subsist (e.g. Augustson et al. 2012, who found that it would scale inversely with Ω in the case of F-type stars).

Eq. (5.25) can thus be rewritten as:

$$D_{\text{Tach}}(t) = C \times 0.02 \left(\frac{\Omega^{0.4}}{N^{1/2}} \right) (4\nu_H K_T)^{1/2} \quad (5.26)$$

where we make explicit the proportionality coefficient adopted and the actual expression used in our computations for the ratio $\hat{\Omega}/\Omega$.

The treatment of the tachocline was implemented during the PhD thesis with both approaches, time-dependent or not. We computed, self-consistently, the thickness of the tachocline and the coefficient for tachocline mixing in Chapter 8.

5.3.3 Parametric turbulent transport

The physical turbulent processes generating chemical mixing in radiative interiors, and more specifically in the radiative regions bordering convective ones, cannot all be accounted for, given our current state of knowledge. Instead, these processes are parameterised to simulate diffusive turbulent mixing and may be applied as constraints to physical models of turbulence.

During the thesis, and in the framework of the previous studies already achieved to reproduce the Li evolution in Population I stars by rotational-mixing, we included the option of a purely parametric turbulent mixing. Specifically, we follow Richer et al. (2000) and Richard et al. (2005) who discussed the use of additional turbulence competing with atomic diffusion, respectively for observed abundance anomalies in Am and Fm stars (e.g. van't-Veer-Menneret et al. 1988) and for the lithium abundances of some Population II halo low-mass stars (e.g. Boesgaard et al. 1998; King et al. 1998). In both classes of objects, atomic diffusion can be very efficient, and comparing models with observations calls for additional transport processes to be able to counteract its effects, as already anticipated in different kinds of stars by a vast literature (e.g. Eddington 1929; Vauclair 2013; Michaud et al. 2015).

Richer et al. (2000) and Richard et al. (2005) propose a purely parametric approach to model turbulence, with no assumptions on the underlying physical mechanism (see also Talon et al. 2006 who was able to reproduce the observations using a rotation-induced mixing, consistent with the turbulent model of Richer et al. (2000)). Their diffusion coefficient is proportional to ρ^{-3} (see Proffitt & Michaud 1991) and attached to a specific temperature or to the density at the base of the convective envelope. These fixed points allow to drive where the turbulence is generated and thus the mixing depth. The parametric diffusivities D_{T_0} and D_{PMa_0} correspond to equations (2) and (3) of Richard et al. (2005), respectively:

$$D_{T_0} = 400 D_{\text{He}}(T_0) \left[\frac{\rho(T_0)}{\rho} \right]^3, \quad (5.27)$$

where T_0 is a free parameter corresponding to the temperature at which the diffusivity is set to be 400 times larger than the atomic diffusion coefficient for He (e.g. $D_{\text{He}}(T_0)$), which is computed

with the analytical approximation

$$D_{He}(T) = \frac{3.3 \times 10^{-15} T^{2.5}}{4\rho \ln\left(1 + \frac{1.125 \times 10^{-16} T^3}{\rho}\right)}, \quad (5.28)$$

as advised by Richer et al. (2000), and $\rho(T_0)$ is the density at the location where $T \equiv T_0$, and:

$$D_{PMa_0} = a_0 \left[\frac{\rho_{bcz}}{\rho} \right]^3. \quad (5.29)$$

Here a_0 is a free factor and ρ_{bcz} is the density at the base of the convective zone.

The two parametric diffusivities were implemented during the thesis. Results are presented in Chapter 8.

5.4 To go beyond

Processes described in the previous sections have to be considered in the framework of several candidates to transport chemicals and/or angular momentum. Alone, they are missing a complete physical explanation, and we know that others effects can be a part of the solution to the problem. The effects of internal gravity waves or the influence of magnetic field and magnetic instabilities have been invoked ("Type II rotational transport") but no clear answer has been found yet. We are not studying directly these processes; however, the tests and results of the thesis are a step forward. More details for these processes are given in the Appendix F of the thesis and references therein. Fig. (5.4) provides the schematic view when adding these processes.

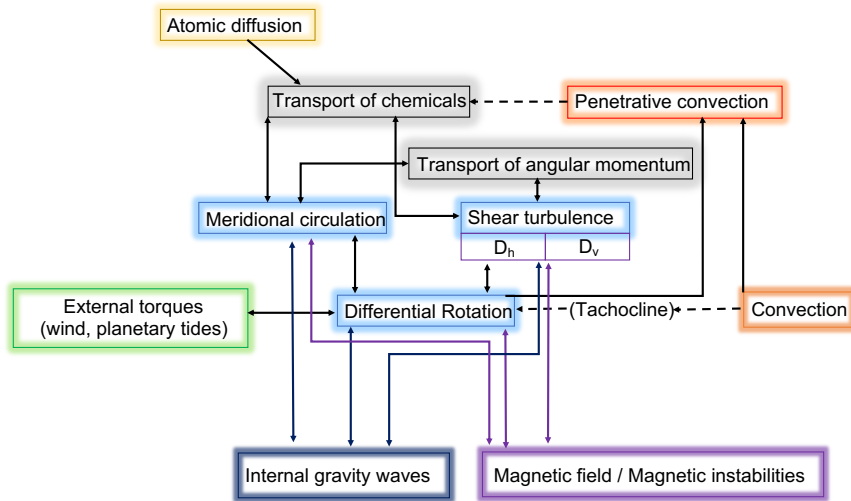


Figure 5.4: Scheme of the dynamical processes and their interaction that lead to transport of chemicals and of angular momentum in the star (freely inspired by Fig. 1 from Mathis et al. 2007)). Compared to Fig. 5.1, here, we consider the most promising physical phenomenon to transport chemicals and/or angular momentum with the addition of internal gravity waves (dark blue frame) and of magnetic processes (purple frame).

Part III

Non-standard stellar evolution models: Results

Validation of the scheme for atomic diffusion

In Chapter 4, we described atomic diffusion and two approaches to describe and implement this phenomenon in a 1D stellar evolution code. We implemented the formalism of Thoul et al. (1994) in STAREVOL. The aim of the present Chapter is to validate this choice and its implementation. In Section 6.1 we present the Montréal/Montpellier code (hereafter MoMo), which will be used in the validation process, and present the stellar structure produced by this code for benchmarking the atomic diffusion formalisms. Then, in Section 6.2, we present the impact of the different improvements made on the original Thoul et al. (1994). The comparison of the results obtained with the Thoul's algorithm as implemented in STAREVOL and the MoMo code and other codes is presented in Section 6.3. Then, Sections 6.4 and 6.5 will be dedicated to the general effects of atomic diffusion on Population I and Population II stars¹, respectively.

6.1 The Montréal/Montpellier stellar evolution code

The validation is achieved using solar evolution models from STAREVOL and models computed with MoMo by Olivier Richard (collaboration with LUPM - Montpellier France) considering a similar set of physics (AGSS09 abundances, grey atmosphere) but with a different formalism for atomic diffusion, described in Proffitt & Michaud (1991) and Turcotte et al. (1998b).

6.1.1 Input physics of MoMo

Models of MoMo are computed as described in Turcotte et al. (1998a). They include the input physics described in Tab. 6.1. **The Montréal/Montpellier stellar evolution code includes a complete and self-consistent formalism for atomic diffusion that fully solves Burgers equations (Burgers 1969, with the option to include radiative accelerations; see Appendix E)** according to the scheme detailed by Proffitt & Michaud (1991); Michaud & Proffitt (1993). In comparison, in the formalism from Thoul et al. (1994), the solution of the Burgers equations is an approximation. This is why we consider the MoMo results as a reference to which compare our models with the improved Thoul et al. (1994) formalism. The MoMo code was used to study the effects of atomic diffusion and radiative accelerations in several case including: the Sun (Turcotte et al. 1998b), more massive F-type stars (Turcotte et al. 1998a), chemically peculiar Am- and Fm-type stars (Turcotte

¹The observed metallicity evolution between stars of different age has led to the determination of a classification of stars into three main populations. Population I refers to stars with solar metallicity or metal-rich stars, Population II refers to metal-poor stars, Population III refers to stars composed only of primordial elements: hydrogen, helium and small amounts of lithium and beryllium.

Table 6.1: Comparative inputs physics in stellar evolution codes used for the validation of the atomic diffusion formalism.

Model	EOS	Opacity	Nuclear reaction rate	Atmosphere
STAREVOL	Modified PTEH95	OPAL (and F05)	NACRE II	Grey
MoMo	CEFF	OPAL (and Kurucz93)	BP92	Grey
MESA	SCVH, OPAL06, HELM, PC	OPAL (and F05)	JINA ReacliB	Grey
CLES	CEFF	OPAL (and F05)	NACRE	Grey

References. PTEH95: Eggleton et al. (1973) and Pols et al. (1995), CEFF: Eggleton et al. (1973) including the Coulomb correction Christensen-Dalsgaard & Daeppen (1992), SCVH: (Saumon et al. 1995), OPAL06: (Rogers & Nayfonov 2002), HELM: (Timmes & Swesty 2000), PC: (Potekhin & Chabrier 2010), OPAL database: Rogers et al. (1996), Kurucz93: see Proffitt (1994, for $T < 12000$ K), BP92: Bahcall & Pinsonneault (1992), F05: Ferguson et al. (2005), NACRE II: Xu et al. (2013b), JINA ReacliB: Cyburt et al. (2010), NACRE: Angulo et al. (1999).

et al. 2000; Richer et al. 2000), B- and A-type stars (Richard et al. 2001) and also for the specific case of Pop. II stars (Richard et al. 2002b; VandenBerg et al. 2002; Richard et al. 2002a). These different studies highlighted the main impact of atomic diffusion and radiative accelerations.

6.1.2 Structure for benchmarking

To make our comparison, we test the two algorithms on the same stellar structure. This structure is generated by MoMo from calibrated solar model (courtesy of O. Richard) at two different evolutionary stages. The first one gives a structure at the ZAMS² (core hydrogen mass fraction $X_c = 0.71$) and the second one corresponds to the structure at the age of the Sun (4.57 Gyrs) or $X_c = 0.35$.

We use the corresponding physical quantities (radius, pressure, temperature, density, mass) to compute atomic diffusion terms and showed Fig. 6.1, to the mass fraction profiles showed Fig. 6.2 and the mean charge profile (Z_{mean}) showed Fig. 6.4. Thereafter, the structure is used as an input for the atomic diffusion routines, extracted from STAREVOL (post-processing), and where we can compute atomic diffusion with the scheme we implemented and presented Section 4.3.2.

The main output obtained with the atomic diffusion routines for the two formalisms are the diffusion velocities that are computed for the different elements followed³ in each code. To achieve the comparison and the validation of our scheme of atomic diffusion, we will consequently focus on the diffusion velocities of a few light elements followed in both codes and the consecutive changes in surface abundances. Thereafter, we will focus on: ${}^3\text{He}$, ${}^4\text{He}$, ${}^{12}\text{C}$, ${}^{13}\text{C}$, ${}^{14}\text{N}$, ${}^{16}\text{O}$.

²Zero Age Main Sequence.

³STAREVOL code follows 54 chemical species from ${}^1\text{H}$ to ${}^{37}\text{Cl}$. MoMo follows elements from ${}^1\text{H}$ to ${}^{58}\text{Ni}$, but we have no access to the different light isotopes (except ${}^2\text{H}$, ${}^6\text{Li}$, ${}^4\text{He}$, ${}^{13}\text{C}$) as in STAREVOL.

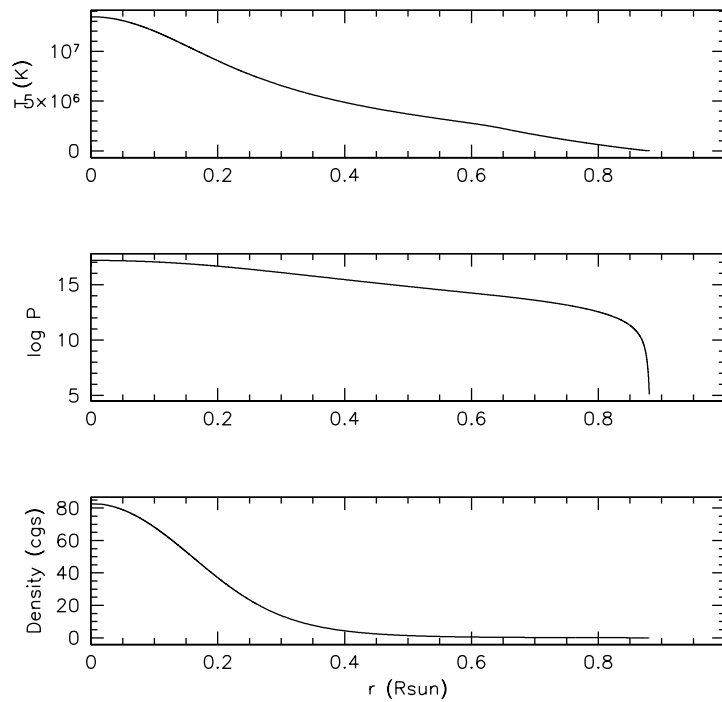


Figure 6.1: (Top) Temperature profile - T (K), (Middle) Pressure profile - P ($\text{dyn}\cdot\text{cm}^{-2}$), (Bottom) Density profile - ρ ($\text{g}\cdot\text{cm}^{-3}$). Structure at ZAMS from a $1M_{\odot}$ star at Z_{\odot} with the MoMo stellar evolution code.

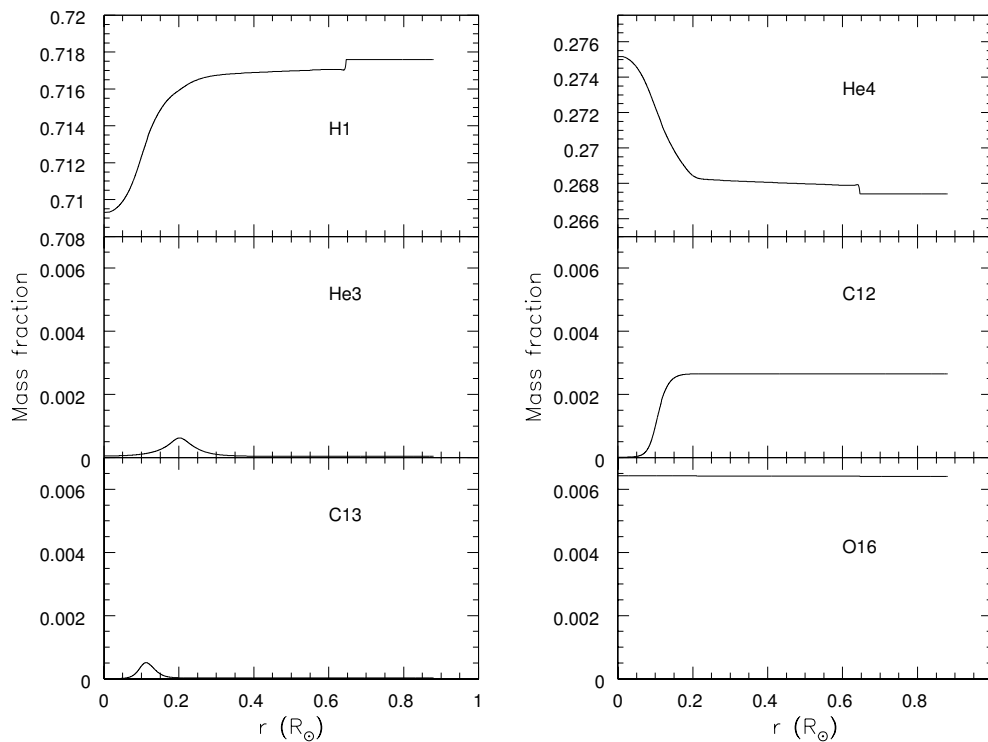


Figure 6.2: Mass fraction profiles within the MoMo stellar evolution code for ^3He , ^4He , ^{12}C , ^{13}C and ^{16}O for the same structure as in Fig. 6.1.

6.2 Improvements on the original Thoul et al. (1994) algorithm

6.2.1 Partial ionisation and Paquette's coefficients

In a first step, starting from the structure at ZAMS, we tested the effects of total/partial ionisation (see Section 3.3) and of the computation with the coefficients of Paquette et al. (1986), described Section 4.2.2, to assess the improvement on the atomic diffusion formalism of Thoul et al. (1994) (see Section 4.3.2). Fig. 6.3 shows the diffusion velocity of ${}^4\text{He}$ (upper panel) and ${}^{16}\text{O}$ (lower panel) close to the ZAMS ($X_c = 0.71$) for each case. Atomic diffusion with and without including the coefficients of Paquette are respectively in red and in blue. Partial ionisation is shown by dashed-lines and total ionisation is shown by dotted-lines.

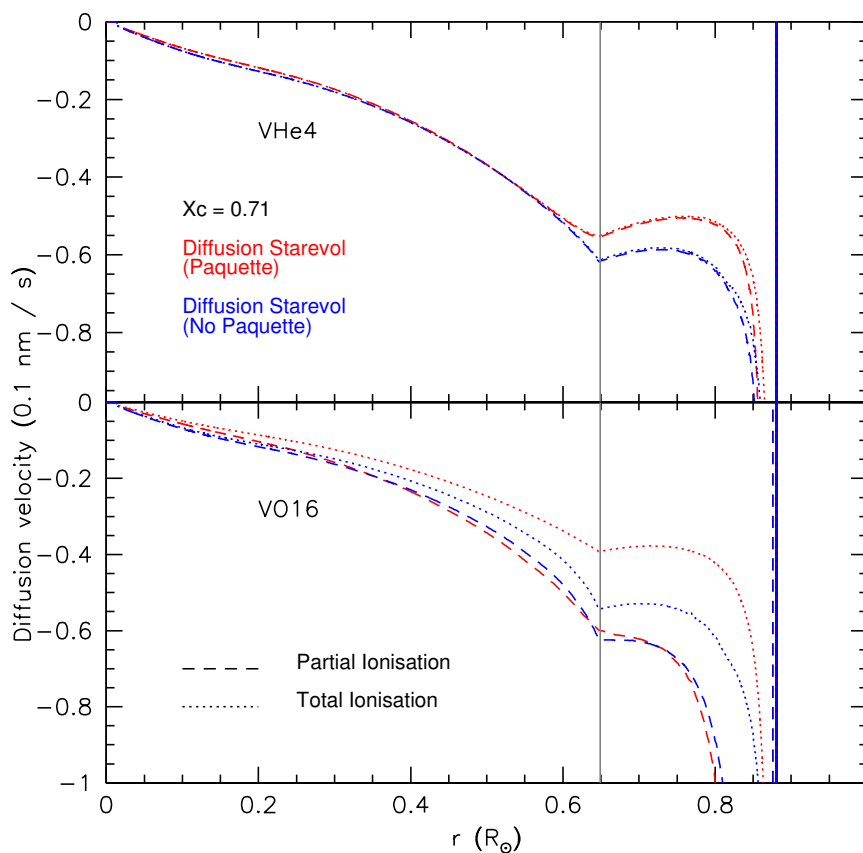


Figure 6.3: Diffusion velocities (in $0.1\text{nm}\cdot\text{s}^{-1}$) of ${}^4\text{He}$ and ${}^{16}\text{O}$ at ZAMS following the diffusion scheme as implemented in the STAREVOL code with Paquette's coefficients (red) and without Paquette's coefficients (blue). The two cases of ionisation (total: dotted-line and partial: dashed-line) are also plotted. The grey line indicates the base of the convective envelope.

The main impact of both updates is, in particular, visible at the base of the convection zone where the degree of ionisation change rapidly⁴. Ionisation affects both the electrical field E proportional to the ion charge and the ion-collision cross-section (Gorshkov & Baturin 2008). With Paquette's coefficients, the helium velocity is decreased from $-0.060\text{nm}\cdot\text{s}^{-1}$ to $-0.055\text{nm}\cdot\text{s}^{-1}$ and the oxygen velocity from $-0.055\text{nm}\cdot\text{s}^{-1}$ to $-0.040\text{nm}\cdot\text{s}^{-1}$. At the opposite, when considering the partial ion-

⁴See also Baturin et al. (2006) concerning the discontinuity at the base of the convective zone and the impact of the different atomic diffusion coefficients.

isation instead of the total ionisation, the velocity is increased but only for ^{16}O . Due to its small number of electrons, including partial ionisation has a negligible effect on ^4He . The inclusion of Paquette’s coefficients and partial ionisation leads to a small absolute increase of the velocity of ^4He and ^{16}O ($\approx 8\%$). The combined effect leads to a stronger effect for heavy elements. In Section 6.2.2 and 6.3.2, I analyse what are the specific terms (i.e. pressure gradient, thermal gradient, concentration gradient) which are the most impacted by these updates.

Partial ionisation of elements changes the velocity of ^{16}O by $\approx 16\%$ without Paquette’s coefficients and up to $\approx 48\%$ when including Paquette’s coefficient. The partial ionisation of elements cannot be neglected, a fortiori for heavy elements. Fig. 6.4 gives the ionisation states as a function of $\log(T)$ for ^4He , ^{12}C , ^{14}N and ^{16}O , and obtained with the codes STAREVOL and MoMo (and where we added the results of MESA stellar evolution code (Paxton et al. 2011, 2018) that use a combined EOS (see Tab. 6.1); each used depending on temperature and density). Although the EOS is different between the codes, the agreement between the three is good, except a shift of the MoMo code close to $\log T = 5$ for ^{12}C , ^{14}N and ^{16}O compared to STAREVOL and MESA and a shift of the three codes at about $\log T = 6.4$ for the same three elements. However, we remind that in STAREVOL we consider total ionisation for $\log T > 6.5$ whereas MoMo code does not reach a total ionisation for elements heavier than helium (we note that ionisation in MoMo comes directly from the OPAL-EOS Rogers & Nayfonov 2002). For both low and high temperatures, differences can be explained by the different formalisms of the EOS used in the codes. For the coming comparison we adopt the $Z_{\text{mean}} = Z_{\text{ionise}}/Z$ profiles from MoMo to discard this difference for our comparison of atomic diffusion algorithms.

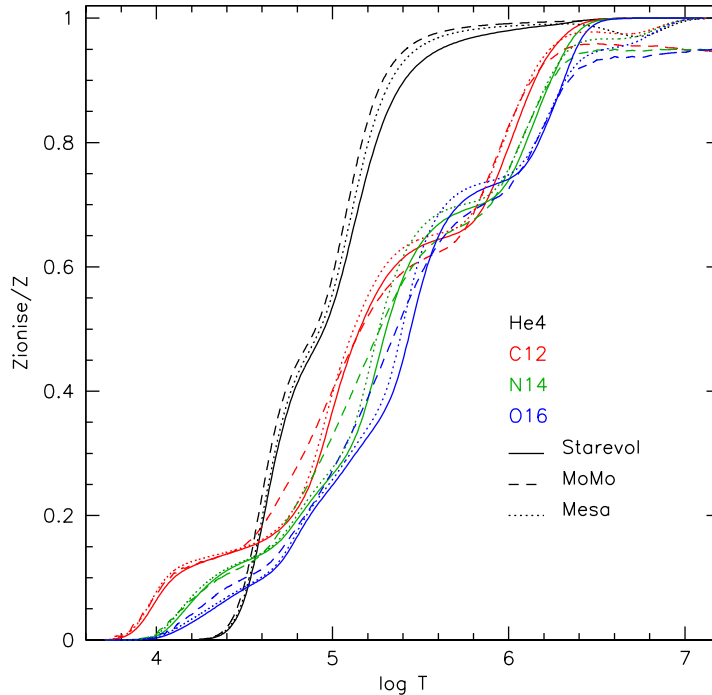


Figure 6.4: Normalised ionisation rate versus logarithm of temperature for ^4He , ^{12}C , ^{14}N and ^{16}O in STAREVOL code (solid line), Montreal/Montpellier code (dashed line) and MESA (dotted line).

6.2.2 Terms involved in the diffusion velocity

As seen previously, the diffusion velocity is a combination of three main components: the pressure term, the temperature (or thermal) term and the concentration term. These terms depend on the abundances, the pressure, the temperature, the density, the element mean charge (Z_{mean}) and the coefficients of Paquette.

We plan to use the same structure to compute diffusion velocities with the two approaches of STAREVOL and MoMo. The MoMo code does not provide these coefficients as outputs, but we can extract these terms thanks to STAREVOL and evaluate the impact of each of them on the diffusion velocities.

Figure 6.5 shows on the left side the profiles of A_t (temperature coefficient) and A_p (pressure coefficient)⁵ for ${}^4\text{He}$ and ${}^{12}\text{C}$ elements⁶, and, on the right side, the contributions to diffusion velocity of the three main terms (pressure, temperature and concentration gradients). If the coefficients

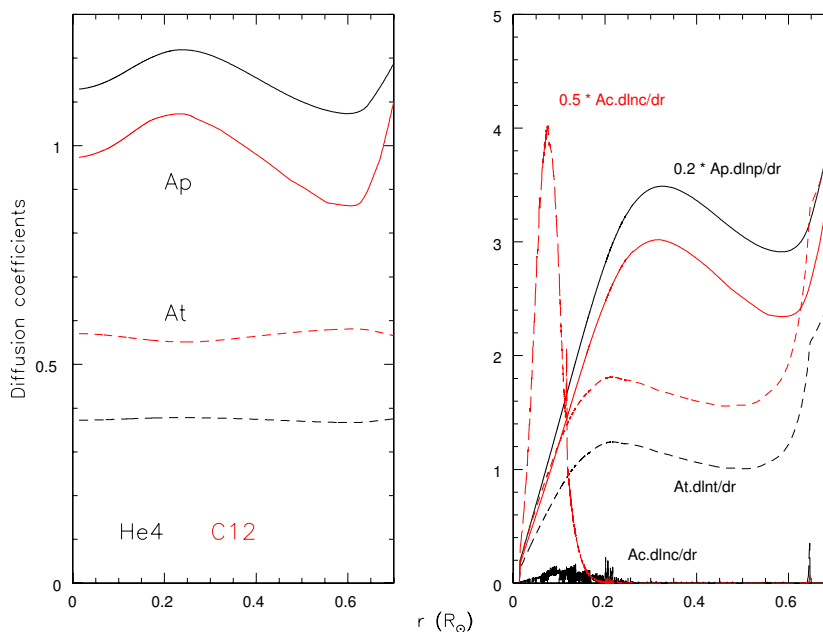


Figure 6.5: Contribution of the different terms involved in atomic diffusion at $X_c = 0.71$: the pressure term (Δ_P), the temperature term (Δ_T) and the concentration term (Δ_C) are plotted in solid, short-dashed and long-dashed line, respectively. (Left) Diffusion coefficients A_p and A_t for ${}^4\text{He}$ (black) and ${}^{12}\text{C}$ (red). (Right) Diffusion gradients for ${}^4\text{He}$ (black) and ${}^{12}\text{C}$ (red). For a better read of the figure, a factor of 0.5 is applied to the concentration gradient of ${}^{12}\text{C}$ and a factor of 0.2 is applied to the pressure gradient for both elements.

A_t and A_p are of the same order, although $A_p > A_t$, the gradient terms are quite different. The pressure term appears to be preponderant compared to the two others, in agreement with the results of Thoul et al. (1994), see for instance their Figure 6, and of Baturin et al. (2006), see their Figure 4. However, the situation is quite different regarding the considered element. For the case of ${}^4\text{He}$, the pressure term is the highest and the two others are small (temperature term) or negligible (concentration term). For the case of carbon, the pressure term is weaker and the temperature

⁵Corresponding to α_i and β_i , respectively, in Eq. 4.45 and where i is the considered element.

⁶The concentration term is a sum over all the elements' contributions, we do not extract each contribution but only the gradient term $Ac \frac{d \ln(c)}{dr}$ for each element. That is why it is not shown here. We note that Ac corresponds to γ_{ij} in Eq. 4.45

one is stronger, although $A_p \frac{d \ln(p)}{dr}$ stays preponderant except at the centre of the star. Indeed, for carbon, the concentration term becomes preponderant between the centre and about $0.1 - 0.15 R_\odot$. As the pressure gradient term dominates the diffusion velocity in the radiative region outside the nuclear core, a modification of this term by the use of the Paquette' coefficient should impact the final diffusion velocity (see also Section 6.3).

The influence of Paquette's coefficients is shown in Figs. 6.6 and 6.7.

Figures 6.6 and 6.7 display A_p and A_t profiles, respectively for ${}^3\text{He}$, ${}^4\text{He}$, ${}^{12}\text{C}$, ${}^{13}\text{C}$ and ${}^{16}\text{O}$. We computed these coefficients with/without Paquette's coefficients and with partial/total ionisation. The use of Paquette's coefficients leads to a systematic increase of A_p coefficients, and to a greater extent, of A_t coefficient for all elements considered here. While the coefficients A_p and A_t of the He isotopes remain unchanged when accounting for partial ionisation, the coefficient A_p are systematically higher for C and O isotopes when partial ionisation is accounted for. A_t coefficients are not affected by partial ionisation in the radiative interior. Using coefficients from Paquette et al. (1986), and at lower level partial ionisation, leads to an increase of the weight of the pressure term for the diffusion velocity. These two updates of the formalism of Thoul et al. (1994) highlight the sensitivity of the diffusion velocity to the way the different involved terms are computed or in other words of what are the approximations we considered for ionisation and particles interaction (through Paquette et al. (1986) coefficients).

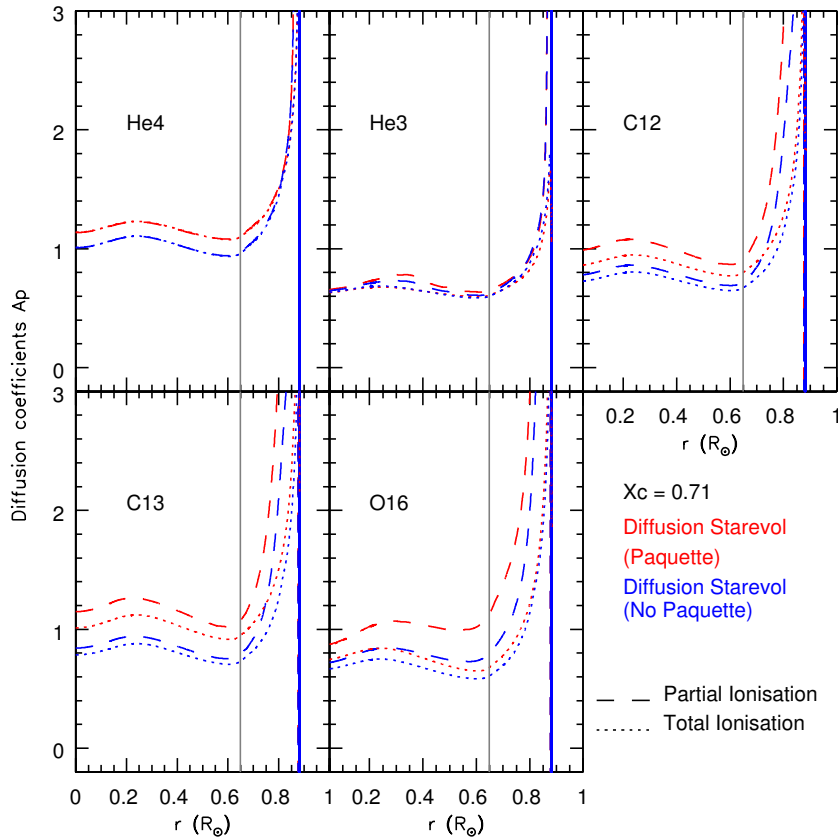


Figure 6.6: Pressure coefficient (A_p) profile at ZAMS for ${}^4\text{He}$, ${}^3\text{He}$, ${}^{12}\text{C}$, ${}^{13}\text{C}$ and ${}^{16}\text{O}$. Atomic diffusion according to Thoul et al. (1994) with coefficients from Paquette et al. (1986) (red) or without (blue). Dotted lines and dashed lines refer to total and partial ionisation, respectively. The grey line indicates the base of the convective envelope.

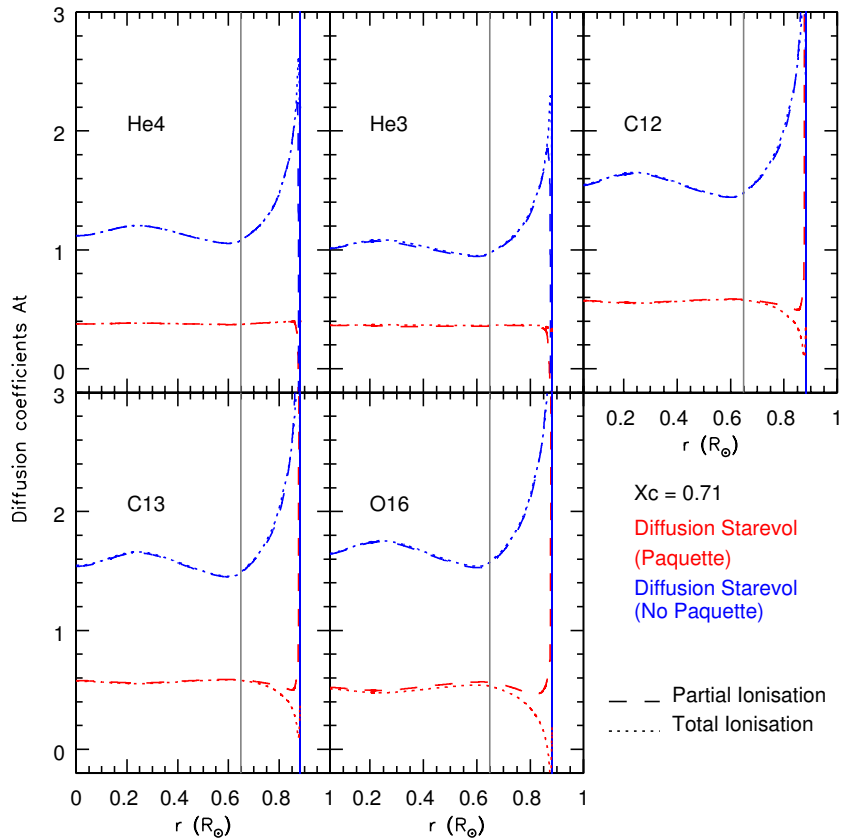


Figure 6.7: Temperature coefficient (At) profile at ZAMS for ${}^4\text{He}$, ${}^3\text{He}$, ${}^{12}\text{C}$, ${}^{13}\text{C}$ and ${}^{16}\text{O}$. Atomic diffusion according to Thoul et al. (1994) with coefficients from Paquette et al. (1986) (red) or without (blue). Dotted lines and dashed lines refer to total and partial ionisation, respectively. The grey line indicates the base of the convective envelope.

Finally, Fig. 6.8 shows that the gradient of concentration has an important effect on several elements in the core. Fig. 6.8 gives diffusion velocity profiles between the centre and $0.3R_{\odot}$ for ${}^4\text{He}$, ${}^{12}\text{C}$, ${}^{13}\text{C}$ and ${}^{16}\text{O}$. Velocities are given with and without the concentration gradient. There is no visible effect on helium and oxygen but there is a clear impact on the two isotopes of carbon. This behaviour is due to the gradient of the chemical composition due to nuclear reactions in the core (Baturin et al. 2006) and by the effect of the CN(O) cycle (see also Fig. 6.17 where ${}^{12}\text{C}$ and ${}^{14}\text{N}$ central abundances are changed due to nuclear reactions).

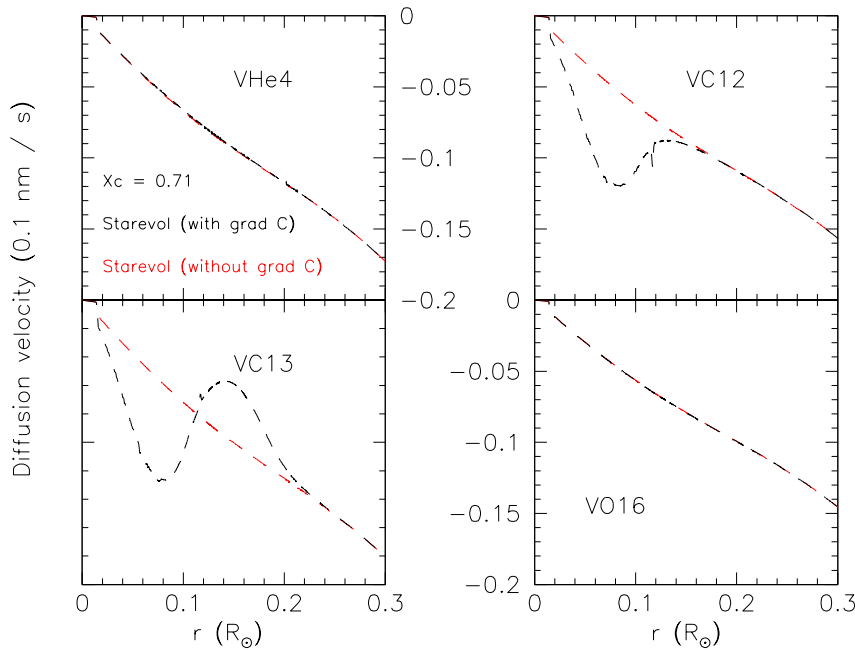


Figure 6.8: Diffusion velocities of ${}^4\text{He}$, ${}^{12}\text{C}$, ${}^{13}\text{C}$ and ${}^{16}\text{O}$ at ZAMS. Black dashed lines and red dashed lines give the diffusion velocity with and without the concentration term, respectively.

6.3 Benchmarking of the Thoul et al. (1994) formalism

6.3.1 Comparison of the diffusion schemes: STAREVOL and MoMo

From now on, our models include partial ionisation and Paquette’s coefficients. We now compare our results with MoMo.

We remind that velocities output from MoMo do not include the concentration gradient term (see Eq. 4.34) which is considered as an additional diffusion coefficient (only added when solving the diffusion equation). Our implementation in STAREVOL allows to discriminate the different terms of diffusion. As a result, the following tests are only based on the determination of the gradients of pressure and temperature and of their associated coefficients $A_p(i)$ and $A_t(i)$. The addition of the gradient of concentration and its associated coefficient $A_c(i)$ will be realised at the end of Sections 6.3.2.

In this section we compare the algorithms for atomic diffusion including Paquette’s coefficients used in STAREVOL and MoMo, for the stellar structure computed with MoMo at ZAMS. We compute the velocities obtained from the addition of the pressure and the temperature gradients and compare to results of MoMo. We present the two cases with partial and total ionisation for both algorithm.

Figure 6.9 shows the diffusion velocity within the radiative zone for ${}^3\text{He}$, ${}^4\text{He}$, ${}^{12}\text{C}$, ${}^{13}\text{C}$, ${}^{16}\text{O}$. Red lines give the results obtained using the formalism of Thoul et al. (1994) as implemented in STAREVOL and green lines give the results obtained using the formalism as implemented in the Montréal/Montpellier code (Proffitt & Michaud 1991).

In their work, Turcotte et al. (1998b) found 20-30 % of difference between MoMo and the analytical fits of Thoul et al. (1994) for oxygen and iron elements at the age of the Sun. Comparing their own results with previous works from Bahcall & Loeb (1990) and Michaud & Proffitt (1993), Thoul et al. (1994) also found differences of the order 15-30% depending on the model and the element. Here,

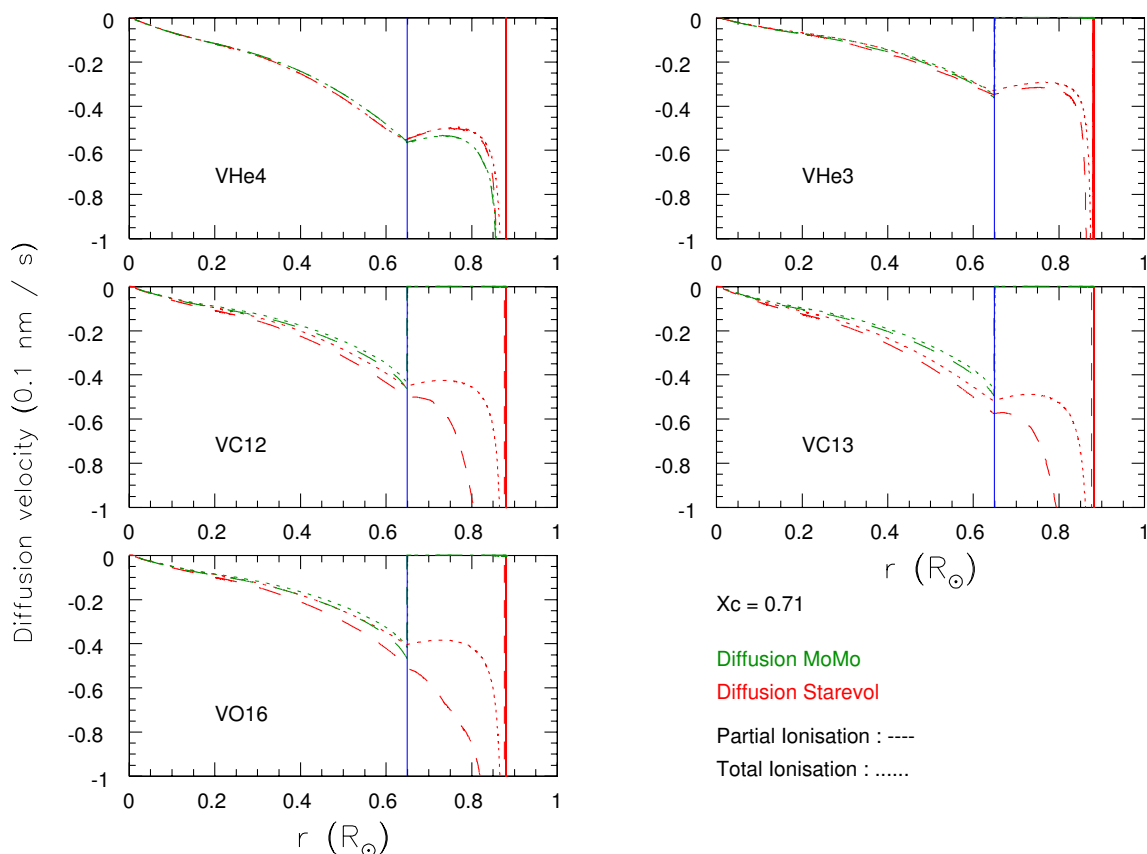


Figure 6.9: Diffusion velocities (in $0.1 \text{ nm} \cdot \text{s}^{-1}$) at ZAMS for ${}^3\text{He}$, ${}^4\text{He}$, ${}^{12}\text{C}$, ${}^{13}\text{C}$ and ${}^{16}\text{O}$ according to STAREVOL (red) and Montréal/Montpellier (green) without considering the concentration term. The two cases of ionisation (total : dotted line and partial : dashed line) are also represented. The blue line indicates the base of the convective envelope.

we reach a better agreement for the case of ${}^3\text{He}$ and ${}^4\text{He}$ with relative difference smaller than 10% at the ZAMS and at the age of the Sun (see Tab. 6.2). Concerning the others elements, differences can be seen between from about $r=0.4R_{\odot}$ and the base of the convective zone at about 10-30 %. For each element the highest difference is reached in the radiative zone before a decrease of the difference at the limit between the convective envelope and the radiative zone. Diffusion velocity in the convective zone is not considered as atomic diffusion is negligible compared to convective turbulent transport in the convective envelope⁷ (see also Baturin et al. 2006).

Also, the effect of partial ionisation of elements is stronger in the formalism implemented in STAREVOL than in MoMo, despite using the same Z_{mean} profile in the comparison. However, accounting for partial ionisation leads a similar and consistent behaviour. Finally, while we took the same given structure, we obtained higher velocities with the formalism implemented in STAREVOL. This difference between the two schemes had already been observed by e.g. Turcotte et al. (1998a) (difference of about 20-30 %) as noticed previously. They explained a part of this difference by the use in MoMo of the coefficients of Paquette et al. (1986) for the computation of collision integrals. However, in our case we include these coefficients and the difference then cannot be only explained by that even if our differences are at a smaller percentage (see at $X_c = 0.35$ in Tab. 6.2).

⁷We note that MoMo consequently does not compute atomic diffusion velocity of elements heavier than helium in the convective envelope.

Table 6.2: Relative difference between diffusion velocities (V) computed by STAREVOL and MoMo at $X_c = 0.71$ and $X_c = 0.35$ (in percentage). Differences are indicated in green if velocities from STAREVOL are higher and in red if they are smaller.

$(V_{\text{MoMo}} - V_{\text{STAREVOL}})/V_{\text{MoMo}}$	ZR	ZR/ZC
$X_c = 0.71$		
${}^3\text{He}$	$\leq 7\%$	$\leq 4\%$
${}^4\text{He}$	$\leq 8\%$	$\leq 2\%$
${}^{12}\text{C}$	$\leq 22\%$	$\leq 9\%$
${}^{13}\text{C}$	$\leq 29\%$	$\leq 16\%$
${}^{16}\text{O}$	$\leq 18\%$	$\leq 11\%$
$X_c = 0.35$		
${}^3\text{He}$	$\leq 8\%$	$\leq 2\%$
${}^4\text{He}$	$\leq 7\%$	$\leq 2\%$
${}^{12}\text{C}$	$\leq 21\%$	$\leq 8\%$
${}^{13}\text{C}$	$\leq 28\%$	$\leq 14\%$
${}^{16}\text{O}$	$\leq 18\%$	$\leq 11\%$

Indeed, we saw that using these coefficients leads to a decrease of the diffusion velocity. However, a reasonable shift remains that could be explained by a difference in the sensitivity of the algorithms to the partial ionisation. Regarding the literature, numerical differences from the way formalisms have been implemented could also be part of the answer.

6.3.2 Comparison at two different evolution stages

Until now, we focused on one given structure corresponding to the ZAMS. We now add the time evolution in our comparison. We have access to a second structure from MoMo for $X_c = 0.35$ near the solar age.

Figure 6.10 shows results obtained with STAREVOL for the two evolutionary steps (ZAMS and solar age) and gives the diffusion velocities (Left) for ${}^4\text{He}$ and ${}^{12}\text{C}$ and pressure and temperature gradient coefficients profiles for the same elements (Right). From ZAMS stage to Solar age, there is a slight increase of the effective temperature and the convection zone becomes shallower (see the blue and cyan lines in Fig. 6.10). Atomic diffusion is then expected to be more efficient. Indeed, we observe an increase of the absolute amplitude velocity especially for helium and, in particular, at the base of the convection zone.

Furthermore, we observe a difference in the core of the star, concerning the A_p coefficient of ${}^4\text{He}$ and the A_p and A_t coefficients of ${}^{12}\text{C}$. Indeed, we see some bumps that appear in the core of the star. This can be explained by the chemical evolution in the core due to nuclear reactions. The nuclear reactions that occur during the evolution lead to changes in abundances profiles and by this way on velocity profiles. The increase of A_p and A_t coefficients of ${}^{12}\text{C}$ in the core leads to an increase of the absolute diffusion velocity in the core. Therefore, we note that ${}^4\text{He}$ reacts in an opposite way compared to ${}^{12}\text{C}$ in the core, mostly for A_p ⁸.

Figure 6.11 shows the comparison of the diffusion velocities between STAREVOL and MoMo. Comparing to Fig. 6.9, the diffusion velocity (in absolute value) increases with age (as the convective envelope retreats) in both cases. The differences between the results of both algorithms do not evolve significantly with time (see Tab. 6.2).

⁸In this context, several tests were realised regarding the use of Nacre I or Nacre II (See Appendix B.3) but they were not conclusive.

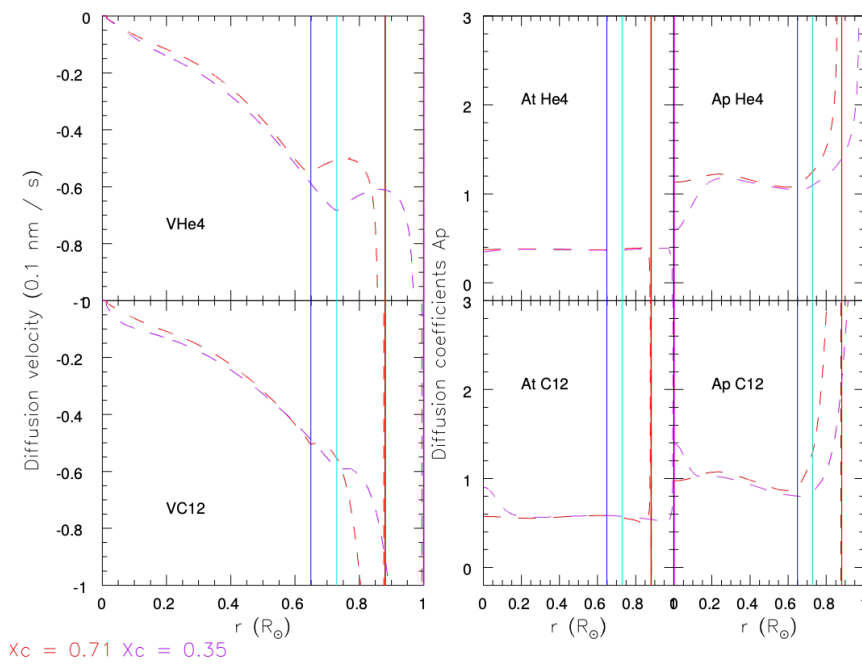


Figure 6.10: (Left) Profile comparisons at two different stages: $X_c = 0.71$ (red) and $X_c = 0.35$ (violet) for ${}^4\text{He}$ (top panels) and ${}^{12}\text{C}$ (bottom panels) computed according to our formalism of atomic diffusion in STAREVOL. *Left*: Diffusion velocity; *Middle*: coefficient A_t , and *Right* coefficient A_p . The blue line and the cyan line delimit the radiative zone and the convective zone, respectively for $X_c = 0.71$ and $X_c = 0.35$.

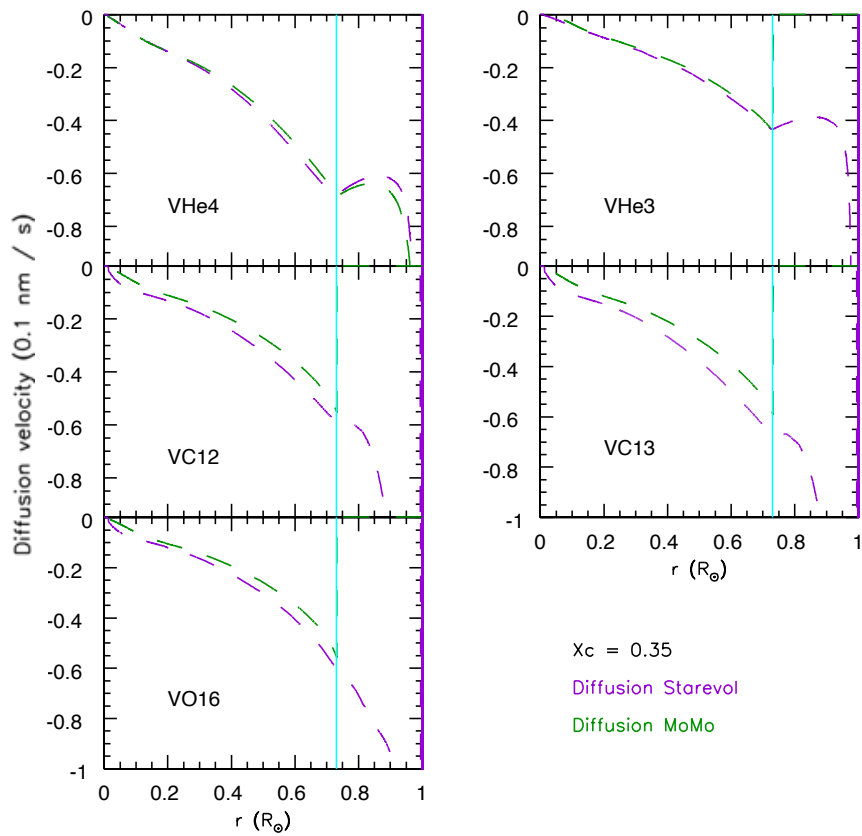


Figure 6.11: Diffusion velocities (in $0.1\text{nm}\cdot\text{s}^{-1}$) at evolutionary phase corresponding to $X_c = 0.35$ for ${}^3\text{He}$, ${}^4\text{He}$, ${}^{12}\text{C}$, ${}^{13}\text{C}$ and ${}^{16}\text{O}$ using the algorithm used in STAREVOL (violet) and that used in the MoMo code (green) without considering the concentration term. The cyan line indicates the base of the convective envelope.

6.3.3 Comparison for different stellar evolution codes at $X_c = 0.35$

In this section, we compare the results obtained for the full evolution of a $1M_\odot$ model at solar metallicity computed with STAREVOL including atomic diffusion as discussed previously (Thoul et al. (1994) with Paquette's coefficient and partial ionisation) at the age of the Sun ($X_c = 0.35$) to that obtained with other stellar evolution codes as listed in Table 6.1. **Contrary to the comparisons presented so far, here we do not limit the comparison to the algorithms, but compare outputs of full stellar evolution models.** In addition of STAREVOL and MoMo outputs, Fig. 6.12 reports tracks from Paxton et al. (2011) and Thoul et al. (1994) as crosses, and we also added the results obtained with the stellar evolution code CLES of Liège (courtesy of G. Buldgen, see also Scuflaire et al. 2008, and Tab. 6.1).

Figure 6.12 gives:

- STAREVOL in red;
- MoMo in green;
- CLES in blue;
- Thoul et al. (1994) fits with black crosses (according to their Figure 9 where velocities are computed exactly from the structure of the contemporary Sun);
- MESA with purple crosses (according to Fig. 7 from Paxton et al. (2011)).

In this figure, the diffusion velocity of STAREVOL includes the gradient of concentration, but it is not the case for MoMo.

The velocity we obtain in STAREVOL is slightly higher than MoMo's one, except between about $r=0.2 R_\odot$ and $r=0.5 R_\odot$. The addition of diffusion velocities computed with other codes allows a complementary comparison showing that differences exist also between the others codes. CLES and MESA are using the formalism of Thoul et al. (1994) but they do not distinguish all the elements. In CLES and in MESA, a system of "classes" is used, in other words, they defined classes of elements where a reference element is the representative isotope that define the velocity for all elements in the same class. We note that classes in CLES and MESA are also different.

Models from STAREVOL, CLES and MoMo finally result of small differences of a few percents in the diffusion velocity of oxygen, in particular, in the core and close to the base of the convective envelope, and although the differences of input physics. MESA and STAREVOL share also a similar formalism and implementation for the treatment of atomic diffusion and results are close mainly at the centre and only of a few percent of difference near the base of the convective zone where MESA diffusion velocities are higher. We note, however, that at $r < 0.2R_\odot$ where the gradient of concentration is efficient, only STAREVOL shows a bump. The treatment of the nuclear reactions in STAREVOL could be at the origin of this difference, as seen previously.

We observe a good agreement between STAREVOL and the analytical fits from Thoul et al. (1994) but with a smaller velocity in STAREVOL. It was already showed that analytical fits from Thoul et al. (1994) were in general too high due to its approximations (see for instance Turcotte et al. 1998a; Gorshkov & Baturin 2008; Hu et al. 2010).

Finally, if the differences between the STAREVOL code and the MoMo code exist, they are consistent with the range of the results obtained from different stellar evolution codes as already observed by previous comparative studies: for instance Thoul et al. (1994); Turcotte et al. (1998a); Hu et al. (2010); Paxton et al. (2011) or see also Gorshkov & Baturin (2008). This last figure confirms that these differences can be mainly attributed to the inputs physics used (EOS, Opacity tables), to

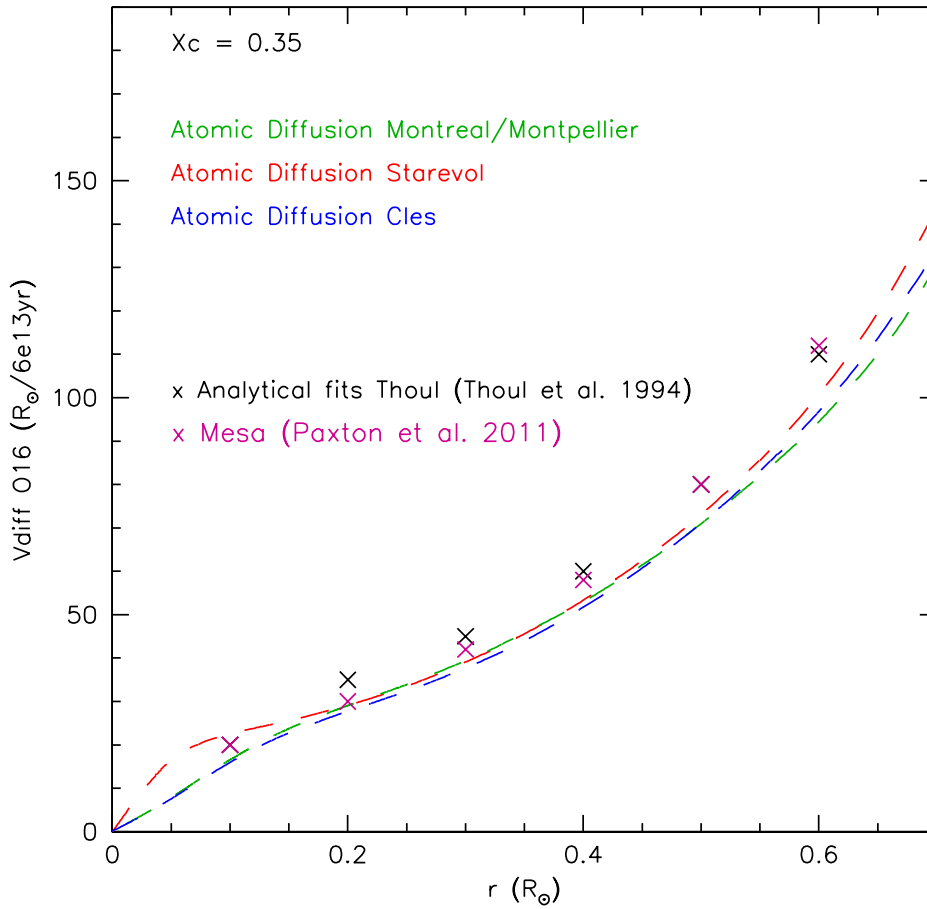


Figure 6.12: Diffusion velocity of ^{16}O at the age of the Sun ($X_c = 0.35$) and from STAREVOL code (red), MoMo code (green), CLES code (blue, courtesy of G. Buldgen), MESA code (purple crosses, Paxton et al. (2011)). Black crosses refer to analytical fits from Thoul et al. (1994). Results are plotted in units of R_\odot/τ_θ , where $\tau_\theta = 6 \times 10^{13}$ yrs is the characteristic diffusion timescale for the Sun (Thoul et al. 1994).

the sensitivity to ionisation of the formalism used, and also to the way the implementation of each formalism is done in each code with, in particular, the way to discriminate the elements.

Consequently, we consider that our implementation of the formalism from Thoul et al. (1994), involving partial ionisation and coefficients from Paquette et al. (1986) to compute the diffusion velocity is validated. The results of a new solar calibration including our updates on atomic diffusion will also be confronted with the ones usually determined in the literature (see Chapter 7). SSM and NSSM models in the coming Chapters of the thesis will include atomic diffusion according to this implementation.

6.4 Population I stars: evolution and structure

In this Section, I focus on the effects of atomic diffusion along evolution of a Population I star of $1 M_{\odot}$ and Z_{\odot} . The results are obtained from the full evolution computed by STAREVOL or by MoMo.

6.4.1 Evolution tracks and surface abundance variations

Figure 6.13 shows the evolution tracks in the HRD of models computed with STAREVOL in black and by MoMo in green⁹ for the two cases: with atomic diffusion (dashed line) or without atomic diffusion (solid line).

The resulting tracks are in good agreement with a shift of only a few K. In both codes, the addition of atomic diffusion leads to a shift to colder temperatures and smaller luminosity. It is expected from the changes in the opacity that result from the transport of elements and mainly of helium abundance that decreases at the surface (see Fig. 6.15). In particular, beyond the solar age, atomic diffusion in STAREVOL leads to a decrease of about 30-40 K close to the Turn-off. Besides, and as expected from the transport of hydrogen to external layers and of helium to the centre (see Fig. 6.14), the stellar lifetime decreases for both codes. At the age of the Sun, the lifetime is decreased by about 6.5 % and about 3.2 % for MoMo and STAREVOL, respectively. Effective temperatures are decreased when atomic diffusion is active (see bottom-panel Fig. 6.14). The H-burning time is shorter for both code but MoMo model is hotter and the efficiency of atomic diffusion is stronger. This explains the difference of ages at the same core hydrogen content between STAREVOL and MoMo. It is not negligible but the impact of the input physics, likely the choice for the EOS, the opacities, the metallicity or the mixing length, for instance, is also a possible origin of this difference.

Chemical composition is also strongly affected by atomic diffusion. Figure 6.15 shows the surface abundance evolution as a function of central hydrogen mass fraction X_c for STAREVOL and MoMo models; it gives the relative evolution of ${}^4\text{He}$, ${}^{12}\text{C}$, ${}^{14}\text{N}$, ${}^{16}\text{O}$, ${}^{20}\text{Ne}$, ${}^{23}\text{Na}$, ${}^{24}\text{Mg}$ and ${}^{27}\text{Al}$. For $X_c = 0.35$ (approximately corresponding to the evolutionary stage of the Sun), ${}^4\text{He}$ is decreased by about 9-10% in STAREVOL and by about 11-12% in MoMo which is consistent with previous studies (e.g. Turcotte et al. 1998a; Buldgen et al. 2019) who estimated about 10% of decrease for helium at solar age. Heavier elements also decreased by about 8-10% depending on each element. Table 6.3 summarises the relative variation during the MS of each element for STAREVOL and MoMo. We remind that now, the stellar structure of each code is different but similar results are obtained with MoMo and STAREVOL. The larger decrease in the MoMo model can be partly explained by the higher effective temperatures reached by the model (see Fig. 6.14). However, differences between the two codes are less important for the three heaviest elements of the sample (${}^{23}\text{Na}$, ${}^{24}\text{Mg}$ and ${}^{27}\text{Al}$), a possible explanation is a different treatment of nuclear reactions (see Tab. 6.1, with in particular the way how isotopes are discriminated).

⁹Here, evolutionary models from MoMo stop at solar age.

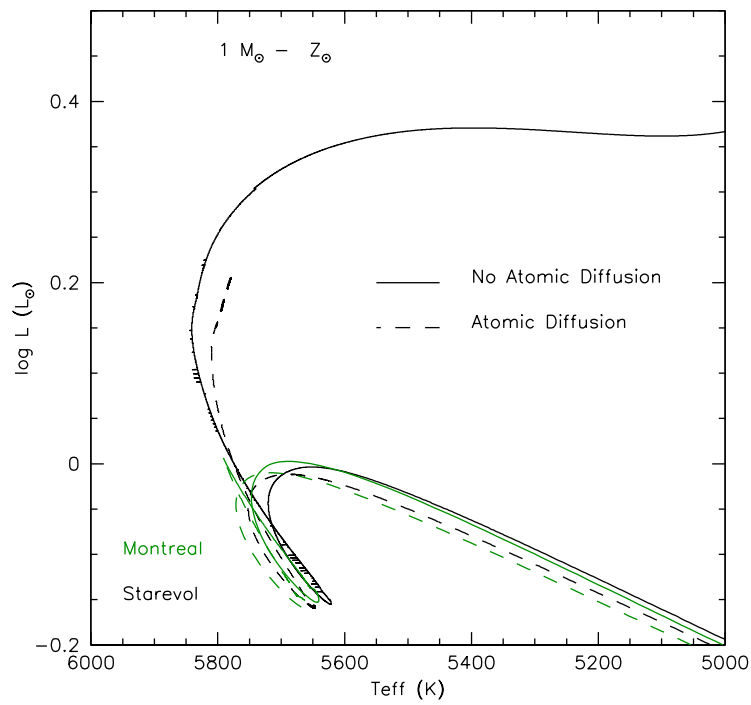


Figure 6.13: Evolutionary tracks in the Hertzsprung-Russell diagram for STAREVOL (black) and MoMo (green) solar models with or without atomic diffusion (dashed and solid line respectively).

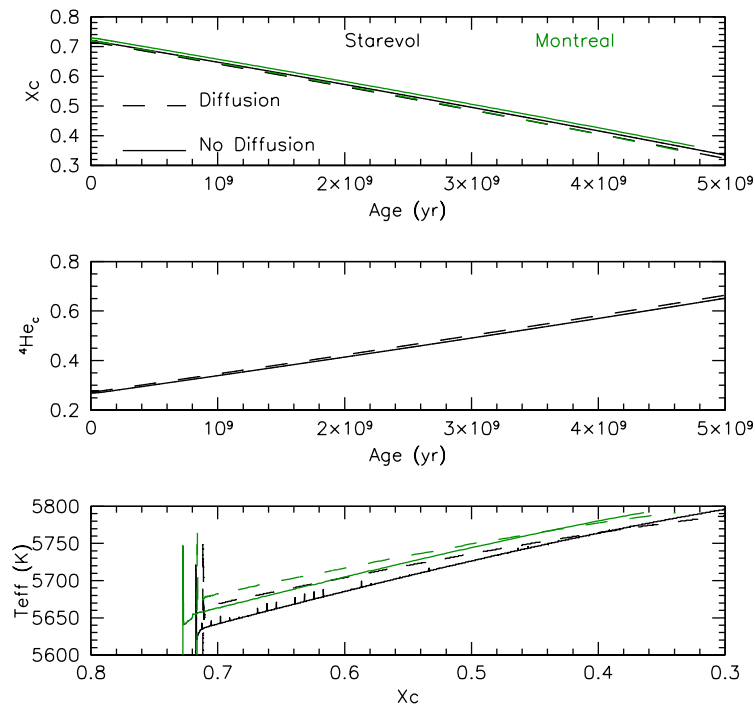


Figure 6.14: (Top) Time evolution of central hydrogen abundance (X_c). (Middle) Time evolution of central helium abundance (${}^4\text{He}_c$). (Bottom) Effective temperature T_{eff} (K) versus X_c . STAREVOL (black) and MoMo (green) tracks are reported.

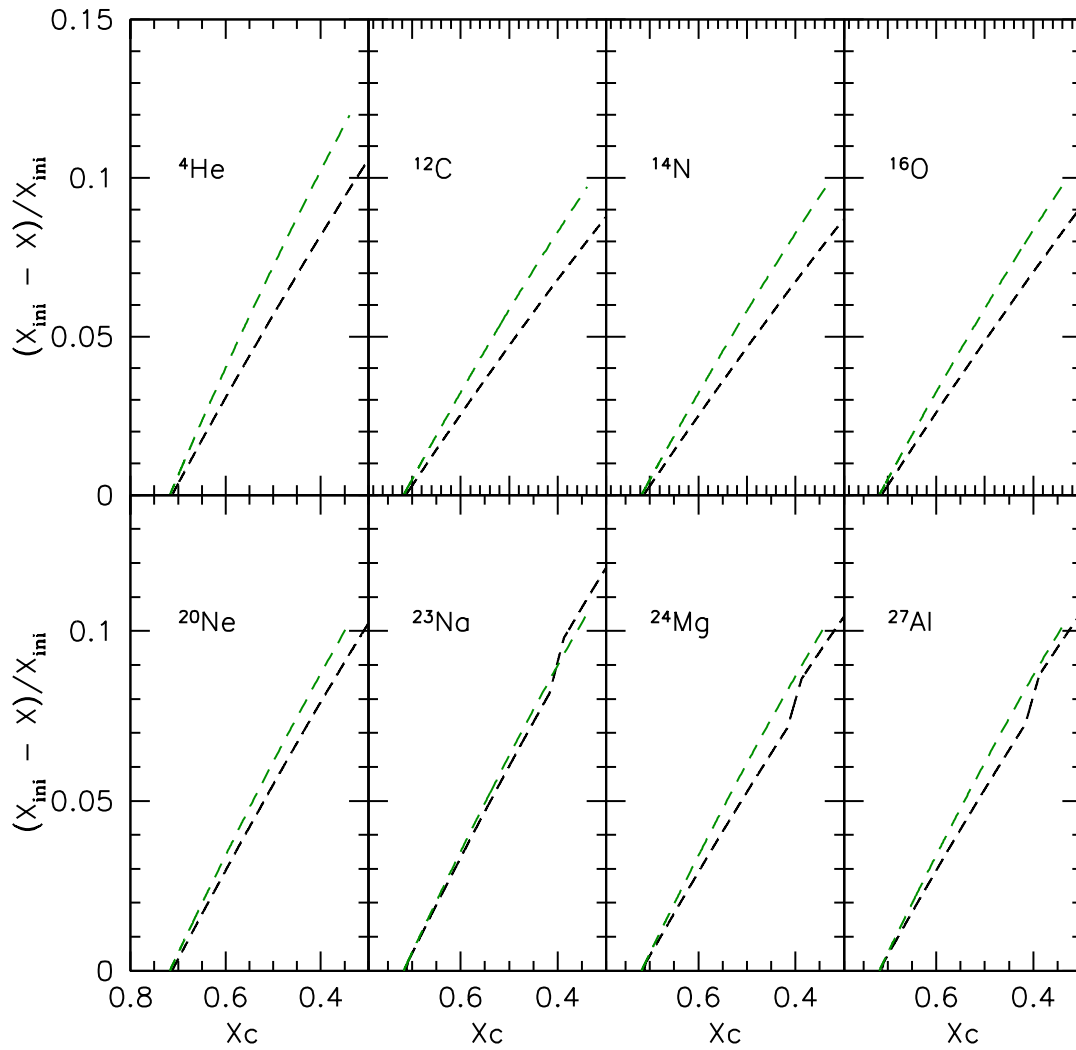


Figure 6.15: Relative variation (decrease) of surface abundances as a function of central hydrogen mass fraction X_c for $1M_{\odot}$ Pop. I models of STAREVOL (black) and MoMo (green), for ${}^4\text{He}$, ${}^{12}\text{C}$, ${}^{14}\text{N}$, ${}^{16}\text{O}$, ${}^{20}\text{Ne}$, ${}^{23}\text{Na}$, ${}^{24}\text{Mg}$ and ${}^{27}\text{Al}$.

Table 6.3: Relative decrease of surface abundances between the initial abundances and those at $X_c = 0.35$ for STAREVOL (left) and MoMo (right).

Element	$X_{\text{ini}} - X_{X_c=0.35} / X_{\text{ini}}$ (%) - Starevol	$X_{\text{ini}} - X_{X_c=0.35} / X_{\text{ini}}$ (%) - MoMo
${}^4\text{He}$	9.5	11.5
${}^{12}\text{C}$	7.8	9.6
${}^{14}\text{N}$	7.8	9.3
${}^{16}\text{O}$	8.2	9.5
${}^{20}\text{Ne}$	9.1	10.1
${}^{23}\text{Na}$	10.6	10.3
${}^{24}\text{Mg}$	9.4	9.9
${}^{27}\text{Al}$	9.5	9.9

6.4.2 Structure: abundances, diffusion velocity and base of the convective envelope

Atomic diffusion also leads to important changes in the stellar structure. In particular, it affects the location of the Base of the Convective Zone (hereafter BCZ).

Figure 6.16 shows the physical parameters of the BCZ: the radius R_{bcz} and the temperature T_{bcz} with and without atomic diffusion for the models from STAREVOL and MoMo. The top panel

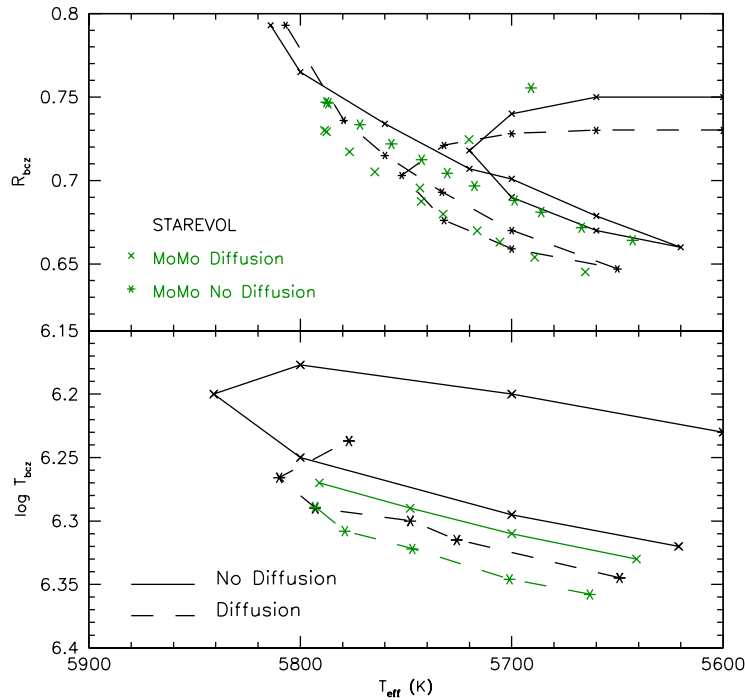


Figure 6.16: Evolution with T_{eff} of radius at the base of the convective zone (R_{bcz}) and temperature at the base of the convective zone (T_{bcz}) for the two codes STAREVOL (in black) and MoMo (in green).

of Fig. 6.16 shows a good agreement between the two codes for R_{BCZ} . When atomic diffusion is active, BCZ is deeper (-2.1% and -2.2% in radius at $X_c=0.35$ for STAREVOL and MoMo, respectively), and hotter. This change is due to the transport of elements by atomic diffusion described previously. The transport of elements, and mainly of helium (abundant and an important contributor to opacity: Blancard et al. 2012) leads to a change of the opacity profile below the convective envelope and consequently to the redefinition of the BCZ location.

Table 6.4 gives the initial and solar age parameters of each of the models. Each model have been calibrated on the Sun (see Chapter 7). The main result of SSM model compared to CSM for STAREVOL and MoMo is a decrease of helium and an increase of hydrogen abundance at the surface of the star. As expected this simultaneous transport of chemicals leads to a different structure of the star and a larger convective envelope ($\approx -2\%$ deeper in radius). With the addition of atomic diffusion, results are in better agreement with the helioseismic estimation of R_{BCZ} . For STAREVOL, the BCZ is located at $0.747 R_{\odot}$ for the CSM model and at $0.731 R_{\odot}$ for the SSM one, to compare to the seismic estimation $0.713 \pm 0.003 R_{\odot}$ according to Kosovichev & Fedorova (1991); Christensen-Dalsgaard et al. (1991). Besides, results for the helium abundance in the convective envelope are in good agreement with the seismic estimation. The addition of atomic diffusion leads to a decrease of about 8% from 0.2689 (CSM) to 0.2481 (SSM), in mass fractions. This second

value is close to the seismic value, estimated at ${}^4He_{ZC} = 0.2485 \pm 0.0035$ according to Basu & Antia (1995).

These results confirm that the optimisation, presented in Chapter 4, for atomic diffusion leads to good results for solar-type stars and also low-mass stars presenting such convective envelope. If differences remain between codes, they can be interpreted as the impact of the choice of the input physics in each code.

Table 6.4: Results of the calibrations computed for two solar models of STAREVOL and MoMo for models with (SSM) or without (CSM) atomic diffusion. X_{surf} , Y_{surf} and Z_{surf} are, respectively the surface hydrogen, helium and metal mass fractions at the age of the Sun, $\frac{Z_{\text{surf}}}{X_{\text{surf}}}$ is the ratio of heavy element and the hydrogen mass fractions, X_{ini} , Y_{ini} , Z_{ini} are, respectively the initial hydrogen, helium and heavy elements mass fraction, α_{MLT} is the mixing length parameter, $\frac{\Delta Y}{\Delta Z}$ is the helium enhancement ratio and R_{BCZ} and ${}^4He_{ZC}$ are, respectively the radius and the helium mass fraction at the base of the convective zone.

Model	STAREVOL CSM	STAREVOL SSM	MoMo CSM	MoMo SSM
X_{surf}	0.7175	0.7484	0.7278	0.7492
Y_{surf}	0.2690	0.2481	0.2589	0.2373
Z_{surf}	0.013446	0.013393	0.013214	0.013562
$\frac{Z_{\text{sol}}}{X_{\text{sol}}}$	0.0187	0.0181	0.0182	0.0181
X_{ini}	0.7175	0.7123	0.7278	0.7169
Y_{ini}	0.2690	0.2733	0.2589	0.2681
Z_{ini}	0.013446	0.014395	0.013214	0.015008
α_{MLT}	1.6602	1.7727	1.5162	1.6562
$\frac{\Delta Y}{\Delta Z}^\dagger$	1.53	1.73	0.80	1.31
R_{BCZ}^*	0.747	0.731	0.746	0.729
${}^4He_{ZC}^{**}$	0.2689	0.2481	0.2590	0.2373

Notes.

† Results are obtained using the primordial abundances according to Coc & Vangioni (2017) where $Y_0 = 0.2484$.

* Helioseismic estimations of radius: $R_{\text{BCZ}} = 0.713 \pm 0.003$ (Kosovichev & Fedorova 1991; Christensen-Dalsgaard et al. 1991)

** Helioseismic estimation of helium in the convective envelope: ${}^4He_{ZC} = 0.2485 \pm 0.0035$ (Basu & Antia 1995).

Figure 6.17 shows the profiles of a few main light elements at $X_c = 0.35$ from the models of STAREVOL (Left) and MoMo (Right) with and without atomic diffusion in dashed-line and solid line, respectively. The two codes are in good agreement at a few percent level. Every element is affected by atomic diffusion, but it is mainly efficient for 1H and 4He at the base of the BCZ. Hydrogen is decreased in the core and increased in the envelope while heavier elements mass fractions are increased in the core and decreased in the envelope. We note that the plateau observed for Li, in the MoMo code, is due to the total destruction of this element by nuclear reactions. The difference of the nuclear reactions between the two is at the origin of this specific difference between STAREVOL and MoMo.

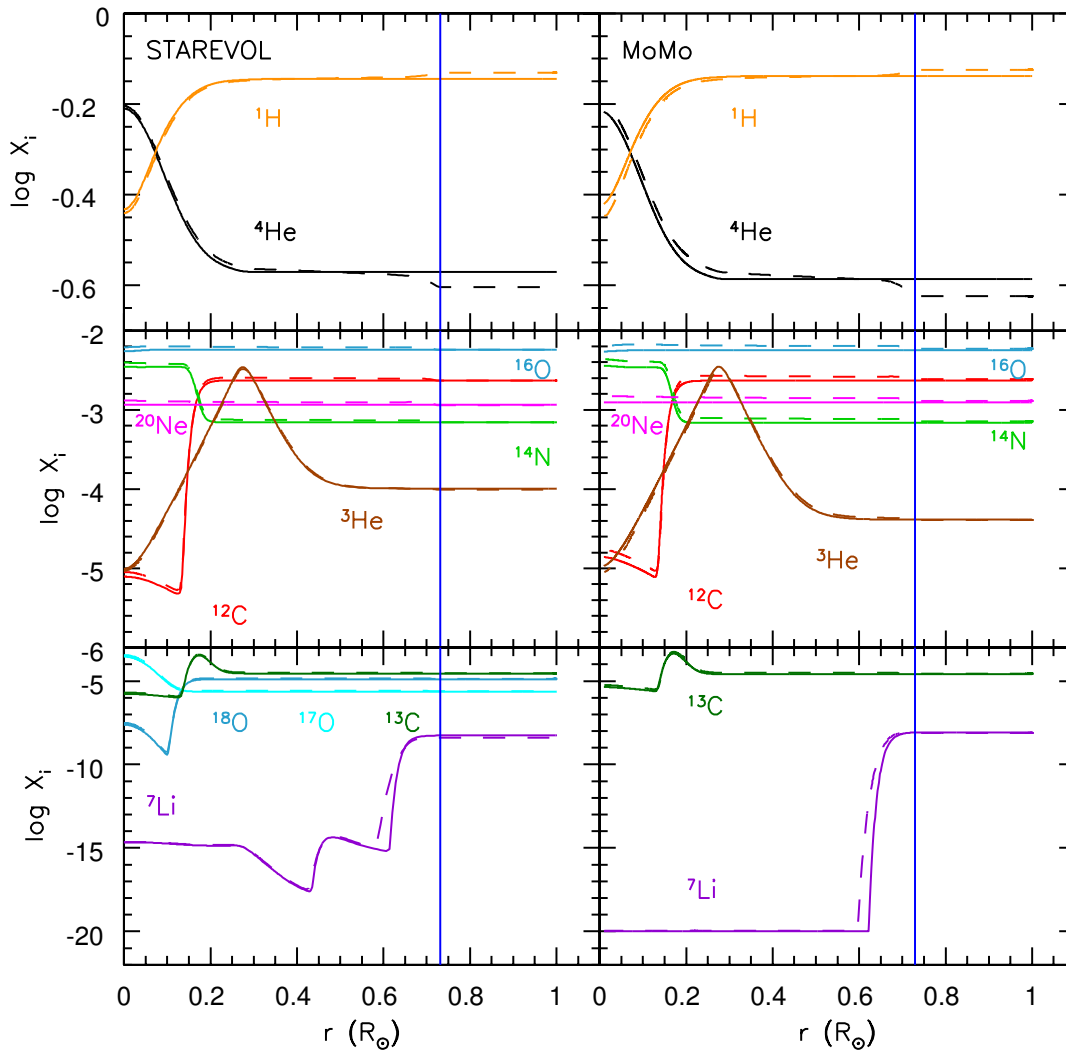


Figure 6.17: Mass fraction profiles of the main light elements (colour-coded) at solar age ($X_c=0.35$). Solid line and dashed line refer to model without and with atomic diffusion, respectively. (Left) STAREVOL, (Right) MoMo. The blue line indicates the base of the convective envelope.

Finally, Fig. 6.18 shows the diffusion velocities profiles obtained from STAREVOL (with and without the gradient of concentration) and MoMo at the age of the Sun. Diffusion velocities are close between the two codes with only a few percents of difference as already seen in Section 6.3.3, although velocities computed by MoMo are smaller in absolute value than STAREVOL ones, in particular at the BCZ.

To conclude on this section, the differences between results of the different stellar evolution codes are of the same order of what was already found in previous comparative studies. For instance, we have a few percent of difference for the luminosity and the effective temperature between STAREVOL and MoMo, in agreement of what was obtained by Lebreton et al. (2007) who found differences of 1-2% for luminosity and effective temperature, comparing six stellar evolution codes. Concerning surface abundances, for the case of the surface helium abundance we find a difference between STAREVOL and MoMo of about 5% at $X_c = 0.35$. Montalbán et al. (2007), comparing CLES and CESAM stellar evolution codes, found a difference of about 8% for the surface helium abundance. These differences are in agreement with the results showed in previous Sections of

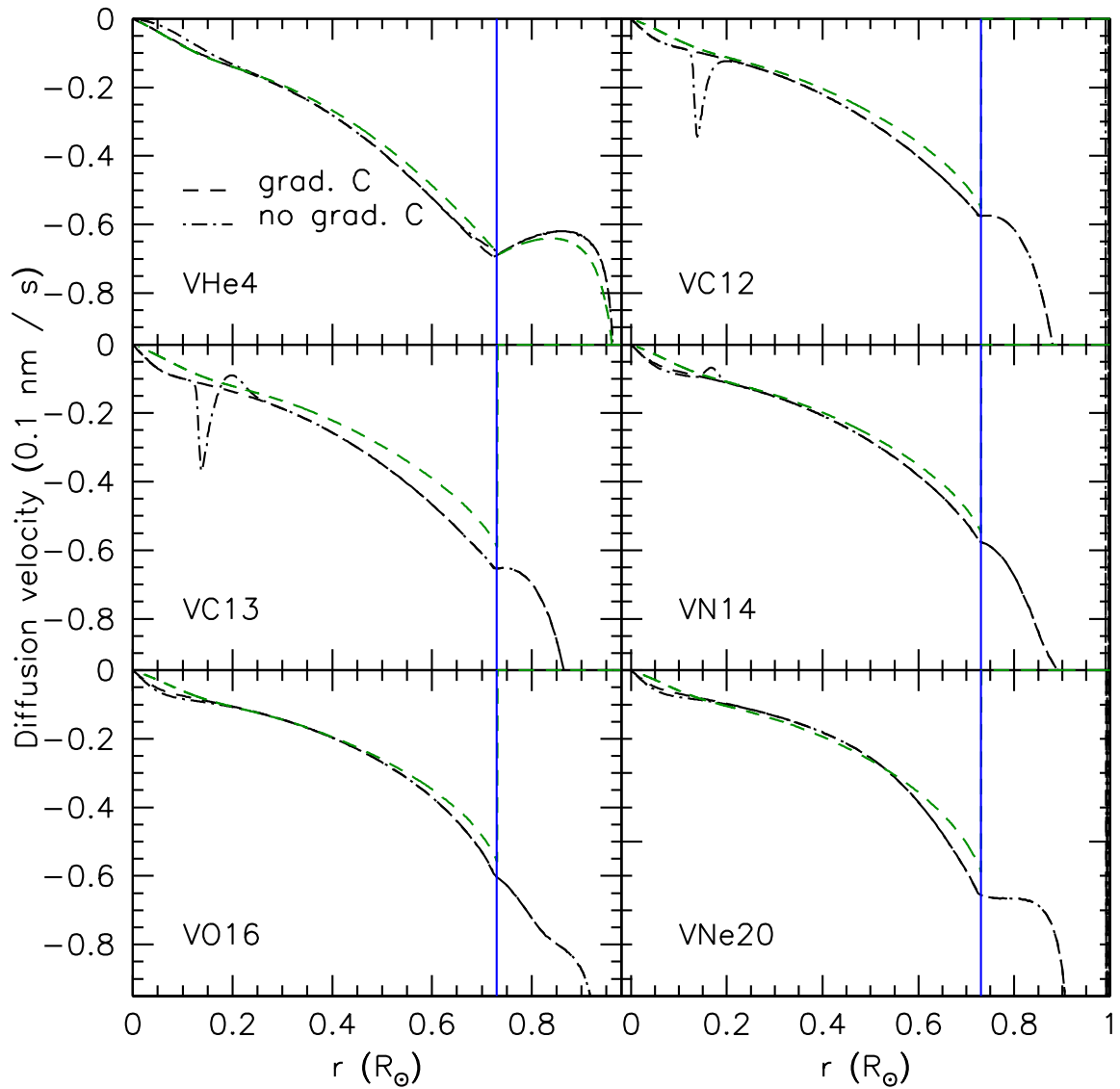


Figure 6.18: Diffusion velocities profile (in $0.1\text{nm}\cdot\text{s}^{-1}$) of ${}^4\text{He}$, ${}^{12}\text{C}$, ${}^{14}\text{N}$, ${}^{16}\text{O}$ and ${}^{20}\text{Ne}$ at $X_c = 0.35$. STAREVOL (black) and MoMo (green) are reported. Dashed-dotted-lines (dashed-lines) indicate that the gradient of concentration is (not) considered. The blue line indicates the base of the convective envelope of STAREVOL model structure.

this Chapter, when testing the formalism for atomic diffusion. It is consequently also the case for the change of abundances in the star.

6.5 Population II stars: evolution and structure

The fundamental effects of atomic diffusion have been illustrated in Section 6.4 for Pop. I stars. Hereafter, we give an overview of the effects at a lower metallicity, i.e. Pop II. stars. A change of metallicity, at a given mass, leads to important changes along the stellar evolution with, in particular, a change of opacity. At a given mass, atomic diffusion is expected to be more efficient and to have a key impact for Pop. II stars as they exhibit higher temperatures than their Pop. I counterparts. In this section, we computed STAREVOL models for $0.8M_{\odot}$ stars with a metallicity equivalent to $[\text{Fe}/\text{H}] = -1.75$, typical of globular clusters low-mass turn-off stars. We have also access to the results of MoMo code for identical stars (courtesy of O. Richard) that will allow to continue the comparison.

To compute models at such a metallicity, we computed a new set of initial abundances obtained from the initial abundances given Tab. 6.4. New initial abundances are given in Tab. 6.5. They are obtained from the solar calibration realised for our model (see Chapter 7). In particular, it allows to determine the helium enhancement ratio $\Delta Y/\Delta Z$ (see Section 7.2). From this ratio, we can determine the abundances corresponding to the value of $[\text{Fe}/\text{H}]$ required. We also note that, at this $[\text{Fe}/\text{H}]$ we applied an α -enhancement (Reddy et al. 2006), $[\alpha/\text{Fe}] = +0.3$ according to Chantreau et al. (2015).

Table 6.5: Parameters of the Population II, $[\text{Fe}/\text{H}] = -1.75$, $M = 0.8M_{\odot}$ models of STAREVOL and MoMo for models with (SSM) or without (CSM) atomic diffusion.

Model	STAREVOL CSM	STAREVOL SSM	MoMo CSM	MoMo SSM
X_{ini}	0.7508	0.7508	0.7515	0.7515
Y_{ini}	0.2487	0.2487	0.2480	0.2480
Z_{ini}	4.00×10^{-4}	4.23×10^{-4}	4.00×10^{-4}	4.00×10^{-4}
α_{MLT}	1.6602	1.7727	1.5162	1.6562
At the Turn-off ($X_c = 10^{-7}$)				
X_{surf}	0.7508	0.8719	0.7515	0.9703
Y_{surf}	0.2487	0.1279	0.2480	0.030
Z_{surf}	4.00×10^{-4}	2.26×10^{-4}	4.00×10^{-4}	3.95×10^{-5}
$\log L (L_{\odot})$	0.47	0.46	0.49	0.47
T_{eff}	6474	6351	6474	6333
Age (yrs)	12.78×10^9	12.55×10^9	12.10×10^9	11.62×10^9
$R_{\text{BCZ}} (R_{*})$	0.888	0.856	0.893	0.889
$\log T_{\text{BCZ}}$	5.57	5.66	5.54	5.50
$M_{\text{BCZ}} (M_{\odot})$	0.797	0.797	-	-

Notes.

X_{ini} , Y_{ini} , Z_{ini} are, respectively the initial hydrogen, helium and heavy elements mass fraction, α_{MLT} is the mixing length parameter, X_{surf} , Y_{surf} and Z_{surf} are, respectively the surface hydrogen, helium and metal mass fractions at the turn-off, L is the luminosity, T_{eff} the effective temperature (K), Age is the time at the Turn-off (years), and R_{BCZ} , T_{BCZ} and M_{BCZ} are the radius, the temperature and the mass at the base of the convective zone at the turn-off.

Fig. 6.19 shows the evolutionary tracks in the HR diagram for Pop. II models of STAREVOL and MoMo with or without atomic diffusion. As observed for the model of a Solar-like star, models without atomic diffusion are hotter than models with atomic diffusion. However, models of Pop. II stars reach hotter temperatures than their Pop. I. counterpart and the impact of atomic diffusion

is more efficient. Indeed, at the Turn-off (i.e. $X_c = 10^{-7}$), the shift of effective temperature is of about 140 K and 135 K for STAREVOL and MoMo, respectively. Models from MoMo are hotter at the surface and in the core, atomic diffusion is then more efficient than in STAREVOL models but results in similar T_{eff} and L variations. The lifetime is decreased by about 2% and by about 4% for STAREVOL and MoMo, respectively. This appears in Fig. 6.20 that shows the core hydrogen decrease with time (Top), the effective temperature evolution (Middle) and the evolution of core temperature versus core density. We note that if temperatures are higher in the MoMo models than in STAREVOL along the evolution, at the turn-off, the tracks cross each other.

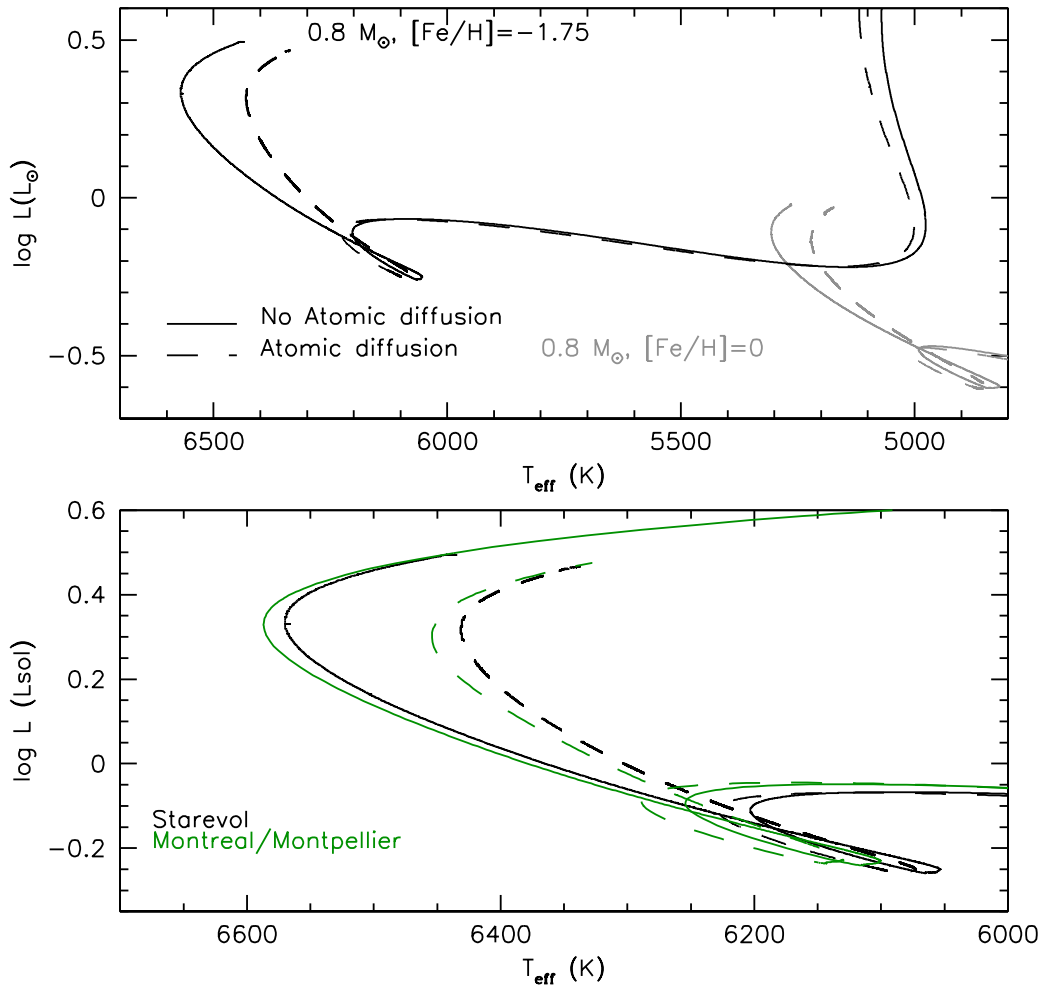


Figure 6.19: Evolutionary tracks in the Hertzsprung-Russell diagram for Population II stars at $0.8M_{\odot}$ and $[\text{Fe}/\text{H}] = -1.75$. STAREVOL-Pop.II (black) and MoMo-Pop.II (green) are indicated with or without atomic diffusion (dashed and solid lines respectively). The STAREVOL-Pop.I counterpart is also shown in grey for comparison.

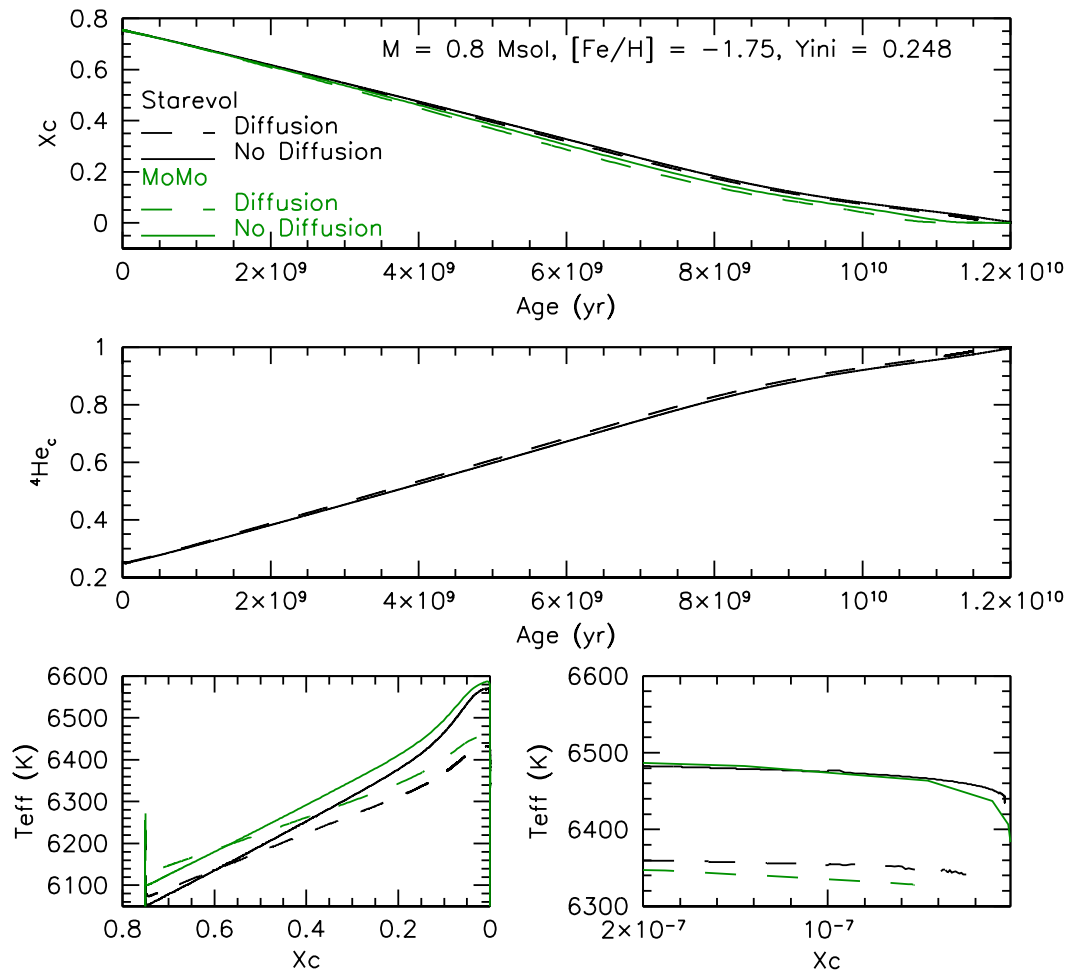


Figure 6.20: (Top) Time evolution of central hydrogen mass fraction (X_c). (Middle) Time evolution of central helium mass fraction (${}^4\text{He}_c$). (Bottom) Effective temperature T_{eff} versus X_c . STAREVOL (black) and MoMo (green) are reported with (dashed-line) or without (solid line) atomic diffusion.

At a given mass, due to hotter temperatures, the convective envelope is shallower and chemical evolution is, consequently, more affected than for Pop.I stars by atomic diffusion. Figure 6.21 shows the relative surface abundance evolution as a function of central hydrogen mass fraction X_c for STAREVOL and MoMo. Figure 6.21 gives the relative evolution of ${}^4\text{He}$, ${}^{12}\text{C}$, ${}^{14}\text{N}$, ${}^{16}\text{O}$, ${}^{20}\text{Ne}$, ${}^{23}\text{Na}$, ${}^{24}\text{Mg}$ and ${}^{27}\text{Al}$. At the turn-off, Tab. 6.6 summarises the relative decrease of several light elements for STAREVOL and MoMo. Similar results are obtained with MoMo and STAREVOL although the decrease is stronger for MoMo for which we observed a more efficient atomic diffusion (see temperatures in Tab. 6.5).

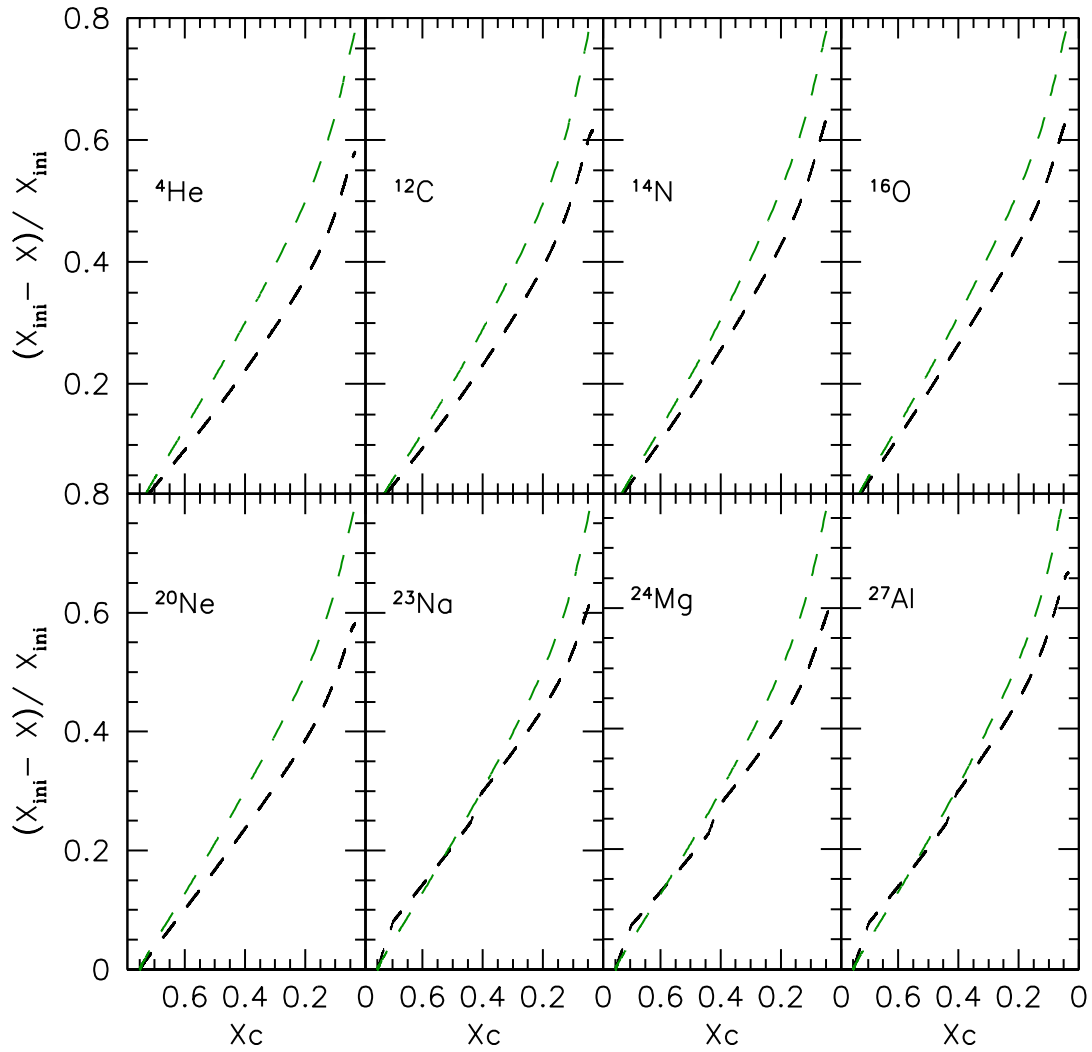


Figure 6.21: Relative variation (decrease) of surface abundances as a function of central hydrogen mass fraction X_c for $0.8M_{\odot}$, $[\text{Fe}/\text{H}]=-1.75$ models for STAREVOL (black) and MoMo (green), for ${}^4\text{He}$, ${}^{12}\text{C}$, ${}^{14}\text{N}$, ${}^{16}\text{O}$, ${}^{20}\text{Ne}$, ${}^{23}\text{Na}$, ${}^{24}\text{Mg}$ and ${}^{27}\text{Al}$.

Table 6.6: Relative decrease of surface abundances between the initial abundances and those at $X_c = 10^{-7}$ for STAREVOL (left) and MoMo (right).

$X_{\text{ini}} - X_{X_c=10^{-7}} / X_{\text{ini}}$ (%)	STAREVOL	MoMo
${}^4\text{He}$	60	80
${}^{12}\text{C}$	62	85
${}^{14}\text{N}$	65	85
${}^{16}\text{O}$	65	85
${}^{20}\text{Ne}$	60	83
${}^{23}\text{Na}$	63	84
${}^{24}\text{Mg}$	60	80
${}^{27}\text{Al}$	66	87

Solar calibrated models

In Chapter 3, I defined three different type of stellar models: Classical (CSM), Standard (SSM, including atomic diffusion) and Non-Standard (NSSM, including atomic diffusion and rotation). The choice of such or such a type, as well as the choice for the EOS, the opacities or the atmosphere for instance, affects model predictions (radius, temperature, abundances, lifetime, evolution tracks), see for instance Lebreton et al. (2014a,b). For a given set of input physics, it is usual to make a solar calibration, or in other words, to reproduce the solar radius and luminosity. The accuracy of the solar calibration should correspond to the accuracy of the solar radius, luminosity, and metallicity observational determination. It is done adjusting the mixing length parameter and the initial helium content (see e.g. Christensen-Dalsgaard 1982; Serenelli 2016). For this work, we make a solar calibration for each type of model in order to be allowed to confront each of them to the observations.

7.1 Solar Calibration

All the elements cannot be measured by the way of spectroscopy. For instance, noble gas like helium or neon cannot be measured in the solar photosphere or confidently measured in meteorites (Asplund et al. 2009)¹. However, in the Sun, the ratio Z/X can be determined (where X refers to hydrogen, Y refers to helium and Z refers to metals) at the surface and used to calibrate stellar models.

A solar calibration consists of reach for a one solar mass model at solar metallicity and solar age ($\approx 4.57\text{Gyr}$) the luminosity L_{\odot} , the radius R_{\odot} and the $(Z/X)_{\odot}$ ratio² of the Sun. When performing the solar calibration, one has to adjust the helium mass fraction Y to obtain the value of Z/X for the reference solar mixture, at the age of the sun. However, a change of the helium abundance leads to a change in the global opacity in the star and to changes in temperature and luminosity for a same metallicity (Charbonnel & Lebreton 1993; Lebreton et al. 2014a)³. Helium is, indeed, one of the main contributors to stellar opacity (Blancard et al. 2012).

The calibration is achieved with the help of three free parameters: the initial helium mass fraction (or Y_{ini}), the initial ratio Z/X_{ini} and the mixing length parameter (or α_{MLT}). In this calibration procedure the mixing length parameter α_{MLT} and the initial chemical composition are adjusted

¹With the help of helioseismology, a helium solar value in the convective zone has however been measured at $Y_{\odot} = 0.2485 \pm 0.0035$ according to Basu & Antia (1995)

²By the mean of this ratio it is possible to infer the relative metal abundance knowing that $X+Y+Z=1$.

³In the framework of globular cluster stars with $[\text{Fe}/\text{H}]=-1.75$, the helium was shown to have a main impact with hotter temperatures, shorter lifetimes and with an impact on the stellar remnant of metal-weak low-mass stars (see: Chantreau et al. 2015, 2016, 2017)

Table 7.1: Solar calibration results for different input physics: Classical Model (CSM - no transport other than convection), Standard Model (SSM - atomic diffusion) and Non-Standard Model (NSSM - atomic diffusion and type I rotation-induced transport). When included, rotation in R1 and R1'' models is computed with the prescription Dv from Zahn (1992) and the prescription Dh from Mathis et al. (2018), and rotation in R2'' is computed with the prescription Dv from Talon & Zahn (1997) and the prescription Dh from Zahn (1992). Models C, D and R1 are the same as in Chapters 8 and 9.

Model	Type	Abundances	Atom. diffusion	Rotation	Atmosphere	α	Y_{ini}	Z_{ini}
C'	CSM	AGSS09	off	off	Grey	1.6602	0.2690	0.0135
C''	CSM	AGSS09	off	off	KS66	2.1069	0.2686	0.0135
C	CSM	AY18	off	off	KS66	2.1100	0.2685	0.0135
D'	SSM	AGSS09	on	off	Grey	1.7727	0.2733	0.0144
D''	SSM	AGSS09	on	off	KS66	2.2573	0.2716	0.0141
D	SSM	AY18	on	off	KS66	2.2357	0.2679	0.0136
R1''	NSSM	AGSS09	on	on	KS66	2.1987	0.2701	0.0139
R2''	NSSM	AGSS09	on	on	KS66	2.1787	0.2701	0.0139
R1	NSSM	AY18	on	on	KS66	2.2236	0.2718	0.0142

so as to reproduce the solar radius and the solar luminosity at the age of the Sun (4.57 Gyr) with a relative accuracy on the difference (luminosity (dL), radius (dR) and $\frac{Z}{X}$ ratio (dZsX)) between the model prediction at the age of the Sun and the reference values of the Sun. The best calibration is determined for the set of the three parameters that minimises the three differences by the use of a χ^2 test. The three calibrated values are then used in our stellar models.

We use the following reference solar values:

- Radius $R_{\odot} = 6.9599 \times 10^{10}$ cm (Allen 1976);
- Luminosity $L_{\odot} = 3.846 \times 10^{33}$ erg.s⁻¹ (Bahcall et al. 1995);
- Age = 4.57×10^9 yrs (Bahcall et al. 1995);
- $(Z/X)_{\odot} = 0.0181$ (Asplund et al. 2009), 0.0188 (Young 2018).

During the PhD thesis, we realised eight solar calibrations for different assumptions, as described in Tab. 7.1. For each one, we provide the corresponding values of Y_{ini} , $(Z/X)_{ini}$ and α_{MLT} .

Table 7.1 gives the input parameters for the calibrations realised for two solar reference abundances: AGSS09 (Asplund et al. 2009) and the solar reference abundance added in STAREVOL during the PhD thesis, AY18 (Asplund et al. (2009) + Ne from Young 2018). The other ingredients are as described in Chapter 3. The values of Y_{ini} and α_{MLT} are highly impacted by the addition of atomic diffusion or by the choice of the atmosphere. Indeed, these two parameters impact the temperature and the luminosity of the star.

Concerning the specific case of NSSM models, we computed two calibrations for two sets of prescription Dh/Dv, and considering AGSS09 abundances. Parameters obtained from the calibration using the prescriptions Dh: Mathis et al. (2018) / Dv: Zahn (1992) (R1'') and parameters obtained using the prescriptions Dh: Zahn (1992) / Dv: Talon & Zahn (1997) (R2'') are shown in Tab. 7.1. We note that the two different prescriptions used to describe the turbulence shear in rotating models lead to close results. The impact is negligible on the calibration parameters, and we then keep the calibration corresponding to the model with Dh: Mathis et al. (2018)/Dv: Zahn (1992) (R1) for all the models including rotation.

7.2 A few elements of comparison: CSM, SSM and NSSM models

As each type of models is now calibrated (see detailed parameters of each model in Tab. 7.2), it is possible to give a brief view of the effects of the different inputs of physics on a solar model. We are using the solar abundances of Asplund et al. (2009) with the enhancement of Ne abundance according to Young (2018): we refer to this mixture as AY18 (see Section 3.5).

Calibrations with a grey atmosphere were done during the phase of implementation and validation of the atomic diffusion (Chapter 6) and are not shown here. The choice of an analytical $T(\tau)$ relation for the atmosphere as the Krishna Swamy (1966, KS66) one leads mainly to an increase of the MLT parameter for the solar calibration and to a shift of temperature during the PMS and the MS as seen in Fig. 3.4, Section 3.8. These results⁴ are in agreement with previous studies from, for instance, VandenBerg et al. (2008) and Amard et al. (2019).

Hereafter, I give a few elements of comparison between the models.

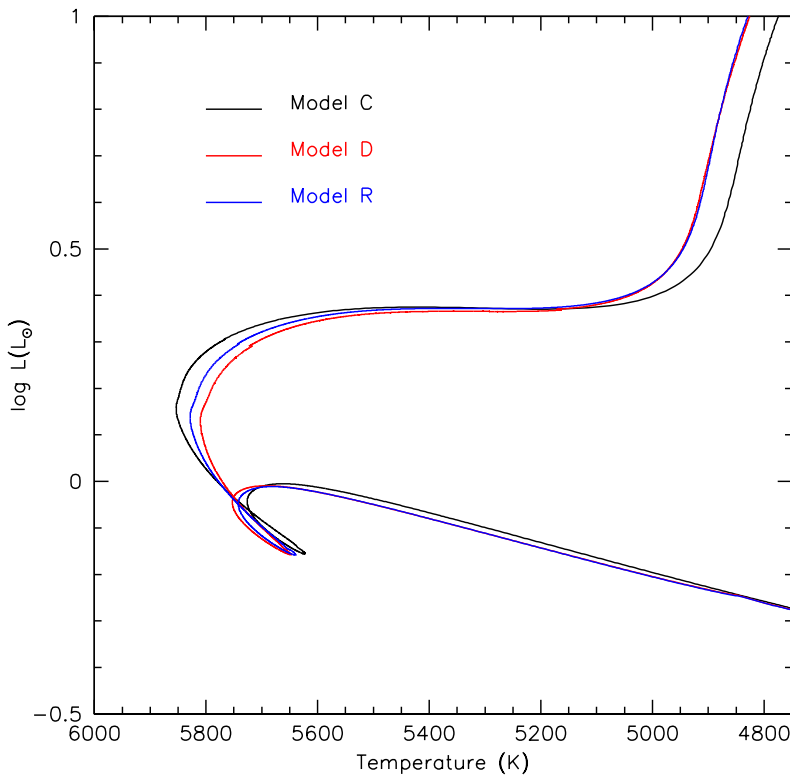


Figure 7.1: Evolutionary tracks in the Hertzsprung-Russell diagram for the calibrated C model (black line), D (Atomic diffusion, red line) model and R1 (Rotation+Atomic diffusion, blue line) model computed using input parameters of Tab. 7.1.

Fig 7.1 gives the evolutionary tracks in the Hertzsprung-Russell diagram for the three types of models with KS66 atmosphere and AY18 abundances. At the age of the Sun, and because of the solar calibration, tracks cross each others, but before and after this age, effects of the involved physics are visible. At the turn-off, Fig. 7.1 shows: i) a shift to a lower effective temperature when one adds the atomic diffusion; ii) a shift to a higher effective temperature when one adds the rotation.

⁴The key impact of the choice of atmosphere for PMS and Giant phases is also highlighted with the changes in the surface temperature as observed in Fig. 3.4, see also for instance works from Choi et al. (2018); Salaris et al. (2018).

Besides, as expected from the settling of helium towards deeper layers of the star, the helium abundance at the surface is smaller when atomic diffusion is activated (see Fig. 7.2). It leads to an

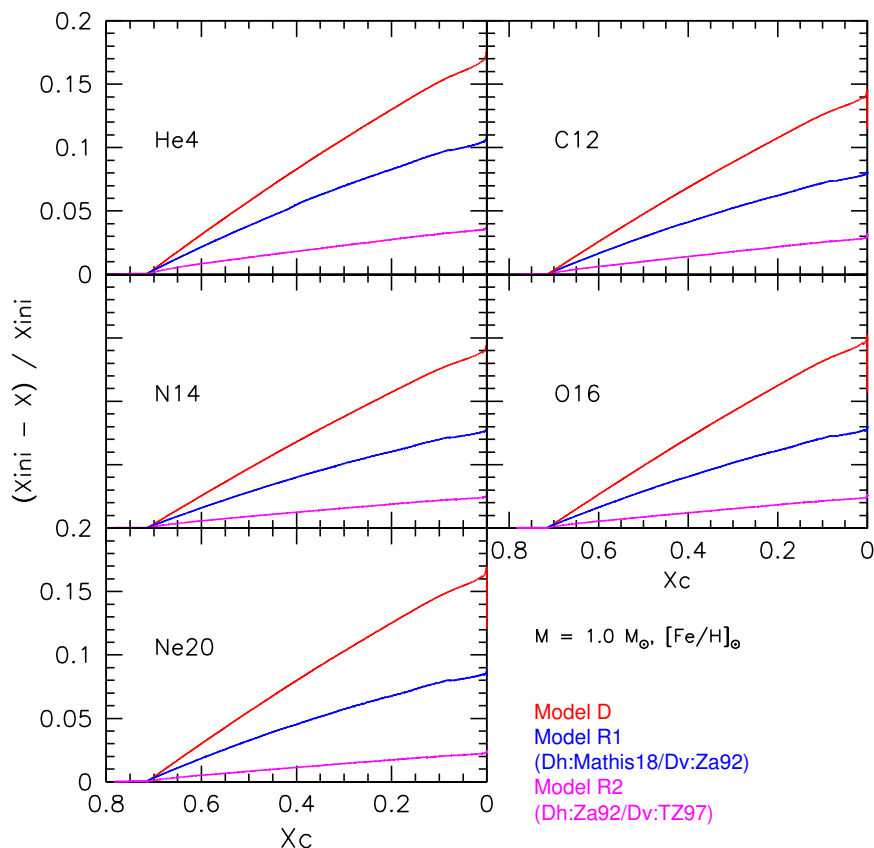


Figure 7.2: Relative Surface abundances evolution of ${}^4\text{He}$, ${}^{12}\text{C}$, ${}^{14}\text{N}$, ${}^{16}\text{O}$ and ${}^{20}\text{Ne}$ versus the mass fraction of central hydrogen for solar models. The D, R1 and R2 models are represented in red, blue and magenta, respectively.

increase of the opacity in the external layers and hence to a shift towards a colder part of the HR diagram in Fig. 7.1. Close to the turn-off, the standard model displays a lower effective temperature than the classical one ($\approx -40\text{K}$). The non-standard model exhibits an intermediate effective temperature ($\approx -20\text{K}$). The NSSM model appears between the two others models due to the effects of rotational-mixing that counteract atomic diffusion. It leads to a larger surface helium abundance (Fig. 7.2) and to a higher effective temperature (Fig. 7.1) than in the SSM. The predictions for the evolution of the surface abundance of ${}^4\text{He}$, ${}^{12}\text{C}$, ${}^{14}\text{N}$, ${}^{16}\text{O}$ and ${}^{20}\text{Ne}$ are shown as a function of the central hydrogen mass fraction X_c in Fig. 7.2. The model C model is not represented as there is no transport in the radiative zone. The red line shows the evolution of the surface element abundances when considering only atomic diffusion and the blue (magenta) line shows the evolution of the surface element abundances when considering atomic diffusion and rotation R1 (R2⁵). Atomic diffusion leads to a strong decrease of the abundances at the surface of about 10% at the age of the Sun (and of about 15% at the turn-off). Adding rotation leads to a lower decrease of the abundances of about 6% (3%) for ${}^4\text{He}$ and of about 5% (1%) for R1 (R2) model. The vertical shear diffusivity defined by TZ97 is stronger than the one defined by Za92 (see Chapter 8) and leads to a weaker decrease of surface element abundances.

⁵R2 includes the prescription Dv from Talon & Zahn (1997) and the prescription Dh from Zahn (1992) but the calibration parameters of model R1.

7.2. A few elements of comparison: CSM, SSM and NSSM models

Table 7.2: Results of the calibrations for the three models C, D and R1 and adopted observational data for the Sun. X_{surf} , Y_{surf} and Z_{surf} are, respectively the surface hydrogen, helium and metal mass fractions at the age of the Sun, $\frac{Z_{\text{surf}}}{X_{\text{surf}}}$ is the ratio of heavy element and the hydrogen mass fractions, T_{eff} is the effective temperature (K), T_c and ρ_c are, respectively the temperature and the density in the centre at solar age, dR is the relative radius difference, dL is the relative luminosity difference, dZsX is the relative $\frac{Z_{\text{surf}}}{X_{\text{surf}}}$ difference, X_{ini} , Y_{ini} , Z_{ini} are, respectively the initial hydrogen, helium and heavy elements mass fraction, α_{MLT} is the mixing length parameter, $\frac{\Delta Y}{\Delta Z}$ is the helium enhancement ratio⁴ and R_{bcz} , T_{bcz} and ${}^4\text{He}_{\text{zc}}$ are, respectively the radius, the temperature and the helium mass fraction at the base of the convective envelope.

Model	Sun	C	D	R1
Abundances	-	AY18	AY18	AY18
Atmosphere	-	KS66	KS66	KS66
Atomic diffusion	-	off	on	on
Rotation	-	off	off	Dh: Mathis 18 / Dv: Zahn 92
X_{surf}	0.7381 ¹	0.7179	0.7396	0.7306
Y_{surf}	0.2485 ²	0.2685	0.2465	0.2557
Z_{surf}	0.0134 ¹ / 0.0139 ³	0.0134	0.0139	0.0137
$\frac{Z_{\text{surf}}}{X_{\text{surf}}}$	0.0188 ³	0.0188	0.0187	0.0188
T_{eff}	5777 K	5775 K	5777 K	5778 K
T_c	-	1.536e7	1.550e7	1.547e7
ρ_c	-	149	153	152
dR	-	10 ⁻⁶	2.1 × 10 ⁻³	6.3 × 10 ⁻⁴
dL	-	10 ⁻⁶	1.3 × 10 ⁻³	3.0 × 10 ⁻⁵
dZsX	-	-	8.2 × 10 ⁻⁵	5.3 × 10 ⁻⁵
X_{ini}	-	0.7180	0.7140	0.7139
Y_{ini}	-	0.2685	0.2716	0.2718
Z_{ini}	-	0.013446	0.014451	0.014227
α_{MLT}	-	2.1100	2.2600	2.2236
$\frac{\Delta Y}{\Delta Z}$ *	-	1.50	1.61	1.65
R_{bcz}	0.713 ± 0.003 ⁴	0.742	0.731	0.731
log T_{bcz}	-	6.28	6.29	6.30
${}^4\text{He}_{\text{zc}}$	0.2485 ± 0.0035 ²	0.2685	0.2466	0.2558

Notes.

¹ Asplund et al. (2009)

² Helioseismic estimation in the convective zone to Basu & Antia (1995)

³ Young (2018)

⁴ Helioseismic estimations according to Kosovichev & Fedorova (1991), Christensen-Dalsgaard et al. (1991)

* The results are obtained using the primordial abundances according to Coc & Vangioni (2017) where $Y_0 = 0.2484$ (see details in text).

Table 7.2 gives all the quantities for the three models C, D and R1.

Model D, with atomic diffusion, has a deeper convective envelope than C model. R_{bcz} : 0.742 R_{\odot} and 0.731 R_{\odot} for model C and model D, respectively. This, has to be compared to the seismic estimation of about 0.713 R_{\odot} . Similarly, for ${}^4\text{He}_{\text{zc}}$, we obtained for the mass fraction: 0.2685 and 0.2466 for model C and model D, respectively, to be compared to the seismic estimation of about

0.2485. As already shown in Chapter 6, taking into account atomic diffusion is a fundamental step to the correct modelling of the Sun and of solar-type stars (see also for instance Richard et al. 1998; Turcotte et al. 1998b; Michaud et al. 2015).

When adding rotation, in consequence of rotational-mixing, the effects of atomic diffusion are counterbalanced and it results of an intermediate value of helium mass fraction in the convection zone at about 0.2558 for model R1. This value is quite higher than the measured solar value but it remains acceptable within the framework of our work. As described in Chapters 4 and 6, atomic diffusion and rotation also lead to changes in the structure and evolution of the star.

Finally, Tab. 7.2 gives also the helium enhancement ratio as a function of the metallicity $\frac{\Delta Y}{\Delta Z}$ with the help of the helium primordial abundance provided by Coc & Vangioni (2017)⁶. This ratio allows to obtain an estimate for the current helium abundance of a star with respect to its metal abundance, and it accounts for the chemical galactic evolution in the interstellar medium (Valcarce et al. 2013; Lebreton et al. 2014a). Depending on the physics used, the helium enhancement will change and regarding the main effect of helium abundance on stellar evolution, it is of a main importance when studying stars with metallicities different from the solar one (see for instance Salaris et al. 2000; Portinari et al. 2010). Then, the estimate of helium can be biased in models that do not include both atomic diffusion and rotation, because of different value for the ratio $\frac{\Delta Y}{\Delta Z}$.

Table 7.3 gives the differences between models C, D and R1, at three different evolutionary steps of the solar evolution. The model with atomic diffusion (D; SSM) exhibits at each step of evolution a higher T_{bcz} and a deeper convection zone than the C (CSM) model. When including rotation, we find intermediate values. Also, as already seen in Chapter 6, we find a shorter duration of the core H-burning phase when including atomic diffusion but the addition of rotation increases this duration as the result of opposite transport of elements than atomic diffusion. The lifetime is mainly affected by the atomic diffusion. The age at the turn-off is decreased by about 2.5 % when activating the atomic diffusion and by about 2.2 % when activating atomic diffusion and rotation. These results agree with the increased of luminosity observed in Fig. 7.1 for the case with only atomic diffusion of the SSM (model D). Indeed, it results of the transport of hydrogen to external layers, leading to a decrease of the central hydrogen abundance (or X_c). The lifetime is consequently smaller. However, when considering the rotation, the effects of atomic diffusion are weaker and more hydrogen is available in the core allowing a longer duration of the MS.

⁶ $\frac{\Delta Y}{\Delta Z} = \frac{Y_{ini} - Y_0}{Z_{ini}}$ where $Y_0 = 0.2484$ is the primordial helium abundance.

Table 7.3: Effective temperature T_{eff} , radius at the base of the convective envelope R_{bcz} , temperature at the base of the convective envelope T_{bcz} , mass at the base of the convective envelope M_{bcz} corresponding to the CSM, SSM and NSSM models. (Top) ZAMS. (Middle) Solar age. (Bottom) Turn-off with also the indication of age. (ZAMS: defined either by a central mass fraction of hydrogen X_c decreased by 0.6% compared to its surface value or by a core temperature that has reach 3×10^7 , Solar age: 4.57 Gyrs and Turn-off is defined when $X_c < 10^{-7}$)

At ZAMS	C	D	R1
T_{eff} (K)	5622	5651	5641
R_{bcz}	0.745	0.740	0.738
$\log T_{\text{bcz}}$	6.32	6.34	6.34
M_{bcz}	0.979	0.976	0.976
At Solar age	C	D	R1
T_{eff} (K)	5775	5777	5778
R_{bcz}	0.742	0.731	0.731
$\log T_{\text{bcz}}$	6.28	6.29	6.30
M_{bcz}	0.983	0.980	0.981
At Turn-off	C	D	R1
Age	10.58	10.30	10.33
T_{eff} (K)	5759	5717	5740
R_{bcz}	0.708	0.680	0.681
$\log T_{\text{bcz}}$	6.19	6.24	6.24
M_{bcz}	0.980	0.973	0.976

Finally, Fig 7.3 shows the mass fraction profiles of a few light elements as a function of the mass coordinate for a star at the turn-off for the three types of model. The chemical transport is illustrated between the three types of models. Due to atomic diffusion, hydrogen is increased at the surface of the star and heavy elements are decreased. As seen previously, the effects are mainly visible at the core where heavy elements and helium are transported and at the base of the convective envelope where hydrogen is transported. Besides, rotation has a weak effect on the profiles in the radiative interior, and its effects can only be seen at the base of the convective envelope.

In this Chapter, we described the solar calibrations realised during the PhD thesis for the three types of models (CSM, SSM and NSSM). We briefly discussed the impact of atomic diffusion and rotation on the structure and evolution of a $1 M_{\odot}$, and confirmed results from the literature. If the addition of atomic diffusion appears necessary to reproduce the helioseismic constraints, like the size of the convective envelope or the helium amount in the convective envelope, it is necessary to consider rotation and its effects in order to counteract the strong pure effect of atomic diffusion. The combined effect is important, in particular, at the base of the convection zone where dynamical processes and instabilities are best seen. For the commings Chapters, we will then focus on the NSSM models that include both processes and the more complete stellar modelling.

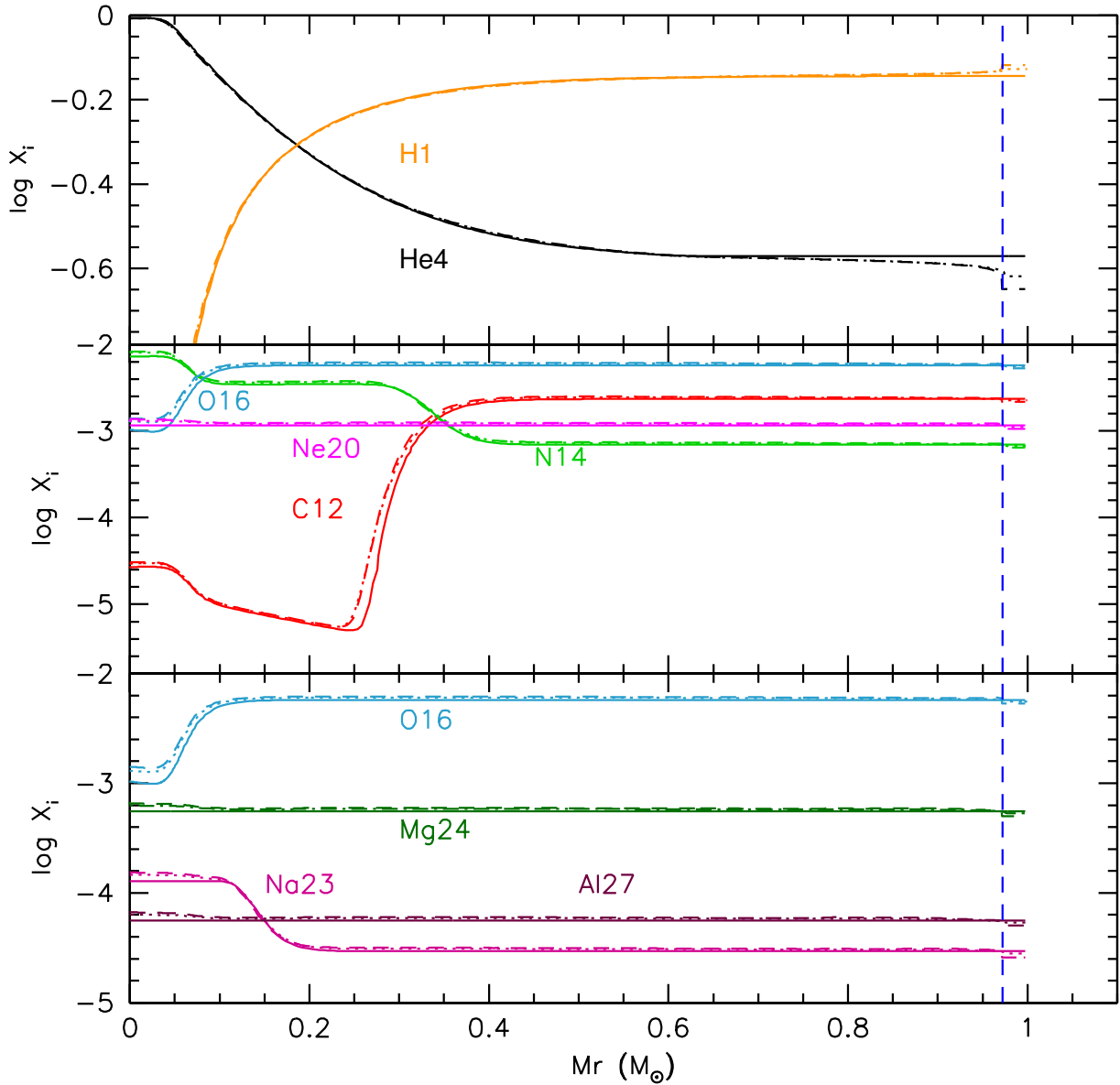


Figure 7.3: Mass fraction profiles of the CSM (full line), SSM (dashed-line) and NSSM-R1 (dotted-dashed line) models at the turn-off. (Top) ^1H (orange), ^4He (black). (Middle) ^{12}C (red), ^{14}N (light green), ^{16}O (light blue) and ^{20}Ne (pink). (Bottom) ^{16}O (light blue), ^{23}Na (magenta), ^{24}Mg (green) and ^{27}Al (purple). The blue vertical dashed line delimits the radiative zone and the convective zone of the CSM model.

Lithium depletion and transport of angular momentum in solar-type stars

In Chapter 1, we described the observational constraints on the surface Li abundance and on rotational evolution. In Chapter 2, we saw that the evolution of Li in different range of mass or age gives rise to several discrepancies between observations and models predictions.

In this Chapter, we present the results obtained by confronting the observational data described in Chapter 1 to models including combinations of dynamical processes that transport chemicals and angular momentum in solar-type stars. Our results were published in Dumont et al. (2021) (Astronomy&Astrophysics; see Section 8.2). In order to introduce this work, I will firstly give a few preliminary elements in Section 8.1.

8.1 Preliminary work

I computed and compared six different STAREVOL models: one CSM model (C), one SSM model (D) and four NSSM models¹. Those NSSM models include different prescriptions for horizontal and vertical shear diffusivities, as described in Tab. 8.1² They are referred as R1, R2, R3 and R4. They are all computed with magnetic braking from Matt et al. (2015a) ($m=0.22$, $p=2.1$, $\chi = 14$, $K = 7.5 \times 10^{30}$ erg), disc coupling timescale of 2.5 Myr and with initial angular velocity of $\Omega_{\text{surf}} = 1.60 \times 10^{-5} \text{ s}^{-1}$.

Table 8.1: Prescriptions for horizontal and vertical shear diffusivities

Name	Prescription D_h	Prescription D_v
R1	Mathis et al. (2018) - Mathis18	Zahn (1992) - Za92
R2	Zahn (1992) - Za92	Talon & Zahn (1997) - TZ97
R3	Mathis et al. (2004) - MPZ04	Zahn (1992) - Za92
R4	Mathis et al. (2004) - MPZ04	Talon & Zahn (1997) - TZ97

Figure 8.1 shows the results obtained for the six models as a function of time. The top-panel gives

¹CSM: Classical Stellar Model, SSM: Standard Stellar Model, NSSM: Non-Standard Stellar Model.

²As pointed out by Amard (2016), when considering the D_h prescription from Mathis et al. (2018) and the D_v prescription from Talon & Zahn (1997), the two coefficients are interdependent. The result is that the diffusion coefficient of horizontal turbulence and the diffusion coefficient of vertical turbulence are of the same order. Consequently, the assumption of turbulence anisotropy is not true any more. Then these two prescriptions are currently not compatible and not tested here.

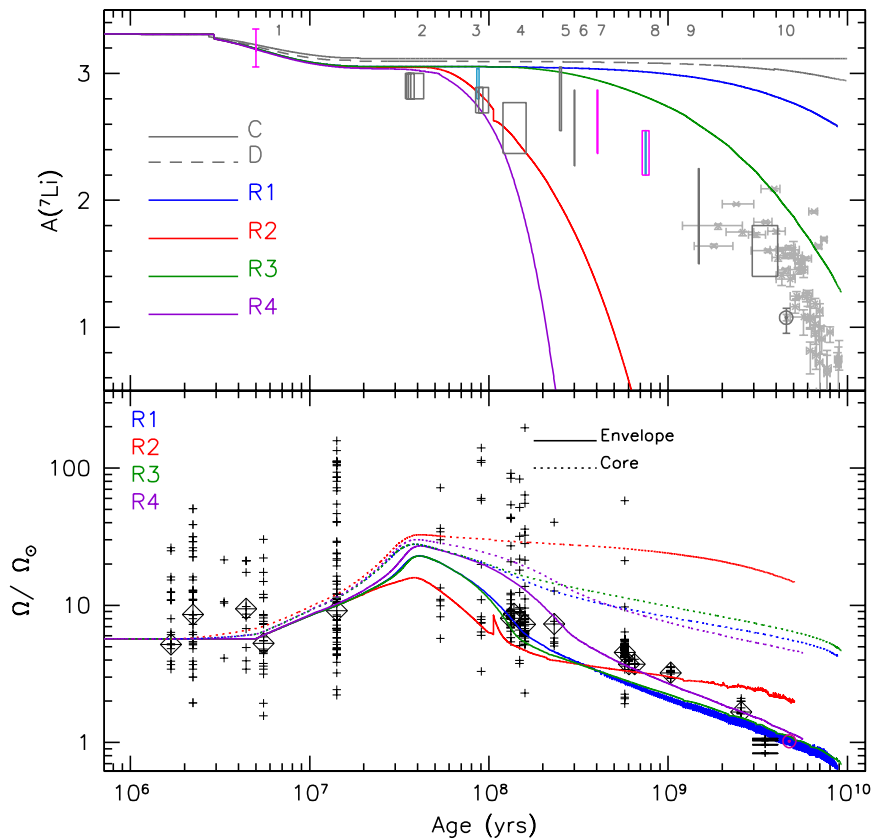


Figure 8.1: (Top) Li surface abundance evolution with time for the CSM (C), SSM (D) and NSSM (R1, R2, R3 and R4) models (colour-coded). Individual points are data for solar twins (Carlos et al. 2019). Boxes are for Li observations of solar-mass stars in different open clusters (Sestito & Randich 2005; Carlos et al. 2020) with ages from Bossini et al. (2019)). The numbers 1 to 10 identify the clusters [1) NGC 2264, 2) IC2391, IC2602 and IC4665, 3) α Per, Pleiades and Blanco I, 4) NGC2516, 5) M34, 6) NGC6475, 7) M35, 8) Praesepe and NGC6633, 9) NGC752 and 10) M67] and the color-boxes indicate their $[\text{Fe}/\text{H}]$ value (Netopil et al. 2016, : pink: -0.17 to -0.05; grey: -0.05 to 0.05; light blue: 0.05 to 0.16). (Bottom) Evolution of the angular velocity (in solar units; $\Omega_\odot = 2.86 \times 10^{-6} \text{s}^{-1}$) versus the age for R1, R2, R3 and R4 models. The observational data comes from Gallet & Bouvier (2015) except the four stars of M67 that comes from Barnes et al. (2016). Crosses are for individual stars; open diamonds show the 50th percentiles of the observed rotational distribution in each cluster.

the surface Li abundance, the bottom-panel gives the surface and mean internal angular velocity; observational data are the same as described in Fig. 1.3.

The light depletion, between 3×10^6 and $2 - 3 \times 10^7$ years, is due to the high temperature reached in the convective zone during the PMS phase that allows to burn Li. When rotation is considered, transport of matter develops in the radiative zone. Li is transported toward hotter layers of the stars and is burned. The transport takes place, in particular, at the end of the PMS, when differential rotation becomes important between the surface and the core as observed in Fig. 8.1. This induces Li depletion on the MS in addition to the PMS one.

The main difference between the four rotation models is due to the choice of D_v prescription that dominates the transport of chemicals. The vertical shear coefficient by Talon & Zahn (1997) drives a

too strong Li-depletion due to a strong differential rotation (models R2 and R4). Figure 8.2 shows the profile of the total transport coefficient $D_{\text{tot}} = D_{\text{eff}} + D_v$ at 8×10^7 years. D_{tot} is, indeed, stronger for models R2 and R4 than for models R1 and R3. When using the vertical shear coefficient by Zahn (1992) (models R1 and R3), at the opposite, the Li-depletion is too weak.

Besides, in all cases, the coupling between surface and core is too weak, or in other words, the

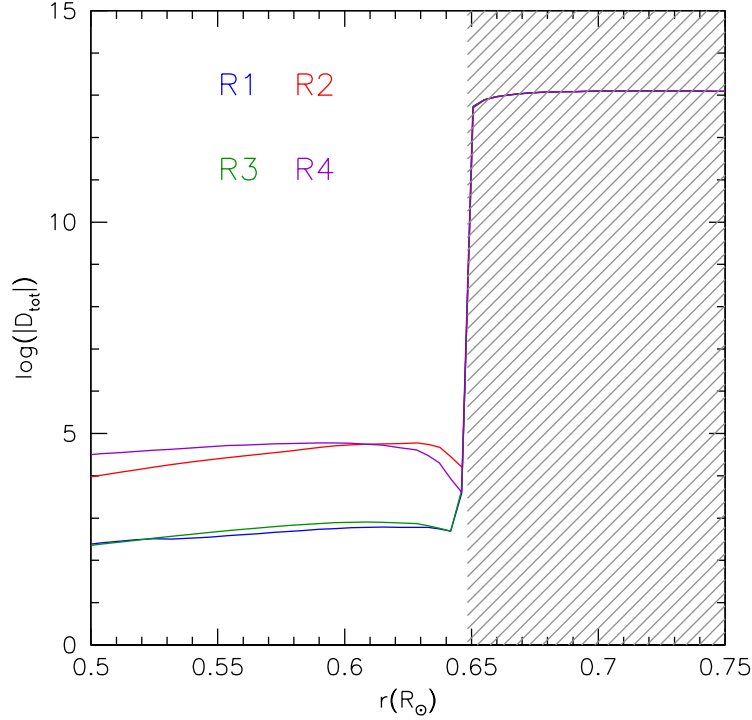


Figure 8.2: Profiles of the logarithm of the total transport coefficient $D_{\text{tot}} = D_{\text{eff}} + D_v$ at 8×10^7 years. Hatched areas correspond to convective regions.

surface angular velocity is very slow compared to the core angular velocity, and the angular velocity is far from the flat solar rotation profile at the age of the Sun. It is confirmed in Fig. 8.3 that shows the rotation profiles of the NSSM-R1 model at four different phases: ZAMS, Sun-Age, Turn-off and 11.5 Gyrs (RGB). At the age of the Sun, the model predicts a fast rotating core and a slow rotating surface, in contradiction with observational data. Moreover, on the RGB the same model predicts a very steep rotation profile (fast rotating core) due to the contraction of the core at the end of the MS. It is also in contradiction with the analysis of mixed modes in solar-mass SGB and RGB presenting solar-like oscillations that shows a low degree of radial differential rotation in the core indicating that the strong coupling found at the solar age is essentially maintained during further evolution (Eggenberger et al. 2012b, 2017, 2019a; Mathis et al. 2018; Aerts et al. 2019).

Finally, if the Li evolution before the ZAMS (≈ 100 Myr) is unaffected by rotational mixing as already pointed out by Amard et al. (2016), the choice of the shear diffusivities strongly impact the MS surface evolution of Li. However, whatever the choice of rotational prescription, in regard to the observational data, the results of NSSM models highlight the need of additional dynamical processes to transport both chemical elements and angular momentum.

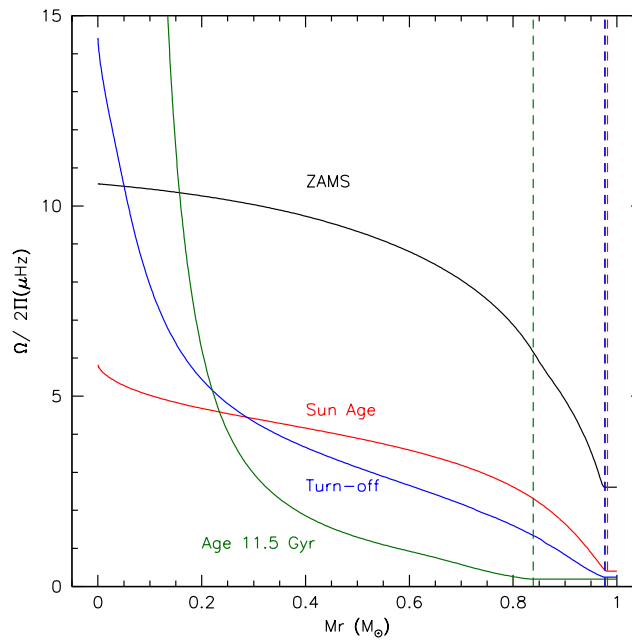


Figure 8.3: Angular velocity profiles function of the relative mass fraction for the NSSM-R1 model. Profiles are represented at ZAMS, Sun-Age, Turn-off and 11.5 Gyrs (Giant branch) and the mass at the base of the convective zone is indicated with dashed line (colour-coded).

8.2 Dumont et al. (2021, A&A, 646, A48)

In Dumont et al. (2021), we focused on solar-type stars. We tested different rotational prescriptions and dynamical processes to transport chemicals and angular momentum. We showed that the inclusion of rotational dependent overshoot as proposed by Augustson & Mathis (2019) is a key process to transport chemicals along the PMS. However, the reproduction of the depletion of Li abundance in the MS, as observed in solar-type stars, and of the rotational profile of the Sun can only be achieved when adding additional transport processes (for R1 models): one for chemicals and one for angular momentum.

We determined a model with an optimal combination of prescriptions to reproduce simultaneously the surface Li abundance with age, the surface angular velocity with age and an almost flat rotation profile at the age of the Sun. This model involves three additional transports in the NSSM model: the overshoot process by Augustson & Mathis (2019), an additional turbulence for chemicals as proposed by Richer et al. (2000) and Richard et al. (2005), and an additional viscosity for angular momentum (ν_{add}) as proposed by Eggenberger et al. (2012b, 2019b). We determined a value for the additional viscosity of $\nu_{\text{add}} = 3.5 \times 10^4 \text{ cm}^2 \cdot \text{s}^{-1}$ that allows to reproduce the almost flat rotation profile of the Sun (see Fig.8.4 that shows the angular velocity profile at the age of the Sun for a model R1 for different efficiency of the additional viscosity ν). Figure 8.5 shows the results obtained with the optimal model called $\nu R1_A^{T6.425}$, computed for three different initial rotation periods: 1.6, 4.5, and 9.0 days, referred to as the fast (*F*), median (*M*), and slow (*S*) rotating models. Our optimal model reproduces well the observations (see the discussion in Dumont et al. 2021)³.

In addition, for the first time, we computed self-consistently the tachocline thickness and found a good agreement with helioseismic estimation (Elliott & Gough 1999), although the resulting

³See also the resulting surface abundances for ^4He and ^{12}C for the different models tested in Fig. 8.6.

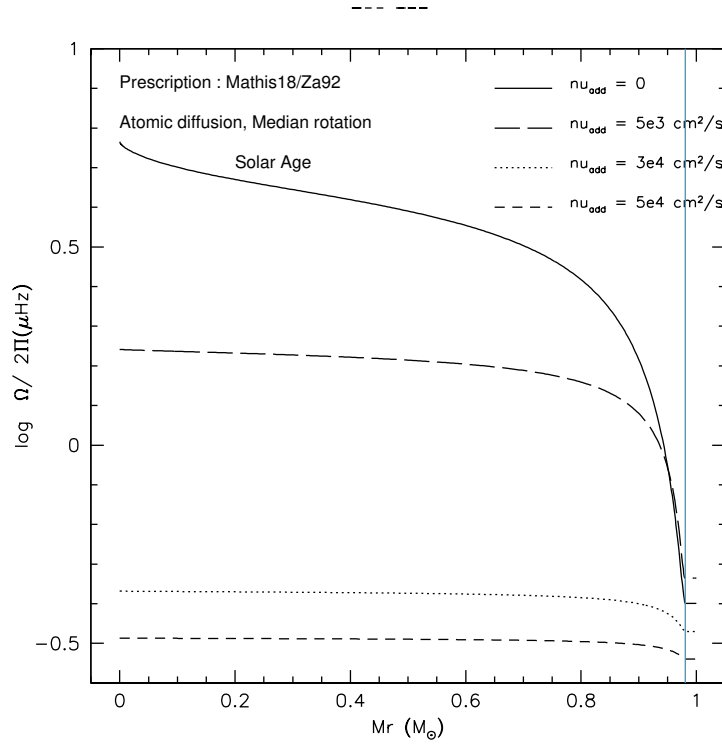


Figure 8.4: Angular velocity profiles versus the radius at solar age for model R1 computed with different values of additional viscosity ν_{add} . The blue line indicates the base of the convective envelope.

tachocline mixing stays too weak to reproduce Li abundance in solar-type stars. It is thus not included in our optimal model.

Finally, the Sun appears to be Li-poor compared to observational data of solar twins confirming that the Sun might not be the best benchmark for solar-type stars (Randich 2009; Carlos et al. 2020). A weaker parametric turbulence is needed when considering the solar twins in place of the Sun. We obtained model $\nu R1_A^{T6.42}$ in Fig. 8.5. Finally, we note that the different processes included in our optimal model leads also to change in the surface abundances of the others elements. Figure 8.6 gives the relative variations (decrease) of surface abundances for ${}^4\text{He}$ and ${}^{12}\text{C}$ as a function of age for the different models tested in Chapter 8. This shows the strong effect of pure atomic diffusion, then counteracted by rotation and by the additional processes added in our optimal model $\nu R1_A^{T6.425}$.

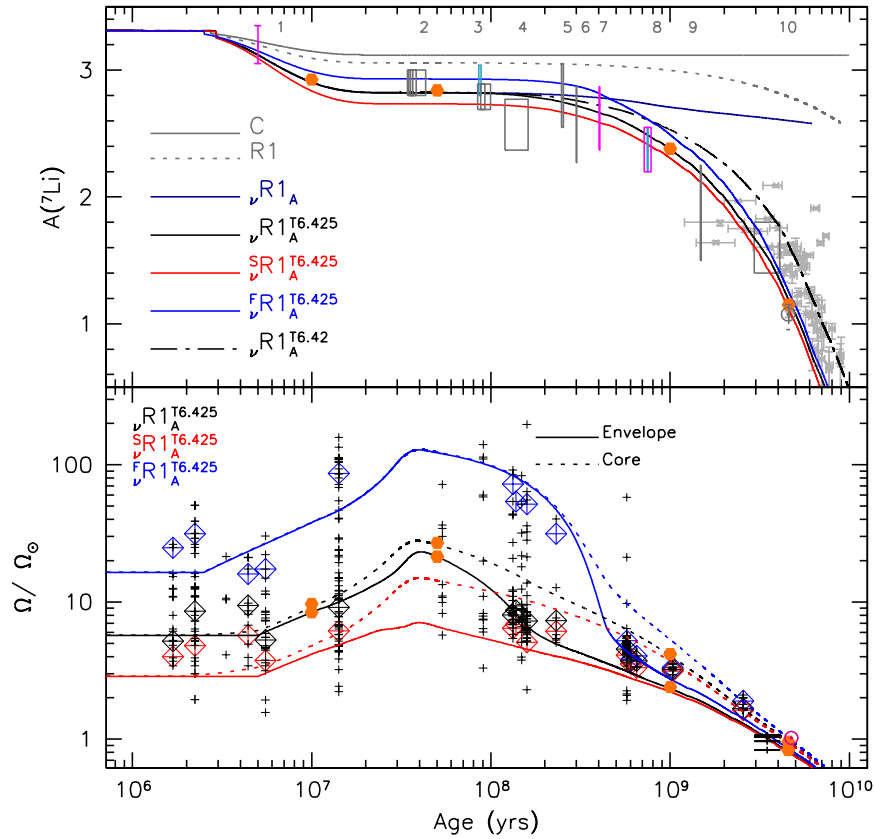


Figure 8.5: Same as Fig. 8.1 with the same C, D and R1 model as Fig. 8.1 and with the addition of the optimal model ($\nu R1_A^{T6.425}$) computed for three different initial velocities (*F*: fast, *M*: median and *S*: slow). The optimal model includes overshoot as proposed by Augustson & Mathis (2019): *A*, parametric turbulence as proposed by Richer et al. (2000) and Richard et al. (2005): *T6.425* (*T6.42* for solar twins), and additional viscosity ν_{add} as proposed by Eggenberger et al. (2012b, 2019b): ν . The orange dots refer to the four ages at which the diffusion coefficient profiles are shown in Fig. 7 in Dumont et al. (2021). The red, black, and blue open squares show the 25th, 50th and 90th percentiles of the observed rotational distributions in each cluster.

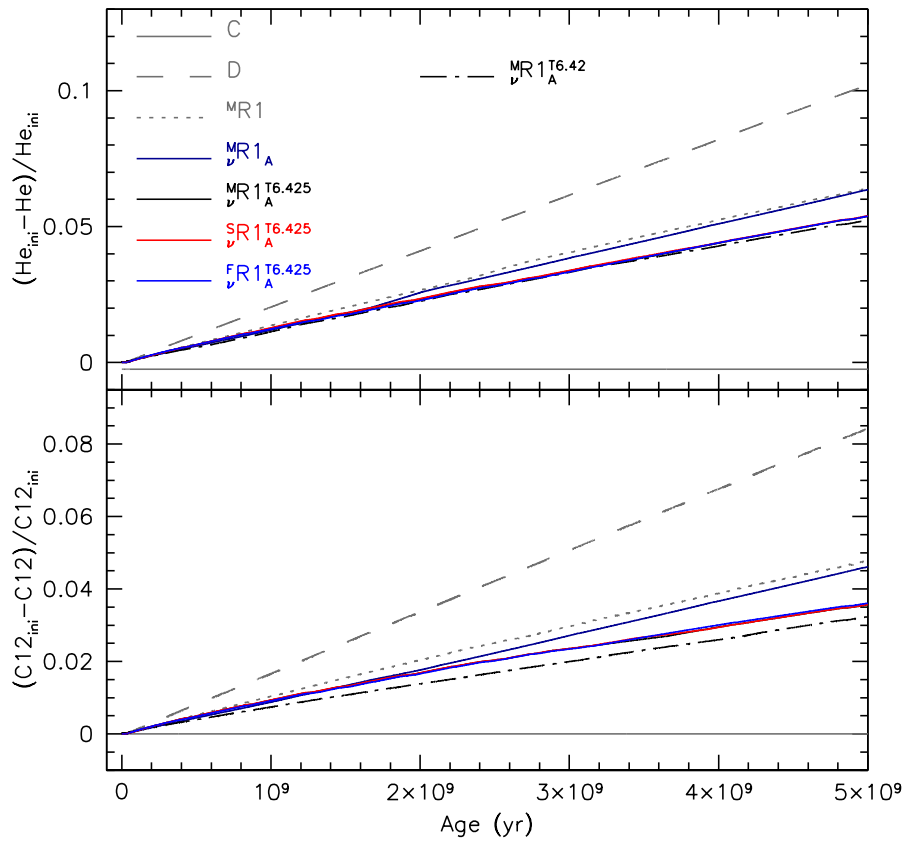


Figure 8.6: Relative variations (decrease) of surface abundances for ${}^4\text{He}$ and ${}^{12}\text{C}$ as a function of age for C, D, ${}^M R1$, $\nu R1_A$, $\nu R1_A^{T6.425}$, $\nu SR1_A^{T6.425}$, $\nu FR1_A^{T6.425}$ and $\nu R1_A^{T6.42}$ models.

Lithium depletion and angular momentum transport in solar-type stars

T. Dumont^{1,2}, A. Palacios², C. Charbonnel^{1,3}, O. Richard², L. Amard⁴, K. Augustson⁵, and S. Mathis⁵

¹ Department of Astronomy, University of Geneva, Chemin des Maillettes 51, 1290 Versoix, Switzerland
 e-mail: thibaut.dumont@unige.ch

² LUPM, Université de Montpellier, CNRS, Place Eugène Bataillon, 34095 Montpellier, France

³ IRAP, UMR 5277 & Université de Toulouse, 14 avenue Edouard Belin, 31400 Toulouse, France

⁴ University of Exeter, Department of Physics and Astronomy, Stocker Road, Devon, Exeter EX4 4QL, UK

⁵ AIM, CEA, CNRS, Université Paris-Saclay, Université Paris-Diderot, Sorbonne Paris Cité, 91191 Gif-sur-Yvette Cedex, France

Received 24 September 2020 / Accepted 24 November 2020

ABSTRACT

Context. Transport processes occurring in the radiative interior of solar-type stars are evidenced by the surface variation of light elements, in particular ${}^7\text{Li}$, and the evolution of their rotation rates. For the Sun, inversions of helioseismic data indicate that the radial profile of angular velocity in its radiative zone is nearly uniform, which implies the existence of angular momentum transport mechanisms that are efficient over evolutionary timescales. While there are many independent transport models for angular momentum and chemical species, there is a lack of self-consistent theories that permit stellar evolution models to simultaneously match the present-day observations of solar lithium abundances and radial rotation profiles.

Aims. We explore how additional transport processes can improve the agreement between evolutionary models of rotating stars and observations for ${}^7\text{Li}$ depletion, the rotation evolution of solar-type stars, and the solar rotation profile.

Methods. Models of solar-type stars are computed including atomic diffusion and rotation-induced mixing with the code STAREVOL. We explore different additional transport processes for chemicals and for angular momentum such as penetrative convection, tachocline mixing, and additional turbulence. We constrain the resulting models by simultaneously using the evolution of the surface rotation rate and ${}^7\text{Li}$ abundance in the solar-type stars of open clusters with different ages, and the solar surface and internal rotation profile as inverted from helioseismology when our models reach the age of the Sun.

Results. We show the relevance of penetrative convection for the depletion of ${}^7\text{Li}$ in pre-main sequence and early main sequence stars. The rotational dependence of the depth of penetrative convection yields an anti-correlation between the initial rotation rate and ${}^7\text{Li}$ depletion in our models of solar-type stars that is in agreement with the observed trend. Simultaneously, the addition of an ad hoc vertical viscosity ν_{add} leads to efficient transport of angular momentum between the core and the envelope during the main sequence evolution and to solar-type models that match the observed profile of the Sun. We also self-consistently compute for the first time the thickness of the tachocline and find that it is compatible with helioseismic estimations at the age of the Sun, but we highlight that the associated turbulence does not allow the observed ${}^7\text{Li}$ depletion to be reproduced. The main sequence depletion of ${}^7\text{Li}$ in solar-type stars is only reproduced when adding a parametric turbulent mixing below the convective envelope.

Conclusions. The need for additional transport processes in stellar evolution models for both chemicals and angular momentum in addition to atomic diffusion, meridional circulation, and turbulent shear is confirmed. We identify the rotational dependence of the penetrative convection as a key process. Two additional and distinct parametric turbulent mixing processes (one for angular momentum and one for chemicals) are required to simultaneously explain the observed surface ${}^7\text{Li}$ depletion and the solar internal rotation profile. We highlight the need of additional constraints for the internal rotation of young solar-type stars and also for the beryllium abundances of open clusters in order to test our predictions.

Key words. stars: abundances – stars: rotation – stars: interiors – stars: evolution – stars: solar-type

1. Introduction

Solar-type stars (e.g., stars with an initial mass of $1 \pm 0.1 M_{\odot}$ and a value of $[\text{Fe}/\text{H}] = 0 \pm 0.2$ dex, but possibly not the same age as the Sun) have been extensively used to constrain and study transport processes of chemicals and angular momentum in stellar interiors (e.g., Pinsonneault et al. 1989; Zahn 1992; Richard et al. 1996; Talon et al. 2002; Talon & Charbonnel 2003, 2005; Eggenberger et al. 2005, 2019a; Charbonnel & Talon 2008; Castro et al. 2009; Amard et al. 2016; Baraffe et al. 2017). Currently the main challenge is to simultaneously explain the time evolution of their photospheric ${}^7\text{Li}$ (hereafter Li) abundances, and of the rotation of their surface and interior.

Several hints point to rotation-induced transport and mixing processes as the cause for Li depletion in the Sun and in main sequence (MS) solar-type stars (e.g., Lebreton & Maeder 1987; Pinsonneault et al. 1990; Charbonnel et al. 1992; Richard et al. 1996; Do Nascimento et al. 2009), although other mechanisms have been invoked, such as penetrative convection (Böhm 1963; Schlattl & Weiss 1999; Baraffe et al. 2017; Jørgensen & Weiss 2018); tachocline mixing (Brun et al. 1999); mass loss (Guzik & Mussack 2010); planet accretion (Montalbán & Rebolo 2002); and mixing by internal gravity waves (Montalbán 1994). On the other hand, the currently available prescriptions for anisotropic turbulence and meridional circulation that are induced by rotation and that transport both chemicals and angular momentum

fail to reproduce the internal rotation rates evidenced by helio- and asteroseismology (e.g., Mosser et al. 2012; Deheuvels et al. 2012, 2014, 2015, 2020; Ceillier et al. 2013; Marques et al. 2013; Benomar et al. 2015; Eggenberger et al. 2017, 2019a; Gehan et al. 2018; García & Ballot 2019; Mathis et al. 2018; Amard et al. 2019; Aerts et al. 2019). More efficient mechanisms are required for the transport of angular momentum, which could be driven by internal gravity waves or magnetic processes and instabilities (e.g., Schatzman 1993; Spruit 2002; Charbonnel & Talon 2005; Mathis & Zahn 2005; Eggenberger et al. 2005, 2010, 2019b,c; Denissenkov et al. 2010; Charbonnel et al. 2013; Belkacem et al. 2015; Pinçon et al. 2017; Fuller et al. 2019). These mechanisms also impact the transport of chemicals induced by rotation and influence the way Li is depleted with time in solar-type stars (e.g., Charbonnel & Talon 2005; Talon & Charbonnel 2005).

In this work we explore the possibilities to reproduce simultaneously the chemical and rotational constraints for solar-type stars along their evolution up to the end of the MS. In Sect. 2 we present the observational data that we aim to account for with our stellar evolution models. In Sect. 3 we describe the input physics of the models and recall the state-of-the-art expressions from the literature for the different transport processes implemented in the stellar evolution code STAREVOL, and tested in this work. In Sect. 4 we compare the predictions of the so-called Type I models for rotating stars (which only include meridional circulation, shear induced turbulence, and atomic diffusion) to the observational constraints for solar-type stars over a broad age range. In Sect. 5 we probe for effects of penetrative convection and tachocline turbulence using for the first time some rotation-dependent prescriptions. This allows us to quantify the efficiency of still missing processes that we simulate in the form of a vertical diffusivity for the transport of angular momentum, and of an ad hoc turbulence for the transport of chemicals. We summarise our results and conclude in Sect. 6.

2. Observational constraints

To best constrain the physics at play in the interior of solar-type stars along their evolution up to the MS turnoff, we use both chemical and rotational data.

2.1. Lithium abundances

Lithium has long been claimed to be a useful and constraining element that can be used to understand the transport of chemicals and of angular momentum in stellar interiors (e.g., Wallerstein & Conti 1969; Boesgaard 1976; Vauclair et al. 1978; Spite & Spite 1982; Baglin et al. 1985; Vauclair 1988; Lebreton & Maeder 1987; Baglin & Lebreton 1990; Boesgaard 1991; Charbonnel et al. 1992, 1994; Deliyannis et al. 2000; Montalbán & Schatzman 1996; Montalbán & Schatzman 2000; Piau & Turck-Chièze 2002; Charbonnel & Talon 2005; Talon & Charbonnel 2010). Because of its relatively low burning temperature (~ 2.5 MK, close to the temperature at the base of the convective zone in solar-type stars), Li is indeed easily destroyed by proton capture in stellar interiors. According to classical stellar evolution theory, this destruction is expected to manifest itself at the surface of solar-type stars during the pre-main sequence (PMS) in the form of a decrease in the surface Li abundance. Classical models that include no transport processes beyond convection predict no further surface Li variation until the first dredge-up episode when the stars evolve towards the red giant branch.

Spectroscopic observations, however, show that the abundance of lithium at the surface of field and open cluster solar-type stars decreases along the main sequence (e.g., King et al. 1997; Sestito & Randich 2005; Chen & Zhao 2006; Takeda et al. 2010; Smiljanic et al. 2011; Xing & Xing 2012; Delgado Mena et al. 2014; Waite et al. 2017; Cummings et al. 2017; Beck et al. 2017; Harutyunyan et al. 2018; Carlos et al. 2020). In the case of the Sun, Li has decreased from its original (i.e. meteoritic) value of $A(^7\text{Li}) = 3.31^1$ down to $A(^7\text{Li}) = 1.05$ (Greenstein & Richardson 1951; Schwarzschild et al. 1957; Asplund et al. 2009). Solar twins (solar-type stars with ages close to that of the Sun, i.e. 4.6 ± 0.5 Gyr) all present significant Li depletion, with non-negligible dispersion, and with the Sun being among the most Li-depleted (e.g., Takeda et al. 2007; Meléndez & Ramírez 2007; Carlos et al. 2019).

In this work we use a consistent set of lithium abundances provided by Sestito & Randich (2005) for a group of open clusters with $[\text{Fe}/\text{H}]$ between -0.21 and $+0.14$ dex: NGC 2264, IC 2391, IC 2602, IC 4665, α Per, Pleiades, Blanco I, NGC 2516, M 34, NGC 6475, M 35, Praesepe, NGC 6633, and NGC 752. We identify the solar-type stars as those that have an effective temperature as derived by Sestito & Randich (2005), corresponding to the effective temperature ± 100 K of our model including atomic diffusion and rotation at the age of the corresponding cluster. We assume the cluster ages given by Bossini et al. (2019). Given the relatively large uncertainty on actual age determination, this slight inconsistency with the ages that would be derived with our models should not affect our conclusions. In Fig. 1 (also appearing in Figs. 2, 3, 6, and 8) we show the corresponding Li range for the solar-type stars with the observational boxes, and indicate the age uncertainty for each cluster. We also consider and show the Li data for M 67 and field solar twins by Carlos et al. (2019, 2020).

2.2. Surface and internal rotation

2.2.1. Surface rotation

Many observations exist of the rotation rates of solar-type stars of different ages (e.g., Stauffer & Hartmann 1986; McQuillan et al. 2014; García et al. 2014; Gallet & Bouvier 2015; dos Santos et al. 2016; Lorenzo-Oliveira et al. 2020). They clearly establish that the surface rotation of these stars evolves with time under the effect of multiple processes. Magnetic interactions between the star and its accretion disc early on the PMS and later with its wind are successfully invoked to explain the evolution and the dispersion of the rotation periods provided by photometric surveys (e.g., Matt et al. 2015; Amard et al. 2016; Gallet et al. 2019, and references therein).

To constrain the surface rotation of the models we use the observational data set gathered by Gallet & Bouvier (2015) for a large number of solar-type stars in open clusters of various ages. We also use the data from Barnes et al. (2016) for a subsample of four stars of M67, selected because their magnitudes are close to the solar value, with a magnitude $B - V \in [0.6; 0.7]$.

2.2.2. Internal rotation

The internal rotation of the Sun is constrained by helioseismology. It is assumed to be similar for other solar-type stars, and asteroseismology constrains it for stars in more advanced

¹ $A(X) = \log_{10}(N_X/N_H) + 12$ (where N_X is the number density of element X).

T. Dumont et al.: Lithium depletion and angular momentum transport in solar-type stars

evolutionary stages beyond the MS (i.e. subgiant and red giant stars; e.g., Mosser et al. 2012; Deheuvels et al. 2012, 2014, 2015; Benomar et al. 2015; Gehan et al. 2018; García & Ballot 2019). The analysis of p -modes gives access to the rotation profile of the Sun between about $R = 0.2 R_{\odot}$ and the surface (Kosovichev 1988; Elsworth et al. 1995; Thompson et al. 2003; Mathur et al. 2008; Eff-Darwich et al. 2008). The inverted rotation profile is compatible with solid-body rotation in the radiative zone. Moreover, the analysis of mixed modes in solar-mass subgiant and red giant stars (hereafter SGB and RGB) presenting solar-like oscillations also points to a low degree of radial differential rotation in the core indicating that the strong coupling found at the solar age is essentially maintained during further evolution (Eggenberger et al. 2017, 2019a; Mathis et al. 2018; Aerts et al. 2019). No observational clue exists yet regarding the structure of the internal rotation during the PMS and the early MS evolution, although there are hints that the quasi solid-body rotation of the solar interior may not be an exception from the analysis of asteroseismic data for solar-type stars (Nielsen et al. 2014) and for F to late G main sequence stars (Benomar et al. 2015).

We thus require that our best models reach an internal rotation profile similar to the solar profile at the age of the Sun as this is basically the only proper constraint for the phases investigated in this paper. For this profile we use the results of the inversion of MDI-GOLF-GONG² data by Eff-Darwich et al. (2008).

3. Stellar evolution models

We use an updated version of the stellar evolution code STAREVOL (for general information and previous versions, see Siess et al. 2000; Palacios et al. 2006; Decressin et al. 2009; Lagarde et al. 2012; Amard et al. 2019). All our models are evolved without accretion starting prior to the deuterium birth-line on the PMS from initial structures corresponding to homogeneous polytropes. This sets the time zero of our computations.

3.1. Input physics

We adopt the solar reference abundances from Asplund et al. (2009) including the enhancement of neon recommended by Young (2018) as reported in Table 1. The opacities are interpolated within the OPAL opacity tables (Iglesias & Rogers 1996) when $T > 8000$ K and the low-temperature opacity tables from the Wichita opacity database when $T < 8000$ K (Ferguson, priv. comm.) that are fully consistent with the adopted solar reference abundances.

The equation of state is analytical and follows Eggleton et al. (1973) and Pols et al. (1995), as described in Siess et al. (2000). We use the nuclear reactions rates from the NACRE2 database generated using the NetGen web interface (Xu et al. 2013a,b).

In the current version of STAREVOL the full set of stellar structure equations is solved for the whole star; there is no decoupling between the interior and the envelope (where the diffusion approximation becomes valid). The surface boundary conditions are treated using the Hopf function $q(\tau)$, which provides a correction to the grey approximation (see Hopf 1930;

² MDI: Michelson Doppler Imager (Scherrer et al. 1995), GOLF: Global Oscillations at Low Frequencies (Gabriel et al. 1995). These instruments are on board the SOLar and Heliospheric Observatory (SOHO) spacecraft of ESA/NASA (Domingo et al. 1995). GONG: Global Oscillation Network Group (e.g., Howe et al. 2020, and references therein).

Table 1. Initial chemical mixture adopted for the different solar calibrated models.

Model element	C	R
¹ H	7.18×10^{-1}	7.14×10^{-1}
⁴ He	2.69×10^{-1}	2.72×10^{-1}
⁷ Li (*)	1.03×10^{-8}	1.03×10^{-8}
⁹ Be (†)	1.66×10^{-10}	1.65×10^{-10}
¹¹ B	3.13×10^{-9}	3.31×10^{-9}
¹² C	2.26×10^{-3}	2.40×10^{-3}
¹⁴ N	6.68×10^{-4}	7.07×10^{-4}
¹⁶ O	5.54×10^{-3}	5.86×10^{-3}
¹⁹ F	4.89×10^{-7}	5.17×10^{-7}
²⁰ Ne	1.58×10^{-3}	1.68×10^{-3}
²³ Na	2.83×10^{-5}	3.00×10^{-5}
²⁴ Mg	5.35×10^{-4}	5.66×10^{-4}
²⁷ Al	5.39×10^{-5}	5.71×10^{-5}
²⁸ Si	5.92×10^{-4}	6.27×10^{-4}
³¹ P	5.65×10^{-6}	5.97×10^{-6}
³² S	2.84×10^{-4}	3.01×10^{-4}
³⁵ Cl	6.73×10^{-8}	7.12×10^{-8}
Others (**)	1.49×10^{-3}	1.58×10^{-3}

Notes. Initial abundances are given in mass fraction for the classical model (C) and the rotation model (R). Each model has been calibrated on the Sun (see Table 2). The mass fraction of metals Z is $Z_C = 0.0134$ and $Z_R = 0.0142$ for the classical and rotating calibrated solar models, respectively. (*) $A_{\text{ini}}(^7\text{Li}) = 3.31$; (†) $A_{\text{ini}}(^9\text{Be}) = 1.41$; (**) refers to elements heavier than chlorine.

Morel et al. 1994)

$$\frac{4}{3} \left(\frac{T(\tau)}{T_{\text{eff}}} \right)^4 = q(\tau) + \tau \quad (1)$$

at a given optical depth τ , T_{eff} being the temperature of the equivalent black body and $T(\tau)$ the temperature profile. We use the analytical expression from Krishna Swamy (1966) for $q(\tau)$, as is also done in Pietrinferni et al. (2013) and Zhang et al. (2019), for instance. The numerical surface is set at $\tau_0 = 0.005$, as in Amard et al. (2019), and the connection to the atmosphere is made at $\tau_{\text{ph}} = 2$.

The models without rotation take into account mass loss starting at the ZAMS³ following the empirical relation by Reimers (1975), with $\eta_R = 0.5$, as advocated by McDonald & Zijlstra (2015) and Guo et al. (2017) for solar-type stars from observational constraints on the red giant branch. When the effects of rotation are taken into account, we use the mass loss prescription by Cranmer & Saar (2011), as in Amard et al. (2019).

Heat transport by convection follows the Mixing Length Theory (MLT; Böhm-Vitense 1958; Cox & Giuli 1968). The convective boundaries are determined with the Schwarzschild criterion. When included, the effect of penetrative convection is treated as overshoot (without changing the temperature gradient in the concerned region; see Zahn 1991) below the convective envelope.

3.2. Model calibration

The abundances of helium and metals vary according to the input physics of the models; in other words, they depend on the

³ Zero Age Main Sequence.

Table 2. Solar calibration results for the STAREVOL classical model (C: no transport other than convection) and rotating model (R: atomic diffusion and type I rotation-induced transport).

	Sun	Model C	Model R
Y_{surf}	0.2485 ^(a)	0.2685	0.2559
Z_{surf}	0.0134 ^(b)	0.0134	0.0134
$\frac{Z_{\text{surf}}}{X_{\text{surf}}}$	0.0181 ^(b)	0.0186	0.0183
$T_{\text{eff}}(\text{K})$	5777	5775	5779
$L_{\odot}(10^{33} \text{ erg s}^{-1})$	3.846 ^(c)	3.846	3.845
$R_{\odot}(10^{10} \text{ cm})$	6.9599 ^(d)	6.9599	6.9555
Relative luminosity accuracy: dL	...	10^{-6}	3.0×10^{-4}
Relative radius accuracy: dR	...	10^{-6}	6.3×10^{-4}
Y_{ini}	...	0.2685	0.2718
Z_{ini}	...	0.0134	0.0142
α_{MLT}	...	2.110	2.223

Notes. Y_{surf} and Z_{surf} are respectively the surface helium and heavy element mass fraction, $\frac{Z_{\text{surf}}}{X_{\text{surf}}}$ is the ratio of heavy element to the hydrogen mass fractions, T_{eff} is the effective temperature (K), L_{\odot} is the luminosity (in solar units), R_{\odot} is the radius (in solar units), Y_{ini} and Z_{ini} are respectively the initial helium and heavy element mass fractions, and α_{MLT} is the mixing length parameter. ^(a)Helioseismic estimation in the convective zone from Basu & Antia (1995); ^(b)Asplund et al. (2009); ^(c)Bahcall et al. (1995); ^(d)Allen (1976).

mixing processes considered. Consequently, for each case the initial chemical composition needs to be evaluated so that the ratio $Z_{\text{surf}}/X_{\text{surf}}$ from Asplund et al. (2009) is reproduced at the age of the Sun. In this calibration procedure the mixing length parameter α_{MLT} and the initial chemical composition are calibrated so as to reproduce the solar radius and solar luminosity at the age of the Sun (4.57 Gyr) with a relative accuracy of the order of 10^{-4} – 10^{-6} . We make two different calibrations depending on the physics of the models (see Table 2). The classical model (C) is without any transport processes in the radiative region and the rotating model (R) includes atomic diffusion and rotational mixing with the assumptions made for model R1 (Table 3) and the median rotation rate (see Sect. 3.4), but it does not include overshoot. The calibration corresponding to model R1 is then used for all the models produced including rotation, in particular for models ${}^a R_c^d$ which include additional transport processes for angular momentum and chemicals (see Sect. 4 and the Appendix for further details). Details on the models resulting from these calibrations are given in Table 2 and the initial chemical mixtures for each calibration are reported in Table 1.

3.3. Evolution of chemical abundances: General equation and atomic diffusion

Chemical abundances within the star evolve under the effect of nuclear reactions and transport processes. This is described by the general diffusion equation (e.g., Maeder 2009), which involves the different physical processes operating in the star

$$\rho \frac{\partial X_i}{\partial t} = \frac{1}{r^2} \frac{\partial}{\partial r} \left(r^2 \rho D \frac{\partial X_i}{\partial r} \right) - \frac{1}{r^2} \frac{\partial}{\partial r} \left(r^2 \rho X_i v_i \right) + m_i \left[\sum_j r_{ji} - \sum_k r_{ik} \right], \quad (2)$$

where ρ is the density; X_i refers to the mass fraction of element i ; r is the radius; $D = \sum_j D_j$ is the total coefficient for turbulent diffusion, written as the sum of the j different diffusion coefficients describing turbulent processes such as shear, penetrative convection, or any other unidentified process (see Sects. 3.4.1, 3.5, and 3.6); v_i is the diffusion velocity of element i ; m_i is the

mass of nuclei i ; and r_{ij} the reaction rate producing nuclei j from nuclei i .

Atomic diffusion is implemented in STAREVOL with the formalism of Thoul et al. (1994) to solve the Burgers equations and compute the individual atomic diffusion velocities of each element taken into account in STAREVOL (see Table 1). The computation of the collision integrals is done according to Paquette et al. (1986). We take into account the partial ionisation of chemical elements for temperatures lower than 5×10^6 K (Schlattl 2002). Radiative accelerations are not taken into account in our models. According to Turcotte et al. (1998) their impact on abundances for light elements in the solar case is only about 2%. Radiative accelerations mainly impact the heavy elements such as iron, and become important for stars more massive than solar-type stars (Richer et al. 1998; Richard et al. 2002; Deal et al. 2018).

3.4. Angular momentum evolution and rotation-induced mixing

Stellar rotation, and in particular differential rotation, is a potent trigger of transport for both angular momentum and chemicals in stellar radiation zones. It generates the large-scale currents of the meridional circulation and several large-scale hydrodynamical instabilities that induce turbulence such as the vertical and horizontal shear instabilities, which are the ones included in our models (Zahn 1992; Maeder & Zahn 1998; Mathis & Zahn 2004; Mathis et al. 2004). This ensemble is referred to as Type I rotational mixing as it does not include the transport by magnetohydrodynamic (MHD) instabilities and magnetic fields or transport by internal gravity waves (see e.g., Mathis 2013; Aerts et al. 2019 for a description of these processes).

3.4.1. Prescriptions for shear induced turbulent transport

Stellar rotation is implemented in STAREVOL as described by Amard et al. (2016, 2019). We use the formalism of the shellular rotation hypothesis developed by Zahn (1992), Maeder & Zahn (1998), and Mathis & Zahn (2004) to describe the transport of angular momentum and chemicals by meridional circulation and turbulent shear (vertical and horizontal). The transport of angular

T. Dumont et al.: Lithium depletion and angular momentum transport in solar-type stars

Table 3. Parameters of the rotating models.

Model	D_h	D_v	Overshoot	d_{ov}	K (erg)	v_{add} (cm ² s ⁻¹)	v_0, α	Turbulence
solid R_A	–	–	D_A	0.0325	1.1×10^{31}	–	–	–
R1	Mathis et al. (2018)	Zahn (1992)	–	–	7.5×10^{30}	–	–	–
R1 B,S	Mathis et al. (2018)	Zahn (1992)	D_B	0.340	7.5×10^{30}	–	–	–
R1 B,E	Mathis et al. (2018)	Zahn (1992)	D_B	0.100	7.5×10^{30}	–	–	–
R1 A	Mathis et al. (2018)	Zahn (1992)	D_A	0.0325	7.5×10^{30}	–	–	–
R1 K	Mathis et al. (2018)	Zahn (1992)	D_K	0.055	7.5×10^{30}	–	–	–
v R1 A	Mathis et al. (2018)	Zahn (1992)	D_A	0.0325	7.5×10^{30}	3.5×10^4	–	–
v .spada $R1_A$	Mathis et al. (2018)	Zahn (1992)	D_A	0.0325	1.2×10^{30}	2.5×10^5	–	–
v .spada(r) $R1_A$	Mathis et al. (2018)	Zahn (1992)	D_A	0.0325	7.5×10^{30}	–	$2.5 \times 10^4, 0.5$	–
v 2.spada(r) $R1_A$	Mathis et al. (2018)	Zahn (1992)	D_A	0.0325	7.5×10^{30}	–	100, 12	–
v R1 A ^{T6.425}	Mathis et al. (2018)	Zahn (1992)	D_A	0.0325	7.5×10^{30}	3.5×10^4	–	$D_{T6.425}$
v R1 A ^{T6.42}	Mathis et al. (2018)	Zahn (1992)	D_A	0.0325	7.5×10^{30}	3.5×10^4	–	$D_{T6.42}$
v R1 A ^{PM5000}	Mathis et al. (2018)	Zahn (1992)	D_A	0.0325	7.5×10^{30}	3.5×10^4	–	D_{PM5000}
v R1 A ^{Tach}	Mathis et al. (2018)	Zahn (1992)	D_A	0.0325	7.5×10^{30}	3.5×10^4	–	D_{Tach}
R2 A	Zahn (1992)	Talon & Zahn (1997)	D_A	0.0325	7.5×10^{30}	–	–	–
R2 A'	Zahn (1992)	Talon & Zahn (1997)	D_A	0.0325	3.0×10^{30}	–	–	–
v R2 A''	Zahn (1992)	Talon & Zahn (1997)	D_A	0.0325	4.5×10^{30}	2.5×10^4	–	–
R3 A	Mathis et al. (2004)	Zahn (1992)	D_A	0.0325	7.5×10^{30}	–	–	–
v R3 A	Mathis et al. (2004)	Zahn (1992)	D_A	0.0325	7.5×10^{30}	3.5×10^4	–	–

Notes. Models (Col. 1) related to the prescriptions for horizontal and vertical turbulent viscosities (Cols. 2 and 3 respectively), the formalism for the overshoot (Col. 4), the value adopted for the free parameter d_{ov} that controls the depth of the overshooting (Col. 5), the wind torque K (Col. 6), the value of the additional constant viscosity v_{add} (Col. 7), the parameters describing its evolution (v_0 and α) according to Eq 20 (Col. 8), and the adopted turbulence coefficient (Col. 9). References. D_B : Baraffe et al. (2017), D_A : Augustson & Mathis (2019), D_K : Korre et al. (2019), $D_{T.425}$: Richard et al. (2005), $D_{T.42}$: Richard et al. (2005), D_{PM5000} : Richard et al. (2005), D_{Tach} : Brun et al. (1999)

momentum obeys the advection-diffusion equation

$$\rho \frac{d}{dt}(r^2 \Omega) = \frac{1}{5r^2} \frac{\partial}{\partial r} (\rho r^4 \Omega U_2) + \frac{1}{r^2} \frac{\partial}{\partial r} \left(v_v r^4 \frac{\partial \Omega}{\partial r} \right), \quad (3)$$

where ρ , r , Ω , U_2 , and v_v are the density, radius, angular velocity, meridional circulation velocity, and vertical shellular component of the turbulent viscosity, respectively. Meridional circulation appears through its velocity U_2 in Eq. (3), and can be described as a diffusion coefficient D_{eff} in Eq. (2) for the transport of chemicals, as shown by Chaboyer & Zahn (1992) when assuming a strong turbulent transport in the horizontal direction. The turbulent shear in the vertical and horizontal directions appears as a viscosity v_v (v_h) in Eq. (3) and as a diffusivity D_v (D_h) in Eq. (2), that is assumed to be proportional to the corresponding viscosity, with a proportionality factor of 1 as usually assumed in stellar evolution models (Zahn 1992; Mathis et al. 2018; Eggenberger et al. 2008; Ekström et al. 2012). Several prescriptions exist for both (D_v , v_v) and (D_h , v_h), and stellar evolution models computed with different combinations of these prescriptions can be found in the literature. As demonstrated by Meynet et al. (2013) and Amard et al. (2016), this choice strongly affects the outcome of the models. To explore this aspect we compute models with three different combinations listed in Table 3 and referred to as R1, R2, and R3. We used these combinations in our previous works (e.g., Talon & Charbonnel 2005; Amard et al. 2016; Mathis et al. 2018), motivated by the outcomes of numerical simulations (e.g., Prat & Lignières 2013, 2014; Prat et al. 2016; Garaud et al. 2017; Gagnier & Garaud 2018). The nomenclature of the models and the detailed expressions of the different turbulent diffusion coefficients are given in Appendices A and B, respectively.

3.4.2. Magnetic braking and initial rotation velocities

The extraction of angular momentum at the stellar surface due to magnetised winds is accounted for following the formalism by

Matt et al. (2015). We use the prescription as written in Eqs. (7)–(9) in Amard et al. (2019) with the following values for the parameters $m = 0.22$ and $p = 2.1$, which refer respectively to an exponent related to the magnetic field geometry and the exponent relating rotation and activity. We take $\chi = 14 \equiv \frac{Ro_{\odot}}{Ro_{sat}}$, the ratio of the solar Rossby number to the saturation value of the Rossby number⁴, at which the magnetic activity indicators saturate. They are fitted on the clusters of different ages to reproduce the rotation velocity dispersion according to Amard et al. (2019). Finally, a last complement parameter linked to magnetised wind braking, K , is calibrated so as to reproduce the solar surface rotation at the age of the Sun. We use a value of $K = 7.5 \times 10^{30}$ erg for our models unless otherwise indicated (see also Appendix A).

The models with rotation are computed as in Amard et al. (2019) for three values of the initial rotation period on the PMS: 1.6, 4.5, and 9.0 days, which will be referred to as the fast (^FR), median (R), and slow (^SR) rotating models, respectively. The disc coupling timescale is set at $\tau_{disc} = 2.5$ Myr for the fast rotators and at $\tau_{disc} = 5$ Myr for the median and the slow rotators. These values are chosen in agreement with Gallet & Bouvier (2015) in order to reproduce the observed rotation spread of open clusters stars.

3.5. Overshooting and penetrative convection

Using the MLT formalism associated with the Schwarzschild criterion for the instability to describe the extent of the convective regions, which is a classical approach in stellar evolution codes, is known to be flawed as the convective edges are defined according to null acceleration instead of null velocity of convective eddies. Convection actually penetrates in the sub-adiabatic

⁴ The Rossby number is defined here according to Matt et al. (2015) as $Ro = (\Omega \tau_{cz})^{-1}$, where τ_{cz} is the convective turnover timescale, characterised by the size of the studied convective region divided by the convective velocity.

layers below (for the convective envelopes) the superadiabatic unstable region, which generates mixing beyond the convective region down to where convective eddies are braked or eroded (e.g., Zahn 1991). Several formalisms for penetrative convection exist; we test three recent ones with an associated turbulent diffusion coefficient that scales with depth. We assume that the transport of angular momentum is not impacted by this process. The diffusion coefficients given below enter the expression of D in Eq. (2).

3.5.1. Baraffe et al. (2017)

The formalism proposed by Baraffe et al. (2017) is based on 2D and 3D hydrodynamic simulations of a young Sun on the PMS at 1 Myr and at solar metallicity (Pratt et al. 2017). These simulations allow them to characterise the depth of the penetrative convection below the convection zone; they show the existence of extreme events (deep penetrating plumes), which can have an outsized impact on transport mechanisms, especially ones that are meant to be inviscid. The diffusion coefficient obtained by Pratt et al. (2017) and reproduced here in Eq. (4), describes the mixing in the penetration layers and is characterised by the cumulative distribution function of the maximum penetration depth obtained in the simulations:

$$D_B(r) = D_0 \left[1 - \exp \left(- \exp \left(- \frac{r_{bcz} - r}{R} - \mu \right) \right) \right]. \quad (4)$$

Here $D_0 = (v_{\text{conv}} \times H_p \times \alpha_{\text{MLT}})/3$ is the convective turbulent diffusivity (with v_{conv} the mean velocity of the convective elements obtained from MLT and α_{MLT} the mixing length parameter), r is the local radius, r_{bcz} is the radius at the base of the convective zone, and R is the total radius of the star. The coefficients $\lambda = 6 \times 10^{-3}$ and $\mu = 5 \times 10^{-3}$ are as prescribed by Baraffe et al. (2017) and obtained from the simulations of Pratt et al. (2017). They are assumed to be independent of the stellar structure and age. All physical quantities are in cgs units (here and throughout the paper). The penetration depth of the overshooting is limited by the free parameter d_{ov} linked to the pressure scale-height and adjusted to take into account the limiting effect of stellar rotation. Baraffe et al. (2017) determined that this parameter should be $d_{\text{ov}} \approx 0.30H_p - 0.35H_p$ to reproduce the solar lithium abundance.

3.5.2. Augustson & Mathis (2019)

We tested for the first time in a stellar evolution code including rotation the description of penetrative convection by Augustson & Mathis (2019), which is based on a new model of rotating convection in stellar interiors. Contrary to Eq. (4), the penetration depth is now based on the one obtained by Zahn (1991). In his work Zahn (1991) linearised the equations of motion in the region of penetration, and the depth of penetration is then solved for given the velocity at the upper boundary of that region, which is assumed to reside in the convection zone. In Augustson & Mathis (2019) the impact of rotation on the convection is accounted for by using a modal convection model for rotating Rayleigh-Benard convection (Barker et al. 2014) where it is assumed to be locally valid in the region of penetration. This model has the asymptotic property that the velocity scales as $(v/v_0) \propto \text{Ro}^{1/5}$, with Ro the Rossby number, which is inversely proportional to the angular velocity in the convective region. The depth of the overshooting zone then depends on the pressure scale-height, the convective Rossby number (hence angular

velocity), and the thermal diffusivity, and is dynamically estimated. Using this model for penetrative convection and the functional form proposed by Pratt et al. (2017), Augustson & Mathis (2019) derive a new expression for the diffusion coefficient (their Eq. (70)), an approximation of which we use in this paper:

$$D_\Lambda(r) \approx D_0 \left[1 - \exp \left(- \exp \left(\frac{r - r_{bcz}}{d_{\text{ov}} \times \left(\frac{v}{v_0} \right)^{3/2}} + \frac{\mu}{\lambda} \right) \right) \right]. \quad (5)$$

Here D_0 , μ , and λ are the same as in Eq. (4); d_{ov} is the free parameter for controlling the depth of the overshoot; and (v/v_0) is the ratio of the velocity of the convective elements when taking rotation into account to the non-rotating inviscid value. The scaling between the velocity scales and the angular velocity implies that the diffusion coefficient in Eq. (5) is smaller when the star rotates faster, mimicking the fact that fast rotation inhibits convective motions to penetrate deep into the stably stratified region below. Thus, this model is a combination of the Baraffe et al. (2017) fit to their numerical stellar convective penetration simulations and those theoretical results of Augustson & Mathis (2019).

3.5.3. Korre et al. (2019)

Korre et al. (2019) propose a diffusive prescription suitable for 1D stellar evolution codes based on hydrodynamical simulations of penetrative convection and overshooting in a non-rotating Boussinesq spherical shell. In comparison to the simulations of Pratt et al. (2017), these simulations include an explicit diffusion, being the Navier-Stokes equations rather than an approximation of the Euler equations. The prescription is given by their Eq. (45),

$$D_K(r) = D_0 \exp \left(- \frac{(r - r_{bcz})^2}{2\delta_G^2} \right), \quad (6)$$

where D_0 (denoted D_{cz} in the original paper) is the same as in Eq. (4) and δ_G controls the depth of the penetration and writes

$$\delta_G \approx 1.2 \left(\frac{E_0 \text{Pr}}{S \text{Ra}_0} \right)^{1/2}, \quad (7)$$

where E_0 is the energy in the non-rotating convection zone, $\text{Pr} = \nu/\kappa$ is the Prandtl number defined as the ratio of the viscosity ν to the thermal diffusivity κ , S is the stiffness that measures the stability of the interface between the radiative zone and the convective zone, and Ra_0 is the Rayleigh number defined by Eq. (11) in Korre et al. (2019) as

$$\text{Ra}_0 = \frac{\alpha_{\text{th}} g \left| \frac{dT_0}{dr} - \frac{dT_{\text{ad}}}{dr} \right| r_0^4}{\kappa \nu}, \quad (8)$$

with α_{th} the thermal expansion coefficient, g the gravity, $\frac{dT_{\text{ad}}}{dr}$ the adiabatic temperature gradient, $\frac{dT_0}{dr} = \frac{dT_{\text{ad}}}{dr} |_{r=r_0}$, r_0 the outer radius of the convection zone, κ the thermal diffusivity, and ν the viscosity.

In this work we used Eq. (9) (instead of Eq. (6)), which is a result of fits to the numerical penetrative convection simulations carried out in Korre et al. (2019) where the overshooting length is adapted to contain information about the local rotation rate through the convective model of Augustson & Mathis (2019) and its implications for a linearised convective penetration model

$$D_K(r) \approx D_0 \exp \left(- \frac{(r - r_{bcz})^2}{d_{\text{ov}}^2 \times \left(\frac{v}{v_0} \right)^2} \right), \quad (9)$$

T. Dumont et al.: Lithium depletion and angular momentum transport in solar-type stars

where δ_G is approximated using the same principle as for $D_A(r)$ and adding the velocity dependence (v/v_0) (Augustson & Mathis 2020)

$$\delta_G \approx d_{ov} \times \frac{v}{v_0}, \quad (10)$$

Due to this inverse dependence on rotation, $D_K(r)$ is also smaller when the star rotates faster. Regarding the initial numerical simulation of Korre et al. (2019), the way that we adapted the rotational dependence with the help of the Augustson & Mathis (2019) should be taken with precautions. However, in the framework of slow-rotators, it is a relevant assumption.

3.6. Additional transports of chemicals

3.6.1. Tachocline turbulence

The tachocline is a shear layer located at the base of the solar convection zone where the radial rotation profile goes from differential in the convective envelope to flat in the radiative interior (Christensen-Dalsgaard & Schou 1988). First modelled by Spiegel & Zahn (1992) in a hydrodynamical framework, it is considered to be the seat of strong turbulence, with an associated diffusion coefficient that can be parametrised with respect to the Brunt-Väisälä frequency, the thickness of the tachocline, and the horizontal turbulent viscosity within it. Here we present models including the time-dependent expression given by Eqs. (15) and (16) in Brun et al. (1999),

$$D_{\text{Tach}}(\zeta) = \frac{1}{180} \frac{1}{4} \left(\frac{8}{3}\right)^2 \nu_H \left(\frac{d}{r_{bcz}}\right)^2 \mu_4^6 Q_4^2 \exp(-2\zeta) \cos^2(\zeta), \quad (11)$$

where ν_H is the horizontal turbulent viscosity; r_{bcz} is the radius at the base of the convective envelope; $\zeta = \mu_4(r_{bcz} - r)/d$ is a non-dimensional depth; $\mu_4 = 4.933$; $Q_4 \approx \hat{\Omega}/\Omega$, with $\hat{\Omega} = d\Omega(r, \theta)/d\theta$ the latitudinal differential rotation at the base of the convective envelope; and d is a measure of the tachocline thickness $h \approx d/2$:

$$d(t) = r_{bcz} \left(\frac{2\Omega}{N}\right)^{1/2} \left(\frac{4K_T}{\nu_H}\right)^{1/4}. \quad (12)$$

The depth of the convective envelope r_{bcz} , the angular velocity Ω , the horizontal viscosity ν_H , the thermal diffusivity K_T , and the Brunt-Väisälä frequency N all vary in time, as predicted by the structure and rotation equations. Defining

$$C = \frac{1}{180} \frac{1}{4} \left(\frac{8}{3}\right)^2 \mu_4^6 \exp(-2\zeta) \cos^2(\zeta), \quad (13)$$

we can compute the fully time-dependent equation of D_{Tach} as

$$D_{\text{Tach}}(t) = C \times \nu_H \left(\frac{d}{r_{bcz}}\right)^2 \left(\frac{\hat{\Omega}}{\Omega}\right)^2 \propto \Omega \nu_H^{1/2} \left(\frac{\hat{\Omega}}{\Omega}\right)^2. \quad (14)$$

The treatment of the meridional circulation in the framework of Zahn's theory is based on the expansion of all the physical quantities, including meridional circulation, in Legendre polynomials. The meridional circulation velocity is expanded to the second-order Legendre polynomials in the original works by Zahn (1992) and Maeder & Zahn (1998), which is the formalism adopted in STAREVOL. In that case, as shown by Mathis & Zahn (2004), the differential rotation in latitude is not explicitly accounted for. An expansion to the fourth-order of the departures from spherical symmetry is required to simultaneously treat the bulk of a radiative region and its tachocline, which is beyond

the scope of this study. Hence, we need a prescription to evaluate $\hat{\Omega}/\Omega$, and we adopt the same proportionality as in Brun et al. (1999), namely $\hat{\Omega} \propto \Omega^{0.7 \pm 0.1}$, which in turn comes from the paper from Donahue et al. (1996), and has been confirmed since then (e.g., Saar 2009; Brun et al. 2017), even if some uncertainties subsist (e.g., Augustson et al. 2012, who found that it would scale inversely with Ω in the case of F-type stars).

Equation (14) can thus be recast as

$$D_{\text{Tach}}(t) = C \times 0.02 \left(\frac{\Omega^{0.4}}{N^{1/2}}\right) (4\nu_H K_T)^{1/2}, \quad (15)$$

where we make explicit the proportionality coefficient adopted and the actual expression used in our computations for $\hat{\Omega}/\Omega$.

3.6.2. Parametric turbulent transport coefficients

The physical turbulent processes generating chemical mixing in radiative interiors, and more specifically in the radiative regions bordering convective ones, cannot all be accounted for given our current state of knowledge. Instead, these processes are parametrised to simulate diffusive turbulent mixing. Specifically, we follow Richer et al. (2000) and Richard et al. (2005) who discussed the use of additional turbulence competing with atomic diffusion to account respectively for observed abundance anomalies in Am and Fm stars and for the lithium abundances of Population II halo low-mass stars. In both classes of objects, atomic diffusion can be very efficient, and comparing models with observations calls for additional transport processes to be able to counteract its effects, as already anticipated in different kinds of stars by a vast amount of literature (e.g., Eddington 1929; Vauclair 2013; Michaud et al. 2015). Richer et al. (2000) and Richard et al. (2005) propose a purely parametric approach to model turbulence, with no assumptions on the underlying physical mechanism (see also Talon et al. 2006 for a comparison with rotation-induced mixing). Their diffusion coefficient is proportional to ρ^{-3} (see Proffitt & Michaud 1991) and attached to a specific temperature or to the density at the base of the convective envelope. These fixed points control where the turbulence is generated and thus the mixing depth. The parametric diffusivities D_{T_0} and D_{PMa_0} correspond to Eqs. (2) and (3) of Richard et al. (2005), respectively,

$$D_{T_0} = 400 D_{\text{He}}(T_0) \left[\frac{\rho(T_0)}{\rho}\right]^3, \quad (16)$$

where T_0 is a free parameter corresponding to the temperature at which the diffusivity is set to be 400 times larger than the atomic diffusion coefficient for He (e.g., $D_{\text{He}}(T_0)$), which is computed with the analytical approximation, as advised by Richer et al. (2000), and $\rho(T_0)$ is the density at the location where $T \equiv T_0$:

$$D_{\text{PMa}_0} = a_0 \left[\frac{\rho_{bcz}}{\rho}\right]^3 \quad (17)$$

Here a_0 is a free factor and ρ_{bcz} is the density at the base of the convective zone. To avoid numerical issues a minimum value of 1 is imposed on D_{T_0} and D_{PMa_0} .

4. Type I rotating models with atomic diffusion and penetrative convection

As discussed in the introduction, classical models do not account for the evolution of Li with time observed in solar-type stars. However, we computed such a model for comparison purposes

(C models, see Table 2), but we focus our discussion on models including rotation (R models), which all include atomic diffusion. In this section we present Type I rotating models, where the transport of angular momentum is driven only by meridional circulation and shear turbulence (Sect. 3.4); we focus on median rotators (see Sect. 3.4.2). We discuss the impact of the initial rotation rate in Sect. 5.

4.1. General behaviour

We start with model R1⁵ for which we adopt the same prescriptions for the horizontal and vertical shear induced turbulent viscosities (Mathis et al. 2018 and Zahn 1992, respectively; see Table 3), the same initial rotation period (4.5 days), and the same disc lifetime (5 Myr) as for the 1 M_{\odot} , Z_{\odot} median rotator model of Amard et al. (2019). The predicted evolution of the Li surface abundance and of the mean core and envelope angular velocities is shown in Fig. 1. As the envelope is convective and is assumed to rotate as a solid body, we have $\bar{\Omega}_{\text{conv}}(t) \equiv \Omega_{\text{surf}}(t)$. The averaged core angular velocity represents the angular velocity of a solid body of equal angular momentum to that of the entire radiation zone, and is defined as in Amard et al. (2019),

$$\bar{\Omega}_{\text{rad}} = \frac{\int_0^{M_{\text{BCE}}} r^2 \Omega dm}{\int_0^{M_{\text{BCE}}} r^2 dm}, \quad (18)$$

with M_{BCE} the mass coordinate at the base of the convective envelope.

As discussed in Amard et al. (2019), such a model reproduces well the 50th percentiles of the period distributions of most of the clusters for solar-type stars in open clusters from the early PMS to the age of the Sun and beyond. This behaviour is mainly driven by the extraction of angular momentum at the surface via magnetised winds modelled following Matt et al. (2015). As seen in Fig. 1, we confirm that the meridional circulation and shear turbulence are too weak to enforce the coupling between the core and the surface, leading to a core spinning too fast at the age of the Sun compared to the internal rotation profile inferred through helioseismology (see Sect. 4.3). On the other hand, the associated transport of chemicals is dominated by vertical shear-induced turbulence, which remains weak during the entire evolution (see Sect. 5.3, and Mathis et al. 2018) and only partially counteracts atomic diffusion. Consequently, at the age of the Sun the predicted lithium abundance is ~ 1.5 dex higher than observed.

4.2. Penetrative convection

As extensively discussed in the literature, model predictions for PMS Li depletion strongly depend on the treatment of convection and of penetrative convection (see e.g., D'Antona & Mazzitelli 1994; Piau & Turck-Chièze 2002; Baraffe et al. 2017; Thévenin et al. 2017). Here we test three different prescriptions for penetrative convection beyond the convective envelope that depend on the evolution of the internal angular velocity profile (Baraffe et al. 2017, Augustson & Mathis 2019, and Korre et al. 2019; see Sect. 3.5 and Table 3). Penetrative convection is assumed to only transport chemicals. It does not affect the surface and internal angular velocity evolution, which behave as in R1 (Fig. 1).

⁵ See Appendix A for model notation.

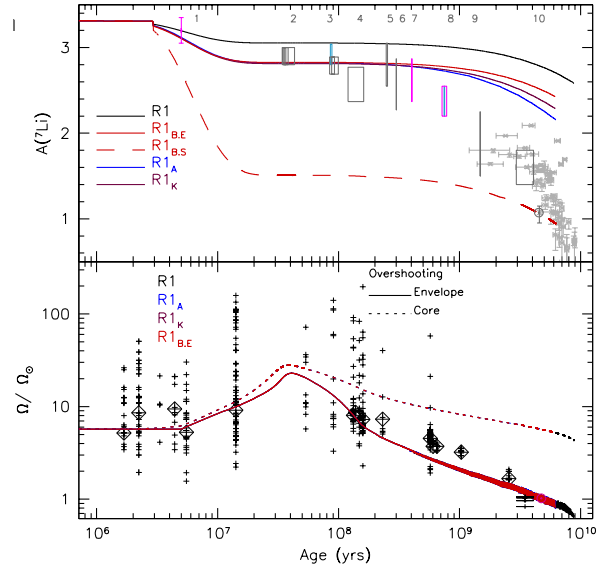


Fig. 1. *Top:* lithium surface abundance evolution with time for the R1 models including different overshoot prescriptions (colour-coded). Individual points are data for solar twins (Carlos et al. 2019). Boxes are for Li observations of solar-type stars in different open clusters (Sestito & Randich 2005; Carlos et al. 2020 for M 67) with ages from Bossini et al. (2019). The numbers 1–10 identify the clusters: (1) NGC 2264, (2) IC 2391, IC 2602 and IC 4665, (3) α Per, Pleiades, Blanco I, (4) NGC 2516, (5) M 34, (6) NGC 6475, (7) M 35, (8) Praesepe, NGC 6633, (9) NGC 752, and (10) M 67. The colour of the boxes indicates the [Fe/H] value: Netopil et al. (2016): pink: -0.17 to -0.05 ; grey: -0.05 to 0.05 ; light blue: 0.05 – 0.16 . *Bottom:* evolution of the angular velocity of the convective envelope and of the radiative core (in solar units $\Omega_{\odot} = 2.86 \times 10^{-6} \text{ s}^{-1}$; solid and dotted lines, respectively) vs age. The observational data is from Gallet & Bouvier (2015), except the four stars of M 67 from Barnes et al. (2016). Crosses are for individual stars; open diamonds show the 50th percentiles of the observed rotational distributions in each cluster.

Concerning the impact on Li, and as already shown by Baraffe et al. (2017), its evolution when assuming a constant value for the extent of the overshoot region d_{ov} does not match the observed Li behaviour with time. As shown in Fig. 1, the models R1_{BS} and R1_{BE} implementing Eq. (4) with $d_{\text{ov}} = 0.34H_p$ and $0.1H_p$, respectively, fit either the solar Li abundance or the Li abundances in the youngest open clusters (between 10 Myr and 100 Myr). Baraffe et al. (2017) thus proposed to vary the depth of the overshooting zone depending on rotation, as supported by numerical studies (Ziegler & Rüdiger 2003; Brummell 2007; Brun et al. 2017). They reproduce the Li temporal evolution fairly well when adopting $d_{\text{ov}} = 0.1H_p$ when the star is rapidly rotating ($\Omega > 5\Omega_{\odot}$, i.e. typically on the late PMS and around the ZAMS, and similarly to what we find) and a much deeper overshooting zone ($d_{\text{ov}} = 1H_p$) for slower, more evolved rotating stars.

We decided not to fine-tune the depth of the overshooting zone for the slow rotators (after ~ 1 Gyr), however, considering that other slow mixing processes may be responsible for Li depletion during this phase (see Sect. 5.2). We found the same behaviour as above with the prescription by Augustson & Mathis (2019) that accounts for the impact of the rotation on penetrative convection efficiency, and with the prescription by Korre et al. (2019). In both cases (models R1_A and R1_K, Fig. 1,

T. Dumont et al.: Lithium depletion and angular momentum transport in solar-type stars

Table 3) we adjusted the free parameter d_{ov} to reproduce the Li behaviour observed in the youngest open clusters around 30 Myr as in model R1_{B.E.}.

The Li evolution in all these models is characterised by a mild decrease from $A(^7\text{Li}) = 3.3$ dex to $A(^7\text{Li}) = 2.8$ dex at ~ 15 Myr, followed by a plateau and a further slow decrease later on the MS. The convective envelope slowly recedes along the MS, which increases the term $(r - r_{bcz})$ in the exponential of Eqs. (4), (5), and (9), leading to an increased efficiency of the slow mixing in the overshooting region that slowly depletes Li at the surface. In models R1_A and R1_K the transport in the overshoot region also depends on the rotation rate, which affects the depth of convective penetration via the ratio (v/v_0) . This results in a multiplying factor to the convective turbulent diffusivity D_0 in Eq. (5) larger than that in Eq. (9), hence a more efficient mixing and a greater Li depletion in model R1_A than in model R1_K.

4.3. Impact of turbulent diffusion modelling

From now on we consider models for median rotators including atomic diffusion, penetrative convection according to Augustson & Mathis (2019) with the calibration described above, and rotation-induced transport of chemicals and angular momentum associated with meridional circulation and shear turbulence. We explore the impact of different sets of prescriptions for the horizontal and vertical shear diffusivities (D_v and D_h , respectively) reported in Table 3. Figure 2 shows the evolution of $A(^7\text{Li})$ and core and envelope angular velocities as a function of age for the corresponding models R1_A (Sect. 4.2), R2_A, R2'_A, and R3_A. Figure 5 presents the internal rotation profiles predicted by these models at the age of the Sun.

Models R2_A and R2'_A include the same prescriptions for D_v and D_h (Talon & Zahn 1997 and Zahn 1992, respectively) as in Charbonnel & Talon (2005), and they differ from each other by the adjustment of the torque parameters to better fit the surface rotation rate (Table 3). In both cases we confirm that these prescriptions fail to reproduce the Li evolution with time and the internal rotation rate of the Sun. In particular, the (too) strong Li depletion is driven by the vertical shear coefficient prescribed by Talon & Zahn (1997), which is much greater than that of Zahn (1992), and which is fed by the very strong differential rotation inside the star during most of its evolution beyond 20 Myr. A similar behaviour for Li was found by Amard et al. (2016) using the same prescription for D_v , but that of D_h from Mathis et al. (2004), although this combination provides a stronger coupling between the core and the surface (which is still irreconcilable with the solar rotation profile). We thus discard the vertical shear diffusivity as prescribed by Talon & Zahn (1997) based on these results on lithium; however, this remains an open question considering that additional transport mechanisms for angular momentum may lead to different conclusions (see e.g., Charbonnel & Talon 2005, who invoke the effects of internal gravity waves).

Model R3_A provides a very good fit of the observed evolution of both the surface rotation period and the Li abundance. The rotational evolution of this model is very similar to that of model R1_A, as it is dominated by vertical shear in the early phases and by the surface extraction of the angular momentum by the magnetised winds beyond the ZAMS. Stronger Li depletion is achieved, however, thanks to a steeper angular velocity profile below the convective envelope (see Fig. 5 for a snapshot at the age of the Sun), which translates into an enhanced turbulent diffusive transport between the base of the convective envelope and the region where Li is destroyed by proton capture. This

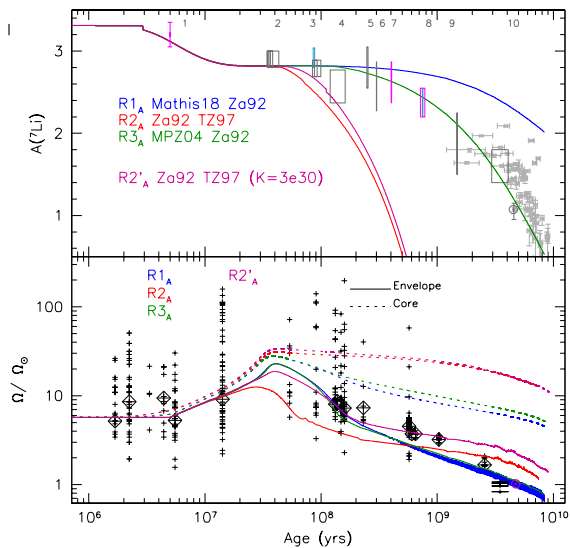


Fig. 2. Same as Fig. 1, but for the R1_A, R2_A, R2'_A, and R3_A models (details in Table 3).

behaviour is directly related to the modelling of the horizontal shear turbulent viscosity. Accounting for an additional source of horizontal shear turbulence when using the Mathis et al. (2018) prescription, as in model R1_A, was shown in this previous paper to lead to a lower vertical shear turbulent viscosity than when using the prescription from Mathis et al. (2004), as in model R3_A. In the absence of astero- and helioseismic constraints R3_A would be the best model. However, it also predicts a strong internal differential rotation at the age of the Sun.

4.4. Conclusions on Type I models

We confirm that all current prescriptions for shear-induced turbulence fail to reproduce simultaneously the internal rotation profile of the Sun and the surface constraints (see e.g., Amard et al. 2016, 2019 and references therein for similar Type I rotating models without atomic diffusion and penetrative convection; see also Ceillier et al. 2013; Marques et al. 2013; Eggenberger et al. 2017, 2019a; Mathis et al. 2018; Aerts et al. 2019; Deheuvels et al. 2020). We favour, however, the prescriptions for D_v and D_h from Mathis et al. (2018) and Zahn (1992), respectively. For the modelling of horizontal turbulence, we recall that the treatment of Mathis et al. (2018) is the first one that accounts for the action of stratification and rotation on horizontal turbulent motions. We couple it with the prescription for the vertical turbulent transport, which is the only one that has been validated by direct numerical simulations (Prat & Lignières 2013; Garaud et al. 2017). Their coupling with angular momentum wind extraction is done with the help of Matt et al. (2015); they reproduce well the evolution of the surface rotation rate with time as observed in solar-type stars in open clusters. Additionally, the three prescriptions that we tested for rotationally dependent penetrative convection help the models more closely fit the Li abundances observed in the youngest clusters (after calibration). Given our choice for the treatment of shear turbulence, accounting for Li in the more advanced stages requires either a very strong dependence between convective penetration depth and rotation, or an additional mixing process that may depend, or not, on the missing transport of angular momentum.

5. Improving the models

In this section we explore the possibilities to fit all the observational constraints by including additional transport processes for both angular momentum and chemical species. All the models discussed in this section include rotation-induced mixing, atomic diffusion, and penetrative convection.

5.1. Transport of angular momentum by additional viscosity

Several processes have been proposed to explain the strong coupling between the core and the surface of low-mass stars, and to flatten the angular velocity profile at the solar age and beyond (in particular, internal gravity waves and processes related to magnetism; Schatzman 1993; Spruit 2002; Charbonnel & Talon 2005; Mathis & Zahn 2005; Eggenberger et al. 2005, 2010, 2019b,c; Denissenkov et al. 2010; Charbonnel et al. 2013; Fuller et al. 2014, 2019; Cantiello et al. 2014; Rüdiger et al. 2015; Belkacem et al. 2015; Pinçon et al. 2017). However, no complete solution has been found yet. Parametric studies thus remain necessary to estimate the efficiency of the missing transport processes, and to potentially determine their nature. This is the approach we chose here.

We follow Eggenberger et al. (2012b, 2019b, see also Lagarde et al. 2014 and Spada et al. 2016) who proposed introducing a parametric vertical viscosity ν_{add} in the equation describing the transport of angular momentum to reproduce the core rotation rates of SGB and RGB stars. In this context, Eq. (3) becomes

$$\rho \frac{d}{dt}(r^2 \Omega) = \frac{1}{5r^2} \frac{\partial}{\partial r} (\rho r^4 \Omega U_2) + \frac{1}{r^2} \frac{\partial}{\partial r} \left((\nu_v + \nu_{\text{add}}) r^4 \frac{\partial \Omega}{\partial r} \right). \quad (19)$$

There ν_{add} was assumed to be either constant in time or dependant on the stellar rotation. Possible variations of ν_{add} within stellar interiors were not considered. We tested both options and in the second case, we followed Spada et al. (2016, their Eq. (3)) and assumed that the angular momentum transport efficiency depends on the radial rotational shear, i.e.

$$\nu_{\text{add}}(t) = \nu_0 \times \left(\frac{\bar{\Omega}_{\text{rad}}}{\bar{\Omega}_{\text{conv}}} \right)^\alpha, \quad (20)$$

where ν_0 and α are free parameters, and $\bar{\Omega}_{\text{rad}}$ and $\bar{\Omega}_{\text{conv}}$ are the mean angular velocity in the radiative interior and convective envelope, respectively, as defined in Sect. 4.1. We computed models with the three different combinations of turbulent shear prescriptions discussed in Sect. 4.3 for different values of ν_{add} and of α and ν_0 (Table 3).

The impact of the additional viscosity on the internal rotation profile and on the Li depletion and surface rotation rate can be seen in Figs. 3–5. In Fig. 4 we show the level of internal differential rotation

$$\Delta\Omega = \frac{\bar{\Omega}_{\text{rad}} - \Omega_{\text{surf}}}{\bar{\Omega}_{\text{rad}} + \Omega_{\text{surf}}}$$

with Ω_{surf} and $\bar{\Omega}_{\text{rad}}$ defined in Sect. 4.1.

Clearly, the higher the value of ν_{add} , or the higher the value of α for a given ν_0 , the earlier and the stronger the coupling between the core and the surface. In our models, the values for ν_{add} required to obtain a flat internal rotation profile at the age of the Sun while accounting for the surface rotation constraints vary between 2.5×10^4 and $4 \times 10^4 \text{ cm}^2 \text{ s}^{-1}$ depending on the adopted prescriptions for D_v and D_h . This is in agreement with the values required for the models to fit the asteroseismic data in subgiants and red giant stars ($\approx 10^4$ to 3×10^4 ;

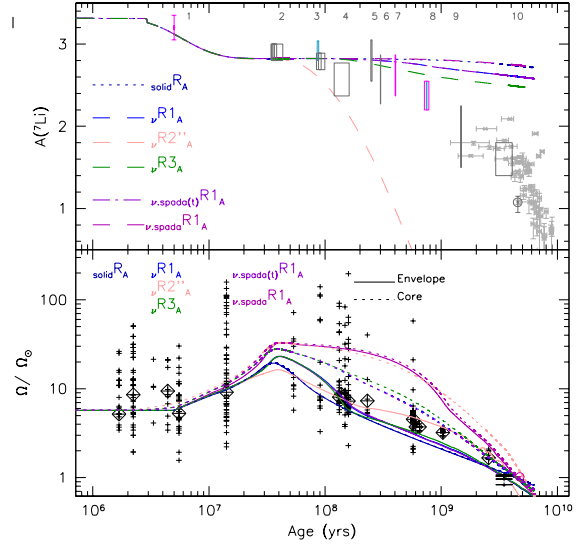


Fig. 3. Same as Fig. 1, but for the models with a fixed viscosity ν_{add} ($\nu R1_A$, $\nu R2'_A$, $\nu R3_A$, and $\nu_{\text{spada}}R1_A$), a time-dependent viscosity ($\nu_{\text{spada}(t)}R1_A$), and a model with enforced solid-body rotation ($\text{solid}R_A$).

Eggenberger et al. 2012b; Spada et al. 2016). In addition, in this case the evolution of the modelled surface rotation rate matches the observed values fairly well all along the evolution of the stars. When we adopt the value of $2.5 \times 10^5 \text{ cm}^2 \text{ s}^{-1}$ (model $\nu_{\text{spada}}R1_A$) advocated by Spada et al. (2016) for their solar benchmark, the internal rotation profile flattens very early in the evolution. In that case, a lower value for the magnetic braking parameter K is needed to fit the solar surface rotation rate⁶, but this destroys the agreement between the model predictions and the observed evolution of the surface rotation rate on the MS (between 100 Myr and 2 Gyr). When assuming a dependency of the transport of angular momentum with the radial rotational shear (Eq. (20)), we obtain a reasonable rotation profile at the age of the Sun with $\nu_0 = 2.5 \times 10^4 \text{ cm}^2 \text{ s}^{-1}$ and $\alpha = 0.5$ (model $\nu_{\text{spada}(t)}R1_A$), where we keep ν_0 of the same order as the constant ν_{add} calibrated above. We also obtain reasonable rotation profiles at solar age with other combinations (e.g., $\nu_0 = 100 \text{ cm}^2 \text{ s}^{-1}$, $\alpha = 12$, model $\nu_{2,\text{spada}(t)}R1_A$, and $\nu_0 = 1000 \text{ cm}^2 \text{ s}^{-1}$, $\alpha = 9$, not shown); in these cases, because of the high value of α , the differential rotation is reduced earlier on the MS and slowly continues receding after 100 Myr. It results in a lower surface rotation velocity than for model $\nu_{\text{spada}(t)}R1_A$ when K is not re-adjusted.

In summary, in the absence of asteroseismic data that could reveal the actual internal rotation profile in MS stars younger than the Sun, we cannot better constrain the efficiency of the transport of angular momentum or the nature of the underlying mechanism. We show, however, that the mean evolution of the surface rotation rate can be fairly well reproduced by the models with moderate values for the additional viscosity and with magnetic braking efficiency in agreement with the calibration value from Matt et al. (2019). However, with the stronger viscosity adopted in model $\nu_{\text{spada}}R1_A$, no value for the magnetic braking parameter K can reconcile the observed periods along the entire evolution. The same problem occurs for the

⁶ $K = 1.2 \times 10^{30} \text{ erg}$ (see Table 3) to be compared with $K = 6.3 \times 10^{30} \text{ erg}$ advised by Matt et al. (2019).

T. Dumont et al.: Lithium depletion and angular momentum transport in solar-type stars

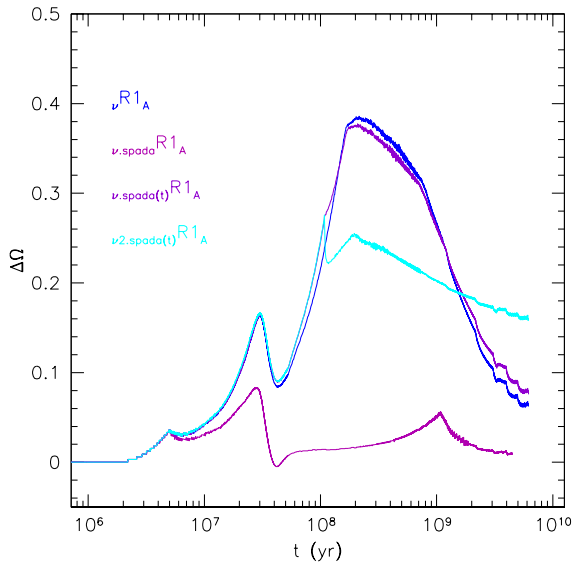


Fig. 4. Differential rotation evolution with time for the $\nu R1_A$, $\nu.spadaR1_A$, $\nu.spada(t)R1_A$, and $\nu2.spada(t)R1_A$ models (details in Table 3).

model where we assume solid-body rotation all along the evolution (models $solidR_A$). This provides a hint that rigid rotation may not be achieved very early on the MS in solar-type stars. This partially agrees with previous works by Gallet & Bouvier (2013, 2015), and by Lanzafame & Spada (2015) and Spada & Lanzafame (2020) for solar-type stars, who find, using two-zone models for the angular momentum transport, that quasi solid-body rotation should be achieved around 1 Gyr in order to fit the same observations. Our models, where the transport of angular momentum is self-consistently treated, resulting in fully resolved angular velocity radial profiles, seem to indicate that quasi rigid rotation may be reached even later in the evolution (see Fig. 4, where $\Delta\Omega = 0$ corresponds to a solid-body rotation and where increasing values of $\Delta\Omega$ correspond to higher differential rotation).

Finally, Li depletion is slightly less efficient in the models with parametric diffusivity than in the corresponding Type I models, due to the weaker turbulent shear. In particular, model $\nu R3_A$ does not reproduce the Li depletion on the MS contrary to what was obtained for model $R3_A$. However, Li depletion remains too strong in model $\nu R2''_A$ as it is dominated by the vertical shear associated with the D_v from Talon & Zahn (1997). In Sect. 4.3 we favoured the prescriptions for D_v and D_h included in models R1 and $\nu R1$. We see that model $\nu R1$ reproduces the evolution of surface rotation along time, and predicts an almost flat rotation profile at the age of the Sun. However, this model does not reproduce the Li depletion observed in open clusters beyond 500 Myr, in solar twins, and in the Sun. An additional transport of chemicals is consequently needed to increase the mixing and the depletion of the lithium during the MS.

5.2. Additional transport for chemicals

5.2.1. Tachocline mixing

As explained in Sect. 3.6.1 the tachocline is the transition layer from the latitudinally differentially rotating convective envelope and the uniformly rotating radiative core. It can be the seat of strong anisotropic turbulent transport when assuming that

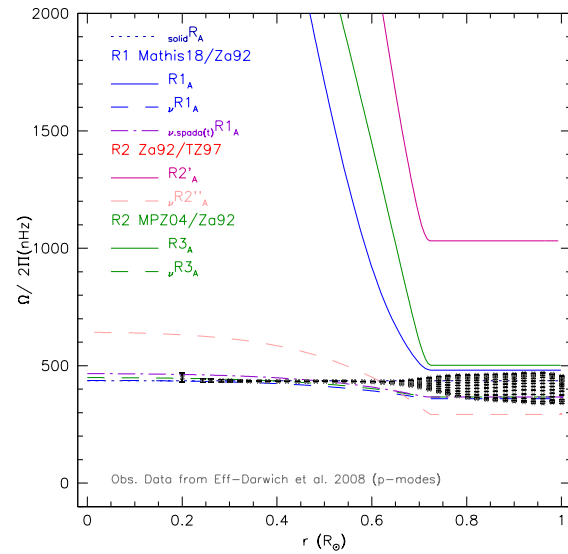


Fig. 5. Angular velocity profiles vs the radius at solar age for models presented in Fig. 3 compared to the rotation profile of the Sun (in dark grey) obtained from helioseismology from Eff-Darwich et al. (2008). The solid line, the dotted line, the dashed line, and the dot-dashed line refer to the differential, solid, ν_{add} , and $\nu_{add}(t)$ rotation cases, respectively.

the dynamics of this layer is driven by hydrodynamical mechanisms (Spiegel & Zahn 1992). We compute a model $\nu R1_A^{Tach}$ using Eqs. (12) and (15). Model $\nu R1_A^{Tach}$ is shown as a medium orange dashed line in Fig. 6. This model implements for the first time the self-consistent computation of the tachocline thickness according to Spiegel & Zahn (1992). It appears to become thinner as the star evolves from the PMS to the age of the Sun⁷ at which time it extends over $0.035 R_\odot$. This value is larger, yet compatible with the estimate of $\approx 0.02 R_\odot$ given by Elliott & Gough (1999) from helioseismology. The efficiency of the transport is also driven by a value of $D_{Tach}(t)$ that varies between $\approx 10^9 - 10^{10} \text{ cm}^2 \text{ s}^{-1}$. At young ages, the transport is very efficient and prevails over the penetrative convection to transport Li because of the deep location of the base of the convective envelope. It leads to an early and strong Li depletion (≈ 1 dex), which is too large to reproduce the Li evolution in young open clusters before 1 Gyr. The same result was obtained by Piau & Turck-Chièze (2002) with a parametric treatment of the tachocline depth and turbulent diffusivity as in Brun et al. (1999). As the star evolves and the convective envelope becomes shallower, the thickness of the tachocline does not increase enough, and even decreases, so that the tachocline becomes inefficient to transport the Li after 20 Myr whatever the value of D_{Tach} . This prediction differs from that of Piau & Turck-Chièze (2002), who achieved a solar Li abundance by the age of the Sun. Such a difference is most probably due to the parametrisation they adopted for the thickness of tachocline.

In its current form and with the adopted description of rotation-induced turbulence in our models, mixing in the tachocline prevents the models from fitting the observed Li evolution in solar-type stars. The efficiency of the turbulent transport in the tachocline as expressed by Eq. (11) remains difficult to model correctly as we lack good estimates of the evolution of

⁷ Age(yr)/h (R_\odot): $10^7/0.05$; $5.10^7/0.065$; $10^9/0.03$; $4.57 \cdot 10^9/0.035$.

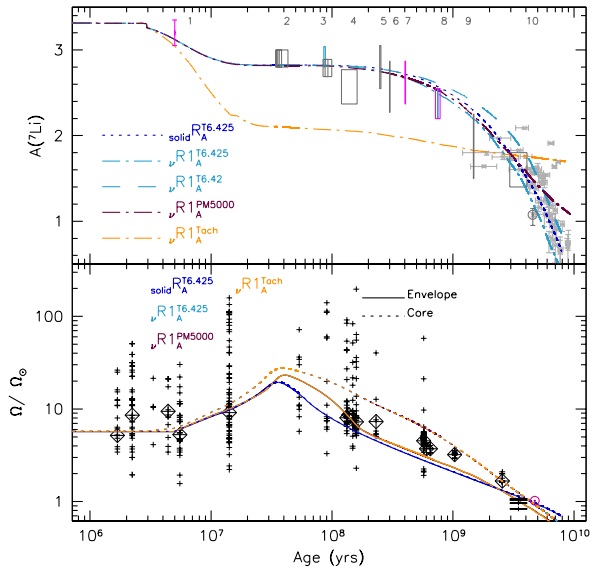


Fig. 6. Same as Fig. 1, but for models $\nu R_A^{T6.425}$, νR_A^{PM5000} , νR_A^{Tach} , and $\text{solid} R_A^{T6.425}$ that include additional turbulence.

the ratio $\hat{\Omega}/\Omega$. A fully consistent model should solve the equations for the structure of the turbulent tachocline as derived by Spiegel & Zahn (1992) with taking into account boundary conditions that describe the variations of the latitudinal differential rotation at the base of the convective envelope as a function of time. This differential rotation is a function of the global rotation of the star (Brun et al. 2017), and will thus evolve all along its evolution.

5.2.2. Parametric turbulence

Following Richard et al. (2005), we use the parametric prescriptions for an additional transport of matter as described by Eqs. (16) and (17). We compute two models, $\nu R_A^{T6.425}$ and νR_A^{PM5000} , for which we adjust the two free parameters of Eqs. (16) and (17) as respectively $\log(T_0) = 6.425$ and $a_0 = 5000$ to best fit the evolution of Li abundance observed at the surface of solar-type stars and the Sun. We consider this to be in rather good agreement with the values obtained by Richard et al. (2005, $\log(T_0) = 6.4$ and $a_0 = 2000$) for their solar model, considering that it did not include rotation and that it was computed with different basic input physics (in particular nuclear reaction rates, eos, opacities).

The parametric turbulent mixing becomes efficient beyond 200–300 Myr, as can be seen from Fig. 6. The form of Eqs. (16) and (17) leads to an increase in the diffusion coefficient between the base of the convective envelope and the Li burning region as the star evolves on the MS. The evolution of the coefficient $D_{T6.425}$ is illustrated alongside that of the other diffusivities at four different ages in Fig. 7. We adopt Eq. (16) included in model $\nu R_A^{T6.425}$ because it is independent of the depth of the convective envelope and is scaled by the atomic diffusion coefficient for ${}^4\text{He}$ in the Li burning region. While the transport by penetrative convection is the main process responsible for surface Li depletion during the PMS (upper left panel of Fig. 7), the coefficient $D_{T6.425}$ dominates the transport within the Li burning region on the MS, as shown in the lower panels of Fig. 7 (at 1 Gyr and

4.57 Gyr). The addition of this mixing process does not affect the predicted evolution of the surface rotation rate (lower panel Fig. 6) because it is independent of rotation. We also tested a solid-body rotating counterpart to model $\nu R_A^{T6.425}$, called model $\text{solid} R_A^{T6.425}$, which is also presented in Fig. 6. It predicts slightly less depletion of Li due to a lower efficiency of the transport in that case.

Model $\nu R_A^{T6.425}$ meets the goal of reproducing the surface evolution of the Li abundance and the angular velocity together with an angular velocity profile compatible with that of the Sun at the solar age.

5.3. Models with optimal prescriptions

We explore the impact of the initial angular velocity on our optimal model $\nu R_A^{T6.425}$ and discuss its predictions for other chemical constraints. We compute ${}^F R_A^{T6.425}$, $\nu R_A^{T6.425}$, and ${}^S R_A^{T6.425}$ for fast, median, and slow rotators, respectively, and present the associated evolution of Li and surface angular velocity in Fig. 8, together with the non-rotating model C (Table 2).

The relation between surface rotation rate and Li abundance in solar-type stars was first observed by Soderblom et al. (1993) in the Pleiades and has been confirmed by more recent studies in several clusters (Bouvier et al. 2018; Arancibia-Silva et al. 2020). The observations indicate that rapidly rotating stars possess higher Li abundances than slowly rotating stars, which is related to the PMS rotational evolution (Bouvier 2008). In particular, it is related to the difference in the disc lifetime between the fast and slow rotators (e.g., Eggenberger et al. 2012a) and/or alternately to the correlation between rotation and penetrative convection efficiency (e.g., Baraffe et al. 2017). Contrary to the models of Amard et al. (2016, 2019) our models comply with the expected behaviour and the PMS Li depletion is larger for slower rotators, as shown in upper panel of Fig. 8. As we use the same treatment for rotational transport and the same disc lifetimes as in Amard et al. (2019), the inclusion of penetrative convection according to Eq. (5) is clearly shaping the Li evolution prior to the ZAMS.

On the MS, when the parametric turbulence takes over the Li transport, all models converge to the solar Li value since we have adjusted the parametric turbulence to fit the Sun. The tracks follow the lower envelope of the data from solar twins (Carlos et al. 2019, 2020). The slightly shallower turbulent mixing used in model $\nu R_A^{T6.42}$ permits us to fit these points. The parameters we adopted for turbulence and magnetic braking lead to a good general agreement between the theoretical and the observed Li behaviour for both field and open cluster solar-type stars.

Regarding surface and internal rotation, the fast, median, and slow models are also in good agreement with the observed velocity distribution (solid lines, bottom panel Fig. 8) in solar-type stars, similar to the models of Amard et al. (2019), which did not include additional viscosity for the transport of angular momentum. Moreover, all the models predict a flat rotation profile in the radiative interior at the age of the Sun due to the extra transport of angular momentum by the adopted ad hoc viscosity ν_{add} , regardless of the initial angular velocity. The evolution of the rotation rate slightly differs, however, depending on the assumed initial rotational rate. The model ${}^F R_A^{T6.425}$ rotates almost as a solid body on the PMS and the early MS. The strong torque exerted by the magnetised winds leads to a sharp deceleration of the surface of this model between 300 Myr and 500 Myr, and differential rotation develops in the interior during that period. When the surface torque becomes

T. Dumont et al.: Lithium depletion and angular momentum transport in solar-type stars

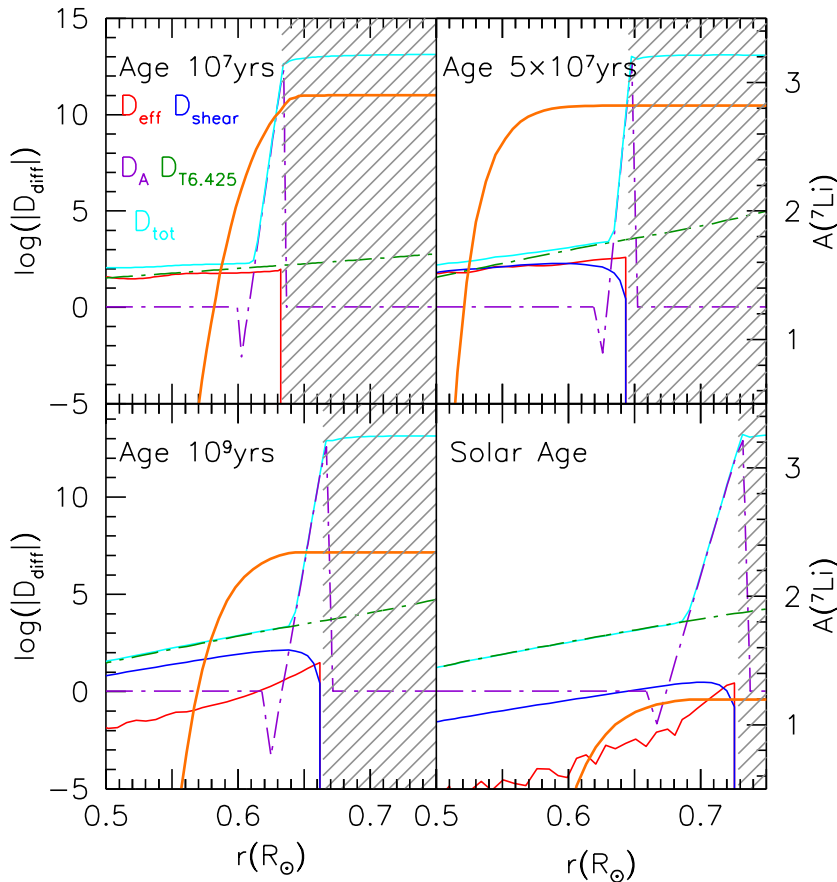


Fig. 7. Profiles of the logarithm of the diffusion coefficients (*left axis*) of the meridional circulation (D_{eff}), the vertical shear ($D_{\text{shear}} = D_v$), the overshoot (D_A), the parametric turbulence ($D_{T6.425}$), and the total transport coefficient ($D_{\text{tot}} = D_{\text{eff}} + D_{\text{shear}} + D_A + D_{T6.425}$) as a function of the radius normalised to solar radius at four different ages (10^7 years, 5×10^7 years, 10^9 years, and solar age) for model $\nu R1_A^{T6.425}$. The abundance profile of $A(^7\text{Li})$ is the orange full line (*right axis*). Hatched areas correspond to convective regions.

inefficient, around 500 Myr, the surface angular velocity evolution settles on a Skumanich-like path (Skumanich 1972) while angular momentum is continuously extracted from the core by the additional transport, modelled here with ν_{add} , so that at the age of the Sun the internal rotation profile agrees with the helioseismic constraint. On the MS the coupling between the core and the surface is larger for larger initial angular velocity (compare $\nu R1_A^{T6.425}$ and $\nu R1_A^{T6.425}$ in Fig. 8). This behaviour differs from what was obtained from bi-zone models (Gallet & Bouvier 2013; Lanzafame & Spada 2015). In slow rotators, the large angular velocity gradient and the small surface angular velocity at the ZAMS and during the early MS evolution lead to the stronger Li depletion discussed above.

Beryllium (hereafter Be) is also easily destroyed in stellar interiors, but at higher temperatures (≈ 3.5 MK) than Li and can thus also be used to further constrain the mixing. Spectroscopic determination of Be in open cluster solar-type stars (e.g., Boesgaard et al. 2003a,b, 2004) indicate that it should be only slightly depleted during the PMS and the MS of solar-like stars. In Fig. 9, we present the evolution of the surface Be abundance as a function of the age for the models shown in Fig. 8. The evolution of Be at the stellar surface is only affected by the parametric turbulent mixing introduced to reproduce the MS depletion of Li in our models. It does not depend on the initial velocity. The parametric turbulent mixing leads to a 0.3 dex depletion of Be by the age of the Sun, which is slightly too large compared to observations. Model $\nu R1_A^{T6.42}$ which better reproduces the Li abundances of solar twins (see previous section), is compatible

within the error bars with the Be abundance at the solar surface. However, the limited number of Be abundance determinations currently prevents us from using this nuclide as a good constraint for internal transport processes.

6. Summary and discussion

We computed models of solar-like stars including atomic diffusion and rotation and we analysed the impact of different internal transport processes on the chemical and rotational evolution of these stars. Our models confirm the need for additional transport processes beyond atomic diffusion and Type I rotation-induced processes (meridional circulation and turbulent shear) for both angular momentum and chemicals in order to reproduce observations of Li and internal rotation for MS solar-type stars. In the framework of our study, we chose to parametrise the action of complex processes and adopt the simpler approach of an additional turbulent viscosity ν_{add} to the angular momentum transport equation, either constant or time-dependent. We follow the propositions by Eggenberger et al. (2012b) and Spada et al. (2016) to account for the low degree of (radial) differential rotation in evolved stars (subgiants and red giant stars). We show that such a parametrisation of a yet-to-be-identified physical process can indeed lead to a strong coupling between the interior and the envelope in solar-type stars at the age of the Sun without significantly modifying the predicted evolution of their surface rotation. Our models also indicate that all the current observational constraints can be satisfied without reaching a full

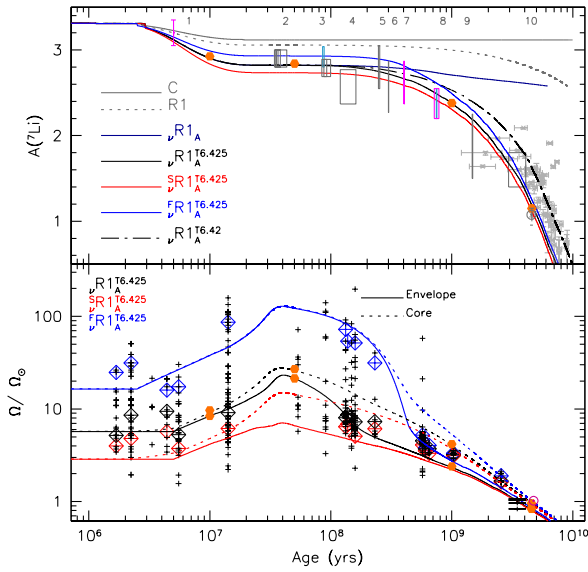


Fig. 8. Same as Fig. 1, but for the different R1 models, the selected $v_A R1_A^{T6.425}$ model with different initial rotation velocities, and the classical model (C). The orange dots refer to the ages at which the diffusion coefficient profiles are shown in Fig. 7. The red, black, and blue open squares show the 25th, 50th and 90th percentiles of the observed rotational distributions in each cluster.

rotational coupling between the core and the envelope until 2–3 Gyr. Moreover, a higher degree of differential rotation is predicted for the slow rotators before this age. Asteroseismic constraints on the internal rotation of young solar-type MS stars would be of great value to test this prediction.

Concerning the transport of chemicals, we confirm that the Li depletion observed in MS solar-type stars of open clusters cannot be reproduced by rotational mixing alone when the solar internal rotation constraint is also taken into account. We implemented for the first time the prescription for penetrative convection dependent on rotation, according to Augustson & Mathis (2019). We show that this process is key to reproducing the surface Li abundance evolution of solar-type stars during the PMS and the very early MS. The dependence of the convective penetration depth on the rotation rate in the convective envelope is the main factor explaining the anti-correlation between the surface rotation rate and Li abundance observed in open clusters. It dominates over the effect of the disc lifetime first pointed out by Eggenberger et al. (2012a).

For the first time since its publication we were able to self-consistently compute the tachocline thickness according to the model by Spiegel & Zahn (1992, their Eq. (12)). Using the parametrisation for the horizontal turbulent viscosity from Mathis et al. (2018), our model predicts a tachocline thickness at the solar age, which is compatible with the helioseismic estimate by Elliott & Gough (1999). On the other hand, the associated turbulent transport as described in Brun et al. (1999) depends on the degree of latitudinal differential rotation, whose evolution remains poorly constrained. Using estimates based on activity indicators from Donahue et al. (1996) leads to very efficient tachocline mixing and an over-depletion of Li surface abundance during the PMS evolution. In addition, the shallow thickness of the tachocline during the MS evolution prevents our models from reproducing the expected Li depletion during this evolutionary

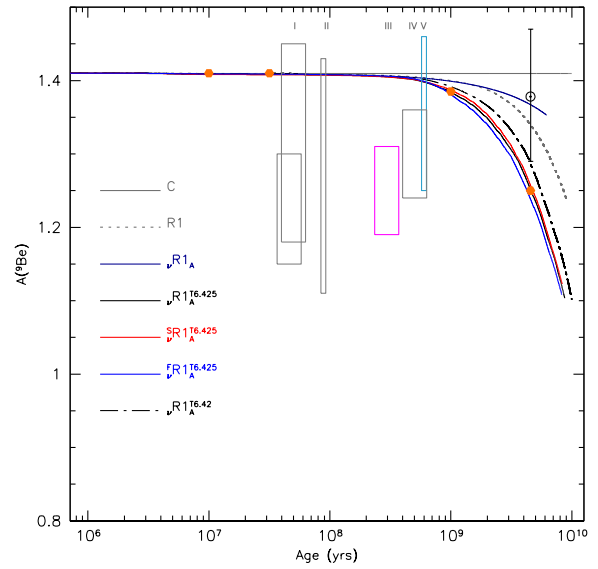


Fig. 9. Same as Fig. 8, but for Be. Boxes are for Be observations of solar-mass stars in different open clusters and are colour-coded according to their metallicity, as in Fig. 1. The numbers I–V identify the clusters: (I) IC 2602 and IC 2391 (Smiljanic et al. 2011), (II) Pleiades (Boesgaard et al. 2003a), (III) Ursa Major (Boesgaard et al. 2003b), (IV) Coma Ber (Boesgaard et al. 2003b), and (V) Hyades (Boesgaard et al. 2004). The solar beryllium with uncertainties comes from Asplund et al. (2009, photospheric value). The orange dots refer to the four profiles extracted from the star evolution shown in Fig. 7.

phase. Furthermore, the models that account self-consistently for the tachocline mixing according to the formalisms of Spiegel & Zahn (1992) and Brun et al. (1999) fail to reproduce the observed evolution of Li abundance in solar-type stars. However, this specific formalism calls for observational constraints on the degree of latitudinal differential rotation. The development of the meridional circulation to the fourth order, as proposed by Mathis & Zahn (2004), was designed to self-consistently include the tachocline region and associated transport in stellar evolution models and could help to sort out the actual impact of tachocline mixing along the evolution of solar-type stars. In this context new developments on the horizontal turbulent transport induced by the instability of the horizontal shear of the differential rotation would be of great importance (Park et al. 2020; Garaud 2020; Cope et al. 2020).

Our optimal models ($v_A R1_A^{T6.425}$) are obtained when including a parametric turbulence according to Richer et al. (2000), which was first proposed as a way to counteract the impact of atomic diffusion with radiative accelerations in F-, A-, and B-type stars for several evolutionary stages. The depth of the turbulence appears to be slightly greater for the Sun than for solar twins based on the comparison of our models ($v_A R1_A^{T6.425}$ and $v_A R1_A^{T6.42}$) to the Li and Be data in open clusters, confirming that the Sun might not be the best benchmark for testing transport processes in solar-type stars (e.g., see also Carlos et al. 2020).

Acknowledgements. We thank J. W. Ferguson for providing us with low-temperature opacity tables adapted to the solar mixture we adopt in this work, P. Eggenberger for fruitful discussions, and the anonymous referee for constructive comments on the manuscript. This work was supported by the Swiss National Science Foundation (Projects 200021-169125 and 200020-192039 P1 C.C.). We thank the Programme National de Physique Stellaire (PNPS) of CNRS/INSU

T. Dumont et al.: Lithium depletion and angular momentum transport in solar-type stars

co-funded by CEA and CNES. This research has made use of NASA's Astrophysics Data System Bibliographic Services. L.A. acknowledges funding from the European Research Council (ERC) under the European Union's Horizon 2020 research and innovation program (Grant agreement No. 682393 AWESoMe-Stars). K.C.A. and S.M. acknowledge support from the ERC SPIRE 647383 grant and PLATO & GOLF CNES Grants at CEA/DAP-AIM. A.P. acknowledge support from the PLATO CNES grant at LUPM.

References

- Aerts, C., Mathis, S., & Rogers, T. M. 2019, *ARA&A*, 57, 35
- Allen, C. W. 1976, *Astrophys. Quantities*,
- Amard, L., Palacios, A., Charbonnel, C., Gallet, F., & Bouvier, J. 2016, *A&A*, 587, A105
- Amard, L., Palacios, A., Charbonnel, C., et al. 2019, *A&A*, 631, A77
- Arancibia-Silva, J., Bouvier, J., Bayo, A., et al. 2020, *A&A*, 635, L13
- Asplund, M., Grevesse, N., Sauval, A. J., & Scott, P. 2009, *ARA&A*, 47, 481
- Augustson, K. C., & Mathis, S. 2019, *ApJ*, 874, 83
- Augustson, K. C., Mathis, S. 2020, in *Stars and their Variability Observed from Space*, eds. C. Neiner, W. W. Weiss, D. Baade, et al., 311
- Augustson, K. C., Brown, B. P., Brun, A. S., Miesch, M. S., & Toomre, J. 2012, *ApJ*, 756, 169
- Baglin, A., & Lebreton, Y. 1990, in *Surface Abundances of Light Elements as Diagnostic of Transport Processes in the Sun and Solar-Type Stars*, eds. G. Berthomieu, & M. Cribier, *Astrophys. Space Sci. Lib.*, 159, 437
- Baglin, A., Morel, P. J., & Schatzman, E. 1985, *A&A*, 149, 309
- Bahcall, J. N., Pinsonneault, M. H., & Wasserburg, G. J. 1995, *Rev. Mod. Phys.*, 67, 781
- Baraffe, I., Pratt, J., Goffrey, T., et al. 2017, *ApJ*, 845, L6
- Barker, A. J., Dempsey, A. M., & Lithwick, Y. 2014, *ApJ*, 791, 13
- Barnes, S. A., Weingrill, J., Fritzewski, D., Strassmeier, K. G., & Platais, I. 2016, *ApJ*, 823, 16
- Basu, S., & Antia, H. M. 1995, *MNRAS*, 276, 1402
- Beck, P. G., do Nascimento, J. D., Duarte, T., et al. 2017, *A&A*, 602, A63
- Belkacem, K., Marques, J. P., Goupil, M. J., et al. 2015, *A&A*, 579, A31
- Benomar, O., Takata, M., Shibahashi, H., Ceillier, T., & García, R. A. 2015, *MNRAS*, 452, 2654
- Boesgaard, A. M. 1976, *PASP*, 88, 353
- Boesgaard, A. M. 1991, *ApJ*, 370, L95
- Boesgaard, A. M., Armengaud, E., & King, J. R. 2003a, *ApJ*, 583, 955
- Boesgaard, A. M., Armengaud, E., & King, J. R. 2003b, *ApJ*, 582, 410
- Boesgaard, A. M., Armengaud, E., & King, J. R. 2004, *ApJ*, 605, 864
- Böhm, K.-H. 1963, *ApJ*, 138, 297
- Böhm-Vitense, E. 1958, *Z. Astrophys.*, 46, 108
- Bossini, D., Vallenari, A., Bragaglia, A., et al. 2019, *A&A*, 623, A108
- Bouvier, J. 2008, *A&A*, 489, L53
- Bouvier, J., Barrado, D., Moraux, E., et al. 2018, *A&A*, 613, A63
- Brummell, N. H. 2007, in *Convection in Astrophysics*, eds. F. Kupka, I. Roxburgh, & K. L. Chan, *IAU Symp.*, 239, 417
- Brun, A. S., Turck-Chièze, S., & Zahn, J. P. 1999, *ApJ*, 525, 1032
- Brun, A. S., Strugarek, A., Varella, J., et al. 2017, *ApJ*, 836, 192
- Cantiello, M., Mankovich, C., Bildsten, L., Christensen-Dalsgaard, J., & Paxton, B. 2014, *ApJ*, 788, 93
- Carlos, M., Meléndez, J., Spina, L., et al. 2019, *MNRAS*, 485, 4052
- Carlos, M., Meléndez, J., do Nascimento, J. D., & Castro, M. 2020, *MNRAS*, 492, 245
- Castro, M., Vauclair, S., Richard, O., & Santos, N. C. 2009, *A&A*, 494, 663
- Ceillier, T., Eggenberger, P., García, R. A., & Mathis, S. 2013, *A&A*, 555, A54
- Chaboyer, B., & Zahn, J. P. 1992, *A&A*, 253, 173
- Charbonnel, C., & Talon, S. 2005, *Science*, 309, 2189
- Charbonnel, C., & Talon, S. 2008, in *The Art of Modeling Stars in the 21st Century*, eds. L. Deng, & K. L. Chan, *IAU Symp.*, 252, 163
- Charbonnel, C., Vauclair, S., & Zahn, J. P. 1992, *A&A*, 255, 191
- Charbonnel, C., Vauclair, S., Maeder, A., Meynet, G., & Schaller, G. 1994, *A&A*, 283, 155
- Charbonnel, C., Decressin, T., Amard, L., Palacios, A., & Talon, S. 2013, *A&A*, 554, A40
- Chen, Y. Q., & Zhao, G. 2006, *AJ*, 131, 1816
- Christensen-Dalsgaard, J., & Schou, J. 1988, in *Seismology of the Sun and Sun-Like Stars*, ed. E. J. Rolfe, *ESA SP*, 286, 149
- Cope, L., Garaud, P., & Caulfield, C. P. 2020, *J. Fluid Mech.*, 903, A1
- Cox, J. P., & Giuli, R. T. 1968, *Principles of Stellar Structure* (New York: Gordon and Breach)
- Cranmer, S. R., & Saar, S. H. 2011, *ApJ*, 741, 54
- Cummings, J. D., Deliyannis, C. P., Maderak, R. M., & Steinhilber, A. 2017, *AJ*, 153, 128
- D'Antona, F., & Mazzitelli, I. 1994, *ApJS*, 90, 467
- Deal, M., Alecian, G., Lebreton, Y., et al. 2018, *A&A*, 618, A10
- Decressin, T., Mathis, S., Palacios, A., et al. 2009, *A&A*, 495, 271
- Deheuvels, S., García, R. A., Chaplin, W. J., et al. 2012, *ApJ*, 756, 19
- Deheuvels, S., Doğan, G., Goupil, M. J., et al. 2014, *A&A*, 564, A27
- Deheuvels, S., Ballot, J., Beck, P. G., et al. 2015, *A&A*, 580, A96
- Deheuvels, S., Ballot, J., Eggenberger, P., et al. 2020, *A&A*, 641, A117
- Delgado Mena, E., Israelian, G., González Hernández, J. I., et al. 2014, *A&A*, 562, A92
- Deliyannis, C. P., Pinsonneault, M. H., & Charbonnel, C. 2000, in *The Light Elements and their Evolution*, eds. L. da Silva, R. de Medeiros, & M. Spite, *IAU Symp.*, 198, 61
- Denissenkov, P. A., Pinsonneault, M., Terndrup, D. M., & Newsham, G. 2010, *ApJ*, 716, 1269
- Do Nascimento, J. D., Castro, M., Meléndez, J., et al. 2009, *A&A*, 501, 687
- Domingo, V., Fleck, B., & Poland, A. I. 1995, *Sol. Phys.*, 162, 1
- Donahue, R. A., Saar, S. H., & Baliunas, S. L. 1996, *ApJ*, 466, 384
- dos Santos, L. A., Meléndez, J., do Nascimento, J. D., et al. 2016, *A&A*, 592, A156
- Eddington, A. S. 1929, *MNRAS*, 90, 54
- Elf-Darwich, A., Korzennik, S. G., Jiménez-Reyes, S. J., & García, R. A. 2008, *ApJ*, 679, 1636
- Eggenberger, P., Maeder, A., & Meynet, G. 2005, *A&A*, 440, L9
- Eggenberger, P., Meynet, G., Maeder, A., et al. 2008, *Ap&SS*, 316, 43
- Eggenberger, P., Meynet, G., Maeder, A., et al. 2010, *A&A*, 519, A116
- Eggenberger, P., Montalbán, J., & Miglio, A. 2012a, *A&A*, 544, L4
- Eggenberger, P., Haemmerlé, L., Meynet, G., & Maeder, A. 2012b, *A&A*, 539, A70
- Eggenberger, P., Lagarde, N., Miglio, A., et al. 2017, *A&A*, 599, A18
- Eggenberger, P., Buldgen, G., & Salmon, S. J. A. J. 2019a, *A&A*, 626, L1
- Eggenberger, P., Deheuvels, S., Miglio, A., et al. 2019b, *A&A*, 621, A66
- Eggenberger, P., den Hartogh, J. W., Buldgen, G., et al. 2019c, *A&A*, 631, L6
- Eggleton, P. P., Faulkner, J., & Flannery, B. P. 1973, *A&A*, 23, 325
- Ekström, S., Georgy, C., Eggenberger, P., et al. 2012, *A&A*, 537, A146
- Elliott, J. R., & Gough, D. O. 1999, *ApJ*, 516, 475
- Ellsworth, Y., Howe, R., Isaak, G. R., et al. 1995, *Nature*, 376, 669
- Fuller, J., Lecoanet, D., Cantiello, M., & Brown, B. 2014, *ApJ*, 796, 17
- Fuller, J., Piro, A. L., & Jermyn, A. S. 2019, *MNRAS*, 485, 3661
- Gabriel, A. H., Grec, G., Charra, J., et al. 1995, *Sol. Phys.*, 162, 61
- Gagnier, D., & Garaud, P. 2018, *ApJ*, 862, 36
- Gallet, F., & Bouvier, J. 2013, *A&A*, 556, A36
- Gallet, F., & Bouvier, J. 2015, *A&A*, 577, A98
- Gallet, F., Zanni, C., & Amard, L. 2019, *A&A*, 632, A6
- Garaud, P. 2020, *ApJ*, 901, 146
- Garaud, P., Gagnier, D., & Verhoeven, J. 2017, *ApJ*, 837, 133
- García, R. A., & Ballot, J. 2019, *Liv. Rev. Sol. Phys.*, 16, 4
- García, R. A., Ceillier, T., Salabert, D., et al. 2014, *A&A*, 572, A34
- Gehan, C., Mosser, B., Michel, E., Samadi, R., & Kallinger, T. 2018, *A&A*, 616, A24
- Greenstein, J. L., & Richardson, R. S. 1951, *ApJ*, 113, 536
- Guo, J., Lin, L., Bai, C., & Liu, J. 2017, *Ap&SS*, 362, 15
- Guzik, J. A., & Musack, K. 2010, *ApJ*, 713, 1108
- Harutyunyan, G., Steffen, M., Mott, A., et al. 2018, *A&A*, 618, A16
- Hopf, E. 1930, *MNRAS*, 90, 287
- Howe, R., Chaplin, W. J., Basu, S., et al. 2020, *MNRAS*, 493, L49
- Iglesias, C. A., & Rogers, F. J. 1996, *ApJ*, 464, 943
- Jørgensen, A. C. S., & Weiss, A. 2018, *MNRAS*, 481, 4389
- King, J. R., Deliyannis, C. P., Hiltgen, D. D., et al. 1997, *AJ*, 113, 1871
- Korre, L., Garaud, P., & Brummell, N. H. 2019, *MNRAS*, 484, 1220
- Kosovichev, A. G. 1988, *Sov. Astron. Lett.*, 14, 145
- Krishna Swamy, K. S. 1966, *ApJ*, 145, 174
- Lagarde, N., Decressin, T., Charbonnel, C., et al. 2012, *A&A*, 543, A108
- Lagarde, N., Eggenberger, P., Miglio, A., & Montalbán, J. 2014, in *SF2A-2014: Proceedings of the Annual meeting of the French Society of Astronomy and Astrophysics*, eds. J. Ballet, F. Martins, F. Bounaud, R. Monier, & C. Rey, 483
- Lanzafame, A. C., & Spada, F. 2015, *A&A*, 584, A30
- Lebreton, Y., & Maeder, A. 1987, *A&A*, 175, 99
- Lorenzo-Oliveira, D., Meléndez, J., Ponte, G., & Galarza, J. Y. 2020, *MNRAS*, 495, L61
- Maeder, A. 2009, *Physics, Formation and Evolution of Rotating Stars* (Berlin Heidelberg: Springer)
- Maeder, A., & Zahn, J.-P. 1998, *A&A*, 334, 1000
- Marques, J. P., Goupil, M. J., Lebreton, Y., et al. 2013, *A&A*, 549, A74
- Mathis, S. 2013, in *Transport Processes in Stellar Interiors*, eds. M. Goupil, K. Belkacem, C. Neiner, F. Lignières, & J. J. Green, 865, 23
- Mathis, S., & Zahn, J. P. 2004, *A&A*, 425, 229
- Mathis, S., & Zahn, J. P. 2005, *A&A*, 440, 653
- Mathis, S., Palacios, A., & Zahn, J. P. 2004, *A&A*, 425, 243

- Mathis, S., Prat, V., Amard, L., et al. 2018, *A&A*, 620, A22
- Mathur, S., Eff-Darwich, A., García, R. A., & Turck-Chièze, S. 2008, *A&A*, 484, 517
- Matt, S. P., Brun, A. S., Baraffe, I., Bouvier, J., & Chabrier, G. 2015, *ApJ*, 799, L23
- Matt, S. P., Brun, A. S., Baraffe, I., Bouvier, J., & Chabrier, G. 2019, *ApJ*, 870, L27
- McDonald, I., & Zijlstra, A. A. 2015, *MNRAS*, 448, 502
- McQuillan, A., Mazeh, T., & Aigrain, S. 2014, *ApJS*, 211, 24
- Meléndez, J., & Ramírez, I. 2007, *ApJ*, 669, L89
- Meynet, G., Ekstrom, S., Maeder, A., et al. 2013, in *Models of Rotating Massive Stars: Impacts of Various Prescriptions*, eds. M. Goupil, K. Belkacem, C. Neiner, et al., 865, 3
- Michaud, G., Alecian, G., & Richer, J. 2015, *Atomic Diffusion in Stars* (Switzerland: Springer International Publishing)
- Montalban, J. 1994, *A&A*, 281, 421
- Montalban, J., & Schatzman, E. 1996, *A&A*, 305, 513
- Montalbán, J., & Schatzman, E. 2000, *A&A*, 354, 943
- Montalbán, J., & Rebolo, R. 2002, *A&A*, 386, 1039
- Morel, P., van't Veer, C., Provost, J., et al. 1994, *A&A*, 286, 91
- Mosser, B., Goupil, M. J., Belkacem, K., et al. 2012, *A&A*, 548, A10
- Netopil, M., Paunzen, E., Heiter, U., & Soubiran, C. 2016, *A&A*, 585, A150
- Nielsen, M. B., Gizon, L., Schunker, H., & Schou, J. 2014, *A&A*, 568, L12
- Palacios, A., Charbonnel, C., Talon, S., & Siess, L. 2006, *A&A*, 453, 261
- Paquette, C., Pelletier, C., Fontaine, G., & Michaud, G. 1986, *ApJS*, 61, 177
- Park, J., Prat, V., & Mathis, S. 2020, *A&A*, 635, A133
- Piau, L., & Turck-Chièze, S. 2002, *ApJ*, 566, 419
- Pietrinferni, A., Cassisi, S., Salaris, M., & Hidalgo, S. 2013, *A&A*, 558, A46
- Pinçon, C., Belkacem, K., Goupil, M. J., & Marques, J. P. 2017, *A&A*, 605, A31
- Pinsonneault, M. H., Kawaler, S. D., Sofia, S., & Demarque, P. 1989, *ApJ*, 338, 424
- Pinsonneault, M. H., Kawaler, S. D., & Demarque, P. 1990, *ApJS*, 74, 501
- Pols, O. R., Tout, C. A., Eggleton, P. P., & Han, Z. 1995, *MNRAS*, 274, 964
- Prat, V., & Lignières, F. 2013, *A&A*, 551, L3
- Prat, V., & Lignières, F. 2014, *A&A*, 566, A110
- Prat, V., Guilet, J., Viallet, M., & Müller, E. 2016, *A&A*, 592, A59
- Pratt, J., Baraffe, I., Goffrey, T., et al. 2017, *A&A*, 604, A125
- Proffitt, C. R., & Michaud, G. 1991, *ApJ*, 380, 238
- Reimers, D. 1975, *Mem. Soc. R. Sci. Liege*, 8, 369
- Richard, O., Vauclair, S., Charbonnel, C., & Dziembowski, W. A. 1996, *A&A*, 312, 1000
- Richer, J., Michaud, G., Rogers, F., et al. 1998, *ApJ*, 492, 833
- Richer, J., Michaud, G., & Turcotte, S. 2000, *ApJ*, 529, 338
- Richard, O., Michaud, G., Richer, J., et al. 2002, *ApJ*, 568, 979
- Richard, O., Michaud, G., & Richer, J. 2005, *ApJ*, 619, 538
- Rüdiger, G., Gellert, M., Spada, F., & Tereshin, I. 2015, *A&A*, 573, A80
- Saar, S. H. 2009, in *Solar-Stellar Dynamos as Revealed by Helio- and Asteroseismology: GONG 2008/SOHO 21*, eds. M. Dikpati, T. Arentoft, I. González Hernández, C. Lindsey, & F. Hill, *ASP Conf. Ser.*, 416, 375
- Schatzman, E. 1993, *A&A*, 279, 431
- Scherrer, P. H., Bogart, R. S., Bush, R. I., et al. 1995, *Sol. Phys.*, 162, 129
- Schlattl, H. 2002, *A&A*, 395, 85
- Schlattl, H., & Weiss, A. 1999, *A&A*, 347, 272
- Schwarzschild, M., Howard, R., & Härm, R. 1957, *ApJ*, 125, 233
- Sestito, P., & Randich, S. 2005, *A&A*, 442, 615
- Siess, L., Dufour, E., & Forestini, M. 2000, *A&A*, 358, 593
- Skumanich, A. 1972, *ApJ*, 171, 565
- Smiljanic, R., Randich, S., & Pasquini, L. 2011, *A&A*, 535, A75
- Soderblom, D. R., Jones, B. F., Balachandran, S., et al. 1993, *AJ*, 106, 1059
- Spada, F., & Lanzafame, A. C. 2020, *A&A*, 636, A76
- Spada, F., Gellert, M., Arlt, R., & Deheuvels, S. 2016, *A&A*, 589, A23
- Spiegel, E. A., & Zahn, J. P. 1992, *A&A*, 265, 106
- Spite, F., & Spite, M. 1982, *A&A*, 115, 357
- Spruit, H. C. 2002, *A&A*, 381, 923
- Stauffer, J. B., & Hartmann, L. W. 1986, *PASP*, 98, 1233
- Takeda, Y., Kawanomoto, S., Honda, S., Ando, H., & Sakurai, T. 2007, *A&A*, 468, 663
- Takeda, Y., Honda, S., Kawanomoto, S., Ando, H., & Sakurai, T. 2010, *A&A*, 515, A93
- Talon, S., & Zahn, J. P. 1997, *A&A*, 317, 749
- Talon, S., & Charbonnel, C. 2003, *A&A*, 405, 1025
- Talon, S., & Charbonnel, C. 2005, *A&A*, 440, 981
- Talon, S., & Charbonnel, C. 2010, in *Light Elements in the Universe*, eds. C. Charbonnel, M. Tosi, F. Primas, & C. Chiappini, *IAU Symp.*, 268, 365
- Talon, S., Kumar, P., & Zahn, J.-P. 2002, *ApJ*, 574, L175
- Talon, S., Richard, O., & Michaud, G. 2006, *ApJ*, 645, 634
- Thévenin, F., Oreshina, A. V., Baturin, V. A., et al. 2017, *A&A*, 598, A64
- Thompson, M. J., Christensen-Dalsgaard, J., Miesch, M. S., & Toomre, J. 2003, *ARA&A*, 41, 599
- Thoul, A. A., Bahcall, J. N., & Loeb, A. 1994, *ApJ*, 421, 828
- Turcotte, S., Richer, J., Michaud, G., Iglesias, C. A., & Rogers, F. J. 1998, *ApJ*, 504, 539
- Vauclair, S. 1988, *ApJ*, 335, 971
- Vauclair, S. 2013, in *EAS Pub. Ser.*, eds. G. Alecian, Y. Lebreton, O. Richard, & G. Vauclair, 63, 233
- Vauclair, S., Vauclair, G., Schatzman, E., & Michaud, G. 1978, *ApJ*, 223, 567
- Waite, I. A., Marsden, S. C., Carter, B. D., et al. 2017, *MNRAS*, 465, 2076
- Wallerstein, G., & Conti, P. S. 1969, *ARA&A*, 7, 99
- Xing, L. F., & Xing, Q. F. 2012, *A&A*, 537, A91
- Xu, Y., Goriely, S., Jorissen, A., Chen, G. L., & Arnould, M. 2013a, *A&A*, 549, A106
- Xu, Y., Takahashi, K., Goriely, S., et al. 2013b, *Nucl. Phys. A*, 918, 61
- Young, P. R. 2018, *ApJ*, 855, 15
- Zahn, J. P. 1991, *A&A*, 252, 179
- Zahn, J. P. 1992, *A&A*, 265, 115
- Zhang, Q.-S., Li, Y., & Christensen-Dalsgaard, J. 2019, *ApJ*, 881, 103
- Ziegler, U., & Rüdiger, G. 2003, *A&A*, 401, 433

T. Dumont et al.: Lithium depletion and angular momentum transport in solar-type stars

Appendix A: Model convention

In order to simplify the notations, we used the following convention to identify the models:

$R_{\text{type}}^{\text{Rot}_{\text{ini}}} M_{\text{type}} X_{\text{Oversh}}^{\text{Turb}}$

where we defined

- Model type (M_{type})
 - . Classical model (C)
 - . Rotational model (R)
- Dh/Dv prescription/adjusted K parameter (X)
 - . Dh = Mathis et al. (2018)/Dv = Zahn (1992)/
 $K = 7.5 \times 10^{30}$ erg (1)
 - . Dh = Zahn (1992)/Dv = Talon & Zahn (1997)/
 $K = 7.5 \times 10^{30}$ erg (2)
 - . Dh = Zahn (1992)/Dv = Talon & Zahn (1997)/
 $K = 3 \times 10^{30}$ erg (2')
 - . Dh = Zahn (1992)/Dv = Talon & Zahn (1997)/
 $K = 4.5 \times 10^{30}$ erg (2'')
 - . Dh = Mathis et al. (2004)/Dv = Zahn (1992)/
 $K = 7.5 \times 10^{30}$ erg (3)

Initial rotation velocity (Rot_{ini})

- . Slow (S)
- . Median (none = default)
- . Fast (F)

Rotation type (R_{type}) – All rotation models include meridional circulation and shear turbulence

- . Impose solid rotation (solid)
- . Addition of a viscosity ν_{add} (ν)
- . Addition of the viscosity ν_{add} advised by Spada et al. (2016) for the Sun (ν_{spada})
- . Addition of the time-dependent viscosity $\nu_{\text{add}}(t)$ according to Spada et al. (2016) ($\nu_{\text{spada}}(t)$ and $\nu_{2.\text{spada}}(t)$)

Turbulence mixing (Turb)

- . Turbulence fixed at temperature T0 (T6.425)
- . Turbulence fixed at the base of the convection zone (PM5000)
- . Tachocline turbulence (Tach)

Overshoot (Oversh)

- . Overshoot from Baraffe et al. (2017) (B)
- . Overshoot from Augustson & Mathis (2019) (A)
- . Overshoot from Korre et al. (2019) (K).

Appendix B: Prescriptions for turbulent viscosities

B.1. Vertical turbulent viscosities

In the framework of the shellular rotation hypothesis and assuming strong anisotropic turbulence, Zahn (1992) proposed defining D_v as

$$D_v = \frac{\text{Ri}_c}{3} \kappa_T \left(\frac{r \sin \theta}{N_T} \frac{d\Omega}{dr} \right)^2, \quad (\text{B.1})$$

with Ri_c the critical Richardson number ($= 1/4$) beyond which the initial instability exists, κ_T the thermal diffusivity, θ a spherical coordinate, and N_T the thermal term of the Brunt-Väisälä frequency.

Talon & Zahn (1997) developed another version of D_v that considers the effect of thermal and chemical stratifications. The Richardson criterion was then modified; it now involves N_μ , the chemical term of the Brunt-Väisälä frequency. The coefficient D_v is defined as

$$D_v = \frac{1}{4} \text{Ri}_c \left(\frac{N_T^2}{K_T + D_h} + \frac{N_\mu^2}{D_h} \right)^{-1} \left(r \sin \theta \frac{d\Omega}{dr} \right)^2, \quad (\text{B.2})$$

where $N^2 = N_T^2 + N_\mu^2$ is the Brunt-Väisälä frequency.

B.2. Horizontal turbulent viscosities

Zahn (1992) defined D_h as

$$D_h = \frac{1}{c_h} r |2V_2 - \alpha U_2|, \quad (\text{B.3})$$

with $\alpha = \frac{1}{2} \frac{d \ln(r^2 \Omega)}{d \ln r}$ the shear rate ($\alpha = 1$ means uniform rotation), V_2 the latitudinal component, and U_2 the radial component of the meridional circulation developed to the second order:

$$V_2 = \frac{1}{6\rho} \frac{d(\rho r^2 U_2)}{dr}, \quad (\text{B.4})$$

$$U_2 = \frac{5}{\rho r^4 \Omega} \left(\Gamma(m) - \rho \nu_v r^4 \frac{d\Omega}{dr} \right). \quad (\text{B.5})$$

Here $\Gamma(m)$ refers to the gain or loss of angular momentum in the isobar enclosing $m(r)$.

Mathis et al. (2004) defined D_h as

$$D_h = \left(\frac{\beta}{10} \right)^{1/2} (r^2 \Omega)^{1/2} [r |2V_2 - \alpha U_2|]^{1/2}, \quad (\text{B.6})$$

where β is a parameter close to 1.5×10^{-5} .

Mathis et al. (2018) accounted for the fact that horizontal turbulence is generated from both horizontal and vertical shears. The coefficient D_h then writes as $D_h = D_{h,h} + D_{h,v}$. The first index means the direction of the transport and the second index refers to the shear that generates the transport. This additional transport ($D_{h,v}$) is active only if the vertical shear does not fulfil the Reynolds criterion ($R_e > R_{e,c}$ with $R_{e,c} = 7\nu_m$ with ν_m the molecular viscosity):

$$D_{h,h} = \left(\frac{\beta}{10} \right)^{1/2} (r^2 \Omega)^{1/2} [r |2V_2 - \alpha U_2|]^{1/2}, \quad (\text{B.7})$$

$$D_{h,v} = \begin{cases} \frac{\tau^2 N^4}{2\Omega^2} D_{v,v} & \text{if } R_e > R_{e,c} \\ 0 & \text{if } R_e < R_{e,c} \end{cases}. \quad (\text{B.8})$$

Here $D_{v,v} \equiv D_v$ from Eq. (B.1), and τ is a characteristic timescale for the turbulence, taken to be equal to the time characterising the radial shear, $\tau = 1/S$, where $S = r \sin \theta \frac{d\Omega}{dr}$, as in Amard et al. (2019).

Lithium depletion and angular momentum transport in F-type and G-type stars in Galactic open clusters

In Chapter 8, we studied the Li-depletion exhibited by the solar-type stars along their evolution and determined an optimal model to reproduce both the observational constraints from surface Li abundance and rotation. In the present Chapter, we aim to extend our study to a larger range of masses from $0.8 M_{\odot}$ to $1.5 M_{\odot}$ for which we have access to surface abundances and surface rotation velocities (see Chapter 1). This range of mass includes stars in the so-called Li-dip, as well as stars on the cold-side of the dip that exhibit a Li-depletion with decreasing mass.

In this Chapter, we present the results obtained by confronting the observational data described in Chapter 1 to models including the optimal combinations of dynamical processes that transport chemicals and angular momentum determined in Chapter 8.

9.1 Dumont et al. 2021 (A&A, revised)

In Dumont et al. 2021 (A&A, revised), we use the optimal model from Dumont et al. (2021) and including transport processes of chemicals and angular momentum (namely, rotation, penetrative convection, parametric turbulence, parametric viscosity, and atomic diffusion) that were tested with respect to Li abundances and surface and internal rotation constraints for solar-type stars. We now apply the prescriptions that were identified to be the most relevant to a broader range in mass and metallicity.

We showed that the optimal model developed for solar-type stars is able to reproduce the cold side of the Li-dip for each cluster, independently of age and metallicity. A metallicity effect is highlighted and we predict a higher depletion at high metallicity than at low metallicity. However, our models are in less good agreement with metal-poor observational data that are more Li-depleted than predicted and would argue for a metal-dependence of the transport processes. Over the entire range of masses, metallicities, and ages explored, we reproduce the evolution of the surface rotation rates, and predict for the first time the observed anticorrelation between surface rotation rate and Li-depletion as a consequence of the penetrative convection prescription. Besides, the model predicts internal rotation profiles in good agreement with asteroseismic constraints in main sequence stars. However, we cannot reproduce the Li-dip observed in few open clusters with the same model because of a too weak depletion of Li for $M > 1.2M_{\odot}$. The Li-dip can only be reproduced considering a different prescription for the shear turbulent mixing and a mass depen-

dent parametric viscosity ν_{add} to transport angular momentum. It is thus mandatory to have a clear theoretical discrimination between the different prescriptions currently available to account for the turbulent shear transport. It also calls for a new exploration of physical processes such as tachocline mixing for the transport of chemicals and internal gravity waves for the transport of angular momentum. Finally, we highlight the key constraint of Beryllium, which also exhibits a dip, correlated with Li. It provides additional and complementary constraints for the missing transport processes involved. We show that with the few data available, it is presently challenging to reconcile simultaneously the Li-dip and the Be-dip. It highlights the need of additional data for the beryllium abundance in main sequence F- and G-type stars of different ages and metallicities.

Lithium depletion and angular momentum transport in F-type and G-type stars in Galactic open clusters

T. Dumont^{1,2,*}, C. Charbonnel^{1,3}, A. Palacios², and S. Borisov^{1,4}

¹ Department of Astronomy, University of Geneva, Chemin Pegasi 51, 1290 Versoix, Switzerland

² LUPM, Université de Montpellier, CNRS, Place Eugène Bataillon, 34095 Montpellier, France

³ IRAP, CNRS UMR 5277 & Université de Toulouse, 14 avenue Edouard Belin, 31400 Toulouse, France

⁴ Sternberg Astronomical Institute, M.V. Lomonosov Moscow State University, Universitetsky prospect 13, Moscow, 119234, Russia

Accepted 14 July 2021

ABSTRACT

Context. Open clusters provide unambiguous clues to understand the evolution of ${}^7\text{Li}$ at the surface of low-mass stars and its possible correlation with stellar rotation, which is a challenge for both stellar hydrodynamics and Galactic chemical evolution.

Aims. We aim at quantifying the efficiency of the transport processes for both angular momentum and chemicals that are required to explain simultaneously the observed behaviour of surface ${}^7\text{Li}$ (and ${}^9\text{Be}$) and rotation as well as the internal rotation profiles inferred from helio- and asteroseismology in F- and G-type main sequence stars.

Methods. We apply the model for the transport of angular momentum and chemicals that we tailored in a previous work for solar-type stars to an extended range of initial masses and metallicities corresponding to F- and G-type stars in a sample of 20 Galactic open clusters. We evaluate its ability to explain the ${}^7\text{Li}$, ${}^9\text{Be}$, and rotation periods observations. This model includes atomic diffusion, rotation-induced processes (for which we test different prescriptions for shear turbulence), penetrative convection with a rotational dependence, parametric viscosity and turbulence, and magnetic braking.

Results. Over the entire range of masses, metallicities, and ages explored, we reproduce the evolution of the surface rotation rates, and predict for the first time the observed anticorrelation between surface rotation rate and ${}^7\text{Li}$ depletion as a consequence of the penetrative convection prescription. The ${}^7\text{Li}$ behaviour and its evolution with time is well reproduced for G-type stars. However, the ability of the model to reproduce the so-called ${}^7\text{Li}$ -dip centered around ~ 6600 K strongly depends on the adopted prescriptions for shear turbulence. It also requires a stellar mass dependence for the parametric viscosity adopted for the transport of angular momentum, similar to the behaviour predicted for the generation and luminosity of internal gravity waves generated by stellar convective envelopes. Finally, the model predicts internal rotation profiles in good agreement with asteroseismic constraints in main sequence stars.

Conclusions. We provide an efficient way to model successfully G-type stars of different ages and metallicities. However, the ${}^7\text{Li}$ and ${}^9\text{Be}$ dips constraints urgently call for further hydrodynamical studies to better model turbulence in stars, and for the exploration of physical processes such as tachocline mixing for the transport of chemicals and internal gravity waves for the transport of angular momentum. Finally, additional data for the internal rotation and for ${}^9\text{Be}$ in main sequence low-mass stars are definitively needed.

Key words. Stars: abundances – Stars: rotation – Stars: evolution – Stars: low-mass – open clusters and associations: general

1. Introduction

Understanding the evolution of ${}^7\text{Li}$ (hereafter Li) in low-mass stars is one of the main challenges for stellar and Galactic astrophysics. Despite Li being a very scarce element, it is a tracer of Galactic chemical evolution (e.g. Spite & Spite 1982; Matteucci et al. 1995; Romano et al. 2001; Travaglio et al. 2001; Prantzos 2012) and of transport processes that occur in stellar interiors (e.g. Charbonneau & Michaud 1990; Montalbán & Schatzman 1996; Montalbán & Schatzman 2000; Charbonnel & Talon 2005; Talon & Charbonnel 2010; Castro et al. 2016; Dumont et al. 2021, hereafter Paper I, and references therein). An overall picture of the different possibly involved processes is described in the reviews by Mathis (2013) and Aerts et al. (2019).

Observations of open clusters have provided numerous Li abundance data for stars of different ages over a large range of masses and metallicities (e.g. Boesgaard 1976; Duncan & Jones 1983; Cayrel et al. 1984; Balachandran et al. 1988, 2011; Soderblom et al. 1990, 1993b; Boesgaard 1991; Thorburn et al.

1993; Garcia Lopez et al. 1994; Swenson et al. 1994; Jones et al. 1999; Boesgaard et al. 2003a,b; Sestito & Randich 2005; Anthony-Twarog et al. 2009, 2018; Cummings et al. 2012, 2017; Deliyannis et al. 2019; Randich et al. 2020). Li depletion has clearly been evidenced to increase with time and to be linked to the stellar mass (e.g. Deliyannis et al. 2000, for a review). At a given age, the Li behaviour as a function of stellar effective temperature (T_{eff}) shows two specific patterns. On one hand, photospheric Li abundances of G-type stars decrease with decreasing effective temperature (decreasing mass). On the other hand, a group of F-type stars with T_{eff} centered around 6600 K fall into the so-called Li-dip which appears in open clusters older than ~ 200 Myrs (e.g. Wallerstein et al. 1965; Boesgaard & Tripicco 1986; Hobbs & Pilachowski 1986; Soderblom et al. 1993a; Balachandran 1995; Steinhauer & Deliyannis 2004; Boesgaard et al. 2016).

Classical stellar evolution (accounting only for convection as a mixing process in stellar interiors) predicts noticeable Li-depletion during the pre-main sequence (PMS) when the base of the convective envelope is deep enough to reach the Li-burning temperature, which happens only for the less massive stars (i.e.,

* e-mail: thibaut.dumont@unige.ch

below $\sim 0.9 - 1.0 M_{\odot}$ at solar metallicity; e.g. Bodenheimer 1965; Pinsonneault 1997). However, it does not predict any further surface Li variation until the first dredge-up occurs after the stars leave the main sequence (MS), in striking contrast with the observational evidence of the steepening along the main sequence of the Li- T_{eff} trend of the cool side of the Li-dip and of the Li-dip itself.

The key role of rotation was pointed out as the cool edge of the Li-dip coincides with the so-called Kraft rotation break as observed for instance in the Hyades (Boesgaard 1987) and in NGC 752 (Hobbs & Pilachowski 1986). The Kraft break (Kraft 1967) corresponds to the transition stellar mass ($\simeq 1.2 M_{\odot}$ at solar metallicity) where important structural changes occur in main sequence star. In particular, stars more massive than the transition value have extremely thin convective envelope, implying weaker, or ineffective, magnetic braking compared to cooler, less massive stars with thick convective envelope that can sustain efficient stellar wind magnetic braking (e.g. Schatzman 1962; Weber & Davis 1967; Matt et al. 2015; Kawaler 1988; Cummings et al. 2017; Deliyannis et al. 2019). The cool side of the dip corresponds also to the transition region where the convective envelope can efficiently generate internal gravity waves that transport angular momentum (Talon & Charbonnel 2003, 2004, 2005), and to an internal structure where the stellar core is radiative while hotter MS stars host a convective core.

Different non-standard mixing-processes (beyond convection) have been explored to explain the observed Li features in F-type and G-type stars: convective overshooting or penetrative convection (Schlattl & Weiss 1999; Brun et al. 2017; Baraffe et al. 2017; Jørgensen & Weiss 2018, Paper I), atomic diffusion (Michaud 1986; Richer & Michaud 1993; Turcotte et al. 1998), mass loss (Guzik & Mussack 2010), planet accretion or migration (Montalbán & Rebolo 2002; Castro et al. 2009), tachocline mixing (Brun et al. 1999, Paper I), internal gravity waves (Montalbán 1994), rotation-induced mixing (Pinsonneault et al. 1990; Charbonnel et al. 1992; Palacios et al. 2003; Eggenberger et al. 2012a; Somers & Pinsonneault 2016; Amard et al. 2016; Zhang et al. 2019), magnetic processes and instabilities (Charbonneau & MacGregor 1993; Ruediger & Kitchatinov 1996; Eggenberger et al. 2005, 2010), as well as different combinations of some of the above mentioned processes where the transports of chemicals and angular momentum are intimately coupled (Richard et al. 1996; Charbonnel & Talon 2005; Talon & Charbonnel 2005; Deal et al. 2020; Semenova et al. 2020, Paper I).

Importantly, Li appears to be only one piece of a bigger puzzle that should also include the constraints from ^9Be (hereafter Be) that burns at a slightly higher temperature than Li (~ 3.5 MK and 2.5 MK, respectively; e.g. Pinsonneault 1997). Indeed, while the Be-dip coincides with the Li-dip (e.g. Deliyannis et al. 1998; Boesgaard et al. 2001, 2004b, 2020), Be is hardly depleted in the Sun, solar-like stars, and G-type stars (Balachandran & Bell 1998; Boesgaard et al. 2003a,b, 2004a, 2016, 2020). The Be behaviour thus brings additional constraints on the possible origin of the observed behaviour of Li in F- and G-type stars and on the depth of the required mixing process. Last but not least, the difficulty is to find the actual connection between the transport of chemicals and the transport of angular momentum at play in stars of different spectral types along their evolution, to account simultaneously for the internal rotation profiles that can be deduced for the Sun and for some other stars thanks to asteroseismology (Kosovichev 1988; Elsworth et al. 1995; Mathur et al. 2008; Eff-Darwich et al. 2008; Marques et al. 2013; Benomar et al. 2015; Eggenberger et al. 2019a; García & Ballot 2019).

In this work, we explore the chemical and rotational evolution of low-mass stars on the PMS and the MS for different stellar masses and metallicities that cover the range of Galactic open clusters with ages between 5 Myrs and 4 Gyrs. We study the effects and the relevance for these stars of different transport processes that we already explored and validated for the specific case of the solar-type stars (Paper I), and that depend on both mass and metallicity. In Sect. 2, we present the observational data that we use to constrain model predictions. In Sect. 3 we describe the input physics of the stellar models and the different processes implemented in the evolution code STAREVOL used for this work. In Sect. 4, we compare the observations for the Hyades and Praesepe open clusters with the predictions for Li, Be, and surface rotation of our non-standard model including meridional circulation, shear induced turbulence, atomic diffusion, overshoot, and parametric viscosity and turbulence. In Sect. 5, we compare the model predictions with Li and rotational periods (P_{rot}) data in a sample of open clusters over a broad range in age and metallicity. In Sect. 6, we discuss model predictions for the internal rotation and compare to asteroseismic measurements. We summarise our results and conclude in Sect. 7.

2. Observational data

We use observational data for a sample of Galactic open clusters. Their names, ages, metallicities, distances to the Galactic centre are given in Table 1 along with bibliographical references from which the Li and Be surface abundances and rotation periods of individual stars were taken. We only take into account non-binary stars with confirmed membership as mentioned or flagged in the reference papers cited in Table 1.

2.1. Lithium and Beryllium abundances

In this work, we consider Li spectroscopic data for a sample of 14 open clusters (see Tab. 1) with $[\text{Fe}/\text{H}]$ values between -0.38 and $+0.16$ dex, and ages between 35 Myrs and 4 Gyrs : IC 2602, IC 2391, Pleiades, α Persei (α Per), M 35, M 50, Coma Berenices (Coma Ber), Ursa Major (UMa), Hyades, NGC 6633, Praesepe, NGC 6819, NGC 2420, M 67 and NGC 2243. We adopt the meteoritic abundance $A(\text{Li}) = 3.31^1$ (Asplund et al. 2009) as the original abundance of lithium.

All the original papers give 1-D LTE Li abundances, except Jeffries et al. (2002), where they give NLTE Li abundances for NGC 6633 stars. As lithium abundances are known to be sensitive to non-LTE effects, we compute the 3-D NLTE corrections (Δ_{NLTE}) to all the 1-D LTE lithium abundances using the code `Breidablik`² by Wang et al. (2021)³. To do so, we use for each star the $[\text{Fe}/\text{H}]$, T_{eff} , and $\log g$ values given in the original papers also providing the lithium abundances (see Tab. 1). In the specific case of the Pleiades, Bouvier et al. (2018) do not give the surface gravity. We thus adopt $\log g = 4.4$ for its stars, which appears to describe well the typical surface gravity of F and G dwarfs⁴. The absolute values of NLTE corrections rarely exceed

¹ $A(X) = \log_{10}(N_X/N_H) + 12$, where N_X is the number density of element X.

² <https://github.com/ellawang44/Breidablik>

³ In the case of the NGC 6633 stars from Jeffries et al. (2002), we first reverse their NLTE correction using the code of Carlsson et al. (1994) to obtain the 1-D LTE abundances and then compute the same 3-D NLTE corrections as for the other data.

⁴ Δ_{NLTE} depends weakly on $\log g$ for most of the studied temperature range. For instance, for $T_{\text{eff}}=6'000$ K, $A(\text{Li})=2.5$ and $[\text{Fe}/\text{H}]=0$,

Table 1. Main properties of the open clusters considered in this work, with the corresponding references for the Li and Be abundances and the rotation periods.

Name	Age (Myrs)	Ref Age	[Fe/H]	Distance (kpc)	Ref Li	Ref Be	Ref P_{rot}
NGC 2362	5	I	0.00	9.11	-	-	a
NGC 2547	35	I	-0.14±0.10	8.39	-	-	b
IC 2602	35	II	-0.02±0.02	8.29	1	-	-
IC 2391	36	II	-0.03±0.02	8.34	1	-	c
Pleiades (Melotte 22)	87	II	-0.01±0.05	8.45	2	-	b;d
α Per (Melotte 20)	87	II	+0.14±0.11	8.48	3;4	-	c
M 35 (NGC 2168)	150	I	-0.17±0.01	9.24	5;6	-	e
M 50 (NGC 2323)	150	I	0.00*	9.10	-	-	b;f
NGC 2516	150	I	-0.06±0.05	8.32	-	-	b
M 37 (NGC 2099)	500	I	+0.02±0.05	9.77	-	-	b;g
Coma Ber (Melotte 111)	570	III	0.00±0.08	8.35	7	-	-
UMa	600	IV	-0.09*	8.37*	7	-	-
Hyades (Melotte 25)	720	III	+0.13±0.05	8.38	8	9	h;i
NGC 6633	770	II	-0.08±0.12	8.00	10;11	-	-
Praesepe (NGC 2632)	750	II	+0.16±0.08	8.48	8	12	b;j;k;l
NGC 6811	950	I	+0.03±0.01	8.20	-	-	b;m
NGC 6819	2000	II	+0.09±0.01	8.03	13	-	n
NGC 2420	2500	V	-0.05±0.02	10.68	14	-	-
M 67 (NGC 2682)	3640	II	-0.01±0.04	8.96	15	-	-
NGC 2243	4000	VI	-0.38±0.04	10.58	16	-	-

Notes.

The [Fe/H] values are from Netopil et al. (2016) and Gutiérrez Albarrán et al. (2020), except for UMa (Boesgaard et al. 2003a) and M 50 (Douglas et al. 2016). Distances to the Galactic centre are from Cantat-Gaudin et al. (2020), except for UMa (Ujjwal et al. 2020) and are based on the Gaia DR2 measurements.

I: Godoy-Rivera et al. (2021); II: Bossini et al. (2019), III: Netopil et al. (2016); IV: Boesgaard et al. (2003a); V: Semenova et al. (2020); VI: Gutiérrez Albarrán et al. (2020). 1: Randich et al. (2001); 2: Bouvier et al. (2018); 3: Boesgaard et al. (2003b); 4: Balachandran et al. (2011); 5: Barrado y Navascués et al. (2001); 6: Jeffries et al. (2021); 7: Boesgaard et al. (2003a); 8: Cummings et al. (2017); 9: Boesgaard et al. (2016); 10: Jeffries (1997); 11: Jeffries et al. (2002); 12: Boesgaard et al. (2004a); 13: Deliyannis et al. (2019); 14: Semenova et al. (2020); 15: Pace et al. (2012); 16: François et al. (2013). a: Irwin et al. (2008); b: Godoy-Rivera et al. (2021); c: Irwin & Bouvier (2009); d: Hartman et al. (2010); e: Meibom et al. (2009); f: Irwin et al. (2009); g: Hartman et al. (2008); h: Delorme et al. (2011); i: Douglas et al. (2016); j: Agüeros et al. (2011); k: Douglas et al. (2017); l: Douglas et al. (2019); m: Meibom et al. (2011); n: Meibom et al. (2015)

• [Fe/H] from Douglas et al. (2016)

★ [Fe/H] from Boesgaard et al. (2003a)

* Distance to the Galactic centre from Ujjwal et al. (2020), assuming the Sun is at a distance of 8.34 kpc from the galactic centre (Cantat-Gaudin et al. 2020)

0.1 dex, we consequently do not expect a significant impact on the results.

We also use as an additional constraint the Be spectroscopic data for the Hyades and Praesepe from Boesgaard et al. (2004a) and Boesgaard et al. (2016). Observations are directly extracted from Boesgaard et al. (2004a, 2016) without any modification. We adopt the meteoritic abundance $A(^9\text{Be}) = 1.41$ (Asplund et al. 2009) as the original abundance of beryllium.

2.2. Age

There is no self-consistent determination in the literature of the ages of all the clusters we consider here, and this task is out of the scope of this work. To be consistent with Paper I, we use the ages from Bossini et al. (2019, when available) for the clusters with Li abundance measurements. For the clusters with rotation period measurements, we use the ages from Godoy-Rivera et al. (2021, when available). For the five clusters with Li data that

$\Delta_{\text{NLTE}}(\log g=4.4) - \Delta_{\text{NLTE}}(\log g=4.0) = -0.0135$ dex, which is negligible. However, for $T_{\text{eff}} \approx 3'900$ K to $4'500$ K this difference is more significant and reaches values of about +0.08 dex. In our sample, only 17 out of the 92 stars of Pleiades are in this temperature range, therefore this should not have a significant impact on the result.

were not studied in these two works, we take the ages quoted in the respective observation papers (see Table 2). Except for the Pleiades, the differences in age determinations from the literature is weakly affecting our conclusions (see discussion in Sect. 5.1).

2.3. Effective temperature T_{eff}

The effective temperatures used in this study are taken from the same original sources as the lithium (or beryllium) abundances for consistency (see Tab. 1). In rare cases, spectroscopic T_{eff} are available (this is the case of M67 and NGC 2420). In most cases, T_{eff} are determined using colour-temperature calibration relations from (B-V), (V- I_c) or (V-K) colour indices. For the 14 open clusters presented in Table 1, at least 6 different relations / methods are used. These relations differ by their metallicity dependence, the zero-point of their temperature scale, the colours used, etc. The relative consistency between the different calibration relations was tested in several previous studies (Huang et al. 2015; Casagrande et al. 2010; Meléndez et al. 2010). These studies emphasize maximum differences of about 100 K can be found when applying the different temperature scales to dwarf stars in the metallicity and photometric domain considered here. We thus consider that the general agreement between the differ-

ent temperature scales adopted in the original papers that we use in this work is satisfactory.

2.4. Surface and internal rotation

We compare the surface rotation predicted by our models with the observational data set gathered by Irwin & Bouvier (2009), Gallet & Bouvier (2015) and Godoy-Rivera et al. (2021) for low-mass stars among a sample of 12 open clusters with ages between 5 Myrs and 2 Gyrs: NGC 2362, NGC 2547, IC 2391, α Per, Pleiades, M 35, M 50, M 37, Hyades, Praesepe, NGC 6811 and NGC 6819 (see details in Table 1).

We constrain our model predictions for internal rotation using the asteroseismic measurements obtained by Benomar et al. (2015) for a sample of MS field stars observed by *Kepler*. We select a sub-sample of four stars with metallicities close to that of the Hyades.

3. Stellar evolution models – Input micro- and macro-physics

3.1. General assumptions

We follow the conclusions of Paper I on different transport processes of chemicals and angular momentum (namely: rotation, penetrative convection, parametric turbulence, parametric viscosity, and atomic diffusion, as described below) that were tested with respect to Li abundances and surface and internal rotation constraints for solar-type stars. We use the nomenclature described in Paper I. For instance, model $\nu^M R_1^A T_0^{6.42}$ is a model computed with R1 prescription for rotation-induced turbulence and parametric viscosity ($\nu=\nu_{\text{add}}$), penetrative convection (A), parametric turbulence down to $\log T_0 = 6.42$, at median initial rotation velocity (M), and with atomic diffusion. All the details about the corresponding prescriptions for the different processes are given below.

We apply to a broader range of masses and metallicities the prescriptions that were identified to be the most relevant for solar-type stars. Models are computed in the mass range between $0.8 M_{\odot}$ and $1.5 M_{\odot}$ ($\delta M = 0.1 M_{\odot}$) for seven values of [Fe/H] (-0.4, -0.2, -0.1, -0.05, 0, +0.10, +0.15) that cover the metallicity range of the Galactic open clusters described in Table 1. Computations start on the Hayashi track at the beginning of the deuterium burning phase on the PMS that we take as the time zero of the evolution.

3.2. Input physics

We use the same updated version of the stellar evolution code STAREVOL as in Paper I (for general informations and previous versions see Siess et al. 2000; Palacios et al. 2006; Decressin et al. 2009; Lagarde et al. 2012; Amard et al. 2019) to which we refer for details and references. The models presented in this work are computed with the same inputs physics (equation of state, opacities, nuclear reactions, model atmosphere, mass loss). We use the same values for the mixing length parameter (α_{MLT} , assuming the Schwarzschild criteria for convective stability) and the initial abundances that resulted from model calibrations on the Sun that were carried out for classical models (no transport of chemicals beyond convection), and for models including both rotation and atomic diffusion (respectively models C and R1 from Paper I).

Article number, page 4 of 17

3.3. Atomic diffusion, penetrative convection, parametric turbulence

Atomic diffusion is implemented according to Paquette et al. (1986) and Thoul et al. (1994). We do not take into account radiative accelerations. Their impact starts however to be non-negligible for stars with effective temperature higher than $\sim 6'800$ K, which corresponds to $\sim 1.4 M_{\odot}$ at solar metallicity (Richer et al. 1998; Richard et al. 2002; Deal et al. 2018, 2020). This will be discussed in Sect. 7.

Penetrative convection is treated as an overshoot and computed following the formalism of Augustson & Mathis (2019) with the following expression for the diffusion coefficient:

$$D_A(r) \approx D_0 \left[1 - \exp \left(- \exp \left(\frac{r - r_{bcz}}{d_{ov} \times \left(\frac{v}{v_0} \right)^{3/2} + \frac{\mu}{\lambda}} \right) \right) \right], \quad (1)$$

where $D_0 = (u_{\text{conv}} \times H_p \times \alpha_{\text{MLT}})/3$ is the convective turbulent diffusivity (with u_{conv} the mean velocity of the convective elements obtained from MLT, α_{MLT} the mixing length parameter, and H_p the pressure scale height), r is the local radius, r_{bcz} is the radius at the base of the convective zone, (v/v_0) is the ratio of the velocity of the convective elements when taking rotation into account to the non-rotating inviscid value, and $d_{ov} = 0.0325$ (as calibrated by Paper I to reproduce the Li abundance in solar-type stars in very young open clusters). The coefficients $\lambda = 6 \times 10^{-3}$ and $\mu = 5 \times 10^{-3}$ are as prescribed by Baraffe et al. (2017) based on the simulations of Pratt et al. (2017).

Parametric turbulence is defined according to Richer et al. (2000) and Richard et al. (2005) with the following prescription for the diffusion coefficient:

$$D_{T_0} = 400 D_{\text{He}}(T_0) \left[\frac{\rho(T_0)}{\rho} \right]^3, \quad (2)$$

where T_0 is a free parameter that sets the depth of the maximum efficiency of the mixing depending on the value of the atomic diffusion coefficient He (D_{He}). Initially introduced by Richer et al. (2000) to counteract a too strong impact of atomic diffusion in AmFm stars, we introduced it in our models with rotation to increase the surface Li depletion predicted on the MS and reproduce the observations for solar type stars and for the Sun. For all the reference models we adopt $\log T_0 = 6.42$ as calibrated by Paper I. We also present a set of models for the Hyades metallicity ([Fe/H] = + 0.15 dex) where we have increased this depth to $\log T_0 = 6.5$.

3.4. Angular momentum evolution and rotation-induced mixing

Stellar rotation is implemented in STAREVOL as described by Amard et al. (2016, 2019) and Paper I. We adopt the shellular rotation hypothesis developed by Zahn (1992), Maeder & Zahn (1998), and Mathis & Zahn (2004) to describe the transport of angular momentum and chemicals by meridional circulation, treated as an advective process for angular momentum, and turbulent shear (vertical and horizontal), treated as diffusive processes. We follow Eggenberger et al. (2012b, 2019b) and Spada et al. (2016) who introduced an additional parametric vertical viscosity ν_{add} in order to flatten the internal rotation profile as evidenced by helio- and asteroseismology of low-mass stars.

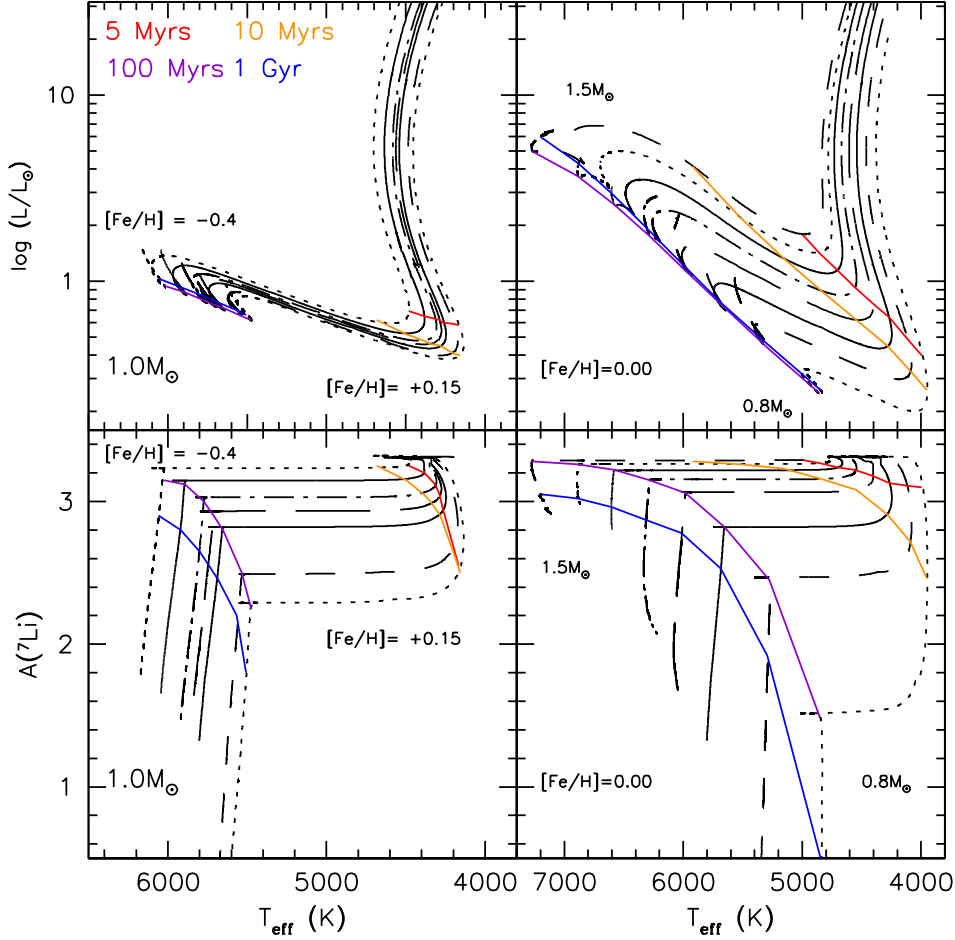


Fig. 1. (Top) Evolutionary tracks in the Hertzsprung-Russell diagram of $^M R1_A^{T6.42}$ models of $1.0M_{\odot}$ computed for seven values of $[\text{Fe}/\text{H}]$ (Left) and of different masses for $[\text{Fe}/\text{H}]=0$ (Right). (Bottom) Surface Li abundance for the corresponding models. The coloured-lines connect points of the same age.

The transport of angular momentum hence obeys the following advection-diffusion equation:

$$\rho \frac{d}{dt}(r^2 \Omega) = \frac{1}{5r^2} \frac{\partial}{\partial r}(\rho r^4 \Omega U_2) + \frac{1}{r^2} \frac{\partial}{\partial r} \left((v_v + v_{\text{add}}) r^4 \frac{\partial \Omega}{\partial r} \right), \quad (3)$$

where ρ , r , Ω , U_2 , and v_v are the density, the radius, the angular velocity, the meridional circulation velocity, and the vertical shellular component of the turbulent viscosity, respectively. For the reference models we adopt $v_{\text{add}} = 3.5 \times 10^4 \text{ cm}^2 \text{ s}^{-1}$ in the entire radiative region. This value was calibrated in Paper I on the solar angular velocity profile provided by helioseismology. We also present a set of models for the Hyades metallicity ($[\text{Fe}/\text{H}] = +0.15$ dex) where we modified this value depending on the initial stellar mass ($v'_{\text{add}} = 3.5 \times 10^5$, 1.0×10^5 , 2.5×10^5 , 6.5×10^5 , and $8.5 \times 10^5 \text{ cm}^2 \text{ s}^{-1}$ for the 1.5, 1.4, 1.35, 1.3, and 1.2 M_{\odot} models respectively). These values are kept constant during the entire evolution.

We explore two combinations of prescriptions for turbulence shear referred to as R1 and R2 as in Paper I. R1 includes pre-

scriptions from Mathis et al. (2018) and Zahn (1992) for the horizontal diffusivity D_h and the vertical diffusivity D_v , respectively. R2 includes prescriptions from Zahn (1992) and Talon & Zahn (1997) for D_h and D_v , respectively. The detailed expressions of the four turbulent diffusion coefficients can be found in Appendix B of Paper I. We use the same parameters as in Paper I for the extraction of angular momentum at the stellar surface due to magnetised winds ($m=0.22$, $p=2.1$, $\chi = 14$, $K = 7.5 \times 10^{30}$ erg unless otherwise indicated) according to Matt et al. (2015) formalism. Models are computed for three values of the initial rotation period on the PMS: 1.6, 4.5 and 9.0 days, which will be referred to as fast ($^F R$), median ($^M R$), and slow ($^S R$) rotating models, respectively. The disc coupling timescale is set at $\tau_{\text{disc}} = 2.5$ Myrs for the fast rotators and at $\tau_{\text{disc}} = 5$ Myrs for the median and the slow rotators, in agreement with Gallet & Bouvier (2015) and Amard et al. (2019).

To summarise, the best models for solar-type stars that we developed in Paper I include the self-consistent treatment of physical processes as well as parametrized additional transports for angular momentum and chemicals as summarised in Tab. 2.

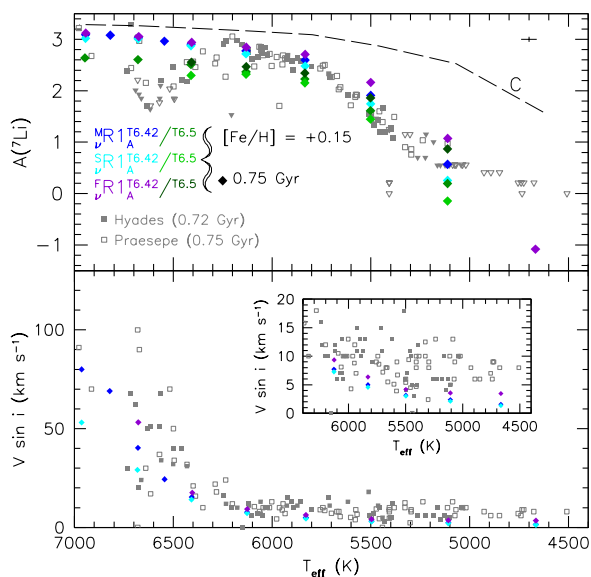


Fig. 2. *Top:* Li surface abundance versus T_{eff} in the Hyades (filled squares) and Praesepe (open squares) from Cummings et al. (2017); downward triangles are for upper limits. Comparison to the predictions at 0.75 Gyr (diamonds) of models with $[\text{Fe}/\text{H}] = +0.15$ computed under several assumptions: classical models (C; dashed black line) and complete models $\nu R1_A^{T_{6.42}}$ (cyan, blue, and violet diamonds for slow, median, and fast initial rotation velocities, respectively) and $\nu R1_A^{T_{6.5}}$ (light green, green, and dark green diamonds for slow, median, and fast initial rotation velocities, respectively). *Bottom:* $V \sin i$ versus T_{eff} in the Hyades (filled squares) and Praesepe (open squares) from Cummings et al. (2017). Comparison to the surface rotation velocity predictions of model $\nu R1_A^{T_{6.42}}$ at 0.75 Gyr. Insert: zoom on the cool side of the Kraft rotation break including model predictions for $0.8\text{--}1.2M_{\odot}$ stars.

The parameters are strongly constrained by observations (see col. 3 Tab. 2) and cannot be varied freely. In the present study, we explore a possible variation of the efficiency of these additional processes with metallicity and initial mass.

4. Model predictions for Li, Be, and surface rotation - The Hyades and Praesepe test case

In this section, we explore the predictions of model $\nu R1_A^{T_{6.42-6.5}}$ over a range of masses and metallicities for three different rotation rates. We recall that this model was developed for the specific case of solar-type stars in Paper I. We discuss the general impact of mass and metallicity on Li depletion, and then we compare the predictions for the behaviour of surface Li, Be, and rotation rates to the observations in the Hyades and Praesepe, and to the predictions of classical models and of model $\nu R2_A^{T_{6.42}}$ computed with different prescriptions for rotation-induced turbulence (see Tab. 3).

4.1. Impact of metallicity and mass on Li evolution

Figure 1 shows the evolutionary tracks in the Hertzsprung-Russell diagram (PMS and MS) and the predicted surface Li abundance as a function of T_{eff} for a selection of models (all computed with median rotation). We see the well-known impact of varying the mass and the metallicity on the evolution tracks,

and the global consequence on Li depletion. When metallicity decreases for a given mass, or when the mass increases for a given metallicity, the model is hotter and brighter. As a consequence, its convective envelope retracts more rapidly at the beginning of the Hayashi track on the PMS, and it is thinner on the MS. Hence, its base is more distant from the layers where Li is burning, which leads to overall lower Li depletion, although the quantitative details depend on the efficiency of the transport process(es) that connect the base of the convective envelope to the Li-free region (see below).

In all the models shown in Fig. 1, Li decreases along two successive episodes, first on the PMS, and later along the MS. The PMS depletion episode is due first to Li burning in the convective envelope at the beginning of the Hayashi track and later to overshoot that are both dependent on the size of the convective envelope and of its timescale for retraction along the PMS. As a consequence, PMS depletion is minute for stars with ZAMS⁵ T_{eff} higher than $\sim 6'500$ K, and it increases with decreasing stellar mass and increasing metallicity.

The MS depletion episode is due to the combined effects of rotation-induced mixing and parametric turbulence. The first process is more efficient in cooler stars (i.e., less massive at a given metallicity, or more metal-rich at a given mass) which undergo more significant extraction of angular momentum by their magnetised winds (see e.g. Fig. 6 in Amard et al. 2019). Similar mass and metallicity dependencies exist in the case of the second process, because in all our models we assume in Eq. (2) the same value for the free parameter T_0 which is closer to the temperature of the base of the convective envelope in less massive or more metal-rich stars. In summary, overall Li depletion is stronger in less massive, more metal-rich stars.

4.2. The Hyades and Praesepe

Here we focus on the well-studied Hyades and Praesepe for which Li, Be, and surface rotation data are available. These two open clusters are close in age (0.72 Gyr and 0.75 Gyr, respectively) and metallicity ($[\text{Fe}/\text{H}] = +0.13 \pm 0.05$ and $+0.16 \pm 0.08$ dex respectively) according to the references quoted in Table 1.

Figure 2 shows the observed Li abundances and rotation velocities ($V \sin i$) as a function of the effective temperature from Cummings et al. (2017). Both clusters exhibit similar patterns, namely the so-called Li-dip between $\sim 6'400$ and $6'800$ K, the Li- T_{eff} decrease in G-type stars on the cool side of the dip, and the well-know break in rotation velocity ($\approx 6'400\text{--}6'500$ K) for dwarf stars later than F4 spectral type (Schatzman 1959, 1962; Kraft 1967; Boesgaard 1987). In the same figure we show the predictions at 0.75 Gyr of the classical models, and of the complete models $\nu R1_A^{T_{6.42}}$ and of $\nu R1_A^{T_{6.5}}$ models computed with $[\text{Fe}/\text{H}] = +0.15$ for three different initial rotation velocities (slow, median, fast) for masses between 0.8 and $1.5 M_{\odot}$ (mass step $0.1 M_{\odot}$), and for median initial rotation velocity for the 1.35 and $1.45 M_{\odot}$ models.

As long known in the literature, and as shown in Fig. 2, classical models (model C) that account solely for convection predict Li-depletion on the PMS only, when the size of the convective envelope is large enough to reach the Li-burning temperatures along the Hayashi track (see Sect. 4.1). While the predicted mass and T_{eff} dependence of the Li abundance after the PMS depletion is similar to the observed pattern for G-type stars, the predicted surface Li abundances are too high compared to the observations

⁵ Zero age main sequence.

Table 2. Transport processes considered in this work.

Process	Quantity	Adjusted parameter	Observational constraints
Atomic diffusion	C	–	–
Meridional circulation	C & AM	–	–
Shear-induced turbulence (R1 or R2)	C & AM	–	–
Magnetic torque	AM	$K = 7.5 \times 10^{30}$ erg	Surface rotation of solar-type stars
Penetrative convection	C	$d_{ov} = 0.0325$	Surface Li abundance of young solar-type stars
Parametric turbulence	C	$\log T = 6.42$	Surface Li abundance of MS solar-type stars
Vertical viscosity	AM	$\nu_{\text{add}} = 3.5 \times 10^4 \text{ cm}^2 \text{ s}^{-1}$	Solar rotation profile

Notes.

Transport processes (Column 1), and values of the free parameters (when relevant) (Column 3) with the corresponding observational constraints adjusted (Column 4) for the best model for solar-type stars (Paper I) and adopted in this study. The flags in Column 2 indicate the transported quantity (C for chemicals and AM for angular momentum)

Table 3. Models computed for the specific case of the Hyades and Praesepe open clusters at $[\text{Fe}/\text{H}] = +0.15$.

Model	ν_{add} ($\text{cm}^2 \cdot \text{s}^{-1}$)	K (10^{30} erg)	Turbulence
C	0	7.5	none
$\nu R1_A^{T6.42}$	3.5×10^4	7.5	$D_{T6.42}$
$\nu R1_A^{T6.5}$	3.5×10^4	7.5	$D_{T6.5}$
$M R2_A^{T6.42}$	3.5×10^4	7.5	$D_{T6.42}$
$\nu R2_A^{T6.42}$	$1.0 - 2.5 - 3.5 - 6.5 - 8.5 \times 10^5$	7.5	$D_{T6.42}$
$M R2_A^{T6.42}$	3.5×10^4	1.5	$D_{T6.42}$
$\nu R2_{A,K}^{T6.42}$	3.5×10^4	1.5	$D_{T6.42}$

in the Hyades and Praesepe, as well as in the other clusters of different ages considered in this work (see Sect. 5).

Models $\nu R1_A^{T6.42}$ and $\nu R1_A^{T6.5}$ predict rotation velocities that account well for the observed $V \sin i$ trends (including the position in effective temperature of the Kraft break) in both open clusters, thanks to the extraction of angular momentum due to magnetised winds (see also Fig. 5). However, on the cool side of the Kraft rotation break (see insert in Fig. 2), models well reproduce the lower observational envelope but not the entire observed spread. It is mainly the case for the lowest stellar masses where the parametric viscosity is more efficient.

Models $\nu R1_A^{T6.42}$ and $\nu R1_A^{T6.5}$ also provide a very good fit of the Li data in G-type stars on the cool side of the Li-dip where angular momentum extraction is maximal, i.e., for stellar masses lower than $1.3M_{\odot}$ for the metallicity of these clusters. At the age of the Hyades/Praesepe, the increased (with respect to the classical model C) Li-depletion is mainly due to penetrative convection (Eq. 1) along the PMS, and only slightly to turbulent mixing at the beginning of the MS. As discussed in Paper I, Augustson & Mathis (2019) expression for penetrative convection leads to larger Li depletion for slow rotators than for fast rotators because of the influence of the rotation rate on the depth of the overshoot via the ratio ν/ν_0 in Eq. (1). This anticorrelation with the rotation rate, which has long been observed (e.g. Bouvier 2008; Bouvier et al. 2018; Arancibia-Silva et al. 2020), is obtained here for the first time for the entire mass range considered at Hyades/Praesepe age ⁶ In addition, the predicted Li spread induced by the different initial rotation rates assumed here (Sect. 3.4) is amplified in lower mass stars where the base of the convective envelope is deeper and closer to the Li burning lay-

ers, which also leads to more efficient parametric turbulence on the lower mass end. For this later process, we present model predictions for two values of the parameter T_0 from Eq. (2), i.e., $\log T_0 = 6.42$ as calibrated in the Sun, and $\log T_0 = 6.5$ which better fits the data spread in cool stars of the Hyades and Praesepe. Overall, our complete model $\nu R1_A^{T6.42-6.5}$ reproduces fairly well the $\text{Li}-T_{\text{eff}}-V \sin i$ trend and the observed Li dispersion on the cool side of the Li-dip (i.e., G-type and late F-type stars). In this T_{eff} domain, it also accounts for the Be data in the Hyades and Praesepe, as shown in Figs. 3 and 4.

However, models $\nu R1_A^{T6.42-6.5}$ predict little Li depletion (both on the PMS and the MS at the ages of the Hyades and Praesepe) for stars more massive than $1.3M_{\odot}$ that have vanishingly small convection zones on the MS and which undergo a negligible angular momentum braking. As a consequence, it does not reproduce the depth of the Li-dip, nor the Li rise on the cool edge of the dip. Around 6'600 K, where many stars have only Li upper limits, the maximum Li depletion predicted reaches only ~ 1 dex in the case where we assume slightly deeper parametric turbulence (i.e. $\log T_0 = 6.5$). This low depletion results mainly from the choice of prescriptions for the horizontal and vertical diffusivities D_h and D_v (taken here from Mathis et al. 2018 and Zahn 1992 respectively; see Sect. 3.4). This is in contrast with previous studies of the hot edge of the Li-dip (Palacios et al. 2003) where the use of the prescriptions by Zahn (1992) and Talon & Zahn (1997) for D_h and D_v , respectively, lead to a good match between model predictions and observations. As can be seen in Fig. 3, much stronger Li and Be depletion is indeed obtained in model $M R2_A^{T6.42}$ where we use the same prescriptions as in that earlier paper. As already evidenced in Paper I for the solar case, this combination leads however to too strong Li depletion in F- and G-type stars for the value of ν_{add} adopted in that paper and here ($3.5 \times 10^4 \text{ cm}^2 \cdot \text{s}^{-1}$). Additionally, reducing the torque parameter K for the wind from Matt et al. (2015), from 7.5×10^{30} erg to 1.5×10^{30} erg improves the comparison on the hot edge of the Li-dip and of the Be-dip, but not on the cool edge as can be seen in Figs. 3 and 4 for model $\nu R2_{A,K}^{T6.42}$.

⁶ This anticorrelation was initially obtained by Somers & Pinsonneault (2015) who invoked a radius inflation dependent on the rotation velocity to explain the anti-correlation at Pleiades age. However, if it has been confirmed in the Pleiades (Somers & Pinsonneault 2016; Somers & Stassun 2017), the effect of this process still needs to be clarified at older ages than Pleiades and for different metallicities (e.g. Jaehnig et al. 2019; Jackson et al. 2019).

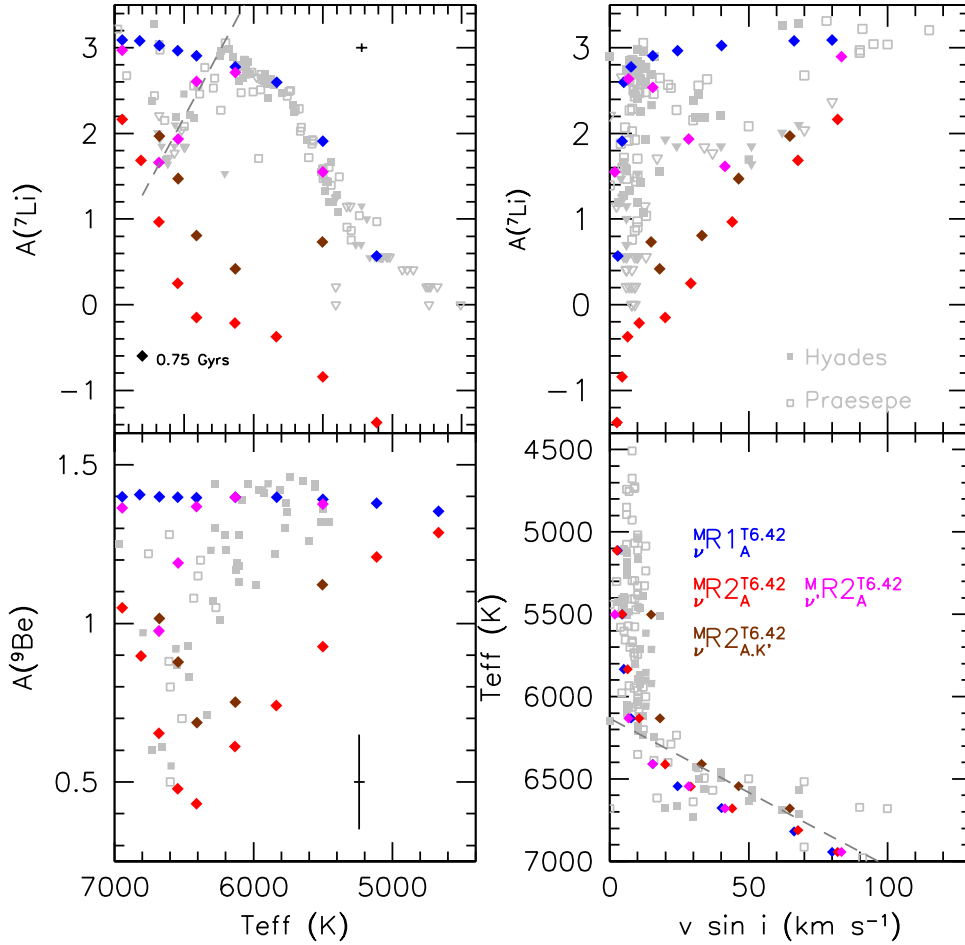


Fig. 3. Comparison of the Li, Be, and $V \sin i$, observations in the Hyades and Praesepe (filled and open grey squares respectively; triangles are for abundance upper limits; see Table 1 for references) with the predictions of models ${}^M R 1_A^{T6.42}$ (blue diamonds) and ${}^M R 2_A^{T6.42}$ for different values of ν'_{add} and K (colour-coded, see also Tab. 3). Model predictions are shown at 0.75 Gyr. The grey dashed line represents the empirical relation in the cold edge of the dip obtained by Cummings et al. (2017).

Talon & Charbonnel (1998) reached similar conclusions than Palacios et al. (2003), using the same turbulence prescriptions (D_h and D_v from Zahn 1992 and Talon & Zahn 1997, respectively). These authors interpreted the rise of Li on the cool edge of the dip as the signature of the appearance of a process that transports angular momentum more efficiently than meridional circulation and turbulent shear. Talon & Charbonnel (2003, 2005) then showed that the generation of internal gravity waves (hereafter IGW) by the stellar convective envelope becomes efficient inside the Li-dip and increases on its cool edge. In their model, the maximum efficiency of the IGWs in terms of angular momentum transport is expected at T_{eff} around 5'800-5'900 K, before it decreases in cooler stars (see Fig. 6 of Talon & Charbonnel 2003 and Fig. 4 of Talon & Charbonnel 2004). Last but not least, their model also accounts for the internal solar rotation (Charbonnel & Talon 2005). It has thus the proper mass and T_{eff} dependence to be the required transport mechanism at act, contrary to other processes that could potentially also transport

angular momentum (e.g. the Taylor-Spruit dynamo Spruit 2002; Eggenberger et al. 2005, 2010).

Following this theoretical trend for IGWs, we computed ${}^M R 2_A^{T6.42}$ of various masses assuming a T_{eff} dependence of the parametric viscosity ν'_{add} (increasing value with decreasing mass on the cool edge of the Li-dip) in order to mimic a transport of angular momentum as predicted for low-mass stars. Although the use of a uniform and constant parametric viscosity within the radiative layers leads to a very different angular momentum profile than that shaped by IGW (compare Fig.7 with Fig.1 of Charbonnel & Talon 2005), higher values of ν'_{add} mimics a more efficient internal transport of angular momentum compared to that driven by meridional circulation and turbulent shear (see Fig. 7 that will be discussed in detail in Sect. 7), hence reducing their efficiency for the transport of chemicals. The ν'_{add} values required to reproduce the shape of the Li-dip are $3.5 \times 10^5 \text{ cm}^2 \cdot \text{s}^{-1}$ and $1.0 \times 10^5 \text{ cm}^2 \cdot \text{s}^{-1}$ for the 1.5 and 1.4 M_{\odot} models, respectively, on the hot edge of the Li-dip, and 2.5×10^5 , 6.5×10^5 , and $8.5 \times 10^5 \text{ cm}^2 \cdot \text{s}^{-1}$ for the 1.35 M_{\odot} , 1.3 M_{\odot} , and 1.2 M_{\odot} on the

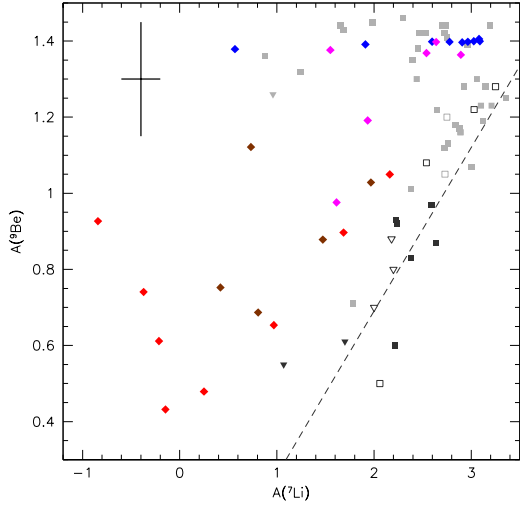


Fig. 4. Comparison of the models ${}^M R1_A^{T6.42}$ (blue diamonds), ${}^M R2_A^{T6.42}$ (red diamonds), ${}^v R1_A^{T6.42}$ (brown diamonds), and ${}^v R2_A^{T6.42}$ (magenta diamonds) with observations of surface Li and Be in the Hyades (filled squares) and Praesepe (open squares) open clusters. Downward triangles are for Li upper limits. Stars corresponding to the Li-dip ($6'400 \text{ K} < T_{\text{eff}} < 6'800$) are represented in dark grey and stars outside of the Li-dip are represented in light grey. Observations are directly extracted from Boesgaard et al. (2004a, 2016) without any modification (no NLTE correction for Li abundances). The dark grey dashed line represents the linear correlations found by Boesgaard et al. (2020) with $A(\text{Be}) = 0.43 \times A(\text{Li}) - 0.17$ for stars in the cold edge of the Li-dip.

cool edge of the dip. On the other hand, the Li abundance in the $1.0 M_{\odot}$ model is well reproduced for $v'_{\text{add}} = 2.5 \times 10^5 \text{ cm}^2 \cdot \text{s}^{-1}$. However for this mass, it leads to a too strong reduction of the surface velocity (see Figs. 5 and 7) which makes it hard to reconcile with P_{rot} measurements in the Hyades and Praesepe. As shown in Figs. 3 and 4, these assumptions explain the Be plateau in cool stars, within the observational uncertainties. However, the ${}^M R2_A^{T6.42}$ models do not account for the large Be depletion in the Be-dip nor in its cool edge. This conclusion holds for all the initial rotation rates explored here.

It thus appears very difficult to reconcile the Li, Be, and surface rotation rate constraints in the test case of the Hyades and Praesepe. While the ${}^v R1_A^{T6.42}$ models account well for the surface rotation over the entire mass domain explored, and for the Li and Be abundances in G-type stars, they fail to explain the Li and Be dips in these two clusters. On the other hand, ${}^M R2_A^{T6.42}$ models with the parametric viscosity for the transport of angular momentum dependent of the stellar mass of the star and adjusted to fit the Li abundances along the entire mass range predict a Be-dip not as deep as the one observed, and lead the $1 M_{\odot}$ model to rotate too slowly at the age of the two clusters (0.72-0.75 Gyr). In Sect. 5 we evaluate the respective compatibility of the models ${}^v R1_A^{T6.42}$ and ${}^M R2_A^{T6.42}$ with the surface Li and rotation rates in a sample of open clusters, before discussing in Sect. 6 the impact of the different assumptions for the transport of angular momentum on the internal rotation profiles of the models under the light of asteroseismic constraints. We present in Sect. 7 a wrap up of the successes and difficulties of the different assumptions, and discuss their meaning in terms of the uncertainties of the different processes involved.

5. Model predictions for Li and surface rotation - Comparison to open clusters of different ages and metallicities

In this section, we compare the predictions of models ${}^v R1_A^{T6.42}$ and ${}^M R2_A^{T6.42}$ to rotation rates and surface Li abundances for a sample of open clusters with different ages and metallicities (see Table 1). Be can not be used here, as there is not enough available data for clusters others than the Hyades and Praesepe. In the ${}^v R1_A^{T6.42}$ case, we computed models for the actual $[\text{Fe}/\text{H}]$ of the individual clusters and for three initial rotation rates (slow, median, fast), while in the ${}^M R2_A^{T6.42}$ case we use the models at the metallicity of the Hyades and Praesepe ($[\text{Fe}/\text{H}] = +0.15$ dex), and for median rotation discussed previously. The values of $A(\text{Li})$, T_{eff} , and P_{rot} predicted by the ${}^M R1_A^{T6.42}$ model are given in Appendix A for the different masses and cluster ages.

5.1. P_{rot} versus Mass

In Fig. 5 we compare the predicted surface rotation periods of the ${}^v R1_A^{T6.42}$ models with relevant $[\text{Fe}/\text{H}]$ to observational data for a sample of 12 open clusters at different ages. We add the ${}^M R2_A^{T6.42}$ model predictions at the $[\text{Fe}/\text{H}]$ of the Hyades for αPer , Hyades, Praesepe, and NGC 6819. The masses of the individual cluster stars were determined by isochrone fitting in the original papers quoted in Table 1 for the P_{rot} . Godoy-Rivera et al. (2021) have studied the difference in mass estimates that can derive from using different families of isochrones and shown that it is quite small ($\Delta M \approx 0.05 M_{\odot}$).

We confirm the conclusions reached in previous studies (e.g. Krishnamurthi et al. 1997; Allain 1998; Irwin & Bouvier 2009; Amard et al. 2016, 2019): the evolution of the rotation period can be divided in several phases that our models succeed to predict. Firstly, the large dispersion at very young ages for all masses (NGC 2362 to IC 2391, first row of Fig. 5) results in our models from the assumption of constant surface angular velocity as long as disc-locking is efficient. Secondly, the progressive slow down of first, slow and median, and finally fast rotators of decreasing mass in clusters of increasing age (from αPer to M 37, second row of Fig. 5) is very well reproduced by our models as the result of the secular evolution of the radius along the PMS and the efficient wind braking on the early MS. Finally, for clusters older than Praesepe (≈ 750 Myrs), we observe the convergence of the three families of rotators into one single sequence recovering the observational law by Skumanich (1972). In addition, the sequence presents a change of slope around $M \approx 1.2 M_{\odot}$ in the P_{rot} vs mass diagram (last row of Fig. 5) resulting from the magnetic braking by the stellar winds. This change of slope corresponds to the Kraft break and to the mass domain where the convective envelope becomes very thin. In the Hyades and Praesepe, we also show the predictions of the model ${}^M R2_A^{T6.42}$ introduced to fit the cool edge of the Li-dip (see Sect. 4.2). The predicted rotation periods for models more massive than $1.2 M_{\odot}$ are fully compatible with observations while the $1 M_{\odot}$ median rotator model is far too slow, as already discussed in Sect. 4.2. As in Amard et al. (2019) who uses the same prescriptions for horizontal and vertical turbulence and for the braking law as in model ${}^v R1_A^{T6.42}$ (with a parameter $K=7.0 \times 10^{30}$ erg instead of 7.5×10^{30} erg) but who does not include the parametric viscosity for the internal transport of angular momentum, our model predictions for the older clusters present a larger negative slope on the lower mass side, with the lower mass models spinning slower than the observed stars. For the more massive stars in NGC 6819, the extraction of angu-

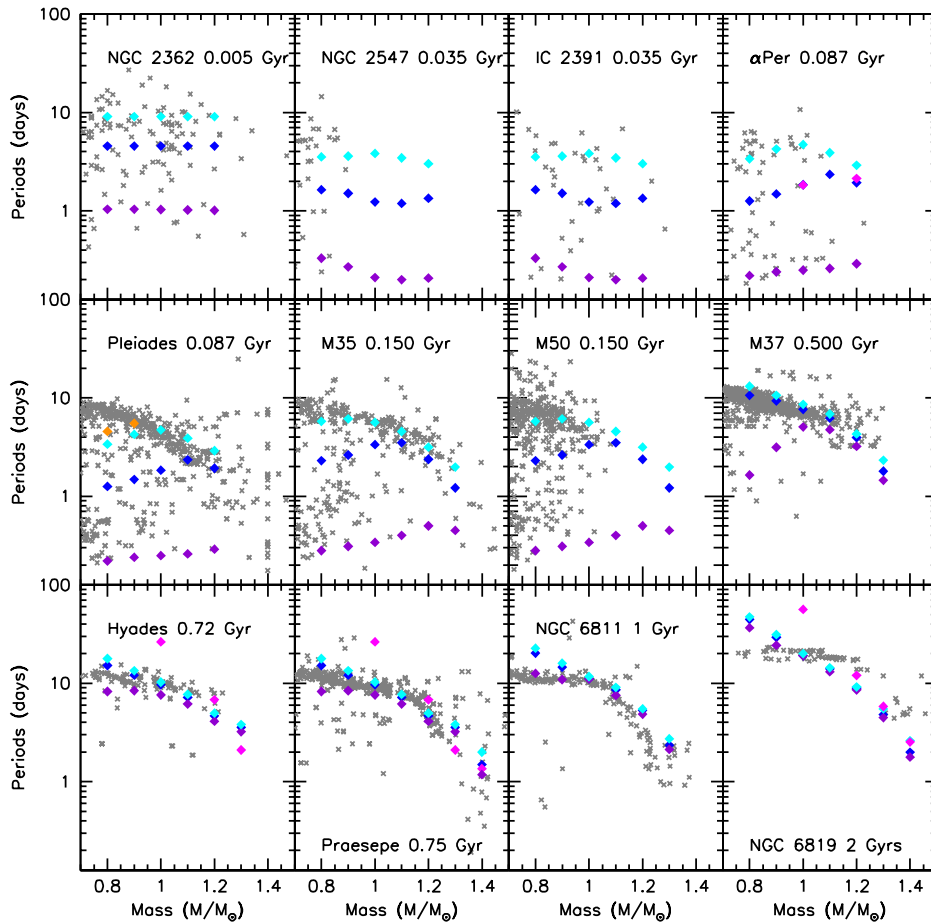


Fig. 5. Surface rotational period versus mass. Comparison of the models $\nu R_1^{T6.42}$ (diamonds) at three different initial velocities: slow (cyan), median (blue) and fast (violet) with the observations for open clusters at different ages and metallicities. The orange diamond for Pleiades corresponds to a slow rotating model at 125 Myrs. In the case of α Per, Hyades, Praesepe, and NGC 6819 we also show the predictions of the ${}^M R_2^{T6.42}$ models (magenta diamonds). Observations references are reported in Table 1.

lar momentum, which is directly linked to the depth of the convective envelope, becomes inefficient in the models, which spin faster than the observed stars. Finally, for the Pleiades we obtain a poor agreement with observations for the lowest stellar masses (0.8 and 0.9 M_\odot) compared to what we get for all the other clusters and to what was obtained in Amard et al. (2019). This is essentially due to the difference in age adopted for this cluster in both studies (125 Myrs from Barrado y Navascués et al. (2004) in Amard et al. (2019) instead of 87 Myrs as assumed here), as shown Fig. 5 where the orange diamonds are the predictions of our models at 125 Myrs, which better account for the data.

To summarise, the comparison between the predictions of our $\nu R_1^{T6.42}$ and ${}^M R_2^{T6.42}$, and the observational data for the rotation period is rather satisfactory, although some peculiar features remain difficult to reproduce without further adjustments. This work confirms the global theoretical behaviour obtained by Amard et al. (2016, 2019) despite the fact that we include an additional diffusive source of transport of angular momentum in the present study.

5.2. Lithium - T_{eff}

In Fig. 6, we compare the predictions of models $\nu R_1^{T6.42}$ for the surface Li abundances to data within the cluster sample (see Sect. 2 and Table 1), and we report the predictions of models ${}^M R_2^{T6.42}$ discussed in Sect. 4 for the most metal-rich clusters (α Per, Hyades, Praesepe, and NGC 6819). Importantly, over the entire mass and metallicity range explored, the faster the initial rotation velocity, the lower the predicted Li depletion. As already discussed in Sect. 4.2, this is due to penetrative convection acting on the PMS, which we simulate with Augustson & Mathis (2019) prescription.

The Li- T_{eff} relation for G-type stars is well reproduced by models $\nu R_1^{T6.42}$ at all ages from the youngest (IC 2602 and IC 2391) to the oldest cluster (M67) with solar or super-solar metallicities. For the young clusters with subsolar metallicity (M35, NGC 6633, and UMa) the cooler models, corresponding to lower mass stars (see Table in Appendix A), predict however larger A(Li) values than observed. In these models, the con-

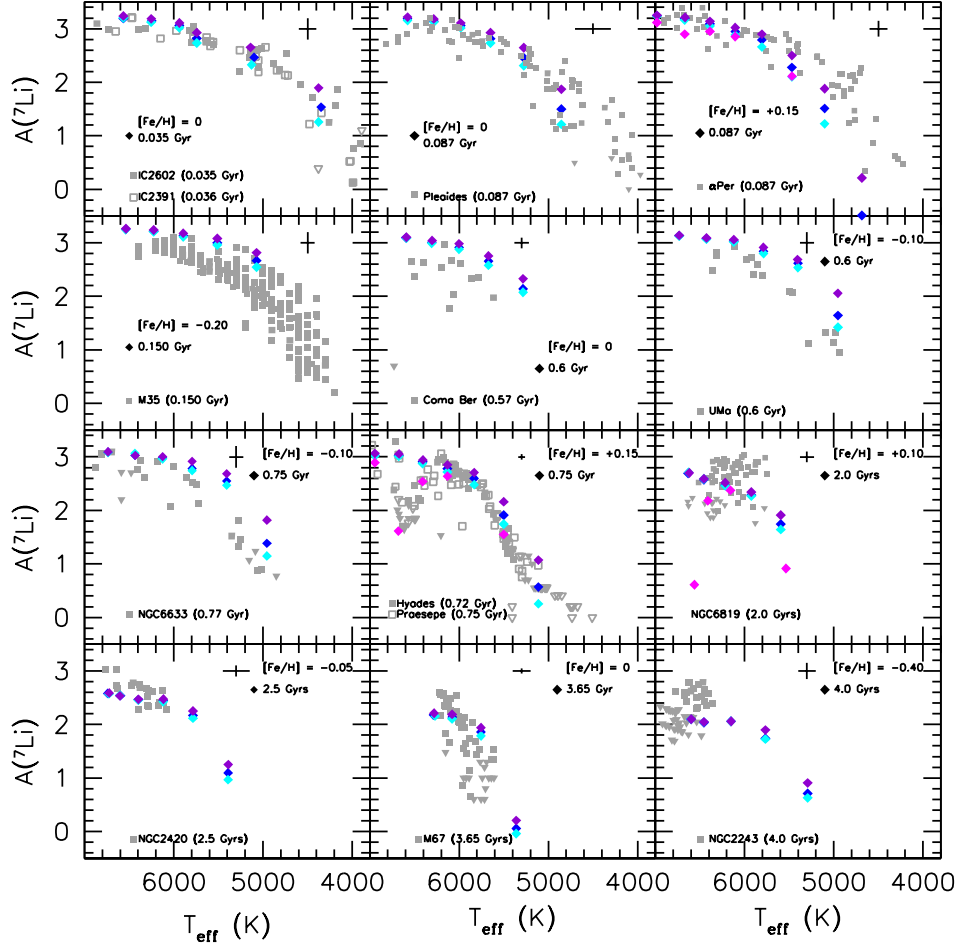


Fig. 6. Li surface abundance versus T_{eff} in open clusters of different ages and $[\text{Fe}/\text{H}]$ (see Table 1 for references; grey squares and triangles are abundance determinations and upper limits respectively). The typical observation errorbars from the original papers are indicated by a cross in each panel. Coloured diamonds are the predictions of the models at the age and metallicity of the corresponding clusters. $\nu R1_A^{T6.42}$ models are shown for three initial velocities (slow, median, and fast are the cyan, blue, and violet diamonds, respectively), and models $M R2_A^{T6.42}$ for median rotation only (magenta diamonds). Models from left to right in each panel correspond to masses between $1.5 M_{\odot}$ (warmer) and $0.8 M_{\odot}$ (cooler).

vective envelope is thinner due to the lower metallicity and the penetrative convection, which is the main process responsible for the Li depletion on the PMS, is less efficient than at higher metallicity. This can be directly seen when comparing the panels showing NGC 6633 / UMa clusters and the Hyades/ Praesepe clusters, which have similar ages but different metallicities. This suggests a stronger metallicity dependence of the Li depletion in cool stars compared to that predicted. Data for the cooler stars in the most metal-poor and oldest cluster (NGC 2243) would be required to confirm this trend at older ages.

We see in Fig. 6 that the Li-dip is not present in the youngest clusters, and that its depth increases with time along the MS (see also Wallerstein et al. 1965; Boesgaard & Tripicco 1986; Hobbs & Pilachowski 1986; Soderblom et al. 1993a; Balachandran 1995; Steinhauer & Deliyannis 2004; Anthony-Twarog et al. 2009; Cummings et al. 2012; Boesgaard et al. 2016). As already discussed in Sect. 4.2, model $\nu R1_A^{T6.42}$ predicts too little Li depletion in the dip, while $M R2_A^{T6.42}$ models (computed only for

$[\text{Fe}/\text{H}] = +0.15$ dex) reproduce both the depth and the shape of the Li-dip in clusters with super-solar metallicities and with ages between 720 Myrs (Hyades) and 2 Gyrs (NGC 6819). For the old low metallicity NGC 2243 cluster, the cold edge of the Li-dip is shifted towards slightly higher T_{eff} compared to the younger higher metallicity clusters (Cummings et al. 2012; François et al. 2013). Since models $\nu R1_A^{T6.42}$ lie below the observational points on the cold edge of the Li-dip we expect that model $M R2_A^{T6.42}$, assuming similar dependence between ν'_{add} and T_{eff} as assumed to fit the Hyades and Praesepe, would predict an even stronger Li-depletion and would be incompatible with the data of NGC 2243.

We thus reach similar conclusions as in Sect. 4.2, for a relatively large range of metallicities and ages. Model $\nu R1_A^{T6.42}$ initially developed to reproduce surface and internal constraints for solar-type stars nicely explains the general trend of the data for both the rotation and Li behaviours over the mass and the metallicity ranges probed in this study, except for the Li-dip.

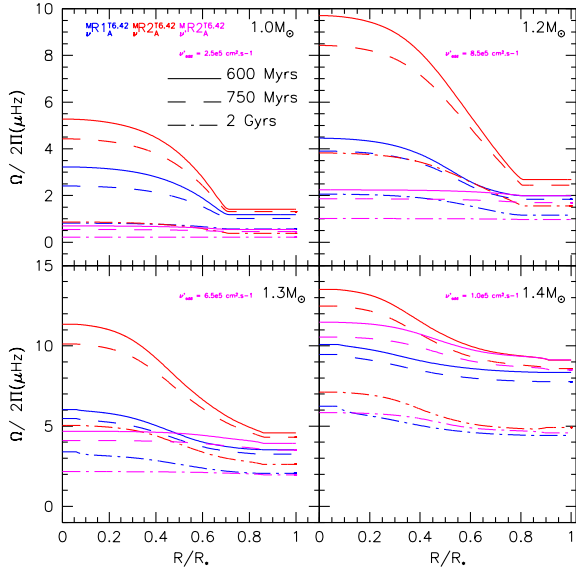


Fig. 7. Angular velocity profiles vs the radius within the star for models ${}^M_{\nu}R1_A^{T6.42}$ (blue), ${}^M_{\nu}R2_A^{T6.42}$ (red), and ${}^M_{\nu}R2_A^{T6.42}$ (magenta) at $[\text{Fe}/\text{H}]=+0.15$ and for four masses: 1.0, 1.2, 1.3, and $1.4M_{\odot}$ (the value of ν'_{add} used is indicated for each mass). The solid, dashed, and dot-dashed lines refer to three different ages (0.6, 0.75, and 2 Gyrs, respectively)

On the other hand, model ${}^M_{\nu}R2_A^{T6.42}$ with turbulent viscosity for the transport of angular momentum parametrised to fit the dip in the Hyades and the Pleiades predicts too slow rotation rates for the lower mass models. Importantly, and for the first time, we predict that over the entire mass and metallicity range explored here, penetrative convection that is efficient at the early stages of the PMS leads to larger Li depletion in the slower rotators. This anticorrelation between the rotation rate and the Li abundance, which builds early on the PMS, remains along time.

6. Models predictions for internal rotation and comparison to asteroseismic constraints

In this section, we present the predictions of models ${}^M_{\nu}R1_A^{T6.42}$, ${}^M_{\nu}R2_A^{T6.42}$, and ${}^M_{\nu}R2_A^{T6.42}$ with $[\text{Fe}/\text{H}] = +0.15$ dex (characteristic of the Hyades, Praesepe, and NGC 6819 clusters) in terms of internal rotation and tentatively compare them to the only available asteroseismic estimates of internal rotation rates in MS field stars of similar metallicity from Benomar et al. (2015).

In Fig. 7, we present the internal rotation profiles for the 1.0, 1.2, 1.3, and $1.4M_{\odot}$ models at three different ages on the MS. For G-type stars, the ${}^M_{\nu}R1_A^{T6.42}$ model that reproduces all surface observational constraints (see previous sections) predicts a small radial differential rotation that decreases with time and is compatible with helioseismic data as already shown in Paper I. For the more massive models corresponding to the Li-dip stars in the Hyades, Praesepe, and NGC 6819, this model predicts the same behaviour. The ${}^M_{\nu}R2_A^{T6.42}$ model predicts larger radial differential rotation for all masses and ages than ${}^M_{\nu}R1_A^{T6.42}$ model, in agreement with the associated strong Li depletion discussed in previous sections. This results from the much higher efficiency of the vertical turbulent shear D , when using Talon & Zahn (1997) prescription (see also Paper I). For the ${}^M_{\nu}R2_A^{T6.42}$ model, which intro-

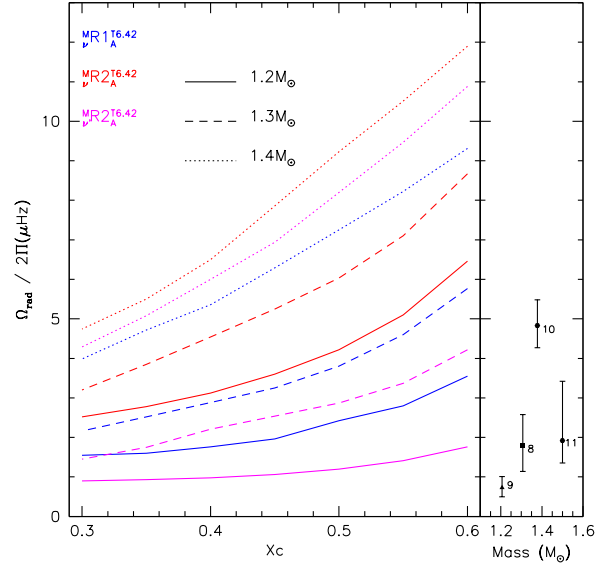


Fig. 8. (Left) Mean angular velocity within the stellar layers in the radiative zone as a function of the remaining central hydrogen mass fraction X_c (time increases from right to left) for the same models as in Fig. 7. Masses 1.2, 1.3, and $1.4M_{\odot}$ are represented by full, dashed, and dotted lines respectively. (Right) Stars observed by Benomar et al. (2015) as indexed in the original paper (8: $M = 1.307 \pm 0.027 M_{\odot}$, 9: $M = 1.206 \pm 0.077 M_{\odot}$, 10: $M = 1.378 \pm 0.028 M_{\odot}$, 11: $1.500 \pm 0.050 M_{\odot}$).

duces an enhanced parametric turbulent transport of angular momentum to fit the cold edge of the Li-dip, the radial differential rotation is strongly reduced at all ages, especially in the $1.2M_{\odot}$ model with the larger value of ν'_{add} , which presents an almost flat rotation profile at all ages displayed on the figure. Concerning the case of the $1.4M_{\odot}$ model, although the angular momentum contrast between the surface and the core is of the same order in models ${}^M_{\nu}R1_A^{T6.42}$ and ${}^M_{\nu}R2_A^{T6.42}$, the angular velocity gradient near the base of the convective envelope is much larger in the later model (see change of slope in magenta profiles around $r = 0.9R_{\star}$ in Fig. 7), thus leading to an enhanced shear and associated turbulent transport in the exact region where the connection between the convective envelope and Li burning zone is made. This leads to the strong Li depletion discussed previously in this model (see Sect. 4.2). On the contrary, the shear is near to null at the base of the convective envelope in model ${}^M_{\nu}R1_A^{T6.42}$, leading to almost no Li depletion.

Fig. 8 shows the mean angular velocity in the radiative interior (i.e. excluding the convective core if present⁷, consistently with asteroseismic data that do not take it into account) as a function of the central hydrogen mass fraction in the 1.2, 1.3, and $1.4M_{\odot}$ models at $[\text{Fe}/\text{H}]=+0.15$ dex. We compare to a selected sub-sample of four field stars with metallicities close to that of the Hyades for which the average rotation in the radiative interior was estimated from asteroseismology by Benomar et al. (2015).

⁷ The expression used is similar to Eq. (18) from Paper I but starting the integration at the outer edge of the convective core when present: $\Omega_{\text{rad}} = \int_{M_{\text{TCC}}}^{M_{\text{BCE}}} r^2 \Omega dm / \int_{M_{\text{TCC}}}^{M_{\text{BCE}}} r^2 dm$, with M_{TCC} the mass coordinate of the top of the convective core and M_{BCE} the mass coordinate at the base of the convective envelope.

Our predictions are of the same order of magnitude as the results from Benomar et al. (2015) but the predicted rotation is faster than the values they inferred for the selected targets. Models ${}^M R_2^{T6.42}$ lead to a better agreement with the values derived from asteroseismic data than models ${}^M R_2^{T6.42}$. A more precise comparison with the results in Benomar et al. (2015) is prevented by the use in their study of MESA stellar models including very different input physics and settings. In particular, core hydrogen mass fractions X_c cannot be compared.

Additional data for different stellar masses would be required to better discriminate between the different prescriptions for the transport of angular momentum, especially for cool stars. Nevertheless, this comparison supports the need of strong transport of angular momentum on the MS for stars in the Li-dip region as obtained when increasing the strength of ν_{add} as assumed in models ${}^M R_2^{T6.42}$.

7. Summary and discussion

The need for additional transport processes beyond atomic diffusion and so-called Type-I rotation-induced processes (turbulent shear and meridional circulation) for the transport of chemicals and angular momentum has long been reported (see references in Sect. 1). This work follows Paper I who analysed the impact of several processes, using state-of-the-art prescriptions for specific mechanisms (rotation-induced turbulence and penetrative convection in particular), as well as parametric prescriptions for others (parametric turbulence for chemicals and parametric viscosity for angular momentum) that were calibrated to reproduce the evolution of the surface Li abundance and rotation rates as well as the internal angular velocity profiles in the Sun and solar-type stars. The aim of the present paper is to study the impact of these processes (using the solar-type calibrations) on F- and G-type MS stars at different metallicities and to test them against data in Galactic open clusters over a large range in ages. Although the adopted ages come from different references and are not fully consistent, our conclusions are robust given the uncertainties on their estimate. Our predictions support however the Pleiades to be older than assumed in this work, which is in agreement with other age determinations for this cluster.

The so-called ${}^{\nu} R_1^{T6.42-6.5}$ models calibrated in Paper I include atomic diffusion, rotation-induced processes (meridional circulation and turbulence), penetrative convection, parametric turbulence for the transport of chemicals, and parametric viscosity for the transport of angular momentum. We also presented ${}^M R_2^{T6.42}$ models which differ by the assumed prescriptions for horizontal and vertical shear-induced turbulence, and that are computed with different values of the parametric viscosity. We analysed the agreement between the theoretical predictions of these two sets of models and observational data for Li, Be, and surface rotation rates available in a sample of open clusters of different ages and metallicities. We also compared the predicted internal rotation profiles with asteroseismic constraints in field MS stars with [Fe/H] close to that of the Hyades.

Both ${}^{\nu} R_1^{T6.42-4.5}$ and ${}^M R_2^{T6.42}$ explain the main general trends observed between Li depletion and stellar mass, age, rotation, and metallicity covered in this study. Thanks to the prescription we use for penetrative convection (Augustson & Mathis 2019), an anticorrelation between Li depletion and surface rotation builds up early on the PMS, and remains along evolution on the MS. Theoretical surface Li abundance and T_{eff} are correlated as observed in cluster stars, with cooler and lower mass stars being more Li depleted than hotter and more massive ones (except in the Li-dip when this feature is present). Our

models also recover the anticorrelation between metallicity and Li-depletion efficiency that is observed in open clusters stars. Metal-poor stars are less Li-depleted than their metal-rich counterparts as expected from the metallicity dependence of the location of the base of the convective envelope that affects the PMS Li-depletion. However, Li-depletion in our metal-poor models is more modest than in open cluster stars.

Model ${}^{\nu} R_1^{T6.42-6.5}$ succeeds to reproduce the Li, Be, and rotation rates observations in G-type stars at all ages, and in F-type stars in the young clusters where the Li-dip has not started to form yet. This is achieved thanks to the combined effects of penetrative convection, rotation-induced processes, and parametric turbulence, whose efficiencies vary with both the stellar mass and the metallicity. The impact of these mechanisms on Li and Be depletion becomes minute in the more massive stars that have very thin convective envelope, more distant from the Li and Be burning layers. As a result, model ${}^{\nu} R_1^{T6.42-6.5}$ is not able to reproduce the Li and the Be dips centered around $\sim 6'600$ K that appear later on the MS, although it reproduces the rotation rates over the entire mass range covered in this study. On the other hand, model ${}^M R_2^{T6.42}$ computed with the same value of the parametric viscosity, but with different prescriptions for horizontal and vertical turbulence (D_h and D_v) that lead to more differential rotation (hence more efficient rotation-induced mixing) in the stellar interior, predicts too much Li depletion on the cool side of the dip, as expected from previous studies.

Building on the assumption that an additional transport process like internal gravity waves would be the main driver for the transport of angular momentum in stellar interiors on the cold edge of the Li-dip, we introduced a mass dependent viscosity ν_{add}' with a maximum efficiency at $\approx 5'900$ K as predicted in Talon & Charbonnel (2003) and Talon & Charbonnel (2004) for the IGW excitation by the convective envelope and their luminosity. Although the assumption we make of a parametric viscosity $\nu_{\text{add}}^{(\cdot)}$ uniform within the radiative interior and constant with time is a very crude parametrisation of a transport of angular momentum within stars, ${}^M R_2^{T6.42}$ model predicts a good agreement with Li abundances on the cold edge of the dip in open clusters of different ages at the metallicity of the Hyades (this was not tested for other metallicities). This is due to the flattening of the angular velocity gradient within the stellar interior, and in particular between the base of the convective envelope and the Li burning depth, implied by higher values of the parametric viscosity. Further improvement of our model now requires the full treatment of the transport of angular momentum by IGWs as in Charbonnel & Talon (2005), taking into account also recent developments on the generation and the behaviour of IGWs (e.g. Pinçon et al. 2016; Augustson et al. 2020; Ratnasingam et al. 2020). The Tayler-Spruit dynamo process that was updated in recent studies (e.g. Fuller et al. 2019; Eggenberger et al. 2019a,b,c) is also a candidate for additional transport of angular momentum and should also be tested regarding the results of the present work. The Be depletion obtained with model ${}^M R_2^{T6.42}$ is on the other hand too modest to explain the depth of the Be-dip observed in a couple of clusters. The acquisition of more Be observational data in open clusters of different ages and metallicities, in addition to those in field stars (e.g. Delgado Mena et al. 2012) would be an important key to better constrain models.

Importantly, the transport of angular momentum simulated with the parametric viscosity values adopted in our different models is much more efficient than that driven by meridional circulation and turbulence. Both the ${}^{\nu} R_1^{T6.42}$ and the ${}^M R_2^{T6.42}$ models predict mean angular rotation velocity in the radiative interior that are compatible with the values inferred from as-

teroseismology in field MS with the same metallicity than the Hyades and the Pleiades. Additional asteroseismic data to probe the internal rotation of young MS stars over a large metallicity range would be valuable.

Reflecting on the modelling of turbulent shear, we have to conclude that none of the combinations for the prescriptions of the horizontal and vertical turbulence (D_h and D_v) we used is able to reconcile all the surface constraints used in this study. Model $\nu R_1^{T6.42-6.5}$, tailored for solar-type stars, includes the Mathis et al. (2018) prescription for the horizontal shear diffusivity D_h , which is the only prescription including the contributions of both the horizontal and vertical shear on the horizontal turbulent transport, and the Zahn (1992) prescription for the vertical shear diffusivity D_v , which does not take into account the effects of thermal and molecular diffusivity on the vertical turbulent transport, but is the only one that has been validated by direct numerical simulations (Prat & Lignières 2013; Garaud et al. 2017). This model thus includes the apparently most robust available prescriptions but it cannot explain the Li-dip even when combined to additional sources for turbulent transport as D_{T_0} and ν_{add} .

On the other hand, the use of the Zahn (1992) prescription for the horizontal shear diffusivity (D_h) and that of Talon & Zahn (1997), which includes the effect of thermal and molecular diffusion, for the vertical shear diffusivity (D_v) in model $\nu R_2^{T6.42}$ requires higher values for the parametric viscosity for the internal transport of angular momentum, with a mass-dependent efficiency as expected from IGW. The choice of these prescriptions thus impacts our ability to constrain the other transport processes (see Meynet et al. 2013; Amard et al. 2016) as additionally illustrated by the predictions obtained in this work and for instance by Semenova et al. (2020) for the specific case of NGC 2420. Insight and validation of the different available prescriptions for the vertical turbulent shear transport from hydrodynamicists and multi-D numerical simulations, similar to the ongoing work on the horizontal turbulent shear (Park et al. 2020, 2021; Prat & Mathis 2021) is now mandatory in order to overcome this impasse.

Finally, two additional promising leads to understand in particular the formation of the Li and Be dips should be explored, that were neglected here. First, we do not consider radiative accelerations on heavy elements. Their effects are however non-negligible for stars with effective temperature higher than $\approx 6'800$ K, which corresponds to $\approx 1.4 M_{\odot}$ at solar metallicity, close to the hot edge of the Li-dip (e.g. Richer & Michaud 1993; Deal et al. 2018, 2020). Their impact on the stellar opacity could partly modify some of our conclusions concerning the most massive models. Second, the process sustaining the parametric turbulence used in in this work and others in the literature has yet-to-be-identified. In particular, even if the tachocline mixing (Spiegel & Zahn 1992; Brun et al. 1999; Garaud 2020) was shown to not be adapted in solar-type stars (Paper I), this process could play a role in the building of the Li and Be dips because of its dependence at the latitudinal differential rotation that is predicted to scale inversely with rotation for F-type stars (Augustson et al. 2012) compared to G-type stars.

Acknowledgements. We thank J.W. Ferguson for providing us with low-temperature opacity tables adapted to the solar mixture we adopt in this work, E. Semenova for providing us observational data for NGC 2420 open cluster, J.D. Cummings and collaborators for providing the log g values for their Hyades and Praesepe sample, L. Amard and P. Eggenberger for fruitful discussions, and the anonymous referee for constructive comments on the manuscript. This work was supported by the Swiss National Science Foundation (Project 200020-192039 PI C.C.), by CNES (funding of AP at LUPM) focussed on the PLATO mission, and by the Agence Nationale de la Recherche grant POPSYPOLY num-

ber ANR-19-CE31-0022. This research has made use of NASA's Astrophysics Data System Bibliographic Services.

References

- Aerts, C., Mathis, S., & Rogers, T. M. 2019, *ARA&A*, 57, 35
 Agüeros, M. A., Covey, K. R., Lemonias, J. J., et al. 2011, *ApJ*, 740, 110
 Allain, S. 1998, *A&A*, 333, 629
 Amard, L., Palacios, A., Charbonnel, C., Gallet, F., & Bouvier, J. 2016, *A&A*, 587, A105
 Amard, L., Palacios, A., Charbonnel, C., et al. 2019, *A&A*, 631, A77
 Anthony-Twarog, B. J., Deliyannis, C. P., Harmer, D., et al. 2018, *AJ*, 156, 37
 Anthony-Twarog, B. J., Deliyannis, C. P., Twarog, B. A., Croxall, K. V., & Cummings, J. D. 2009, *AJ*, 138, 1171
 Arancibia-Silva, J., Bouvier, J., Bayo, A., et al. 2020, *A&A*, 635, L13
 Asplund, M., Grevesse, N., Sauval, A. J., & Scott, P. 2009, *ARA&A*, 47, 481
 Augustson, K. C., Brown, B. P., Brun, A. S., Miesch, M. S., & Toomre, J. 2012, *ApJ*, 756, 169
 Augustson, K. C. & Mathis, S. 2019, *ApJ*, 874, 83
 Augustson, K. C., Mathis, S., & Astoul, A. 2020, *ApJ*, 903, 90
 Balachandran, S. 1995, *ApJ*, 446, 203
 Balachandran, S., Lambert, D. L., & Stauffer, J. R. 1988, *ApJ*, 333, 267
 Balachandran, S. C. & Bell, R. A. 1998, *Nature*, 392, 791
 Balachandran, S. C., Mallik, S. V., & Lambert, D. L. 2011, *MNRAS*, 410, 2526
 Baraffe, I., Pratt, J., Goffrey, T., et al. 2017, *ApJ*, 845, L6
 Barrado y Navascués, D., Deliyannis, C. P., & Stauffer, J. R. 2001, *ApJ*, 549, 452
 Barrado y Navascués, D., Stauffer, J. R., & Jayawardhana, R. 2004, *ApJ*, 614, 386
 Benomar, O., Takata, M., Shibahashi, H., Ceillier, T., & García, R. A. 2015, *MNRAS*, 452, 2654
 Bodenheimer, P. 1965, *ApJ*, 142, 451
 Boesgaard, A. M. 1976, *PASP*, 88, 353
 Boesgaard, A. M. 1987, *PASP*, 99, 1067
 Boesgaard, A. M. 1991, *ApJ*, 370, L95
 Boesgaard, A. M., Armengaud, E., & King, J. R. 2003a, *ApJ*, 583, 955
 Boesgaard, A. M., Armengaud, E., & King, J. R. 2003b, *ApJ*, 582, 410
 Boesgaard, A. M., Armengaud, E., & King, J. R. 2004a, *ApJ*, 605, 864
 Boesgaard, A. M., Armengaud, E., King, J. R., Deliyannis, C. P., & Stephens, A. 2004b, *ApJ*, 613, 1202
 Boesgaard, A. M., Deliyannis, C. P., King, J. R., & Stephens, A. 2001, *ApJ*, 553, 754
 Boesgaard, A. M., Lum, M. G., & Deliyannis, C. P. 2020, *ApJ*, 888, 28
 Boesgaard, A. M., Lum, M. G., Deliyannis, C. P., et al. 2016, *ApJ*, 830, 49
 Boesgaard, A. M. & Tripicco, M. J. 1986, *ApJ*, 302, L49
 Bossini, D., Vallenari, A., Bragaglia, A., et al. 2019, *A&A*, 623, A108
 Bouvier, J. 2008, *A&A*, 489, L53
 Bouvier, J., Barrado, D., Moraux, E., et al. 2018, *A&A*, 613, A63
 Brun, A. S., Strugarek, A., Varela, J., et al. 2017, *ApJ*, 836, 192
 Brun, A. S., Turck-Chièze, S., & Zahn, J. P. 1999, *ApJ*, 525, 1032
 Cantat-Gaudin, T., Anders, F., Castro-Ginard, A., et al. 2020, *A&A*, 640, A1
 Carlsson, M., Ratten, R. J., Bruls, J. H. M. J., & Shchukina, N. G. 1994, *A&A*, 288, 860
 Casagrande, L., Ramírez, I., Meléndez, J., Bessell, M., & Asplund, M. 2010, *A&A*, 512, A54
 Castro, M., Duarte, T., Pace, G., & do Nascimento, J. D. 2016, *A&A*, 590, A94
 Castro, M., Vauclair, S., Richard, O., & Santos, N. C. 2009, *A&A*, 494, 663
 Cayrel, R., Cayrel de Strobel, G., Campbell, B., & Dappen, W. 1984, *ApJ*, 283, 205
 Charbonneau, P. & MacGregor, K. B. 1993, *ApJ*, 417, 762
 Charbonneau, P. & Michaud, G. 1990, *ApJ*, 352, 681
 Charbonnel, C. & Talon, S. 2005, *Science*, 309, 2189
 Charbonnel, C., Vauclair, S., & Zahn, J. P. 1992, *A&A*, 255, 191
 Cummings, J. D., Deliyannis, C. P., Anthony-Twarog, B., Twarog, B., & Maderak, R. M. 2012, *AJ*, 144, 137
 Cummings, J. D., Deliyannis, C. P., Maderak, R. M., & Steinhauer, A. 2017, *AJ*, 153, 128
 Deal, M., Alecian, G., Lebreton, Y., et al. 2018, *A&A*, 618, A10
 Deal, M., Goupil, M. J., Marques, J. P., Reese, D. R., & Lebreton, Y. 2020, *A&A*, 633, A23
 Decressin, T., Mathis, S., Palacios, A., et al. 2009, *A&A*, 495, 271
 Delgado Mena, E., Israelian, G., González Hernández, J. I., Santos, N. C., & Rebolo, R. 2012, *ApJ*, 746, 47
 Deliyannis, C. P., Anthony-Twarog, B. J., Lee-Brown, D. B., & Twarog, B. A. 2019, *AJ*, 158, 163
 Deliyannis, C. P., Boesgaard, A. M., Stephens, A., et al. 1998, *ApJ*, 498, L147
 Deliyannis, C. P., Pinsonneault, M. H., & Charbonnel, C. 2000, in *IAU Symposium*, Vol. 198, *The Light Elements and their Evolution*, ed. L. da Silva, R. de Medeiros, & M. Spite, 61

- Delorme, P., Collier Cameron, A., Hebb, L., et al. 2011, *MNRAS*, 413, 2218
- Douglas, S. T., Agüeros, M. A., Covey, K. R., et al. 2016, *ApJ*, 822, 47
- Douglas, S. T., Agüeros, M. A., Covey, K. R., & Kraus, A. 2017, *ApJ*, 842, 83
- Douglas, S. T., Curtis, J. L., Agüeros, M. A., et al. 2019, *ApJ*, 879, 100
- Dumont, T., Palacios, A., Charbonnel, C., et al. 2021, *A&A*, 646, A48
- Duncan, D. K. & Jones, B. F. 1983, *ApJ*, 271, 663
- Eff-Darwich, A., Korzennik, S. G., Jiménez-Reyes, S. J., & García, R. A. 2008, *ApJ*, 679, 1636
- Eggenberger, P., Buldgen, G., & Salmon, S. J. A. J. 2019a, *A&A*, 626, L1
- Eggenberger, P., Deheuvels, S., Miglio, A., et al. 2019b, *Astronomy and Astrophysics*, 621, A66
- Eggenberger, P., den Hartogh, J. W., Buldgen, G., et al. 2019c, *A&A*, 631, L6
- Eggenberger, P., Haemmerli, L., Meynet, G., & Maeder, A. 2012a, *A&A*, 539, A70
- Eggenberger, P., Maeder, A., & Meynet, G. 2005, *A&A*, 440, L9
- Eggenberger, P., Meynet, G., Maeder, A., et al. 2010, *A&A*, 519, A116
- Eggenberger, P., Montalbán, J., & Miglio, A. 2012b, *Astronomy and Astrophysics*, 544, L4
- Elsworth, Y., Howe, R., Isaak, G. R., et al. 1995, *Nature*, 376, 669
- François, P., Pasquini, L., Biazzo, G., Bonifacio, P., & Palsa, R. 2013, *A&A*, 552, A136
- Fuller, J., Piro, A. L., & Jermyn, A. S. 2019, *MNRAS*, 485, 3661
- Gallet, F. & Bouvier, J. 2015, *A&A*, 577, A98
- Garaud, P. 2020, *Astrophysics and Space Science Proceedings*, 57, 207
- Garaud, P., Gagnier, D., & Verhoeven, J. 2017, *ApJ*, 837, 133
- García, R. A. & Ballot, J. 2019, *Living Reviews in Solar Physics*, 16, 4
- García Lopez, R. J., Rebolo, R., & Martín, E. L. 1994, *A&A*, 282, 518
- Godoy-Rivera, D., Pinsonneault, M. H., & Rebull, L. M. 2021, *arXiv e-prints*, arXiv:2101.01183
- Gutiérrez Albarrán, M. L., Montes, D., Gómez Garrido, M., et al. 2020, *A&A*, 643, A71
- Guzik, J. A. & Mussack, K. 2010, *ApJ*, 713, 1108
- Hartman, J. D., Bakos, G. Á., Kovács, G., & Noyes, R. W. 2010, *MNRAS*, 408, 475
- Hartman, J. D., Gaudi, B. S., Holman, M. J., et al. 2008, *ApJ*, 675, 1254
- Hobbs, L. M. & Pilachowski, C. 1986, *ApJ*, 309, L17
- Huang, Y., Liu, X. W., Yuan, H. B., et al. 2015, *MNRAS*, 454, 2863
- Irwin, J., Aigrain, S., Bouvier, J., et al. 2009, *MNRAS*, 392, 1456
- Irwin, J. & Bouvier, J. 2009, in *The Ages of Stars*, ed. E. E. Mamajek, D. R. Soderblom, & R. F. G. Wyse, Vol. 258, 363–374
- Irwin, J., Hodgkin, S., Aigrain, S., et al. 2008, *MNRAS*, 384, 675
- Jackson, R. J., Jeffries, R. D., Deliyannis, C. P., Sun, Q., & Douglas, S. T. 2019, *MNRAS*, 483, 1125
- Jaehnig, K., Somers, G., & Stassun, K. G. 2019, *ApJ*, 879, 39
- Jeffries, R. D. 1997, *MNRAS*, 292, 177
- Jeffries, R. D., Jackson, R. J., Sun, Q., & Deliyannis, C. P. 2021, *MNRAS*, 500, 1158
- Jeffries, R. D., Totten, E. J., Harmer, S., & Deliyannis, C. P. 2002, *MNRAS*, 336, 1109
- Jones, B. F., Fischer, D., & Soderblom, D. R. 1999, *AJ*, 117, 330
- Jørgensen, A. C. S. & Weiss, A. 2018, *MNRAS*, 481, 4389
- Kawaler, S. D. 1988, *ApJ*, 333, 236
- Kosovichev, A. G. 1988, *Soviet Astronomy Letters*, 14, 145
- Kraft, R. P. 1967, *ApJ*, 150, 551
- Krishnamurthi, A., Pinsonneault, M. H., Barnes, S., & Sofia, S. 1997, *ApJ*, 480, 303
- Lagarde, N., Decressin, T., Charbonnel, C., et al. 2012, *A&A*, 543, A108
- Maeder, A. & Zahn, J.-P. 1998, *A&A*, 334, 1000
- Marques, J. P., Goupil, M. J., Lebreton, Y., et al. 2013, *A&A*, 549, A74
- Mathis, S. 2013, *Transport Processes in Stellar Interiors*, ed. M. Goupil, K. Belkacem, C. Neiner, F. Lignières, & J. J. Green, Vol. 865, 23
- Mathis, S., Prat, V., Amard, L., et al. 2018, *Astronomy and Astrophysics*, 620, A22
- Mathis, S. & Zahn, J. P. 2004, *A&A*, 425, 229
- Mathur, S., Eff-Darwich, A., García, R. A., & Turck-Chièze, S. 2008, *A&A*, 484, 517
- Matt, S. P., Brun, A. S., Baraffe, I., Bouvier, J., & Chabrier, G. 2015, *ApJ*, 799, L23
- Matteucci, F., D'Antona, F., & Timmes, F. X. 1995, *A&A*, 303, 460
- Meibom, S., Barnes, S. A., Latham, D. W., et al. 2011, *ApJ*, 733, L9
- Meibom, S., Barnes, S. A., Platais, I., et al. 2015, in *American Astronomical Society Meeting Abstracts*, Vol. 225, American Astronomical Society Meeting Abstracts #225, 449.09
- Meibom, S., Mathieu, R. D., & Stassun, K. G. 2009, *ApJ*, 695, 679
- Meléndez, J., Schuster, W. J., Silva, J. S., et al. 2010, *A&A*, 522, A98
- Meynet, G., Ekstrom, S., Maeder, A., et al. 2013, *Models of Rotating Massive Stars: Impacts of Various Prescriptions*, ed. M. Goupil, K. Belkacem, C. Neiner, F. Lignières, & J. J. Green, Vol. 865, 3
- Michaud, G. 1986, *ApJ*, 302, 650
- Montalbán, J. 1994, *A&A*, 281, 421
- Montalbán, J. & Rebolo, R. 2002, *A&A*, 386, 1039
- Montalbán, J. & Schatzman, E. 1996, *A&A*, 305, 513
- Montalbán, J. & Schatzman, E. 2000, *A&A*, 354, 943
- Netopil, M., Paunzen, E., Heiter, U., & Soubiran, C. 2016, *A&A*, 585, A150
- Pace, G., Castro, M., Meléndez, J., Théado, S., & do Nascimento, J. D., J. 2012, *A&A*, 541, A150
- Palacios, A., Charbonnel, C., Talon, S., & Siess, L. 2006, *A&A*, 453, 261
- Palacios, A., Talon, S., Charbonnel, C., & Forestini, M. 2003, *A&A*, 399, 603
- Paquette, C., Pelletier, C., Fontaine, G., & Michaud, G. 1986, *ApJS*, 61, 177
- Park, J., Prat, V., & Mathis, S. 2020, *A&A*, 635, A133
- Park, J., Prat, V., Mathis, S., & Bugnet, L. 2021, *A&A*, 646, A64
- Pinçon, C., Belkacem, K., & Goupil, M. J. 2016, *A&A*, 588, A122
- Pinsonneault, M. 1997, *ARA&A*, 35, 557
- Pinsonneault, M. H., Kawaler, S. D., & Demarque, P. 1990, *ApJS*, 74, 501
- Prantzos, N. 2012, *A&A*, 542, A67
- Prat, V. & Lignières, F. 2013, *A&A*, 551, L3
- Prat, V. & Mathis, S. 2021, *A&A*, 649, A62
- Pratt, J., Baraffe, I., Goffrey, T., et al. 2017, *A&A*, 604, A125
- Randich, S., Pallavicini, R., Meola, G., Stauffer, J. R., & Balachandran, S. C. 2001, *A&A*, 372, 862
- Randich, S., Pasquini, L., Franciosini, E., et al. 2020, *A&A*, 640, L1
- Ratnasingham, R. P., Edelmann, P. V. F., & Rogers, T. M. 2020, *MNRAS*, 497, 4231
- Richard, O., Michaud, G., & Richer, J. 2005, *The Astrophysical Journal*, 619, 538
- Richard, O., Michaud, G., Richer, J., et al. 2002, *ApJ*, 568, 979
- Richard, O., Vauclair, S., Charbonnel, C., & Dziembowski, W. A. 1996, *A&A*, 312, 1000
- Richer, J. & Michaud, G. 1993, *ApJ*, 416, 312
- Richer, J., Michaud, G., Rogers, F., et al. 1998, *ApJ*, 492, 833
- Richer, J., Michaud, G., & Turcotte, S. 2000, *The Astrophysical Journal*, 529, 338
- Romano, D., Matteucci, F., Ventura, P., & D'Antona, F. 2001, *A&A*, 374, 646
- Ruediger, G. & Kitchatinov, L. L. 1996, *ApJ*, 466, 1078
- Schatzman, E. 1959, in *The Hertzsprung-Russell Diagram*, ed. J. L. Greenstein, Vol. 10, 129
- Schatzman, E. 1962, *Annales d'Astrophysique*, 25, 18
- Schlattl, H. & Weiss, A. 1999, *A&A*, 347, 272
- Semenova, E., Bergemann, M., Deal, M., et al. 2020, *A&A*, 643, A164
- Sestito, P. & Randich, S. 2005, *A&A*, 442, 615
- Siess, L., Dufour, E., & Forestini, M. 2000, *A&A*, 358, 593
- Skumanich, A. 1972, *ApJ*, 171, 565
- Soderblom, D. R., Fedele, S. B., Jones, B. F., Stauffer, J. R., & Prosser, C. F. 1993a, *AJ*, 106, 1080
- Soderblom, D. R., Oey, M. S., Johnson, D. R. H., & Stone, R. P. S. 1990, *AJ*, 99, 595
- Soderblom, D. R., Pilachowski, C. A., Fedele, S. B., & Jones, B. F. 1993b, *AJ*, 105, 2299
- Somers, G. & Pinsonneault, M. H. 2015, *MNRAS*, 449, 4131
- Somers, G. & Pinsonneault, M. H. 2016, *ApJ*, 829, 32
- Somers, G. & Stassun, K. G. 2017, *AJ*, 153, 101
- Spada, F., Gellert, M., Arlt, R., & Deheuvels, S. 2016, *A&A*, 589, A23
- Spiegel, E. A. & Zahn, J. P. 1992, *A&A*, 265, 106
- Spite, F. & Spite, M. 1982, *Astronomy and Astrophysics*, 115, 357
- Spruit, H. C. 2002, *A&A*, 381, 923
- Steinhauer, A. & Deliyannis, C. P. 2004, *ApJ*, 614, L65
- Swenson, F. J., Faulkner, J., Rogers, F. J., & Iglesias, C. A. 1994, *ApJ*, 425, 286
- Talon, S. & Charbonnel, C. 1998, in *Astronomical Society of the Pacific Conference Series*, Vol. 154, *Cool Stars, Stellar Systems, and the Sun*, ed. R. A. Donahue & J. A. Bookbinder, 973
- Talon, S. & Charbonnel, C. 2003, *A&A*, 405, 1025
- Talon, S. & Charbonnel, C. 2004, *A&A*, 418, 1051
- Talon, S. & Charbonnel, C. 2005, *A&A*, 440, 981
- Talon, S. & Charbonnel, C. 2010, in *IAU Symposium*, Vol. 268, *Light Elements in the Universe*, ed. C. Charbonnel, M. Tosi, F. Primas, & C. Chiappini, 365–374
- Talon, S. & Zahn, J. P. 1997, *Astronomy and Astrophysics*, 317, 749
- Thorburn, J. A., Hobbs, L. M., Deliyannis, C. P., & Pinsonneault, M. H. 1993, *ApJ*, 415, 150
- Thoul, A. A., Bahcall, J. N., & Loeb, A. 1994, *ApJ*, 421, 828
- Travaglio, C., Randich, S., Galli, D., et al. 2001, *ApJ*, 559, 909
- Turcotte, S., Richer, J., & Michaud, G. 1998, *ApJ*, 504, 559
- Ujjwal, K., Kartha, S. S., Mathew, B., Manoj, P., & Narang, M. 2020, *AJ*, 159, 166
- Wallerstein, G., Herbig, G. H., & Conti, P. S. 1965, *ApJ*, 141, 610
- Wang, E. X., Nordlander, T., Asplund, M., et al. 2021, *MNRAS*, 500, 2159
- Weber, E. J. & Davis, Leverett, J. 1967, *ApJ*, 148, 217
- Zahn, J. P. 1992, *Astronomy and Astrophysics*, 265, 115
- Zhang, Q.-S., Li, Y., & Christensen-Dalsgaard, J. 2019, *ApJ*, 881, 103

Appendix A: Models predictions

Table A1. $M_{\nu} R_{A}^{1.642}$ model predictions for the different clusters with lithium abundances presented in Table 1 and in Figs. 5 and 6.

Cluster	Mass (M_{\odot})	T_{eff} (K)	A(Li)	P_{rot} (d)
IC 2602 / IC 2391	0.8	4347	1.54	1.6
	0.9	5099	2.47	1.5
	1.0	5742	2.82	1.2
	1.1	5937	3.06	1.2
	1.2	6247	3.15	1.3
	1.3	6564	3.19	1.1
Pleades	0.8	4855	1.50	1.3
	0.9	5275	2.46	1.5
	1.0	5649	2.81	1.8
	1.1	5982	3.06	2.4
	1.2	6284	3.14	1.9
	1.3	6578	3.19	0.9
α Per	0.8	4685	-0.49	1.3
	0.9	5103	1.51	1.5
	1.0	5470	2.28	1.8
	1.1	5806	2.79	2.4
	1.2	6104	2.95	1.9
	1.3	6388	3.09	0.9
	1.4	6670	3.19	2.3
M 35	0.8	5072	2.67	2.3
	0.9	5512	3.00	2.6
	1.0	5894	3.13	3.4
	1.1	6225	3.22	3.5
	1.2	6538	3.25	2.4
Coma Ber	0.9	5284	2.13	10.5
	1.0	5671	2.66	8.5
	1.1	6001	2.92	6.6
	1.2	6305	3.01	4.3
	1.3	6597	3.10	1.1
UMa	0.8	4953	1.64	11.8
	0.9	5402	2.62	9.3
	1.0	5789	2.84	8.0
	1.1	6121	3.03	5.7
	1.2	6429	3.08	3.2
	1.3	6733	3.14	1.3
Hyades	0.8	4665	-2.11	12.4
	0.9	5108	0.85	10.5
	1.0	5497	1.99	8.5
	1.1	5829	2.65	6.6
	1.2	6127	2.83	4.3
	1.3	6407	2.96	3.3
	1.4	6679	3.07	1.4
1.5	6964	3.08	0.8	
NGC 6633	0.8	4955	1.38	14.3
	0.9	5406	2.55	10.5
	1.0	5793	2.79	9.0
	1.1	6126	2.98	6.3
	1.2	6434	3.03	3.5
	1.3	6737	3.09	1.4
Praesepe	0.8	4667	-2.73	15.2
	0.9	5112	0.57	12.1
	1.0	5501	1.91	9.7
	1.1	5833	2.60	7.2
	1.2	6132	2.78	4.7
	1.3	6410	2.91	3.6
	1.4	6677	3.03	0.9
	1.5	6944	3.03	0.8
NGC 6819	0.9	5198	-1.32	24.3
	1.0	5594	1.74	19.1
	1.1	5925	2.29	13.1

Table A1. continued.

Cluster	Mass (M_{\odot})	T_{eff} (K)	A(Li)	P_{rot} (d)
NGC 6819	1.2	6218	2.47	8.6
	1.3	6457	2.57	4.5
	1.4	6634	2.70	1.8
NGC 2420	0.9	5391	1.10	29.1
	1.0	5785	2.17	18.9
	1.1	6118	2.45	11.9
	1.2	6398	2.46	6.9
	1.3	6598	2.54	3.0
	1.4	6741	2.58	1.2
M67	0.9	5369	-0.24	49.5
	1.0	5765	1.78	28.7
	1.1	6083	2.05	17.5
	1.2	6240	2.10	11.7
NGC 2243	0.8	5293	0.71	48.5
	0.9	5766	1.74	26.6
	1.0	6152	2.06	15.3
	1.1	6455	2.04	7.2

Conclusion and perspectives

10.1 Conclusion

During this PhD thesis, we explored how additional transport processes can improve the agreement between evolutionary models of rotating stars and observations for Li depletion, the rotation evolution of solar-type stars, and the solar rotation profile. We used observational constraints of the Sun and of open clusters stars, including solar-type stars and low-mass stars from F- to G-spectral type. The Population I stars are characterised by an important Li-depletion during their evolution from the PMS to the age of the Sun. The observed Li depletion cannot be fully explained by the rotation-induced mixing that is an insufficient process. In addition, the constraints on the rotation velocity evolution in solar-type stars and on the solar rotation profile require a strong coupling between the surface and the internal layers of the stars in order to get closer to the almost solid-body rotation inferred by helioseismology. When considering a larger range of stellar masses, we observe for a few open clusters, like the Hyades, a Li-dip, that appears at about 6600 K, corresponding to F-type stars, and, in addition to the Li-depletion with time, stars in the cold-side of the Li-dip also exhibit a Li-depletion with decreasing masses.

The first task was to optimise the stellar evolution code STAREVOL to compute non-standard models adapted to our study. We optimised the treatment of atomic diffusion through the implementation of more recent formalism, avoiding the trace element assumption, and that we validated via the comparison with others stellar evolution codes. Then, we determined the optimal input physics for our models, including an update of the solar abundance reference, and calibrated our models on the Sun.

The second task was to test these models, and to compare them with the observational data from the Sun and from solar-type stars. It highlighted the deficiency of NSSM models, including Type I rotational mixing and atomic diffusion, to reproduce simultaneously the constraint on Li and on rotation velocity and that additional dynamical processes are needed to transport both angular momentum and chemicals. We implemented and studied the effects of different additional processes in order to determine an optimal combination to reproduce observations. We highlighted that the Li-depletion for solar-type stars can be reproduced in two steps: at the PMS with the addition of a rotation dependent overshoot process and at the MS with the addition of two distinct parametric turbulent mixing processes for angular momentum and for chemicals. We also computed for the first time a model including a self-consistent treatment of the tachocline with the prediction of the same thickness as that was inferred by helioseismology. However, we showed that the turbulent transport resulting from tachocline didn't allow the observed Li depletion to be reproduced, and that we miss a complete analytical development for tachocline. We finally deter-

mined an optimal model that reproduces all the observations at once. We highlighted, however, the need of additional constraints for the internal rotation of young solar-type stars and also for the beryllium abundances of open clusters in order to test the predictions further on.

The third task was to test our optimal model, determined for solar-type stars, in the framework of the larger range of stars including F-type to G-type low mass stars. We showed that our model works well with the cold-side and the hot-side of the Li-dip, independently of the age and the initial rotation velocity. However, the Li-dip itself cannot be reproduced by this model. The Li-dip can only be reproduced considering a different prescription for the shear turbulent mixing and a mass dependent parametric viscosity ν_{add} to transport angular momentum. Even then, the transition between the cold side of the dip and the dip itself remains difficult to predict. This highlights the need to clarify the theory describing shear turbulence in stars and the need to explore other physical processes such as tachoclinic mixing for chemical species transport and internal gravity waves for angular momentum transport. Finally, we highlight the key constraint of Beryllium, which also exhibits a dip, correlated with Li. It provides additional and complementary constraints for the missing transport processes involved. We show that with the few data available, it is presently challenging to reconcile simultaneously the Li-dip and the Be-dip. We highlight the need of additional data for the beryllium abundance in main sequence F- and G-type stars of different ages and metallicities.

In the context of the observational constraints to which we have access, we confirmed that transport processes are needed, in addition to atomic diffusion, meridional circulation and turbulent shear, to explain the behaviour of surface Li abundance and rotation evolution for both solar-like stars and low-mass stars (at the exception of the Li-dip stars) and that additional constraints on the internal rotation and on the beryllium content would be a step forward. The Li-Be correlation in the dip is indeed very promising.

10.2 Perspectives

The work achieved during this thesis opens the path to further analysis in direct continuity of the study of lithium abundance and rotation velocity, but also for the extension to different frameworks where the application of our optimal model could be relevant.

- The first and direct perspective of the present work is to extend our sample of stars with the addition of field stars. The study of field stars, for which Be abundance was inferred for a sample of about a hundred of stars is available in the works of Garcia Lopez & Perez de Taoro (1998); Santos et al. (2002, 2004b,a); Gálvez-Ortiz et al. (2011); Delgado Mena et al. (2012), would bring, in particular, a complementary constraint. Besides, metallicity effects have also been identified. Indeed, it was proposed that metal-rich field stars present a higher Li-depletion than solar metallicity stars (e.g. Guiglion et al. 2016; Fu et al. 2018). Several explanations have been studied like the possible effect of the distance to the galactic centre (Prantzos et al. 2017b) but it is still debated in the community (e.g. Grisoni et al. 2019; Randich et al. 2020);
- The second direct perspective would be to increase the range of mass considered in our studies toward higher masses in order to test the predictions of the models in a wider range of stars. It would imply the implementation of the radiative accelerations that are not negligible any more with increasing mass (or decreasing metallicity, e.g. Deal et al. 2018, 2020, and see the implementation method in Appendix E);

- The third direct perspective would be the study and the implementation of new transport processes to transport chemicals and/or angular momentum. Internal gravity waves (e.g. Charbonnel & Talon 2005; Talon & Charbonnel 2008; Charbonnel et al. 2013), Tayler-Spruit dynamo (Spruit 2002), convective pumping (Kissin & Thompson 2015) are promising;
- The fourth direct perspective of our work is the continuation of our study for the more evolved stars: SGB and RGB stars. Lithium can also be useful for the study of giant evolved stars (do Nascimento et al. 2000; Charbonnel et al. 2000, 2020). The low rotation rate of these stars allows an accurate determination of Li surface abundance. Besides, with the help of asteroseismology, evolved stars have been accurately characterised (mass, radius) and their interior probed by mean of the mixed-modes¹ that give access to the internal rotation of stars (e.g. Mosser et al. 2012; Gehan et al. 2018). That way, mixed-modes opened new windows to study the evolution of transport of angular momentum in stars (see for instance Eggenberger et al. 2017, 2019b);
- Another perspective would be to add directly asteroseismic constraints for MS stars by mean of the study of the acoustic glitches that appear on oscillation modes. Recent methods of analysis allowed Verma et al. (2017); Verma & Silva Aguirre (2019) and also Farnir et al. (2019) to exploit the information provided by the acoustic glitch both for helium and convection zone origins. Following the work done by Monteiro et al. (2000); Appourchaux et al. (2015); Farnir et al. (2019); Verma et al. (2019), the study of the glitches with the help of our non-standard stellar evolution model would be a step forward to understand and constrain the transport processes with the help of internal stellar information.
- A last perspective would be to apply our optimal model in the framework of Pop. II metal-stars with the specific case of globular clusters low-mass stars. The ideal view of globular clusters sharing similar properties such as the initial chemical abundances is now questioned with the detection of Multiple Stellar Populations (e.g. Gratton et al. 2012; Charbonnel 2016; Bastian & Lardo 2018). Indeed, thanks to the Hubble Space Telescope, high-resolution photometric studies allowed to detect multiple sequences at different points of the Color-Magnitude Diagrams (CMD) of the globular clusters (e.g. Bedin et al. 2004; Piotto et al. 2007; Milone et al. 2008; Piotto 2009; Bellini et al. 2017). Thus, several spectroscopic analyses of these MSP brought a new light on their characteristics (Gratton et al. 2001; Carretta et al. 2009; Gratton et al. 2012). These studies identified at least two populations (hereafter 1P and 2P) which present different chemical abundances. The 1P stars present a chemistry comparable to the halo field stars while the 2P stars have an exotic and unique chemistry. The application of our model to the modelling of 1P low-mass stars, combining effects of atomic diffusion and rotation at weak metallicity would be a step forward, after the previous studies by, for instance, Richard et al. (2002b); Charbonnel (2016); Prantzos et al. (2017a); Chantreau et al. (2015), and it would bring new constraints on the polluter scenario.

¹Mixed-modes are the result of the coupling between p-modes and g-modes when the star reaches evolved phases such as SGB and RGB. The mixed characteristics of such modes allow to probe giant stars from the core to the surface.

Generation of new opacity tables

In order to generate new tables of opacities from OPAL database, we have to determine the number fraction for each considered. We have:

Number fraction ϵ :

$$\epsilon_i = \frac{N_i}{\sum_j N_j}, \quad (\text{A.1})$$

where N_i is the number density of element i and N_j is the number density of element j with $j=1, S$ (S the total number of element taken into account);

Mass fraction X_i

$$X_i = \frac{A_i N_i}{\sum_j A_j N_j}, \quad (\text{A.2})$$

where A_i is atomic mass of element i ;
and

$$A(i) = \log \frac{N_i}{N_H} + 12. \quad (\text{A.3})$$

The solar composition from Asplund et al. (2009) (AGSS09) are reported in Tab. A.1. From $\sum_j N_j = N_{\text{tot}} = 7.69 \times 10^{-4}$, we can determine the number fraction asked to generate OPAL opacity tables.

Considering abundances from Young (2018) (AY18), the neon enhancement corresponds to the new value $A(\text{Ne}) = 8.08$ in place of 7.93 for the solar composition reference AGSS09. Then we have $N_{\text{Ne}} = 8.87 \times 10^{-5}$ and $N_{\text{tot}} = 7.95 \times 10^{-4}$. The new number fraction for Ne is then $\epsilon_{\text{Ne}} = 0.1116$.

Table A.1: AGSS09 solar composition

Specy symbol	Z	A(i)	Specy symbol	Z	A(i)
C	6	8.43	Cl	17	5.50
N	7	7.83	Ar	18	6.40
O	8	8.69	K	19	5.03
Ne	10	7.93	Ca	20	6.34
Na	11	6.24	Ti	22	4.95
Mg	12	7.60	Cr	24	5.64
Al	13	6.45	Mn	25	5.43
Si	14	7.51	Fe	26	7.50
P	15	5.41	Ni	28	6.22
S	16	7.12			

Addendum to atomic diffusion implementation

B.1 Friction coefficient with Paquette coefficients

Eq. (22) of Paquette et al. (1986) with $x_i = n_i/n$ and $x_j = n_j/n$:

$$K_{ij} = \frac{n_i}{n} \frac{n_j}{n} n \frac{k_B T}{[D_{ij}]_1} \quad (\text{B.1})$$

Eqs. (5) and (17) are:

$$[D_{ij}]_1 = \frac{3E}{2nm} \quad (\text{B.2})$$

$$E = \frac{k_B T}{8M_i M_j \Omega_{ij}^{11}} \quad (\text{B.3})$$

With Eq. (B.2), Eq. (B.1) becomes:

$$K_{ij} = \frac{n_i}{n} \frac{n_j}{n} n \frac{k_B T}{3E} 2nm \quad (\text{B.4})$$

And with Eq. (B.2), Eq. (B.4) writes:

$$K_{ij} = n_i n_j \frac{2k_B T}{3} m \frac{8M_i M_j \Omega_{ij}^{11}}{k_B T}, \quad (\text{B.5})$$

and finally

$$K_{ij} = \frac{16}{3} n_i n_j \mu_{ij} \Omega_{ij}^{11} \quad (\text{B.6})$$

where we used : $M_i = m_i/m$, $M_j = m_j/m$ and $\mu = m_i m_j / (m_i + m_j)$.

B.2 K0 renormalisation

The perfect gas equation writes:

$$p = nk_bT = \sum_i n_i k_b T \quad (\text{B.7})$$

with $i \in [0, \text{mspec}]$

n : number of particules per cm^3

k_b : Boltzman constant.

$$\rho = \sum_i n_i m_i = m_u \sum_i n_i A_i \quad (\text{B.8})$$

with m_i : mass of particle i

$m_u = \frac{1}{N_A}$: atomic mass unit with N_A : Avogadro number

A_i : atomic mass.

Then, with:

$$c_i = \frac{n_i}{n_e} \quad (\text{B.9})$$

we obtain:

$$p = n_e k_b T \sum_i c_i \quad (\text{B.10})$$

$$\rho = n_e m_u \sum_i c_i A_i \quad (\text{B.11})$$

Multiplying Eq. (B.10) by Eq. (B.11), we have:

$$P\rho = m_u k_b T n_e^2 \sum_i c_i A_i \sum_i c_i \quad (\text{B.12})$$

$$P = m_u k_b T^{-1.5} T^{2.5} n_e^2 \sum_i c_i A_i \sum_i c_i / \rho \quad (\text{B.13})$$

Equation (28) from Thoul et al. (1994) gives:

$$P = 2K0T^{2.5} \sum_i c_i A_i \sum_i c_i / \rho \quad (\text{B.14})$$

From Eqs. (B.13 and (B.14), we have:

$$m_u k_b T^{-1.5} T^{2.5} n_e^2 \sum_i c_i \sum_i c_i A_i / \rho = 2K0T^{2.5} \sum_i c_i A_i \sum_i c_i / \rho \quad (\text{B.15})$$

$$K0 = \frac{m_u k_b}{2} T^{-1.5} n_e^2 \quad (\text{B.16})$$

and we obtain K0 in Thoul units:

$$K0 \approx 1.144 \times 10^{-40} T^{-1.5} n_e^2 \quad (\text{B.17})$$

In Thoul units, Thoul et al. (1994) gives the density ρ in 100 g.cm^3 , the temperature T in $10^7 K$, the distance in $R_\odot = 6.95 \times 10^{10} \text{ cm}$ and the time $\tau_0 = 6 \times 10^{13}$ years. The renormalisation in cgs unit gives:

$$K0 \approx \frac{1.144 \times 10^{-40} T^{-1.5} n_e^2}{\frac{100 R_\odot^2}{(10^7)^{5/2} \tau_0}} \quad (\text{B.18})$$

Finally in cgs units:

$$K0 \approx 1.41 \times 10^{-25} T^{-1.5} n_e^2 \quad (\text{B.19})$$

B.3 Test on Nacre I and Nacre II

In view of the results obtained for the diffusion velocities of different elements in Chapter 6, we highlighted a recurrent shift for their pattern close to the core. Indeed, a bump is shaping for the majority of the light elements (except the particular case of ^4He where the bump is less important and on the reverse side).

As a consequence of its location we suspected this feature may originate from the treatment of the nuclear reactions.

We resume here what is the impact of nuclear data choice, between Nacre II (Xu et al. 2013b) and Nacre I (Arnould et al. 1999).

We give few examples with the velocity and the profile of ^{12}C and ^{13}C on Figs. B.1 and B.2.

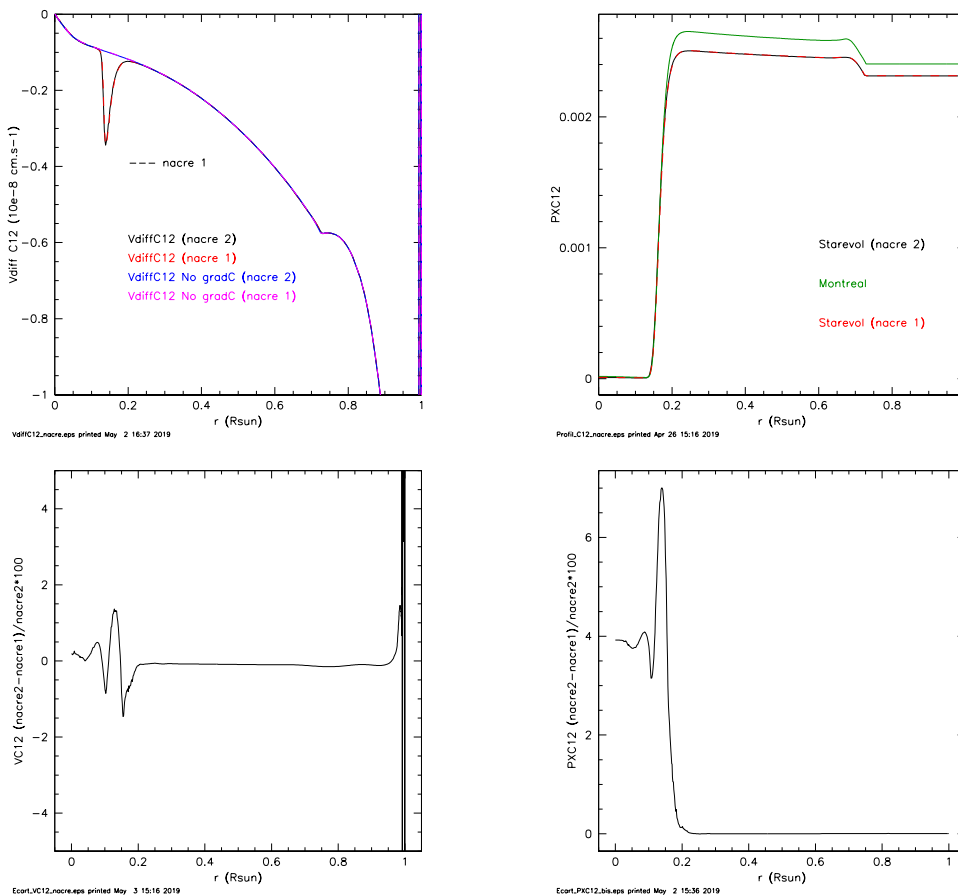


Figure B.1: Comparison of Nacre I or Nacre II for ^{12}C . Top left : Diffusion velocity profile. Top right : Abundance profile. Bottom left : Diffusion velocity difference between Nacre I and Nacre II. Bottom right : Abundance difference between Nacre I and Nacre II.

We obtain similar behaviours with Nacre I and Nacre II for the two carbon isotopes, involved in the CN(O) cycle. Some differences are visible between due to the update from Nacre I to Nacre II. However, the bump observed for the diffusion velocity is visible for both choices in the core, and cannot be attributed by the choice of Nacre I or Nacre II.

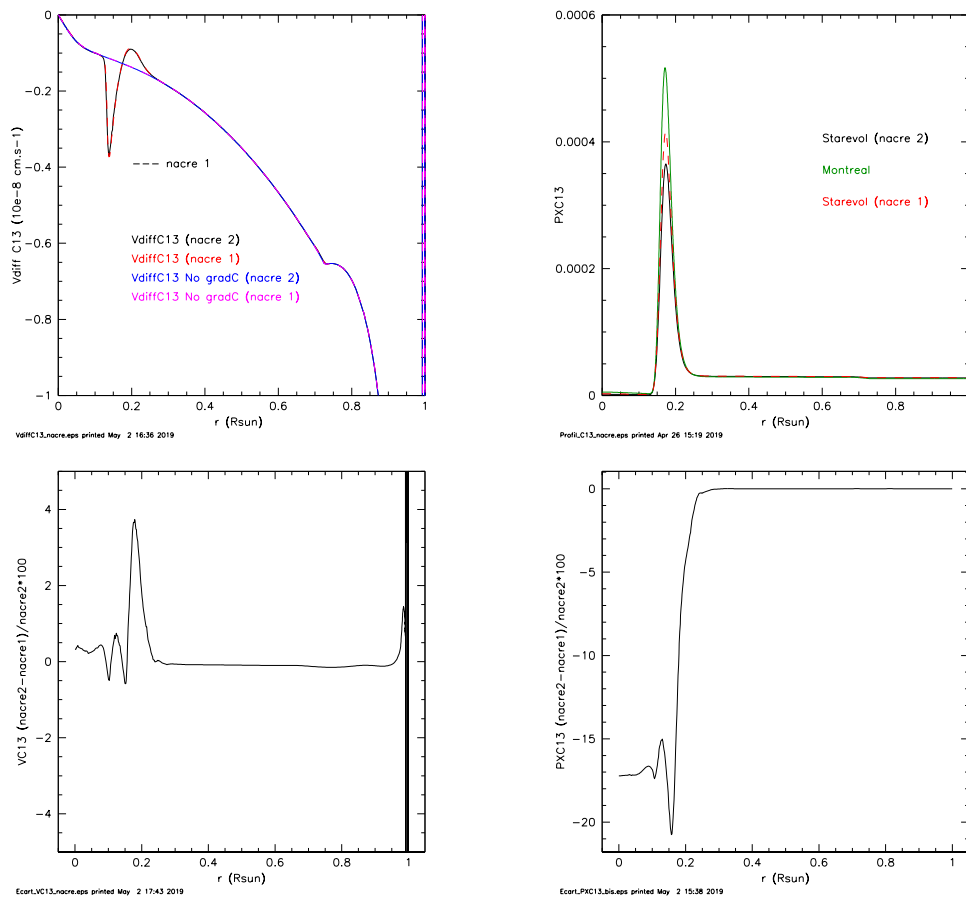


Figure B.2: Comparison of Nacre I or Nacre II for ^{13}C . Top left : Diffusion velocity profile. Top right : Abundance profile. Bottom left : Diffusion velocity difference between Nacre I and Nacre II. Bottom right : Abundance difference between Nacre I and Nacre II.

Period rotation detection

In order to analyse the light curve, the analysis is usually performed in the Fourier domain by means of a power spectrum density (PSD). Fig. C.1 shows the PSD of the HD 52265, observed over 117 days by CoRoT, and with a measured period of 12.3 ± 0.15 days. From the low-frequencies to

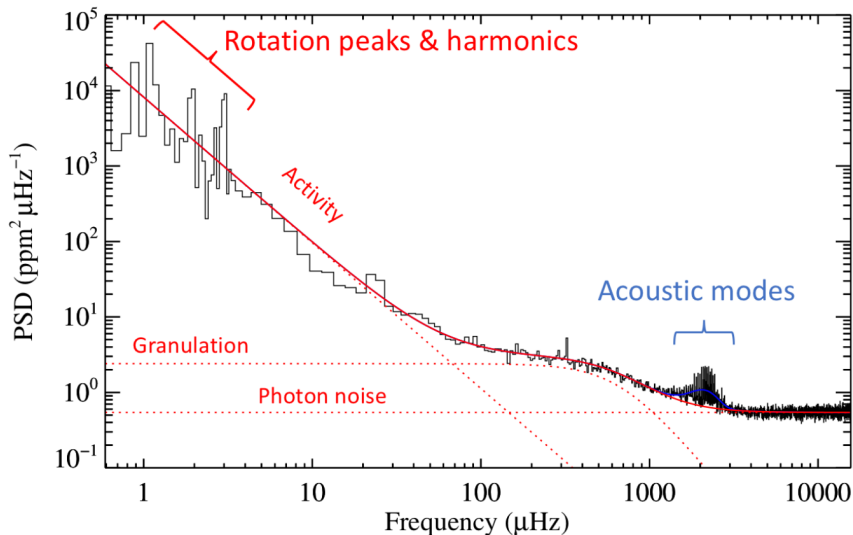


Figure C.1: Power spectrum density (PSD) of the CoRoT target HD 52265 (Ballot et al. 2011). Physical phenomena associated with each region of the PSD are indicated: photon noise, oscillations, convection (granulation), activity related slope, and rotation through the spot modulation of the emitted stellar flux. The continuous red line represents the fitted background components. The blue continuous line is the gaussian fit over the p-mode hump (from García & Ballot 2019).

the high-frequencies, several features can be identified. The peaks at low-frequencies correspond to the spot at the surface of the star, and consequently to the surface rotation. At higher frequency, the acoustic modes are visible. In between, the continuum results of the turbulent surface effect of the star (convection, granulation, magnetic activity). To that, periodic signals from a possible exoplanet or instrumental effect could appear. Then, the challenge is the correct identification of the different features observed and the correct measurement of the period of rotation.

There are several methods to analyse such a signal. Hereafter, we show in Fig. C.2 an analysis of a light curve in order to determine the period of rotation of the star KIC 001570191 observed by *Kepler*. The measurement is realised by means of three different methods: the auto-correlation

of the power spectrum, the wavelet projection and a combination of the two called composite method. Each of them gives a measurement of the period. For KIC 001570191, we measured a period of about 18 days with a good agreement between the three method.

Legend of Fig. C.2: Comparison of three analyses, ACF (Auto-correlation Function), GWPS (Global Wavelet Power Spectrum) and CS (Composite Spectrum, applied for the star KIC 001570191 observed by *Kepler*). The plots are as follows: First line: left-panel shows the long-cadence *Kepler* light curves, where vertical dotted lines indicate the transitions between the observing quarters. The right panel shows the associated power density spectrum as a function of period between 0.5 and 100 days. Second line: Left panel depicts the WPS computed using a Morlet wavelet between 0.5 and 100 days on a logarithmic scale. Right panel: GWPS as a function of the period of the wavelet (black line) and the associated fit composed of several Gaussian functions (green line). The horizontal dashed line designates the position of the retrieved Prot. Third line: panel shows the ACF of the full light curve plotted between 0 and 100 days. The vertical dashed line indicates the returned Prot for the ACF. Fourth line; panel shows the CS obtained from the combination of GWPS and ACF analysis. The vertical dashed line indicates the returned Prot for the CS. Fifth line: Power spectrum in log-log scale obtained from the light curve. The coloured dashed lines indicate the returned Prot for each method. (Collaboration with J. Ballot and R. A. Garcia, see also García et al. (2014))

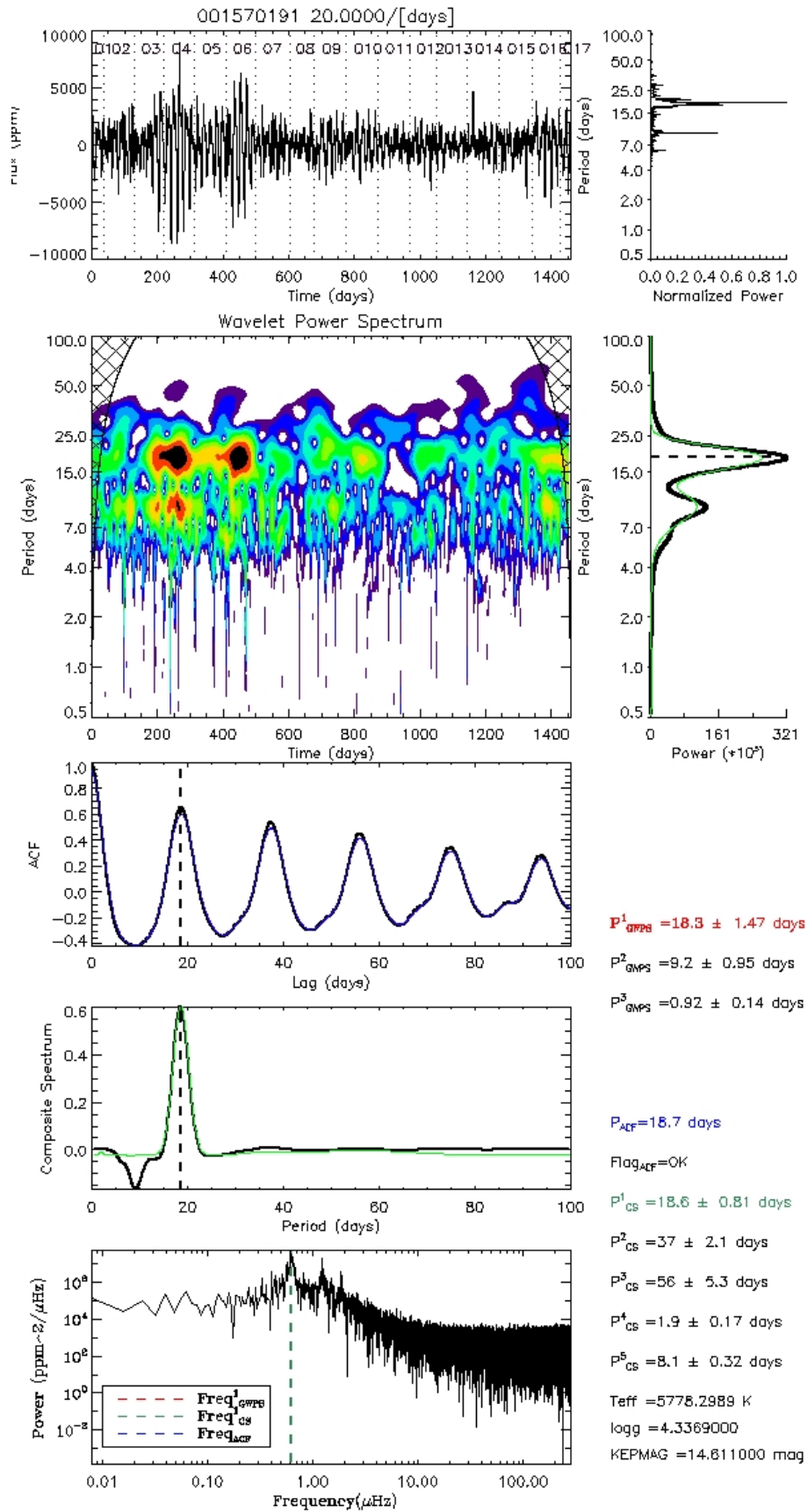


Figure C.2: See description in text.

Asteroseismology

D.1 Introduction

The study of the oscillations of stars allows us to probe their internal structures with a unique access¹. The stellar parameters of stars can be deduced from the frequencies obtained from the observations. Key constraints are now provided with the help of helioseismology and asteroseismology. See the review by Chaplin & Miglio (2013) and by García & Ballot (2019).

The results of asteroseismology give a better measurement of the mass and of the radius of stars and allow to probe different regions in stars presenting solar-like pulsations. When zooming on the p-modes region seen in the PSD of Fig. C.1, we obtain, for instance, the Figure D.1 where the main seismic parameter are identified: the great separation $\Delta\nu$, and the frequency at maximum power ν_{\max} .

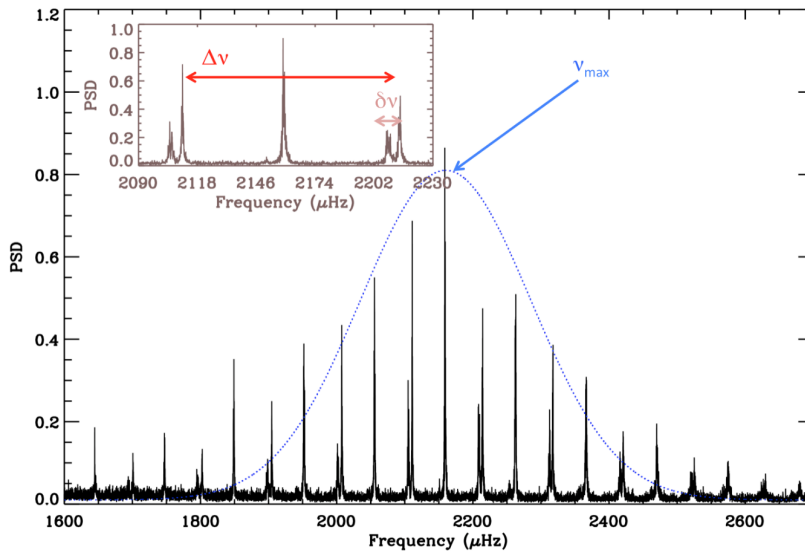


Figure D.1: Power spectrum density (in arbitrary units) of the Kepler target 16 Cyg A. The blue dotted line represents the Gaussian fit to obtain the frequency at maximum power: ν_{\max} . The inset is an enlargement showing the large frequency separation, $\Delta\nu$, between two consecutive modes of angular degree $l=0$ and the small frequency separation, $\delta\nu$, between two modes of angular degree $l=0$ and $l=2$ (from García & Ballot 2019).

¹Spectroscopic and photometric studies are limited to the surface.

D.2 Rotation splittings

The pattern of the p-modes observed in Fig. C.1 can be affected by the rotational splittings and the angle of inclination of the star. Peaks observed in Fig. C.1 are affected as shown in Fig. D.2.

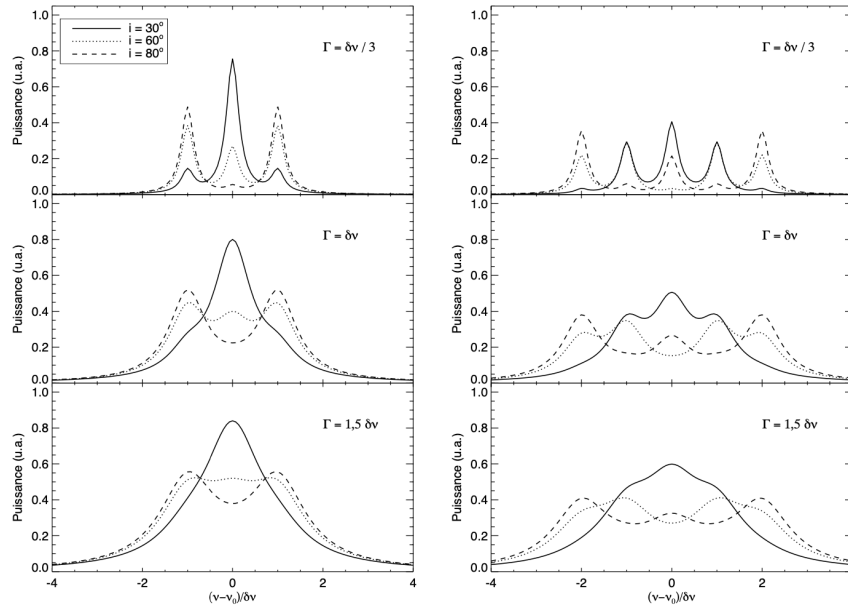


Figure D.2: This figure illustrates the influence of the inclination angle i and of the rotational splitting on the structure of a mode, and more specifically the relative amplitudes multiplet. It shows a mode $l = 1$ (left) and $l = 2$ (right) whose multiplet structure is shown. The visible power is distributed between the $(2l + 1)$ components according to i . Note the difficulty of being able to separate the effect of the angle from that of splitting. ν_0 is the central frequency of a mode, Γ is its width and δ_ν is the splitting (from Ballot et al. 2006).

Radiative accelerations: perspectives and applications

Radiative accelerations are the result of an interaction between photons which radiate in stars and elements which are diffused in the stars. This interaction gives place to a transfer of momentum between the element and radiative field.

The term of radiative accelerations can be added as a complementary term g_{rad} in the equation of the diffusion velocity (Eq. 4.45). The equation for g_{rad} can be formulated as:

$$g_{\text{rad}} = \frac{1}{A_i m_p c} \int_0^\infty \sigma_\nu F_\nu d\nu, \quad (\text{E.1})$$

with F_ν the radiative energy flux in the frequency range $d\nu$ and σ_ν the absorption cross-section. However, this equation does not consider the different states of ionisation and the associated transitions.

Indeed we can divided radiative accelerations into two contributions.

The bound-bound transition:

$$g_{i,\text{line}} = \frac{1}{A_i m_p c N_i} \sum_l N_{i,k} \int_0^\infty \sigma_{i,l} \phi_\nu d\nu. \quad (\text{E.2})$$

The bound-free transition:

$$g_{i,\text{cont}} = \frac{1}{A_i m_p c N_i} \sum_j N_{i-1,j} \int_{\frac{\chi_{i-1,j}}{h}}^\infty f_{i-1,j}(\nu) \sigma_{i-1,j} \phi_\nu d\nu. \quad (\text{E.3})$$

where c is the speed of light, h is the Planck constant, $N_{i,k}$ is the number density of ion X^i in an energetic state k before absorption of a photon from l transition, ϕ_ν is the energetic flux of the photon, $\sigma_{i,l}$ is the cross section of the absorption of the transition l at frequency ν , $f_{i-1,j}$ is a term taking into account that only a part of the momentum is transferred to ion X^i and finally $\chi_{i-1,j}$ is the ionisation potential of the element X from level j .

Finally we have the total acceleration on an element X as:

$$g_{\text{rad},X} = \frac{\sum_i N_i (g_{i,\text{line}} + g_{i,\text{cont}})}{\sum_i N_i} \quad (\text{E.4})$$

A more general equation is also given according to Richard (1999); Michaud et al. (2015), assuming the approximation of a thick medium, as:

$$g_{\text{rad}} = \frac{\pi k_B^4}{2h^3 c^3} \frac{R^2 \bar{\kappa}_R T_{\text{eff}}^4 N_{ik}}{A_i m_p N_i} \int_0^\infty \frac{\sigma_{ikm}}{\kappa} P(u) du \quad (\text{E.5})$$

where $\bar{\kappa}_R$ is the Rosseland mean opacity, κ is the total monochromatic opacity, σ_{ikm} is the cross-section of the transition (k, m) of the element i , R is the stellar radius, and $P(u)$ characterises the radiative transfer with $P(u) = u^4 e^u / (e^u - 1)^2$ and $u = \frac{h\nu}{k_B T}$.

The computation of these equations requires a large database of atomic physics and opacities. This implies a large time-consumption to compute radiative accelerations for each element and at each step. Moreover, Richer et al. (1998); Turcotte et al. (1998b); Deal et al. (2018, 2020) showed that the effect of radiative accelerations is weak for stars with $M < 1.1 - 1.2M_\odot$. Consequently, the contribution of g_{rad} is often neglected for solar-type stars.

Nevertheless, in the recent years a method was developed and updated to compute these terms more quickly (Alecian & LeBlanc 2002; LeBlanc & Alecian 2004; Alecian & LeBlanc 2020). They developed the Single Valued Parameters method (hereafter: SVP) where they assume that we can separate the term of concentration from terms connected to atomic data. This avoids the necessity to recompute all the terms at each variation of the concentration. With the help of this approximation, they rewrite Eq. (E.2):

$$g_{i,\text{line}} = q\phi_i^* (1 + \xi_i^* c_i) \left(1 + \frac{c_i}{p\psi_i^{*2}} \right)^\alpha, \quad (\text{E.6})$$

with

$$q = 5.575 \times 10^{-5} \frac{T_{\text{eff}}^4}{T} \left(\frac{R}{r} \right)^2 \frac{1}{A}, \quad (\text{E.7})$$

and

$$p = 9.83 \times 10^{-23} \frac{n_e T^{-1/2}}{X_H}, \quad (\text{E.8})$$

where X_H is the hydrogen mass fraction and A is the atomic mass in atomic units of the considered species. Parameters ϕ_i^* , ψ_i^* and ξ_i^* are the values of ϕ_i , ψ_i and ξ_i where the relative population of ion i is close to its maximum. Alecian & LeBlanc (2020) gives their expression as:

$$\phi_i = \frac{g_{i,0}}{q}, \quad (\text{E.9})$$

where $g_{i,0}$ is defined in Eq. (11) of Alecian & LeBlanc (2002) and refers to the radiative acceleration of ion i when its concentration is vanishing.

$$\psi_i = \left(\frac{c_{i,S}}{p} \right)^{1/2}, \quad (\text{E.10})$$

where $c_{i,S}$ is defined in Eq. (14) of Alecian & LeBlanc (2002) and refers to the concentration of ion i above which saturation of lines is strong.

$$\xi_i = \frac{N_A}{N_i} \frac{\sum_l (\bar{\delta}_A - \delta_{il}) \left(\frac{\eta_{il}\gamma_{il}}{\kappa_{med}} \right)^{1/2} P_l}{\sum_l \left(\frac{\eta_{il}\gamma_{il}}{\kappa_{med}} \right)^{1/2} P_l}, \quad (\text{E.11})$$

defined in Eq. (15) of Alecian & LeBlanc (2002) and where γ_{il} is a factor dependent on the considered transition, δ_{il} , δ_A are defined in Eq. (5) and η_{il} , P_l are defined in Eq. (7) of Alecian & LeBlanc (2002).

They rewrite E.3 as:

$$g_{i,\text{cont}} \approx 7.16 \times 10^{-26} \frac{N_e T_{\text{eff}}^4}{T^{1.5}} \left(\frac{R}{r A_E} \right)^2 a_i \Theta_i \left(\frac{\chi}{A + \chi} \right)^{b_i}, \quad (\text{E.12})$$

where Θ_i is given (including a_i) in Eq. (5) of LeBlanc & Alecian (2004).

Alecian & LeBlanc (2020) provides all the useful routines and data that can be downloaded from the website <http://gradsvp.obspm.fr>. The routines can be implemented in the STAREVOL code in order to compute radiative accelerations.

This method allows to have good results with an acceptable computing time and we could consequently add this computation to our formalism of atomic diffusion.

At the diffusion point of view, the consideration of radiative accelerations leads to an effect opposed to the gradient of pressure. If gravity leads elements toward the centre of the star, radiative accelerations shall lead elements outward.

This phenomenon stays negligible as long as stellar mass is smaller than approximately 1.1-1.2 M_\odot and for solar metallicity but it becomes important when for metal-poor stars and/or stars with $M > 1.2M_\odot$. See for instance the effects of g_{rad} in Figs. E.1 and E.2. Moreover its effect concerns mainly heavy elements (e.g. Al, Mg, Fe).

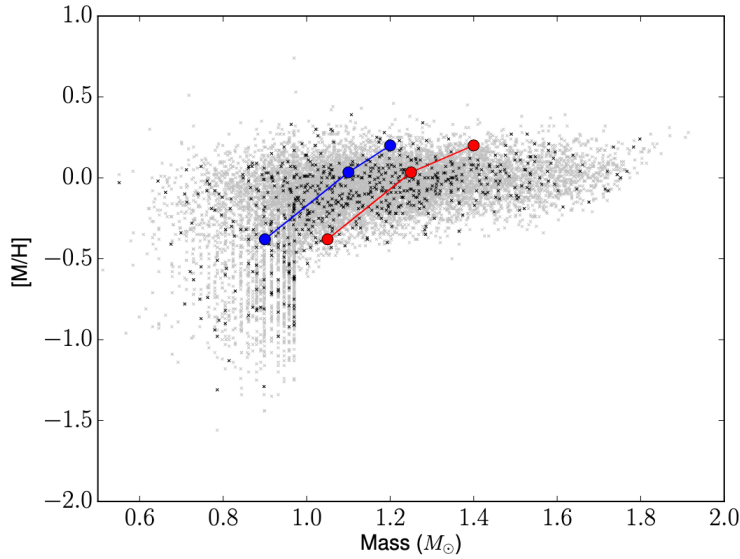


Figure E.1: Metallicity according to the mass of a population simulation of the PLATO (grey crosses) and *Kepler* (black crosses) core programme stars. The selected stars are from K7 to F5 with magnitudes in the range $4 < V < 11$, effective temperature in the range $4030 < T_{\text{eff}} < 6650$ K, and luminosity classes between IV and V. The blue and red points correspond to the models listed in Fig. E.2, which represent masses when g_{rad} needs to be taken into account (from Deal et al. 2018).

Table 4. Mass above which g_{rad} has a non-negligible effect on seismic predictions.

Grid	1	2	3
$[\text{Fe}/\text{H}]_{\text{ini}}$	-0.35	0.035	+0.25
Mass limit A ^a (M_\odot)	0.9	1.1	1.2
Mass limit B ^b (M_\odot)	1.05	1.25	1.4

Notes. ^(a) Limit determined from the differences obtained in $\Delta\nu_0$ with an uncertainty of $0.05 \mu\text{Hz}$ (A). ^(b) Limit determined from the differences in $\Delta\nu_0$ with an uncertainty of $0.2 \mu\text{Hz}$ (B).

Figure E.2: Table 4. extracted from Deal et al. (2018)

Non-standard processes

More efficient mechanisms are required for the transport of angular momentum (and consequently to the indirect transport of chemicals) which could be driven by internal gravity waves or magnetic processes and instabilities (e.g. Schatzman 1993; Spruit 2002; Charbonnel & Talon 2005; Mathis & Zahn 2005; Eggenberger et al. 2005, 2010b, 2019b,c; Denissenkov et al. 2010; Charbonnel et al. 2013; Fuller et al. 2019; Pinçon et al. 2017; Belkacem et al. 2015). However, no current prescription provides a complete solution. The most promising ones are linked to internal gravity waves and to the effect of magnetic instabilities (see Maeder 2009, for a detailed description).

F.1 Internal gravity waves

Internal gravity waves are generated at the interface between the convective and the radiative zone or thanks to the penetration of convective plumes in the radiative zone. They propagate in the central regions of the star and are sensitive to the Coriolis acceleration, and also to the magnetic field as magneto-gravity waves (Mathis et al. 2008; Mathis & de Brye 2012). They have been shown to be an efficient process to transport angular momentum and decrease the rotation of the core (e.g. Charbonnel & Talon 2005; Talon & Charbonnel 2008; Charbonnel et al. 2013). It is a relevant process to include for the evolution of low-mass stars like the Sun. However, we need additional studies to constrain the effect of internal gravity waves in different contexts (for instance different initial stellar velocity, mass loss, magnetic braking). Finally, recent work concerning the generation of internal gravity waves by penetrative convection plume could improve the treatment of internal gravity waves in 1D stellar evolution codes (Pinçon et al. 2016, 2017).

F.2 Tayler-Spruit instability

The effect of magnetic instabilities, mainly the Tayler instability (Tayler 1973), are also studied as promising candidate for the transport of angular momentum. Spruit (2002) proposed a process known as the Tayler-Spruit dynamo from the interaction between the magnetic instability and the differential rotation in the star. It generates an efficient transport of angular momentum that leads to a rotation profile of the Sun that agrees with the one inferred by helioseismology. However, the evolution at more evolved phase seems to be unable to reproduce observational constraints for SGB and RGB stars. A recent revision was proposed by Fuller et al. (2019) where a magnetic cascade is invoked in place of the Tayler-Spruit dynamo. The first results lead to a good agreement with the observational data obtained by asteroseismology for RGB, however Eggenberger et al. (2019c) pointed out that this formalism is unable to reproduce simultaneously the observational

data obtained for both SGB and RGB.

Indeed, one expects a decrease of the angular momentum transport during the SGB phase and an increase of it during the RGB. This inversion represents a challenge for the different hypothesis for the transport of angular momentum.

F.3 Advection-diffusion equation

The advection-diffusion equation that leads the transport of angular momentum can then be written as:

$$\rho \frac{d}{dt}(r^2 \Omega) = \underbrace{\frac{1}{5r^2} \frac{\partial}{\partial r}(\rho r^4 \Omega U_2)}_{\text{Advection term}} + \underbrace{\frac{1}{r^2} \frac{\partial}{\partial r} \left((\nu_v + \nu_B) r^4 \frac{\partial \Omega}{\partial r} \right)}_{\text{Diffusive term}} \pm \underbrace{2 \frac{3}{8\pi} \frac{1}{r^2} \frac{\partial}{\partial r} \mathcal{L}_J(r)}_{\text{Internal gravity waves term}}, \quad (\text{F.1})$$

with the magnetic viscosity term from the Tayler-Spruit dynamo:

$$\nu_B = \frac{\Omega r^2}{q} \frac{\omega_A^3}{\Omega} \frac{\Omega}{N}, \quad (\text{F.2})$$

with the Alfvén frequency $\omega_A^2 = \frac{B^2}{4\pi r^2 \rho}$.

And with the gravity wave luminosity $\mathcal{L}_J(r)$ as:

$$\mathcal{L}_J(r) = \sum_{\sigma, l, m} \mathcal{L}_{J, l, m}(r_e) \exp^{-\tau(r, \sigma, l)} + \sum_{\sigma, l, m} \mathcal{L}_{J, l, m}(r_c) \exp^{-\tau(r, \sigma, l)}, \quad (\text{F.3})$$

with τ the local damping factor as:

$$\tau(r, \sigma, l) = [l(l+1)]^{3/2} \int_r^{r_{cz}} (\kappa_T + \nu_v) \frac{N N_T^2}{\sigma} \left(\frac{N^2}{N^2 - \sigma^2} \right)^{1/2} \frac{dr}{r^3} \quad (\text{F.4})$$

Bibliography

- Aerts, C., Mathis, S., & Rogers, T. M. 2019, *ARA&A*, 57, 35
- Agüeros, M. A., Covey, K. R., Lemonias, J. J., et al. 2011, *ApJ*, 740, 110
- Aigrain, S., Llama, J., Ceillier, T., et al. 2015, *MNRAS*, 450, 3211
- Alecian, G. & LeBlanc, F. 2002, *MNRAS*, 332, 891
- Alecian, G. & LeBlanc, F. 2020, *MNRAS*, 498, 3420
- Allard, F., Homeier, D., & Freytag, B. 2012, in *IAU Symposium*, Vol. 282, *From Interacting Binaries to Exoplanets: Essential Modeling Tools*, ed. M. T. Richards & I. Hubeny, 235–242
- Allen, C. W. 1976, *Astrophysical Quantities*
- Aller, L. H. & Chapman, S. 1960, *ApJ*, 132, 461
- Amard, L. 2016, PhD thesis, Universite de Montpellier, France - Observatoire de Geneve, Suisse
- Amard, L., Palacios, A., Charbonnel, C., Gallet, F., & Bouvier, J. 2016, *A&A*, 587, A105
- Amard, L., Palacios, A., Charbonnel, C., et al. 2019, *A&A*, 631, A77
- Anders, E. & Grevesse, N. 1989, , 53, 197
- Angulo, C., Arnould, M., Rayet, M., et al. 1999, *Nucl. Phys. A*, 656, 3
- Anthony-Twarog, B. J., Deliyannis, C. P., Twarog, B. A., Croxall, K. V., & Cummings, J. D. 2009, *AJ*, 138, 1171
- Appourchaux, T., Antia, H. M., Ball, W., et al. 2015, *A&A*, 582, A25
- Appourchaux, T., Belkacem, K., Broomhall, A. M., et al. 2010, *A&A Rev.*, 18, 197
- Arnould, M., Goriely, S., & Jorissen, A. 1999, *A&A*, 347, 572
- Asplund, M., Grevesse, N., & Sauval, A. J. 2005, in *Astronomical Society of the Pacific Conference Series*, Vol. 336, *Cosmic Abundances as Records of Stellar Evolution and Nucleosynthesis*, ed. I. Barnes, Thomas G. & F. N. Bash, 25
- Asplund, M., Grevesse, N., Sauval, A. J., & Scott, P. 2009, *ARA&A*, 47, 481
- Augustson, K. C., Brown, B. P., Brun, A. S., Miesch, M. S., & Toomre, J. 2012, *ApJ*, 756, 169
- Augustson, K. C. & Mathis, S. 2019, *ApJ*, 874, 83

- Augustson, K. C. & Mathis, S. 2020, in *Stars and their Variability Observed from Space*, ed. C. Neiner, W. W. Weiss, D. Baade, R. E. Griffin, C. C. Lovekin, & A. F. J. Moffat, 311–312
- Baglin, A. & Lebreton, Y. 1990, *Astrophysics and Space Science Library*, Vol. 159, *Surface Abundances of Light Elements as Diagnostic of Transport Processes in the Sun and Solar-Type Stars*, ed. G. Berthomieu & M. Cribier, 437
- Baglin, A., Morel, P. J., & Schatzman, E. 1985, *A&A*, 149, 309
- Bahcall, J. N. & Loeb, A. 1990, *ApJ*, 360, 267
- Bahcall, J. N. & Pinsonneault, M. H. 1992, *Reviews of Modern Physics*, 64, 885
- Bahcall, J. N., Pinsonneault, M. H., & Wasserburg, G. J. 1995, *Reviews of Modern Physics*, 67, 781
- Balachandran, S. 1995, *ApJ*, 446, 203
- Balachandran, S. C., Mallik, S. V., & Lambert, D. L. 2011, *MNRAS*, 410, 2526
- Ballot, J., García, R. A., & Lambert, P. 2006, *MNRAS*, 369, 1281
- Ballot, J., Gizon, L., Samadi, R., et al. 2011, *A&A*, 530, A97
- Baraffe, I., Pratt, J., Goffrey, T., et al. 2017, *ApJL*, 845, L6
- Barker, A. J., Dempsey, A. M., & Lithwick, Y. 2014, *ApJ*, 791, 13
- Barnes, S. A., Weingrill, J., Fritzewski, D., Strassmeier, K. G., & Platais, I. 2016, *ApJ*, 823, 16
- Barrado y Navascués, D., Deliyannis, C. P., & Stauffer, J. R. 2001, *ApJ*, 549, 452
- Bastian, N. & Lardo, C. 2018, *ARA&A*, 56, 83
- Basu, S. & Antia, H. M. 1995, *MNRAS*, 276, 1402
- Basu, S., Antia, H. M., & Narasimha, D. 1994, *MNRAS*, 267, 209
- Baturin, V. A., Gorshkov, A. B., & Ayukov, S. V. 2006, *Astronomy Reports*, 50, 1001
- Beck, P. G., do Nascimento, J. D., J., Duarte, T., et al. 2017, *A&A*, 602, A63
- Bedin, L. R., Piotto, G., Anderson, J., et al. 2004, *ApJL*, 605, L125
- Belkacem, K., Marques, J. P., Goupil, M. J., et al. 2015, *A&A*, 579, A31
- Bellini, A., Milone, A. P., Anderson, J., et al. 2017, *ApJ*, 844, 164
- Benomar, O., Takata, M., Shibahashi, H., Ceillier, T., & García, R. A. 2015, *MNRAS*, 452, 2654
- Blancard, C., Cossé, P., & Faussurier, G. 2012, *ApJ*, 745, 10
- Boesgaard, A. M. 1976, *PASP*, 88, 353
- Boesgaard, A. M. 1987, *PASP*, 99, 1067
- Boesgaard, A. M. 1991, *ApJL*, 370, L95
- Boesgaard, A. M., Armengaud, E., & King, J. R. 2003a, *ApJ*, 583, 955
- Boesgaard, A. M., Armengaud, E., & King, J. R. 2003b, *ApJ*, 582, 410

- Boesgaard, A. M., Armengaud, E., & King, J. R. 2004, *ApJ*, 605, 864
- Boesgaard, A. M., Budge, K. G., & Ramsay, M. E. 1988, *ApJ*, 327, 389
- Boesgaard, A. M., Deliyannis, C. P., Stephens, A., & King, J. R. 1998, *ApJ*, 493, 206
- Boesgaard, A. M., Lum, M. G., & Deliyannis, C. P. 2020, *ApJ*, 888, 28
- Boesgaard, A. M., Lum, M. G., Deliyannis, C. P., et al. 2016, *ApJ*, 830, 49
- Boesgaard, A. M. & Tripicco, M. J. 1986, *ApJL*, 302, L49
- Böhm-Vitense, E. 1958, *Zeitschrift für Astrophysik*, 46, 108
- Bossini, D., Vallenari, A., Bragaglia, A., et al. 2019, *A&A*, 623, A108
- Bouvier, J. 2008, *A&A*, 489, L53
- Bouvier, J., Barrado, D., Moraux, E., et al. 2018, *A&A*, 613, A63
- Breton, S. N., Santos, A. R. G., Bugnet, L., et al. 2021, *A&A*, 647, A125
- Brown, T. M. 1985, *Nature*, 317, 591
- Brummell, N. H. 2007, in *IAU Symposium, Vol. 239, Convection in Astrophysics*, ed. F. Kupka, I. Roxburgh, & K. L. Chan, 417–424
- Brun, A. S., Strugarek, A., Varela, J., et al. 2017, *ApJ*, 836, 192
- Brun, A. S., Turck-Chièze, S., & Zahn, J. P. 1999, *ApJ*, 525, 1032
- Buldgen, G., Salmon, S. J. A. J., Noels, A., et al. 2019, *A&A*, 621, A33
- Burgers, J. M. 1960, *Statistical Plasma Mechanics. Chapter V of Plasma Dynamics*, ed. by FH Clauser
- Burgers, J. M. 1969, *Flow Equations for Composite Gases*
- Caffau, E., Ludwig, H. G., Steffen, M., Freytag, B., & Bonifacio, P. 2011, *Sol. Phys.*, 268, 255
- Capelo, D. & Lopes, I. 2020, *MNRAS*, 498, 1992
- Carlos, M., Meléndez, J., do Nascimento, J.-D., & Castro, M. 2020, *MNRAS*, 492, 245
- Carlos, M., Meléndez, J., Spina, L., et al. 2019, *MNRAS*, 485, 4052
- Carlsson, M., Rutten, R. J., Bruls, J. H. M. J., & Shchukina, N. G. 1994, *A&A*, 288, 860
- Carretta, E., Bragaglia, A., Gratton, R. G., et al. 2009, *A&A*, 505, 117
- Ceillier, T. 2015, PhD thesis, Université Paris-Diderot
- Ceillier, T., Eggenberger, P., García, R. A., & Mathis, S. 2013, *A&A*, 555, A54
- Chaboyer, B. & Zahn, J. P. 1992, *A&A*, 253, 173
- Chandrasekhar, S. 1933, *MNRAS*, 94, 14
- Chantereau, W., Charbonnel, C., & Decressin, T. 2015, *A&A*, 578, A117
- Chantereau, W., Charbonnel, C., & Meynet, G. 2016, *A&A*, 592, A111

- Chantereau, W., Charbonnel, C., & Meynet, G. 2017, *A&A*, 602, A13
- Chaplin, W. J. & Miglio, A. 2013, *ARA&A*, 51, 353
- Chapman, S. 1917a, *MNRAS*, 77, 540
- Chapman, S. 1917b, *MNRAS*, 77, 539
- Chapman, S. & Cowling, T. G. 1970, *The mathematical theory of non-uniform gases. an account of the kinetic theory of viscosity, thermal conduction and diffusion in gases*
- Charbonnel, C. 2016, in *EAS Publications Series, Vol. 80-81, EAS Publications Series*, 177–226
- Charbonnel, C., Decressin, T., Amard, L., Palacios, A., & Talon, S. 2013, *A&A*, 554, A40
- Charbonnel, C., Deliyannis, C. P., & Pinsonneault, M. 2000, in *The Light Elements and their Evolution*, ed. L. da Silva, R. de Medeiros, & M. Spite, Vol. 198, 87
- Charbonnel, C., Lagarde, N., Jasniewicz, G., et al. 2020, *A&A*, 633, A34
- Charbonnel, C. & Lebreton, Y. 1993, *A&A*, 280, 666
- Charbonnel, C. & Talon, S. 2005, *Science*, 309, 2189
- Charbonnel, C., Tosi, M., Primas, F., & Chiappini, C., eds. 2010, *Light Elements in the Universe (IAU S268)*, Vol. 268
- Charbonnel, C., Vauclair, S., Maeder, A., Meynet, G., & Schaller, G. 1994, *A&A*, 283, 155
- Charbonnel, C., Vauclair, S., & Zahn, J. P. 1992, *A&A*, 255, 191
- Chen, Y. Q. & Zhao, G. 2006, *AJ*, 131, 1816
- Choi, J., Dotter, A., Conroy, C., & Ting, Y.-S. 2018, *ApJ*, 860, 131
- Christensen-Dalsgaard, J. 1982, *MNRAS*, 199, 735
- Christensen-Dalsgaard, J. & Daeppen, W. 1992, *A&A Rev.*, 4, 267
- Christensen-Dalsgaard, J., Duvall, T. L., J., Gough, D. O., Harvey, J. W., & Rhodes, E. J., J. 1985a, *Nature*, 315, 378
- Christensen-Dalsgaard, J., Gough, D., & Toomre, J. 1985b, *Science*, 229, 923
- Christensen-Dalsgaard, J., Gough, D. O., & Thompson, M. J. 1991, *ApJ*, 378, 413
- Christensen-Dalsgaard, J., Monteiro, M. J. P. F. G., Rempel, M., & Thompson, M. J. 2011, *MNRAS*, 414, 1158
- Christensen-Dalsgaard, J., Proffitt, C. R., & Thompson, M. J. 1993, *ApJL*, 403, L75
- Christensen-Dalsgaard, J. & Schou, J. 1988, in *ESA Special Publication, Vol. 286, Seismology of the Sun and Sun-Like Stars*, ed. E. J. Rolfe, 149–153
- Coc, A. & Vangioni, E. 2017, *International Journal of Modern Physics E*, 26, 1741002
- Colgan, J., Kilcrease, D. P., Magee, N. H., et al. 2016, *ApJ*, 817, 116
- Cox, A. N., Morgan, S. M., Rogers, F. J., & Iglesias, C. A. 1992, *ApJ*, 393, 272

-
- Cranmer, S. R. & Saar, S. H. 2011, *ApJ*, 741, 54
- Cummings, J. D., Deliyannis, C. P., Anthony-Twarog, B., Twarog, B., & Maderak, R. M. 2012, *AJ*, 144, 137
- Cummings, J. D., Deliyannis, C. P., Maderak, R. M., & Steinhauer, A. 2017, *AJ*, 153, 128
- Cunha, K., Hubeny, I., & Lanz, T. 2006, *ApJL*, 647, L143
- Cyburt, R. H., Amthor, A. M., Ferguson, R., et al. 2010, *ApJS*, 189, 240
- Deal, M., Alecian, G., Lebreton, Y., et al. 2018, *A&A*, 618, A10
- Deal, M., Goupil, M. J., Marques, J. P., Reese, D. R., & Lebreton, Y. 2020, *A&A*, 633, A23
- Decressin, T., Mathis, S., Palacios, A., et al. 2009, *A&A*, 495, 271
- Deheuvels, S., Ballot, J., Beck, P. G., et al. 2015, *A&A*, 580, A96
- Deheuvels, S., Ballot, J., Eggenberger, P., et al. 2020, *A&A*, 641, A117
- Deheuvels, S., Doğan, G., Goupil, M. J., et al. 2014, *A&A*, 564, A27
- Deheuvels, S., García, R. A., Chaplin, W. J., et al. 2012, *ApJ*, 756, 19
- Delgado Mena, E., Israelian, G., González Hernández, J. I., Santos, N. C., & Rebolo, R. 2012, *ApJ*, 746, 47
- Delgado Mena, E., Israelian, G., González Hernández, J. I., et al. 2014, *A&A*, 562, A92
- Deliyannis, C. P., Anthony-Twarog, B. J., Lee-Brown, D. B., & Twarog, B. A. 2019, *AJ*, 158, 163
- Deliyannis, C. P., Pinsonneault, M. H., & Charbonnel, C. 2000, in *The Light Elements and their Evolution*, ed. L. da Silva, R. de Medeiros, & M. Spite, Vol. 198, 61
- Delorme, P., Collier Cameron, A., Hebb, L., et al. 2011, *MNRAS*, 413, 2218
- Denissenkov, P. A., Pinsonneault, M., Terndrup, D. M., & Newsham, G. 2010, *ApJ*, 716, 1269
- Do Nascimento, J. D., J., Castro, M., Meléndez, J., et al. 2009, *A&A*, 501, 687
- do Nascimento, J. D., J., Charbonnel, C., Lèbre, A., de Laverny, P., & De Medeiros, J. R. 2000, *A&A*, 357, 931
- do Nascimento, J. D., J., de Almeida, L., Velloso, E. N., et al. 2020, *ApJ*, 898, 173
- Do Nascimento, J. D., da Costa, J. S., & de Medeiros, J. R. 2010, *A&A*, 519, A101
- Domingo, V., Fleck, B., & Poland, A. I. 1995, *Sol. Phys.*, 162, 1
- Donahue, R. A., Saar, S. H., & Baliunas, S. L. 1996, *ApJ*, 466, 384
- dos Santos, L. A., Meléndez, J., do Nascimento, J.-D., et al. 2016, *A&A*, 592, A156
- Douglas, S. T., Agüeros, M. A., Covey, K. R., et al. 2016, *ApJ*, 822, 47
- Douglas, S. T., Agüeros, M. A., Covey, K. R., & Kraus, A. 2017, *ApJ*, 842, 83
- Douglas, S. T., Curtis, J. L., Agüeros, M. A., et al. 2019, *ApJ*, 879, 100
- Dufour, E. 2000, PhD thesis, Université Joseph Fourier à Grenoble 1
-

- Dumont, T., Palacios, A., Charbonnel, C., et al. 2021, *A&A*, 646, A48
- Eddington, A. S. 1926, *The Internal Constitution of the Stars*
- Eddington, A. S. 1929, *MNRAS*, 90, 54
- Eff-Darwich, A., Korzennik, S. G., Jiménez-Reyes, S. J., & García, R. A. 2008, *ApJ*, 679, 1636
- Eggenberger, P., Buldgen, G., & Salmon, S. J. A. J. 2019a, *A&A*, 626, L1
- Eggenberger, P., Deheuvels, S., Miglio, A., et al. 2019b, *Astronomy and Astrophysics*, 621, A66
- Eggenberger, P., den Hartogh, J. W., Buldgen, G., et al. 2019c, *A&A*, 631, L6
- Eggenberger, P., Haemmerlé, L., Meynet, G., & Maeder, A. 2012a, *A&A*, 539, A70
- Eggenberger, P., Lagarde, N., Miglio, A., et al. 2017, *A&A*, 599, A18
- Eggenberger, P., Maeder, A., & Meynet, G. 2005, *A&A*, 440, L9
- Eggenberger, P., Maeder, A., & Meynet, G. 2009, *Proceedings of the International Astronomical Union*, 5, 381â386
- Eggenberger, P., Maeder, A., & Meynet, G. 2010a, *A&A*, 519, L2
- Eggenberger, P., Meynet, G., Maeder, A., et al. 2008, *Ap&SS*, 316, 43
- Eggenberger, P., Meynet, G., Maeder, A., et al. 2010b, *A&A*, 519, A116
- Eggenberger, P., Montalbán, J., & Miglio, A. 2012b, *Astronomy and Astrophysics*, 544, L4
- Eggleton, P. P., Faulkner, J., & Flannery, B. P. 1973, *A&A*, 23, 325
- Ekström, S., Georgy, C., Eggenberger, P., et al. 2012, *A&A*, 537, A146
- Elliott, J. R. & Gough, D. O. 1999, *ApJ*, 516, 475
- Elsworth, Y., Howe, R., Isaak, G. R., et al. 1995, *Nature*, 376, 669
- Espinosa Lara, F. & Rieutord, M. 2013, *A&A*, 552, A35
- Farnir, M., Dupret, M. A., Salmon, S. J. A. J., Noels, A., & Buldgen, G. 2019, *A&A*, 622, A98
- Ferguson, J. W., Alexander, D. R., Allard, F., et al. 2005, *ApJ*, 623, 585
- Fossat, E., Boumier, P., Corbard, T., et al. 2017, *A&A*, 604, A40
- François, P., Pasquini, L., Biazzo, K., Bonifacio, P., & Palsa, R. 2013, *A&A*, 552, A136
- Fu, X., Romano, D., Bragaglia, A., et al. 2018, *A&A*, 610, A38
- Fuller, J., Lecoanet, D., Cantiello, M., & Brown, B. 2014, *ApJ*, 796, 17
- Fuller, J., Piro, A. L., & Jermyn, A. S. 2019, *MNRAS*, 485, 3661
- Gabriel, A. H., Grec, G., Charra, J., et al. 1995, *Sol. Phys.*, 162, 61
- Gagnier, D. & Garaud, P. 2018, *ApJ*, 862, 36
- Gaia Collaboration, Brown, A. G. A., Vallenari, A., et al. 2018, *A&A*, 616, A1

- Gallet, F. & Bouvier, J. 2013, *A&A*, 556, A36
- Gallet, F. & Bouvier, J. 2015, *A&A*, 577, A98
- Gallet, F., Zanni, C., & Amard, L. 2019, *A&A*, 632, A6
- Gálvez-Ortiz, M. C., Delgado-Mena, E., González Hernández, J. I., et al. 2011, *A&A*, 530, A66
- Garaud, P., Gagnier, D., & Verhoeven, J. 2017, *ApJ*, 837, 133
- García, R. A. & Ballot, J. 2019, *Living Reviews in Solar Physics*, 16, 4
- García, R. A., Ceillier, T., Salabert, D., et al. 2014, *A&A*, 572, A34
- García, R. A., Turck-Chièze, S., Jiménez-Reyes, S. J., et al. 2007, *Science*, 316, 1591
- García Lopez, R. J. & Perez de Taoro, M. R. 1998, *A&A*, 334, 599
- Gehan, C., Mosser, B., Michel, E., Samadi, R., & Kallinger, T. 2018, *A&A*, 616, A24
- Godoy-Rivera, D., Pinsonneault, M. H., & Rebull, L. M. 2021, arXiv e-prints, arXiv:2101.01183
- Gordon, T. A., Davenport, J. R. A., Angus, R., et al. 2021, *ApJ*, 913, 70
- Gorshkov, A. B. & Baturin, V. A. 2008, *Astronomy Reports*, 52, 760
- Gossage, S., Dotter, A., Garraffo, C., et al. 2020, arXiv e-prints, arXiv:2011.02470
- Gough, D. O. & McIntyre, M. E. 1998, *Nature*, 394, 755
- Graboske, H. C., Dewitt, H. E., Grossman, A. S., & Cooper, M. S. 1973, *ApJ*, 181, 457
- Gratton, R. G., Bonifacio, P., Bragaglia, A., et al. 2001, *A&A*, 369, 87
- Gratton, R. G., Carretta, E., & Bragaglia, A. 2012, *A&A Rev.*, 20, 50
- Greenstein, J. L. & Richardson, R. S. 1951, *ApJ*, 113, 536
- Grevesse, N. & Noels, A. 1993, in *Origin and Evolution of the Elements*, ed. N. Prantzos, E. Vangioni-Flam, & M. Casse, 15–25
- Grevesse, N. & Sauval, A. J. 1998, *Space Sci. Rev.*, 85, 161
- Grisoni, V., Matteucci, F., Romano, D., & Fu, X. 2019, *MNRAS*, 489, 3539
- Guiglion, G., de Laverny, P., Recio-Blanco, A., et al. 2016, *A&A*, 595, A18
- Guo, J., Lin, L., Bai, C., & Liu, J. 2017, *Ap&SS*, 362, 15
- Gutiérrez Albarrán, M. L., Montes, D., Gómez Garrido, M., et al. 2020, *A&A*, 643, A71
- Guzik, J. A. & Mussack, K. 2010, *ApJ*, 713, 1108
- Hartman, J. D., Bakos, G. Á., Kovács, G., & Noyes, R. W. 2010, *MNRAS*, 408, 475
- Hartman, J. D., Gaudi, B. S., Holman, M. J., et al. 2008, *ApJ*, 675, 1254
- Harutyunyan, G., Steffen, M., Mott, A., et al. 2018, *A&A*, 618, A16
- Herwig, F., Bloeker, T., Schoenberner, D., & El Eid, M. 1997, *A&A*, 324, L81

- Hobbs, L. M. & Pilachowski, C. 1986, *ApJL*, 309, L17
- Holzer, T. E., Fla, T., & Leer, E. 1983, *ApJ*, 275, 808
- Hopf, E. 1930, *MNRAS*, 90, 287
- Howe, R., Chaplin, W. J., Basu, S., et al. 2020, *MNRAS*, 493, L49
- Hu, H., Glebbeek, E., Thoul, A. A., et al. 2010, *A&A*, 511, A87
- Hu, H., Tout, C. A., Glebbeek, E., & Dupret, M.-A. 2011, *MNRAS*, 418, 195
- Iben, I., J. & MacDonald, J. 1985, *ApJ*, 296, 540
- Iglesias, C. A. & Rogers, F. J. 1996, *ApJ*, 464, 943
- Irwin, J., Aigrain, S., Bouvier, J., et al. 2009, *MNRAS*, 392, 1456
- Irwin, J. & Bouvier, J. 2009, in *The Ages of Stars*, ed. E. E. Mamajek, D. R. Soderblom, & R. F. G. Wyse, Vol. 258, 363–374
- Irwin, J., Hodgkin, S., Aigrain, S., et al. 2008, *MNRAS*, 384, 675
- Jeffries, R. D. 1997, *MNRAS*, 292, 177
- Jeffries, R. D. 2000, in *Astronomical Society of the Pacific Conference Series*, Vol. 198, *Stellar Clusters and Associations: Convection, Rotation, and Dynamos*, ed. R. Pallavicini, G. Micela, & S. Sciortino, 245
- Jeffries, R. D., Jackson, R. J., Sun, Q., & Deliyannis, C. P. 2021, *MNRAS*, 500, 1158
- Jeffries, R. D., Totten, E. J., Harmer, S., & Deliyannis, C. P. 2002, *MNRAS*, 336, 1109
- Kaler, J. B. 1989, *Stars and their spectra. an introduction to spectral sequence*
- Kawaler, S. D. 1988a, *ApJ*, 333, 236
- Kawaler, S. D. 1988b, *ApJ*, 333, 236
- Keen, M. A., Bedding, T. R., Murphy, S. J., et al. 2015, *MNRAS*, 454, 1792
- King, J. R., Deliyannis, C. P., Hiltgen, D. D., et al. 1997, *AJ*, 113, 1871
- King, J. R., Stephens, A., Boesgaard, A. M., & Deliyannis, C. 1998, *AJ*, 115, 666
- Kippenhahn, R., Weigert, A., & Mallik, D. C. V. 1991, *Bulletin of the Astronomical Society of India*, 19, 369
- Kiselman, D. 1997, *ApJL*, 489, L107
- Kissin, Y. & Thompson, C. 2015, *ApJ*, 808, 35
- Kitchatinov, L. L. & Rüdiger, G. 2004, *Astronomische Nachrichten*, 325, 496
- Korre, L., Garaud, P., & Brummell, N. H. 2019, *MNRAS*, 484, 1220
- Kosovichev, A. G. 1988, *Soviet Astronomy Letters*, 14, 145
- Kosovichev, A. G. & Fedorova, A. V. 1991, , 35, 507
- Kraft, R. P. 1967, *ApJ*, 150, 551

- Krishna Swamy, K. S. 1966, *ApJ*, 145, 174
- Kurucz, R. L. 1970, *SAO Special Report*, 309
- Lagarde, N., Decressin, T., Charbonnel, C., et al. 2012, *A&A*, 543, A108
- Lagarde, N., Eggenberger, P., Miglio, A., & Montalbán, J. 2014, in *SF2A-2014: Proceedings of the Annual meeting of the French Society of Astronomy and Astrophysics*, ed. J. Ballet, F. Martins, F. Bounaud, R. Monier, & C. Reylé, 483–486
- Landi, E. & Testa, P. 2015, *ApJ*, 800, 110
- Lanzafame, A. C. & Spada, F. 2015, *A&A*, 584, A30
- LeBlanc, F. & Alecian, G. 2004, *MNRAS*, 352, 1329
- Lebreton, Y., Goupil, M. J., & Montalbán, J. 2014a, in *EAS Publications Series*, Vol. 65, *EAS Publications Series*, 99–176
- Lebreton, Y., Goupil, M. J., & Montalbán, J. 2014b, in *EAS Publications Series*, Vol. 65, *EAS Publications Series*, 177–223
- Lebreton, Y. & Maeder, A. 1987, *A&A*, 175, 99
- Lebreton, Y., Montalbán, J., Christensen-Dalsgaard, J., et al. 2007, in *EAS Publications Series*, Vol. 26, *EAS Publications Series*, ed. C. W. Straka, Y. Lebreton, & M. J. P. F. G. Monteiro, 155–165
- Lind, K., Asplund, M., & Barklem, P. S. 2009, *A&A*, 503, 541
- Lodders, K., Palme, H., & Gail, H. P. 2009, *Landolt Börnrstein*, 4B, 712
- Lorenzo-Oliveira, D., Meléndez, J., Ponte, G., & Galarza, J. Y. 2020, *MNRAS*[[arXiv:2003.13871](https://arxiv.org/abs/2003.13871)]
- Maeder, A. 1997, *A&A*, 321, 134
- Maeder, A. 2003, *A&A*, 399, 263
- Maeder, A. 2009, *Physics, Formation and Evolution of Rotating Stars*
- Maeder, A. & Meynet, G. 2001, *A&A*, 373, 555
- Maeder, A. & Zahn, J.-P. 1998, *A&A*, 334, 1000
- Malherbe, J.-M. 2016, lecture
- Marques, J. P., Goupil, M. J., Lebreton, Y., et al. 2013, *A&A*, 549, A74
- Mathieu, R. D. 2000, in *Astronomical Society of the Pacific Conference Series*, Vol. 198, *Stellar Clusters and Associations: Convection, Rotation, and Dynamos*, ed. R. Pallavicini, G. Micela, & S. Sciortino, 517
- Mathis, S. 2013, *Transport Processes in Stellar Interiors*, ed. M. Goupil, K. Belkacem, C. Neiner, F. Lignières, & J. J. Green, Vol. 865, 23
- Mathis, S. & de Brye, N. 2012, *A&A*, 540, A37
- Mathis, S., Decressin, T., Palacios, A., et al. 2007, *Astronomische Nachrichten*, 328, 1062
- Mathis, S., Palacios, A., & Zahn, J. P. 2004, *A&A*, 425, 243

- Mathis, S., Prat, V., Amard, L., et al. 2018, *Astronomy and Astrophysics*, 620, A22
- Mathis, S., Talon, S., Pantillon, F. P., & Zahn, J. P. 2008, *Sol. Phys.*, 251, 101
- Mathis, S. & Zahn, J. P. 2004, *A&A*, 425, 229
- Mathis, S. & Zahn, J. P. 2005, *A&A*, 440, 653
- Mathur, S., Eff-Darwich, A., García, R. A., & Turck-Chièze, S. 2008, *A&A*, 484, 517
- Matt, S. P., Brun, A. S., Baraffe, I., Bouvier, J., & Chabrier, G. 2015a, *ApJ*, 799, L23
- Matt, S. P., Brun, A. S., Baraffe, I., Bouvier, J., & Chabrier, G. 2015b, *ApJL*, 799, L23
- Matt, S. P., Brun, A. S., Baraffe, I., Bouvier, J., & Chabrier, G. 2019, *ApJL*, 870, L27
- Matt, S. P., MacGregor, K. B., Pinsonneault, M. H., & Greene, T. P. 2012, *ApJL*, 754, L26
- McDonald, I. & Zijlstra, A. A. 2015, *MNRAS*, 448, 502
- McQuillan, A., Mazeh, T., & Aigrain, S. 2014, *ApJS*, 211, 24
- Meibom, S., Barnes, S. A., Latham, D. W., et al. 2011, *ApJL*, 733, L9
- Meibom, S., Barnes, S. A., Platais, I., et al. 2015, in *American Astronomical Society Meeting Abstracts*, Vol. 225, *American Astronomical Society Meeting Abstracts #225*, 449.09
- Meibom, S., Mathieu, R. D., & Stassun, K. G. 2009, *ApJ*, 695, 679
- Meynet, G., Ekstrom, S., Maeder, A., et al. 2013, *Models of Rotating Massive Stars: Impacts of Various Prescriptions*, ed. M. Goupil, K. Belkacem, C. Neiner, F. Lignières, & J. J. Green, Vol. 865, 3
- Michaud, G., Alecian, G., & Richer, J. 2015, *Atomic Diffusion in Stars*
- Michaud, G. & Proffitt, C. R. 1993, in *Astronomical Society of the Pacific Conference Series*, Vol. 40, *IAU Colloq. 137: Inside the Stars*, ed. W. W. Weiss & A. Baglin, 246–259
- Milone, A. P., Bedin, L. R., Piotto, G., et al. 2008, *ApJ*, 673, 241
- Mitler, H. E. 1977, *ApJ*, 212, 513
- Mondet, G., Blancard, C., Cossé, P., & Faussurier, G. 2015, *ApJS*, 220, 2
- Montalban, J. 1994, *A&A*, 281, 421
- Montalban, J., Miglio, A., Theado, S., Noels, A., & Grevesse, N. 2006, *Communications in Asteroseismology*, 147, 80
- Montalbán, J. & Rebolo, R. 2002, *A&A*, 386, 1039
- Montalban, J. & Schatzman, E. 1996, *A&A*, 305, 513
- Montalbán, J. & Schatzman, E. 2000, *A&A*, 354, 943
- Montalbán, J., Théado, S., & Lebreton, Y. 2007, in *EAS Publications Series*, Vol. 26, *EAS Publications Series*, ed. C. W. Straka, Y. Lebreton, & M. J. P. F. G. Monteiro, 167–176
- Monteiro, M. J. P. F. G., Christensen-Dalsgaard, J., & Thompson, M. J. 2000, *MNRAS*, 316, 165

- Montmerle, T. & Michaud, G. 1976, *ApJS*, 31, 489
- Morel, P., van't Veer, C., Provost, J., et al. 1994, *A&A*, 286, 91
- Mosser, B., Goupil, M. J., Belkacem, K., et al. 2012, *A&A*, 548, A10
- Netopil, M., Paunzen, E., Heiter, U., & Soubiran, C. 2016, *A&A*, 585, A150
- Nielsen, M. B., Gizon, L., Schunker, H., & Schou, J. 2014, *A&A*, 568, L12
- Pace, G., Castro, M., Meléndez, J., Théado, S., & do Nascimento, J. D., J. 2012, *A&A*, 541, A150
- Palacios, A., Talon, S., Charbonnel, C., & Forestini, M. 2003, *A&A*, 399, 603
- Paquette, C., Pelletier, C., Fontaine, G., & Michaud, G. 1986, *ApJS*, 61, 177
- Paxton, B., Bildsten, L., Dotter, A., et al. 2011, *ApJS*, 192, 3
- Paxton, B., Schwab, J., Bauer, E. B., et al. 2018, *ApJS*, 234, 34
- Piau, L. & Turck-Chièze, S. 2002, *ApJ*, 566, 419
- Pinçon, C., Belkacem, K., & Goupil, M. J. 2016, *A&A*, 588, A122
- Pinçon, C., Belkacem, K., Goupil, M. J., & Marques, J. P. 2017, *A&A*, 605, A31
- Pinsonneault, M. 1997, *ARA&A*, 35, 557
- Pinsonneault, M. H. 2009, *Proceedings of the International Astronomical Union*, 5, 375â380
- Pinsonneault, M. H., Charbonnel, C., & Deliyannis, C. P. 2000, in *The Light Elements and their Evolution*, ed. L. da Silva, R. de Medeiros, & M. Spite, Vol. 198, 74
- Pinsonneault, M. H., Kawaler, S. D., & Demarque, P. 1990, *ApJS*, 74, 501
- Piotto, G. 2009, in *IAU Symposium*, Vol. 258, *The Ages of Stars*, ed. E. E. Mamajek, D. R. Soderblom, & R. F. G. Wyse, 233–244
- Piotto, G., Bedin, L. R., Anderson, J., et al. 2007, *ApJL*, 661, L53
- Pols, O. R., Tout, C. A., Eggleton, P. P., & Han, Z. 1995, *MNRAS*, 274, 964
- Portinari, L., Casagrande, L., & Flynn, C. 2010, *MNRAS*, 406, 1570
- Potekhin, A. Y. & Chabrier, G. 2010, *Contributions to Plasma Physics*, 50, 82
- Prantzos, N., Charbonnel, C., & Iliadis, C. 2017a, *A&A*, 608, A28
- Prantzos, N., de Laverny, P., Guiglion, G., Recio-Blanco, A., & Worley, C. C. 2017b, *A&A*, 606, A132
- Prat, V., Guilet, J., Viallet, M., & Müller, E. 2016, *A&A*, 592, A59
- Prat, V. & Lignières, F. 2013, *A&A*, 551, L3
- Prat, V. & Lignières, F. 2014, *A&A*, 566, A110
- Pratt, J., Baraffe, I., Goffrey, T., et al. 2017, *A&A*, 604, A125
- Proffitt, C. R. 1994, *ApJ*, 425, 849

- Proffitt, C. R. & Michaud, G. 1991, *ApJ*, 380, 238
- Randich, S. 2009, *Proceedings of the International Astronomical Union*, 5, 275â283
- Randich, S., Pallavicini, R., Meola, G., Stauffer, J. R., & Balachandran, S. C. 2001, *A&A*, 372, 862
- Randich, S., Pasquini, L., Franciosini, E., et al. 2020, *A&A*, 640, L1
- Rebull, L. M., Stauffer, J. R., Bouvier, J., et al. 2016, *AJ*, 152, 113
- Reddy, B. E., Lambert, D. L., & Allende Prieto, C. 2006, *MNRAS*, 367, 1329
- Reimers, D. 1975, *Memoires of the Societe Royale des Sciences de Liege*, 8, 369
- Richard, D. & Zahn, J.-P. 1999, *A&A*, 347, 734
- Richard, O. 1999, PhD thesis, Observatoire Midi-Pyrénées – UMR 5572 – 14, Av. E. Belin – 31400 Toulouse, France
- Richard, O., Dziembowski, W. A., Sienkiewicz, R., & Goode, P. R. 1998, *A&A*, 338, 756
- Richard, O., Michaud, G., & Richer, J. 2001, *ApJ*, 558, 377
- Richard, O., Michaud, G., & Richer, J. 2002a, *ApJ*, 580, 1100
- Richard, O., Michaud, G., & Richer, J. 2005, *The Astrophysical Journal*, 619, 538
- Richard, O., Michaud, G., Richer, J., et al. 2002b, *ApJ*, 568, 979
- Richard, O., Vauclair, S., Charbonnel, C., & Dziembowski, W. A. 1996, *A&A*, 312, 1000
- Richer, J., Michaud, G., Rogers, F., et al. 1998, *ApJ*, 492, 833
- Richer, J., Michaud, G., & Turcotte, S. 2000, *The Astrophysical Journal*, 529, 338
- Rieutord, M. 2006, *A&A*, 451, 1025
- Rogers, F. J. & Nayfonov, A. 2002, *ApJ*, 576, 1064
- Rogers, F. J., Swenson, F. J., & Iglesias, C. A. 1996, *ApJ*, 456, 902
- Saar, S. H. 2009, in *Astronomical Society of the Pacific Conference Series*, Vol. 416, *Solar-Stellar Dynamos as Revealed by Helio- and Asteroseismology: GONG 2008/SOHO 21*, ed. M. Dikpati, T. Arentoft, I. González Hernández, C. Lindsey, & F. Hill, 375
- Salaris, M., Cassisi, S., Schiavon, R. P., & Pietrinferni, A. 2018, *A&A*, 612, A68
- Salaris, M., Groenewegen, M. A. T., & Weiss, A. 2000, *A&A*, 355, 299
- Salmon, S., Montalbán, J., Morel, T., et al. 2012, *MNRAS*, 422, 3460
- Santos, N. C., García López, R. J., Israelian, G., et al. 2002, *A&A*, 386, 1028
- Santos, N. C., Israelian, G., García López, R. J., et al. 2004a, *A&A*, 427, 1085
- Santos, N. C., Israelian, G., Randich, S., García López, R. J., & Rebolo, R. 2004b, *A&A*, 425, 1013
- Saumon, D., Chabrier, G., & van Horn, H. M. 1995, *ApJS*, 99, 713
- Schatzman, E. 1962, *Annales d’Astrophysique*, 25, 18

- Schatzman, E. 1993, *A&A*, 279, 431
- Scherrer, P. H., Bogart, R. S., Bush, R. I., et al. 1995, *Sol. Phys.*, 162, 129
- Schlattl, H. 2002, *A&A*, 395, 85
- Schlattl, H. & Weiss, A. 1999, *A&A*, 347, 272
- Schlesinger, F. 1910, *Publications of the Allegheny Observatory of the University of Pittsburgh*, 1, 123
- Schlesinger, F. 1916, *Publications of the Allegheny Observatory of the University of Pittsburgh*, 3, 23
- Schunker, H., Schou, J., Gaulme, P., & Gizon, L. 2018, *Sol. Phys.*, 293, 95
- Schwarzschild, M., Howard, R., & Härm, R. 1957, *ApJ*, 125, 233
- Scuflaire, R., Théado, S., Montalbán, J., et al. 2008, *Ap&SS*, 316, 83
- Seaton, M. J. 2005, *MNRAS*, 362, L1
- Semenova, E., Bergemann, M., Deal, M., et al. 2020, *A&A*, 643, A164
- Serenelli, A. 2016, *European Physical Journal A*, 52, 78
- Serenelli, A. M., Basu, S., Ferguson, J. W., & Asplund, M. 2009, *ApJL*, 705, L123
- Sestito, P. & Randich, S. 2005, *A&A*, 442, 615
- Siess, L., Dufour, E., & Forestini, M. 2000, *A&A*, 358, 593
- Skumanich, A. 1972, *ApJ*, 171, 565
- Smiljanic, R., Randich, S., & Pasquini, L. 2011, *A&A*, 535, A75
- Soderblom, D. R. 2009, *Proceedings of the International Astronomical Union*, 5, 359â360
- Soderblom, D. R., Fedele, S. B., Jones, B. F., Stauffer, J. R., & Prosser, C. F. 1993, *AJ*, 106, 1080
- Somers, G. & Pinsonneault, M. H. 2014, *ApJ*, 790, 72
- Somers, G. & Pinsonneault, M. H. 2015, *MNRAS*, 449, 4131
- Somers, G. & Pinsonneault, M. H. 2016, *ApJ*, 829, 32
- Spada, F., Gellert, M., Arlt, R., & Deheuvels, S. 2016, *A&A*, 589, A23
- Spada, F. & Lanzafame, A. C. 2020, *A&A*, 636, A76
- Spiegel, E. A. & Zahn, J. P. 1992, *A&A*, 265, 106
- Spite, F. & Spite, M. 1982a, *Astronomy and Astrophysics*, 115, 357
- Spite, M. & Spite, F. 1982b, *Nature*, 297, 483
- Spite, M. & Spite, F. 2009, *Proceedings of the International Astronomical Union*, 5, 201â210
- Spruit, H. C. 2002, *A&A*, 381, 923
- Stauffer, J. B. & Hartmann, L. W. 1986, *PASP*, 98, 1233

- Steinhauer, A. 2003, PhD thesis, Indiana University
- Steinhauer, A. & Deliyannis, C. P. 2004, *ApJL*, 614, L65
- Takeda, Y., Honda, S., Kawanomoto, S., Ando, H., & Sakurai, T. 2010, *A&A*, 515, A93
- Talon, S. & Charbonnel, C. 2005, *A&A*, 440, 981
- Talon, S. & Charbonnel, C. 2008, *A&A*, 482, 597
- Talon, S. & Charbonnel, C. 2009, *Proceedings of the International Astronomical Union*, 5, 365–374
- Talon, S. & Charbonnel, C. 2010, in *IAU Symposium*, Vol. 268, *Light Elements in the Universe*, ed. C. Charbonnel, M. Tosi, F. Primas, & C. Chiappini, 365–374
- Talon, S., Richard, O., & Michaud, G. 2006, *ApJ*, 645, 634
- Talon, S. & Zahn, J. P. 1997, *Astronomy and Astrophysics*, 317, 749
- Tassoul, J.-L. 1978, *Theory of rotating stars*
- Tayler, R. J. 1973, *MNRAS*, 161, 365
- Thompson, M. J., Christensen-Dalsgaard, J., Miesch, M. S., & Toomre, J. 2003, *ARA&A*, 41, 599
- Thoul, A. A., Bahcall, J. N., & Loeb, A. 1994, *ApJ*, 421, 828
- Timmes, F. X. & Swesty, F. D. 2000, *ApJS*, 126, 501
- Trimble, V. & Leonard, P. J. T. 1994, *PASP*, 106, 1
- Turcotte, S., Richer, J., & Michaud, G. 1998a, *ApJ*, 504, 559
- Turcotte, S., Richer, J., Michaud, G., & Christensen-Dalsgaard, J. 2000, *A&A*, 360, 603
- Turcotte, S., Richer, J., Michaud, G., Iglesias, C. A., & Rogers, F. J. 1998b, *ApJ*, 504, 539
- Valcarce, A. A. R., Catelan, M., & De Medeiros, J. R. 2013, *A&A*, 553, A62
- VandenBerg, D. A., Edvardsson, B., Eriksson, K., & Gustafsson, B. 2008, *ApJ*, 675, 746
- VandenBerg, D. A., Richard, O., Michaud, G., & Richer, J. 2002, *The Astrophysical Journal*, 571, 487
- van't-Veer-Menneret, C., Burkhardt, C., & Coupry, M. F. 1988, *A&A*, 203, 123
- Vauclair, S. 1988, *ApJ*, 335, 971
- Vauclair, S. 2013, in *EAS Publications Series*, Vol. 63, *EAS Publications Series*, ed. G. Alecian, Y. Lebreton, O. Richard, & G. Vauclair, 233–241
- Vauclair, S. & Vauclair, G. 1982, *ARA&A*, 20, 37
- Vauclair, S., Vauclair, G., Schatzman, E., & Michaud, G. 1978, *ApJ*, 223, 567
- Verma, K., Raodeo, K., Antia, H. M., et al. 2017, *ApJ*, 837, 47
- Verma, K., Raodeo, K., Basu, S., et al. 2019, *MNRAS*, 483, 4678
- Verma, K. & Silva Aguirre, V. 2019, *MNRAS*, 489, 1850

- Vinyoles, N., Serenelli, A. M., Villante, F. L., et al. 2017, *ApJ*, 835, 202
- Vogt, S. S., Allen, S. L., Bigelow, B. C., et al. 1994, in *Society of Photo-Optical Instrumentation Engineers (SPIE) Conference Series*, Vol. 2198, *Instrumentation in Astronomy VIII*, ed. D. L. Crawford & E. R. Craine, 362
- Waite, I. A., Marsden, S. C., Carter, B. D., et al. 2017, *MNRAS*, 465, 2076
- Wallerstein, G. & Conti, P. S. 1969, *ARA&A*, 7, 99
- Wallerstein, G., Herbig, G. H., & Conti, P. S. 1965a, *ApJ*, 141, 610
- Wallerstein, G., Herbig, G. H., & Conti, P. S. 1965b, *ApJ*, 141, 610
- Wang, E. X., Nordlander, T., Asplund, M., et al. 2021, *MNRAS*, 500, 2159
- Weber, E. J. & Davis, Leverett, J. 1967, *ApJ*, 148, 217
- Wildt, R. 1937, *MNRAS*, 97, 225
- Wright, N. J., Drake, J. J., Mamajek, E. E., & Henry, G. W. 2011, *ApJ*, 743, 48
- Xing, L. F. & Xing, Q. F. 2012, *A&A*, 537, A91
- Xu, Y., Goriely, S., Jorissen, A., Chen, G. L., & Arnould, M. 2013a, *A&A*, 549, A106
- Xu, Y., Takahashi, K., Goriely, S., et al. 2013b, *Nucl. Phys. A*, 918, 61
- Young, P. R. 2018, *ApJ*, 855, 15
- Zahn, J. P. 1991, *A&A*, 252, 179
- Zahn, J. P. 1992, *Astronomy and Astrophysics*, 265, 115
- Zhang, Q.-S., Li, Y., & Christensen-Dalsgaard, J. 2019, *ApJ*, 881, 103
- Ziegler, U. & Rüdiger, G. 2003, *A&A*, 401, 433